MICROMAT 2026

XII CONGRESSO BRASILEIRO DE MICROSCOPIA DE MATERIAIS

LIVRO DE RESUMOS

Órgão de Fomento:

FAPESP
FUNDAÇÃO DE AMPARO À PESQUISA DO ESTADO DE SÃO PAULO

Realização:

SBMM
Sociedade Brasileira de Microscopia e Microanálise

LCE

MICROMAT 2026

XII CONGRESSO BRASILEIRO DE MICROSCOPIA DE MATERIAIS

COMITÊ ORGANIZADOR MICROMAT 2026

Prof. Dr. Conrado Ramos Moreira Afonso (Chair) – UFSCar/CCET/DEMa, São Carlos/SP
Prof. Dr. Walter José Botta Filho – UFSCar/CCET/DEMa/LCE, São Carlos/SP
Profa. Dra. Marcia Attias - UFRJ, Rio de Janeiro/RJ
Profa. Dra. Suzana Bottega Peripolli - UERJ, Rio de Janeiro/RJ
Prof. Dr. Lucas Henrique Staffa - UFSCar/CCET/DEMa/LCE, São Carlos/SP
Profa. Dra. Paula Mendes Jardim - UFRJ, Rio de Janeiro/RJ
Dra. Tatiane Oliveira dos Santos - UFG, Goiânia/GO
Profa. Dra. Danielle Cristina Magalhães – UFSCar/CCET/DEMa, São Carlos/SP
Profa. Dra. Beatriz Canabarro - CBPF, Rio de Janeiro/RJ
Prof. Dr. José Eduardo Spinelli - UFSCar/CCET/DEMa, São Carlos/SP
Profa. Dra. Lia Medeiros - Fiocruz, Curitiba/PR
Profa. Dra. Érica Duarte - UFMG, Belo Horizonte/MG

COMITÊ ORGANIZADOR LOCAL MICROMAT 2026

Equipe do LCE/UFSCar

Walter José Botta
Guilherme Zepon
Francisco Gil Coury
Lucas Henrique Staffa
Lucas Barcellos Otani
Diego Davi Coimbrão
Rejeane C. de Luca

COMITÊ CIENTÍFICO MICROMAT 2026

Docentes DEMa

Alberto Moreira Jorge Jr.
Alessandra de Almeida Lucas
Ana Candida Martins Rodrigues
Ana Paula da Luz
André Luiz Vidilli
Andrea Madeira Kliauga
Carlos Alberto Della Rovere
Carlos Henrique Scuracchio
Conrado Ramos Moreira Afonso
Daniel Rodrigo Leiva
Danielle Cristina Camilo Magalhães
Edgar A. Sanches
Edgar Dutra Zanotto
Eduardo Henrique Backes
Eric Marchezini Mazzer
Francys Kley Vieira Moreira
Guilherme dos Santos Vacchi
Guilherme Yuuki Koga
Heloísa Bremm Madalosso
José Alexandrino de Sousa
José Eduardo Spinelli
Juliana Mara Pinto de Almeida
Juliano Marini
Leonardo Bresciani Canto
Lorena Raphael Rodrigues
Marcello Rubens Barsi Andreeta
Marcelo Strozi Cilla
Márcio Raymundo Morelli
Marco Aurélio Liutheviciene Cordeiro
Murilo Camuri Crovace
Piter Gargarella
Rodolfo Foster Klein Gunnewiek
Rodrigo Bresciani Canto
Silvia Helena Prado Bettini
Victor Carlos Pandolfelli

Docentes/Pesquisadores Externos

Diego Rafael Nespeque Corrêa (UNESP/Bauru)
Marcelo Falcão de Oliveira (EESC/USP)
Eduardo Bellini Ferreira (EESC/USP)
Haroldo Cavalcanti Pinto (EESC/USP)
Rafael Salomão (EESC/USP)
Cauê Ribeiro de Oliveira (Embrapa instrumentação)

ORGANIZAÇÃO

AGeventos Assessoria

Editoração

Isabel Kubaski - isabelkubaski@gmail.com

Criação de capa

Rogério Wainer - rogeriowainer@hotmail.com

XII CONGRESSO BRASILEIRO DE MICROSCOPIA DE MATERIAIS (MICROMAT 2026)

O XII Micromat (XII Congresso Brasileiro de Microscopia de Materiais 2026) é um evento científico tradicional, de caráter bienal, realizado com o apoio da Sociedade Brasileira de Microscopia e Microanálise (SBMM), entidade de referência nacional na promoção e consolidação das técnicas de microscopia e microanálise no Brasil. O evento reúne pesquisadores, docentes, estudantes e profissionais interessados no uso de técnicas avançadas de microscopia aplicadas à Ciência e Engenharia de Materiais e outras áreas afins como ciências físicas, química e ciência biológicas entre outras), tendo como objetivo promover um ambiente altamente qualificado para a troca de conhecimentos e o fortalecimento da comunidade científica.

PROGRAMAÇÃO

22/07/2026 (Wednesday)	
	22/07/2026 (Wednesday)
8h00 - 8h30	Mesa de Abertura: Anfiteatro Bento Prado (UFSCar)
Chair Session	Maureen Lagos
8h30 - 9h15	Openning Plenary Talk 1: Daniel Mario Ugarte, Dept. Física Aplicada-Instituto de Física "Gleb Wataghin", Unicamp, Brazil (IFGW UNICAMP): *"Advances in Electron Diffraction Methods for Nanoparticle Characterization"*
9h15 - 9h35	Invited Talk 1: Francisco Gil Coury, Departamento de Engenharia de Materiais, Universidade Federal de São Carlos (LCE/DEMa/UFSCar). *"In-situ transmission electron microscopy with heating and cooling at UFSCar"*
9h35 - 9h55	Invited Talk 2: Caio Gomide Otoni, Department of Chemistry / State University of Campinas (UNICAMP), Campinas, Brazil. *"Nanoscale force microscopy for probing interfacial interactions in multicomponent polymer systems"*
9h55 - 10h25	Advancements in TEM Technology for Challenging Material Problems Tim Eldred - JEOL USA (30min)
9h55 - 10h25	Advancements in TEM Technology for Challenging Material Problems Tim Eldred - JEOL USA (30min)
10h25 - 10h50	Coffee-break (Biblioteca Comunitária da UFSCar - BCo)
Chair Session	Cleiton Silva
10h50 - 11h10	Invited Talk 3: Augusta Cerceau Isaac Neta, Departamento de Engenharia Metal rgica e de Materiais da Universidade Federal de Minas Gerais (DEMet/ UFMG). *"3D X-ray microscopy applied to in situ investigation of degradation mechanisms in structural materials for energy"*
11h10 - 11h30	Invited Talk 4: Thiago Augusto de Lima Burgo Thiago Augusto de Lima Burgo, Department of Chemistry and Environmental Sciences, São Paulo State University (UNESP), São José do Rio Preto, Brazil. *"AFM as a Bridge Between the Nano- and Macroscale: Forces, Charges, and Interfaces"*
11h30 - 11h45	Oral 1 (4DNT): Bernardo Pompermayer Eduardo, Universidade Feral do Rio de Janeiro (UFRJ), Rio de Janeiro - Brazil. *"Investigation of the microstructure evolution during thermomechanical processing of a Zr-0.6Nb-0.4Mn alloy"*
11h45 - 12h00	Oral 2 (4DM4): Diego Rafael Nespeque Correa, Universidade Estadual Paulista (UNESP - Campus Bauru), Bauru - Brazil. *"In situ forming reactions of multicomponent titanium matrix composites produced by arc melting targeted as biomaterials"*
12h00 - 12h15	Oral 3 (4DNE): Andrea Madeira Kliauga, Departamento de Engenharia de Materiais, Universidade Federal de São Carlos (DEMa/UFSCar), São Carlos - Brazil. *"Grain refinement of a 316 LV austenitic stainless steel by severe plastic deformation: HPT, ECAP and deep burnishing"*
12h35 - 14h00	Almoço/Lunch
Chair Session	Francisco Coury
14h00 - 14h45	Plenary Talk 2: Edson Roberto Leite, Scientific Director of LNNano-CNPEM, Campinas, Brazil and Professor of Chemistry, Universidade Federal de São Carlos, São Carlos, SP, Brazil. *"Characterization of the Role of Small Polarons in the Photoelectrochemical Properties of Hematite"*
14h45 - 15h05	Invited Talk 5: Michael J. Kaufman, Director of Materials and Energy Initiatives at the Colorado School of Mines (CSM). "Dramatic Effects of Small Silver Additions on the Microstructure of Cantor Alloy Thin Films"
15h05 - 15h20	Palestra DP UNION "Da mineralogia à perícia: o MEV de bancada como plataforma de automação" - M. Sc. Sady Lobo Almeida

22/07/2026 (Wednesday) - continuação	
15h20 - 15h35	Palestra DECTRIS "Practical Aspects of Fast 4D-STEM: An Overview of Experiment Design and Data Processing" - Daniel Stroppa
15h35 - 15h50	Oral 4 (4DMM): Julio Sapadotto, Departamento de Engenharia de Materiais, Universidade Federal de São Carlos (DEMa/UFSCar), São Carlos - Brazil. "*Phase Identification in Multiphase Discontinuous Precipitation Colonies in a Cr-Fe-Ni-N Alloy using EBSD Pattern-Matching Indexing*"
15h50 - 16h15	Coffee-break
Chair Session	Luiz Tzei
16h15 - 16h35	Invited Talk 6: Maureen Lagos, Canadian Centre for Electron Microscopy (CCEM), Associate Professor in Materials Science and Engineering (MSE) Department at McMaster University. *"Probing interfacial phonons using atom-wide electron beams"*
16h35 - 16h50	Oral 5 (4DQA): Carlos Roberto Grandini, Universidade Estadual Paulista (UNESP - Campus Bauru), Bauru - Brazil. *"Microstructural Analysis of Novel Metastable β-type Titanium Alloys Aiming at Biomedical Applications"*
16h50 - 17h05	Oral 6 (4DPF): João Gabriel da Cruz Passos, Departamento de Engenharia de Materiais, Universidade Federal de São Carlos (DEMa/UFSCar), São Carlos - Brazil. *"High-temperature oxidation behavior of multicomponent refractory alloys Al15Nb30Ti25V5Mo25 and Al15Nb30Ti25V5Zr25"*.
17h05 - 17h20	Oral 7 (4DPH): Diogo Pedrino Braga, Departamento de Engenharia de Materiais, Universidade Federal de São Carlos (DEMa/UFSCar), São Carlos - Brazil. *"Intergranular Corrosion Susceptibility and Microstructural Evolution of 17Cr Supermartensitic Stainless Steel as a Function of Tempering Conditions"*
17h20 - 18h20	Sessão de Pôsteres/Poster Session

23/07/2026 (Thursday)	
	23/07/2026 (Thursday)
8h00 - 8h30	Anfiteatro Bento Prado (UFSCar)
Chair Session	Paula Jardim
8h30 - 9h15	Plenary Talk 3: Raul Arenal, Universidad de Zaragoza-CSIC, ARAID Researcher, Instituto de Nanociencia y Materiales de Aragon (INMA), Spain. *"Nanoscopic Insights into Low-Dimensional Materials: Recent Progress"*
9h15 - 9h35	Invited Talk 7: Andrea Porto-Carrero, Fédération Sciences Chimiques CP2M, Research Engineer - Aix-Marseille University (AMU), France. Materials Science & Advanced Characterization - CP2M Electron Microscopy Center *"Nanoscale Materials Characterization by High-Resolution SEM with TEM-Comparable Performance"*
9h35 - 9h55	Invited Talk 8: Cleiton Carvalho Silva, Laboratório de Pesquisa e Tecnologia em Soldagem (LPTS), Departamento de Engenharia Metalúrgica e de Materiais (DEMM) da Universidade Federal de Ceará (UFC), Fortaleza, Brazil. *"Advanced micro and nanostructural characterization techniques for the study of Ni-based alloys"*
9h55 - 10h25	Microscopia Tridimensional de Raios-X e suas Aplicações Dr. Ricardo Gonçalves Mendes (INSTRUTECNICA - 15 min)
9h55 - 10h25	Alemnis: Especialistas em Nanoindentação Marcos Padovam (ALTMANN - 15 min)
10h25 - 10h50	Coffee-break (Biblioteca Comunitária da UFSCar - BCo)
Chair Session	Andrea Porto
10h50 - 11h10	Invited Talk 9: Edgar Dutra Zanotto, Vitreous Materials Laboratory (LaMaV), Departamento de Engenharia de Materiais, Universidade Federal de São Carlos (DEMa/UFSCar), São Carlos - Brazil. *"Experimental, theoretical, MD and ML assessment of glass forming ability"*

23/07/2026 (Thursday) - continuação	
11h10 - 11h30	Invited Talk 10: Caue Ribeiro de Oliveira, Senior Researcher, Embrapa Instrumentacao / Brazilian Agricultural Research Corporation, São Carlos – Brazil. *"Structure, Phases, and Interfaces in Copper Oxide Ceramics for Photo- and Electrocatalytic CO2 Conversion"*
11h30 - 11h45	Oral 8 (4DNW): Marcos Farina, Universidade Feral do Rio de Janeiro (UFRJ), Rio de Janeiro – Brazil. *"Enamel prisms organization in rodent incisor teeth: comparison between small and large animals"*
11h45 - 12h00	Oral 9 (4DPD): Danilo Biazon Janes. Centro Nacional de Pesquisa em Energia e Materiais (CNPEM), Campinas, – Brazil. *"Mapping Local Thermal and Electrical Conductivity in Electronic Ceramics: A Correlative Study via AFM"*
12h00 - 12h15	Oral 10 (4DND): Adriane Hoeldtke, Engenharia e Ciência dos Materiais, Centro Politécnico, Universidade Federal do Paraná (UFPR), Curitiba – Brazil. *"Correlating microscopy, composition, and sensing behavior in Ce-doped anatase TiO_2 nanomaterials"*
12h35 - 14h00	Almoço/Lunch
Chair Session	Walter José Botta: Evento 50 anos do LCE – Laboratório de Caracterização Estrutural (*50 Years of LCE – Structural Characterization Laboratory*) Anfiteatro Bento Prado (UFSCar)
14h00 - 14h20	Walter José Botta: *"The Early Years of the LCE: History, Establishment, Milestones, and Key Contributors"* (O início do LCE: histórico, consolidação, marcos e pessoas). Homenagem ao Prof Hans-Jurgen Kestenbach (LCE/DEMa/UFSCar).
14h20 - 14h40	Guilherme Zepon: *"The Current LCE Team (including the Steering Committee and User Committee) The New Equipment Booking System, Key Features Improvements for Users, Facility Access and Usage Workflow, LCE Impact Number of Users, Publications, and Other Performance Metrics"* Equipe atual do LCE (incluindo comitê gestor e comitê de usuários) Novo sistema de agendamento, Funcionalidades, Melhorias para os usuários Fluxo de utilização, Impacto do LCE, Número de usuários, publicações, etc..
14h40 - 15h00	Francisco Gil Coury: *"The Microscopy School: Metrics, Reach, and Annual Activities Introduction to the New TEM Instruments at LCE/DEMa: Instrumentation, Analytical Capabilities, New Holders, and Applications"* New XRD Systems at LCE/DEMa: Key differences compared with the previous XRD instruments New sample chambers and accessories available Expanded analytical capabilities and new application opportunities.
15h00-15h15	Lucas Otani: *"Introduction to the New TEM-FIB Facilities at LCE/DEMa: Instrumentation, Analytical Capabilities, and Applications"*. Introdução aos novos equipamentos MET-FIB LCE/DEMa: Instrumentação, análises, e potencialidades
15h15 - 15h30	Lucas Staffa: *"Introduction to the New Spectroscopic Techniques at LCE/DEMa (XPS and Raman) and Correlative Microscopy Techniques„* Introdução às novas técnicas espectrométricas do LCE/DEMa (XPS, Raman), microscopia confocal e ultramicrotomia.
15h30 - 15h45	Guilherme Zepon: "Introduction to the new XRD systems at LCE/DEMa: Key differences compared to previous equipment; new chambers and accessories available; new analytical possibilities and applications." Introdução aos novos sistemas DRX do LCE/DEMa: Principais diferenças em relação aos equipamentos anteriores; Novas câmaras e acessórios disponíveis; Novas possibilidades analíticas e aplicações
15h45 - 16h15	Coffee-break
Chair Session	Danielle Cristina Camilo Magalhães - Coordinator Mesa Redonda "Mulheres na Microscopia, Ciência e Tecnologia" *Roundtable Discussion: "Women in Microscopy, Science, and Technology"* Anfiteatro Bento Prado (UFSCar)

23/07/2026 (Thursday) - continuação	
16h15 - 17h20	The panel will be moderated by: Danielle Cristina Camilo Magalhães (DEMa/Projeto ATENA/UFSCar) Marcia Attias (UFRJ/SBMM) – Atual Presidente da SBMM Yvonne Mascarenhas (IFSC/USP) Giovanna Machado (CETENE/Futuras Cientistas) Beatriz Canabarro (CBPF/SBMM) - Secretaria da SBMM Iara Souza (UFSCar).
17h20 - 18h20	Sessão de Pôsteres/Poster Session
19h30 - 23h00	Jantar de confraternização – "Conference Dinner" Restaurante Cozinha do Lobo - ADUFSCar

23/07/2026 (Thursday) - Auditório CCET/UFSCar	
	23/07/2026 (Thursday)
8h00 - 8h30	Auditório do CCET/UFSCar
Chair Session	Lucas Staffa
9h15 - 9h35	Plenária 3: Raul Arenal (Anfiteatro Bento Prado (UFSCar) Invited Talk 1: Laura Ximena Lovisa Oliveira, Universidade Federal de Santa Catarina, UFSC - Campus Blumenau – Brazil. *"The Role of Multiscale Microscopy in the Development and Evaluation of Functional Surfaces"*
9h35 - 9h55	Invited Talk 12: Paulo F. P. Fichtner. Departamento de Metalurgia, Escola de Engenharia, Programa de Pós-Graduação em Física, Instituto de Física, Centro de Microscopia e Microanálise Brasil-Sul, Universidade Federal do Rio Grande do Sul (UFRGS), Porto Alegre, Brazil. *"Electron Beams as a Dynamic Tool to Investigate the Thermodynamic Behavior of Small Systems"*
9h55 - 10h15	Invited Talk 13: Leonardo Sales Ara . Metallurgical and Materials Department, Universidade Feral do Rio de Janeiro (UFRJ), COPPE/UFRJ, Rio de Janeiro, Brazil. *"Influence of Y on the microstructure and mechanical properties of the nickel based alloy 718"*
10h15 - 10h30	Oral 11 (4DMZ): Augusto Graceto, Departamento de Engenharia Mecânica (DEMec), Universidade Federal de São Carlos (UFSCar), São Carlos – Brazil. *"Optical Microscopy of Surface Marks Induced by Chatter during Steel Turning"*
10h30 - 11h00	Coffee-break (Biblioteca Comunitária da UFSCar - BCo)
	Anfiteatro Bento Prado (UFSCar)
12h35 - 14h00	Almoço/Lunch

24/07/2026 (Friday)	
	24/07/2026 (Friday)
	Anfiteatro Bento Prado (UFSCar)
Chair Session	Suzana Peripolli
8h30 - 9h15	Plenary Talk 4: Giovanna Machado. Diretora do Centro de Tecnologia Estratégica do Nordeste, Microscopia Eletrônica e Nanotecnologia. (CETENE/MCTIC). *"Nanostructured Materials for Sustainable Green Hydrogen Production".*
9h15 - 9h35	Invited Talk 15: Luiz Henrique Galvao Tizei, Product Manager - Bruker AXS Research Director (DR2) of the CNRS, Université Paris-Saclay. Paris, France. *"Light and Electrons: New Frontiers in Nanoscale Material Characterization"*
9h35 - 9h55	Invited Talk 16: Carlos Alberto Ospina Ramirez. Laboratório Nacional de Nanotecnologia (LNNano), Centro Nacional de Pesquisa em Energia e Materiais (CNPEM), Campinas, Brazil. *"TEM as a Knowledge Infrastructure for Materials: Trends, Multimodal Convergence, and Impacts on Society"*
9h55 - 10h30	Mesa Redonda SBMM e Associados e Encerramento (SBMM and Partner Organizations Roundtable & Closing Ceremony)
10h30 - 11h30	Coffee-break + Exposição das imagens do Concurso da SBMM - MicroMat (Biblioteca Comunitária da UFSCar - BCo)
11h30 - 14h00	Almoço/Lunch

PALESTRANTES CONVIDADOS

Profa. Dra. Andrea Porto Carreiro Campos

Research Engineer – Aix-Marseille University (AMU), France. Materials Science & Advanced Characterization – CP2M Electron Microscopy Center, Fédération Sciences Chimiques Marseille

"Nanoscale Materials Characterization by High-Resolution SEM with TEM-Comparable Performance"

Abstract: Scanning Electron Microscopy (SEM) is a powerful and versatile tool in materials science, capable of providing high-resolution structural and chemical information across a wide range of materials systems. The maximum resolution of a scanning electron microscope depends on several factors, including the size of the incident electron beam and the interaction volume within the sample. Advances in electron optics now enable sub-nanometric resolution even at low accelerating voltages, significantly expanding the analytical capabilities of SEM. Modern low-kV field-emission instruments can, in specific cases, deliver compositional and structural information comparable to that obtained by TEM, while preserving the advantages of simpler sample preparation and greater experimental flexibility. This presentation will focus on the optimization of SEM for high-resolution and multi-analytical performance, including low-voltage secondary and backscattered electron imaging, variable pressure imaging, Energy-Dispersive X-ray Spectroscopy (EDS), Wavelength-Dispersive X-ray Spectroscopy (WDS), Electron Backscatter Diffraction (EBSD), and Transmission Kikuchi Diffraction (TKD). Particular attention will be given to acquisition parameters, signal-to-noise optimization, detector geometry, and beam conditions required to achieve high spatial resolution and reliable analytical data on challenging materials systems. A correlative microscopy approach will be emphasized, integrating SEM-based analyses with TEM, Raman spectroscopy, X-ray diffraction (XRD), Atomic Force Microscopy (AFM) and Atom Probe Tomography (APT) to link morphology, crystallography, chemistry, and surface properties across multiple length scales. Applications include semiconductor and functional thin films, nanostructured and energy-related materials. The talk highlights SEM as a high-resolution, multi-modal platform capable of bridging surface-sensitive imaging, diffraction, and microanalysis for advanced materials research.

Profa. Dra. Augusta Cerceau Isaac Neta

Departamento de Engenharia Metalúrgica e de Materiais da Universidade Federal de Minas Gerais (DEMet/UFMG)

"3D X-ray microscopy applied to in situ investigation of degradation mechanisms in structural materials for energy"

Abstract: Oil and gas exploration in ultra-deep waters poses severe engineering challenges, requiring materials with high mechanical and chemical resistance for application in subsea structures, such as flexible pipelines and transport lines. In this context, understanding the degradation mechanisms that govern the performance of these materials under service conditions is essential to ensure operational reliability and safety. 3D X-ray microscopy (3D-XMR) constitutes an advanced and high-potential approach for investigating these mechanisms. Although frequently associated with tomography, the term "3D microscopy" more accurately describes its ability to reveal, in a non-destructive manner and with high spatial resolution (reaching 500 nm), the morphology and distribution of damage or phases within the material. When integrated with mechanical tests, 3D-XMR allows in situ monitoring of the nucleation, growth, and coalescence of voids, cracks, and other defects, providing a direct view of the interaction between microstructure, environment, and mechanical loading. This presentation showcases studies conducted on carbon fiber reinforced polymer composites, focusing on high-resolution 3D morphological characterization, aiming to evaluate the damage associated with aging in a chemical environment that simulates offshore conditions and during mechanical tests. Additionally, results obtained in high-strength low-alloy (HSLA) steels of the API class, widely used in pipelines for transporting oil and gas containing aggressive species such as H_2S, are discussed. The susceptibility to hydrogen embrittlement in API 5L X65 steel and API 5L X70 steel was evaluated, considering the influence of the microstructure along the thickness of thick plates. The results contribute to a deeper understanding of degradation mechanisms in structural materials and support the development of more robust solutions, aligned with the demands of the oil and gas industry and the challenges of the energy transition.

Prof. Dr. Caio Gomide Otoni

Department of Chemistry / State University of Campinas (UNICAMP), Campinas, Brazil

"Nanoscale force microscopy for probing interfacial interactions in multicomponent polymer systems"

Abstract: Understanding how materials interact at interfaces is essential for designing advanced functional systems, yet many interfacial phenomena occur at length scales that are difficult to access using conventional characterization techniques. In this talk, I will discuss how atomic force microscopy (AFM), particularly using the colloidal-probe approach, can be employed to quantify interfacial interactions between soft polymeric materials with high spatial and force resolution. In this method, a micrometer-sized particle is attached to the AFM cantilever, enabling controlled measurements of adhesion forces between model surfaces. By recording force/distance curves, it becomes possible to determine pull-off forces, adhesion energies, and time-dependent interactions between materials. These measurements provide direct insight into the mechanisms governing interfacial compatibility, including electrostatic interactions, hydrogen bonding, and molecular rearrangements during contact. The technique also enables systematic investigation of how surface chemistry, composition, and the presence of compatibilizing molecules influence nanoscale adhesion. Overall, colloidal-probe AFM provides a powerful and quantitative platform to probe interfacial phenomena in soft polymer systems and to guide the rational design of interfaces in multicomponent materials.

Prof. Dr. Carlos Alberto Ospina Ramirez

Laboratório Nacional de Nanotecnologia (LNNano), Centro Nacional de Pesquisa em Energia e Materiais (CNPEM), Campinas, SP, Brazil

"TEM as a Knowledge Infrastructure for Materials: Trends, Multimodal Convergence, and Impacts on Society"

Abstract: Transmission Electron Microscopy (TEM/TEM) has become one of the main "knowledge infrastructures" of materials science: it not only reveals structure at the atomic scale, but also connects microstructure, composition, defects, and properties in an increasingly quantitative way. The historical evolution of TEM is inseparable from public policies and long-term investments in large equipment and multi-user networks, which have consolidated technical communities and accelerated innovation — an environment in which MicroMat stands out for promoting an immersion in microscopy and microanalysis applied to materials science, including TEM and related techniques. In this plenary session, I discuss three movements that define current trends. First, the shift from "seeing" to measuring, with quantitative methodologies and greater reproducibility. Second, the rise of 4D-STEM, which expands the ability to map internal fields, stresses, and local symmetry, robustly connecting nano-meso scales. Third, the maturity of in situ/operando experiments, allowing the observation of dynamic processes during heating, reaction, field application, or other perturbations relevant to the processing and functioning of materials. These advances benefit from convergence with microanalysis and other modalities present in the scope of MicroMat (SEM/FIB, XRM, SPM, among others), reinforcing an agenda of multimodal and correlative characterization. In addition to the scientific impact, there are concrete social impacts: development of materials for energy and sustainability, improved reliability in devices and advanced manufacturing, and training of highly qualified professionals. I will present recent results obtained in the Transmission Electron Microscopy group at LNNano in advanced techniques such as 4D-STEM, in situ TEM, and phase contrast enhancement in STEM, illustrating how these approaches respond to contemporary challenges in functional materials. I conclude with a strategic vision: the future of TEM will require both advanced instrumentation and analysis, as well as access, training, and data governance policies that amplify the social return on public investment.

Prof. Dr. Cleiton Carvalho Silva

Laboratório de Pesquisa e Tecnologia em Soldagem (LPTS), Departamento de Engenharia Metalúrgica e de Materiais (DEMM) da Universidade Federal de Ceará (UFC)

"Advanced micro and nanostructural characterization techniques for the study of Ni-based alloys"

Abstract: This study aims to elucidate the multiple strengthening mechanisms provided by the heterostructure formed during the solidification and cooling of a novel, compositionally complex Ni-based filler metal alloy (Inconel 680) produced by wire arc additive manufacturing (WAAM), which underlie their remarkable mechanical properties. This material is designed to offer high strength, ductility, toughness and corrosion resistance for various applications, including 3D printing and welding of high-strength materials. Through in-depth microstructural characterization using advanced techniques, we provide detailed information about the structure and chemistry at the nanoscale. Our findings reveal that the most significant solid-solution strengthening elements segregate strongly during the solidification process. The interdendritic volume is supersaturated in Nb and Ti. The combination of thermodynamic conditions, fast cooling rate and multiple heating cycles during deposition leads to the precipitation of γ-Ni_3Nb nanoprecipitates in the interdendritic volume. This heterogeneous microstructure consists of a solid-solution γ -fcc Ni matrix single phase in the dendrite cores and a dual-phase microstructure in the interdendritic region formed by γ-fcc + 23 % of γ-Ni_3Nb phase. The resulting heterogeneous microstructure provides a high yield strength (624.5 MPa measured and 651.9 MPa calculated), outperforming traditional solid solution strengthened Ni-based alloys by approximately 200 MPa, without compromising ductility. This research provides crucial insights for advancing high-performance materials designed for additive manufacturing or welding techniques. It emphasises the importance of fostering heterogeneous microstructures that effectively mitigate the strength-ductility trade-off, thereby enhancing material properties.

Prof. Dr. Daniel Mario Ugarte

Dept. Fís. Aplicada-Instituto de Física "Gleb Wataghin" (IFGW UNICAMP), Brazil

"Advances in Electron Diffraction Methods for Nanoparticle Characterization"

Abstract: The rapidly evolving field of nanotechnology has driven significant advancements in scientific methodologies and instrumentation. Notably, electron microscopy has undergone remarkable development, with progress in areas such as electron optics, automation, reproducibility, and the performance of detectors. Crystalline nanomaterials are unique in that they occupy the intermediate space between amorphous systems, which display short-range order, and bulk crystals, characterized by long-range order. When structural characterization is carried out using diffraction physics, these nanomaterials exhibit notable peak broadening, diminished signal levels, elevated background noise, and increased thermal atom movement. This phenomenon is referred to as the "nanostructure problem," which highlights the lack of sufficient constraints, such as narrow diffraction peaks, on the numerous free variables associated with atomic positions in 3D space. The implementation of structural refinement techniques that enable quantitative comparison of experimental results with various structural models includes a great deal of complexity. To achieve meaningful, quantitative, and statistically robust physical interpretations from experimental results, it is crucial to leverage advanced instrumentation in conjunction with sophisticated physicochemical simulations, machine learning, and big data processing. These integrated approaches maximize the value of experimental data and support more rigorous analyses. Here , we will discuss several studies conducted within our group that focus on the detailed characterization of nanosystems, including nanoparticles, nanowires, and nanotubes. These examples are intended to prompt discussion regarding the necessity of rethinking experimental design, execution, and analysis strategies. The ultimate goal is to foster a shift toward quantitative interpretation of measurements derived from advanced TEM techniques.

Prof. Dr. Edgar Dutra Zanotto

Departamento de Engenharia de Materiais (DEMa), Universidade Federal de São Carlos (UFSCar)

"Experimental, theoretical, MD and ML assessment of glass forming ability"

Abstract: Any liquid can be vitrified by sufficiently rapid cooling, exceeding the critical cooling rate, Rc. However, as George Morey noted in his classical book, "devitrification is the chief factor which limits the composition range of practical glasses; it is an ever-present danger in all glass manufacturing and working." This phrase highlights the persistent challenge of identifying novel good glass-forming compositions with a tailored combination of properties. This talk examines the dichotomy between the intrinsic ability to crystallize, governed by homogeneous crystal nucleation and growth, which determines the Rc and the glass-forming ability (GFA), and the extrinsic (practical) scenario, dominated by heterogeneous nucleation induced by foreign particles and interfaces. We present a comparative analysis of good and reluctant inorganic glass formers, utilizing experimental measurements using optical and electronic microscopy, theoretical calculations, and molecular dynamics (MD) simulations to elucidate the factors controlling devitrification. We will also explore strategies to predict GFA using theoretical calculations and machine learning (ML) to expand the compositional range of practical glasses. Finally, we will dwell on the extreme GFA of albite glass, which does not crystallize even after 4 years of thermal treatment.

Prof. Dr. Edson Roberto Leite

Scientific Director – LNNano-CNPEM, Campinas,SP, Brazil and Professor of Chemistry, Universidade Federal de São Carlos, São Carlos, SP, Brazil (LNNano/CNPEM)

"Characterization of the Role of Small Polarons in the Photoelectrochemical Properties of Hematite"

Abstract: A etapa de nucleação é um processo complexo e fundamental para o controle da síntese de nanocristais de óxidos cerâmicos. Para compreender esse fenômeno em profundidade, utilizamos ferramentas avançadas de microscopia eletrônica de transmissão (TEM), incluindo e-PDF, cryo-EM e TEM in situ com controle de temperatura. A técnica de e-PDF permite a análise da ordem estrutural local em escala atômica, identificando a dinâmica de formação de núcleos e transições de fase, além de revelar como o caminho de cristalização influencia o grau de desordem e a presença de defeitos. Por outro lado, a cryo-EM é crucial para capturar estados intermediários da nucleação durante a síntese em meio líquido, congelando amostras a temperaturas extremamente baixas e preservando sua morfologia e arranjo, semelhantes ao encontrado no estado coloidal. Isso possibilita a visualização de núcleos primários durante o processo de cristalização. O TEM in situ, por sua vez, permite a observação da nucleação em tempo real sob diferentes condições térmicas, revelando como a temperatura afeta a formação de núcleos e a dinâmica de crescimento. A combinação dessas técnicas proporciona uma compreensão abrangente do processo de nucleação, relacionando características estruturais e propriedades funcionais, além de abrir caminhos para o desenvolvimento de novos materiais com aplicações inovadoras em cerâmicas avançadas.

Prof. Dr. Francisco Gil Coury

Departamento de Engenharia de Materiais (LCE/DEMa), Universidade Federal de São Carlos (UFSCar)

"In-situ transmission electron microscopy with heating and cooling at UFSCar"

Abstract: In-situ transmission electron microscopy (TEM) has become a powerful approach for investigating materials under external stimuli, enabling the direct observation of microstructural evolution in real time. In this work, we present the first results obtained using the recently implemented in-situ TEM system at the Federal University of São Carlos (UFSCar), focusing on experiments performed under controlled heating and cooling conditions. The experiments demonstrate the capability to monitor, in real time, different types of phase transformations, including temperature-induced structural changes, nucleation and growth processes, and morphology evolution during thermal cycling. Representative examples from distinct material systems are discussed, highlighting the potential of in-situ TEM to access transient and out-of-equilibrium phenomena that are not accessible through conventional ex-situ approaches.

Profa. Dra. Giovanna Machado

Diretora do Centro de Tecnologias Estratégicas do Nordeste (CETENE/MCTIC)

"Nanostructured Materials for Sustainable Green Hydrogen Production"

Abstract: This work investigates the development and application of advanced nanostructured materials for the production of green hydrogen (H_2) through photo(electro)catalytic processes, aiming to contribute to sustainable and low-carbon energy technologies. Semiconductor and metal oxide materials were synthesized and modified with morphological and structural control, seeking to optimize electronic properties, surface area, and charge separation efficiency. Detailed characterization was performed using advanced electron microscopy techniques and physicochemical analysis, allowing correlation of the nanostructure, chemical composition, and interfaces of the materials with catalytic performance in hydrogen generation. The results demonstrate that interface engineering and nanostructuring play a fundamental role in increasing the efficiency, stability, and durability of catalytic systems under operating conditions. The study highlights the potential of these materials for application in sustainable hydrogen production routes from renewable sources, contributing to scientific and technological advancement in the area of green hydrogen, with a direct impact on the energy transition and decarbonization of the energy matrix.

Profª. Dra. Laura Ximena Lovisa Oliveira

Universidade Federal de Santa Catarina no campus Blumenau (UFSC-BNU) Coordenadoria Especial de Engenharia de Materiais (UFSC)

"The Role of Multiscale Microscopy in the Development and Evaluation of Functional Surfaces"

Abstract: Energy-converting ceramic materials are undergoing significant development and are fundamentally relevant in modern society due to their wide range of applications, such as energy storage, light-emitting diodes, solar cells, photocatalysis, biomarkers, and others. Despite these materials playing an important role in emerging technologies, a better understanding of the relationship between their optical and structural properties and their performance in the aforementioned applications is being sought. To obtain these materials and considering the technical and economic feasibility of their production, alternative, less energy-intensive synthesis routes are being investigated, as well as the use of low-cost precursors to ensure the sustainability of the materials' synthesis process. These synthesis routes have satisfactorily allowed the control of the physicochemical properties of ceramic oxides through the adjustment of particle size and morphology. Given these efforts, it is possible to achieve highly organized structures on a nanometric scale, encompassing potential applications in sectors such as light conversion in optoelectronic devices, as well as the use of semiconductor oxides in environmental remediation through photocatalysis. Among these routes, particle synthesis by chemical methods has proven very efficient due to its reproducibility, as well as a high degree of control over the structural and morphological characteristics of the particles obtained. This presentation aims to correlate the synthesis steps, characterization, and study of the microstructural, photoluminescent, and photocatalytic properties of metal oxide particles doped with rare earth ions. To validate the properties of the produced materials, results from some published works will be presented. The various characterization techniques performed include: X-ray Diffraction, UV-visible Spectroscopy and Photoluminescence Spectroscopy, and in particular, Scanning Electron Microscopy with Field Emission and Energy Dispersive Spectroscopy analyses.

Dr. Luiz Henrique Galvao Tizei

Research Director (DR2) of the CNRS, France

"Light and Electrons: New Frontiers in Nanoscale Material Characterization"

Abstract: Electron spectroscopies, combined with light injection and collection, reveal novel properties of nanoscale materials. This seminar explores nanosecond-resolved spectroscopies for probing material dynamics with nanometer spatial resolution in transmission electron microscopes. Cathodoluminescence excitation spectroscopy (CLE) links electron energy loss spectroscopy (EELS) to cathodoluminescence (CL), providing an efficient measure of relative quantum efficiency [1]. Electron energy gain spectroscopy (EEGS) couples free electrons to a laser beam, achieving <1 meV spectral resolution, surpassing EELS [2]. Finally, a time-resolved pump-probe scheme between laser injection and EELS measures temperature variations in thin materials with nanometer spatial and nanosecond temporal resolution [3]. For this, different spectroscopic signatures, such as phonons, plasmons and excitons are used. Examples from diverse materials will illustrate these methods.
[1] N. Varkentina et al., Sci. Adv 8, abq4947. (2022).
[2] Y. Auad et al., Nat. Comm. 14, 4442. (2023).
[3] F. Castioni et al., Nano Lett. 25, 1601 (2025)

Dr. Maureen Joel Lagos

Research Director (DR2) of the CNRS, France

"Light and Electrons: New Frontiers in Nanoscale Material Characterization"

Abstract: The development of atom-size monochromatic electron beams in transmission electron microscopes has enabled the realization of phonon spectroscopy studies in nanomaterials with (sub)-nanometer spatial sensitivity. These spectroscopy capabilities are also permitting us to unveil physical processes driven by phonons in the realms of nanoscale heat transfer. In this talk, we will describe progress along those directions by highlighting results involving: (i) Hardening of optical phonon modes at AlN/GaN interfaces. The focus is on measuring the dispersive behavior of phonon modes in nanoscale volumes of matter. (ii) Studies of heat transfer across nanoscale gaps. We seek to determine the spectral distribution of the thermal conductance between two objects subjected at different temperatures. These results represent progress towards understanding the role of phonons in physical process such as energy transfer and nanoscale heat transport.

Prof. Dr. Michael J. Kaufman

Director of Materials and Energy Initiatives at the Colorado School of Mines (CSM)

"Dramatic Effects of Small Silver Additions on the Microstructure of Cantor Alloy Thin Films"

Abstract: This work deals with the effect of Ag doping on the microstructure of Cantor alloy thin films deposited by magnetron co-sputtering. The introduction of silver, with its higher enthalpy of mixing exceeding the thermodynamic criterion for stable solid solutions, promotes the coexistence of a crystallized silver face-centered cubic (fcc) phase alongside the Cantor phase. Using X-ray diffraction, scanning and transmission electron microscopy, and energy dispersive X-ray spectroscopy, alongside with thermodynamic modeling through the CALPHAD methodology, we provide a comprehensive analysis of the resulting tweed-like microstructure. The findings underscore the substantial impact of compositional modifications on the microstructural development of high entropy alloys for their diverse applications.

Prof. Dr. Raul Arenal

ARAID Researcher, Instituto de Nanociencia y Materiales de Aragon (INMA), Universidad de Zaragoza-CSIC, Spain

"Nanoscopic Insights into Low-Dimensional Materials: Recent Progress"

Abstract: Uncovering the structural origins of nanomaterial properties requires precise atomic-scale analysis. The combination of aberration-corrected TEM and SR-EELS offers a powerful solution, utilizing a ~1Å electron probe to directly resolve the atomic and chemical landscape of nanostructured systems. This presentation highlights recent studies on the atomic structure and optoelectronic properties of low-dimensional systems, including inorganic nanotubes, 2D nanostructures, and metallic nanoparticles. By leveraging monochromated, aberration-corrected (S)TEM and SR-EELS, we demonstrate the power of high-spatial-resolution spectroscopy. Additionally, I will showcase recent in-situ TEM-EELS experiments that enable the simultaneous characterization of physical and chemical phenomena at the nanoscale

Prof. Dr. Thiago Augusto de Lima Burgo

Department of Chemistry and Environmental Sciences, São Paulo State University (UNESP), São José do Rio Preto, Brazil

"AFM as a Bridge Between the Nano- and Macroscale: Forces, Charges, and Interfaces"

Abstract: In this presentation, Atomic Force Microscopy (AFM) will be introduced as a particularly effective bridge between the nano- and macroscales: an instrument capable of transforming local contrasts (mechanical and electrical) into an understanding of real-world material performance, stability, and functionality. The focus is on electrified interfaces and, in particular, on the nature of charge carriers that emerge under different scenarios: electronic states in dielectrics, electron transfer at contacts, and adsorbed/organized ions within interfacial water layers. This diversity of charge carriers governs friction, adhesion, dissipation, and the persistence of charge "mosaics" generated by triboelectrification and contact electrification at solid–solid and solid–liquid interfaces. Moreover, AFM will be discussed as an intrinsically interdisciplinary tool, valuable to chemists, biologists, engineers, and applied fields, as it enables the integration of morphology, mechanics, and electrical properties within a single measurement platform. Examples will be presented across functional materials and surfaces (including humidity–solid interfaces), biointerfaces (electrostatically mediated adhesion in microorganisms), and dental biomaterials (surface heterogeneity and roughness). Finally, the presentation emphasizes how local measurements can help address still-open questions in electrostatics and why this is relevant for both science and technology.

SUMÁRIO

INVITED LECTURE **19**

Advanced micro- and nanostructural characterisation methods for investigating the processing of Ni-based superalloys. 20
Cleiton C. Silva

Experimental, theoretical, MD and ML simulations of glass-forming ability 21
Edgar Dutra Zanotto

ORAL **22**

Correlating microscopy, composition, and sensing behavior in Ce-doped anatase TiO_2 nanoparticles 23
Adriane Hoeldtke, Renan Barbieri, José Pedro Mansueto Serbena, Ney Mattoso

Enamel prisms organization in rodent incisor teeth: comparison between small and large animals 24
Vilma Lima, Carlos A. Menezes, Jean Pierre dos Santos, Mair M. M. de Oliveira, Marcos Farina

Grain refinement of a 316 LV austenitic stainless steel by severe plastic deformation: HPT, ECAP and deep burnishing. 25
Andrea Madeira Kliauga, Danielle Cristina Camilo Magalhães, Diogo Pedrino Braga, Lucina Montanari

High-temperature oxidation behavior of multicomponent refractory alloys Al15Nb30Ti25V5Mo25 and Al15Nb30Ti25V5Zr25. 26
João Gabriel da Cruz Passos, Carolina Soares, Rodrigo de Oliveira França, David Jose Aviles, Diogo Pedrino Braga, Guilherme dos Santos Vacchi, Carlos Alberto Della Rovere, Artur Mariano de Sousa Malafaia, Marcelo Falcão de Oliveira

In situ forming reactions of multicomponent titanium matrix composites produced by arc melting targeted as biomaterials 27
Carlos Eduardo da Silva, Carlos Roberto Grandini, Vinícius Richieri Manso Gonçalves, Conrado Ramos Moreira Afonso, Diego Rafael Nespeque Correa

Investigation of the microstructure evolution during thermomechanical processing of a Zr-0.6Nb-0.4Mn alloy 28
Bernardo Pompermayer Eduardo, Paula Mendes Jardim, Rafaella Martins Ribeiro

Mapping Local Thermal and Electrical Conductivity in Electronic Ceramics: A Correlative Study via AFM 29
Danilo Biazon Janes, Otavio Berenguel, Bruna Sedaca Camargo de Melo, Carlos Alberto Rodrigues Costa, Tanna Elyn Rodrigues Fiuza, Fabiano Emmanuel Montoro, Jefferson Bettini, Edson Roberto Leite

Microscopia Óptica das Marcas Superficiais Induzidas por Chatter no Torneamento de Aço 30
Augusto de Souza Graceto, Elvis Soares da Silva, Sidney Bruce Shiki, Carlos Eiji Hirata Ventura, Armando Italo Sette Antonialli

Microstructural Analysis of Novel Metastable β-type Titanium Alloys Aiming at Biomedical Applications. 31
Fernanda de Freitas Quadros, Giovana Collombaro Cardoso, Pedro Akira Bazaglia Kuroda, Conrado Ramos Moreira Afonso, Diego Rafael Nespeque Correa, Carlos Roberto Grandini

Phase Identification in Multiphase Discontinuous Precipitation Colonies in a Cr-Fe-Ni-N Alloy using EBSD Pattern-Matching Indexing 32
Julio Spadotto, Francisco Coury, Tristan Manchester, Brian Connolly, Grace Burke, Guillermo Solorzano

PÔSTER 33

Analysis of long-term contact with sea water impacts into gray iron cast microstructure 34
Vinícius Felippe Elias, Leandra Marques, Lorena Maria da Silva, Eric Marchezini Mazzer, Francisco Gil Coury

Analysis of Pitanga-Like Vanadium Oxide Nanostructures Obtained by the Nanoemulsion Method 35
Lucas H. M. Paodjuenas, Fernanda T. L. Serrão, Marco A. L. Cordeiro

Analysis using microscopy techniques of oxide layers formed on the Nb-25Ta-35Ti alloy obtained by micro-arc oxidation. 36
Gabriel Cardoso Rôa, Fernanda de Freitas Quadros, Diego Rafael Nespeque Corrêa, Carlos Roberto Grandini

Biotechnological system based on hybrid hydrogel spheres for the release of Zn and plant growth-promoting bacteria 37
Débora Ribeiro Antunes, Mariana M. L. H. Forini , Heloiza F. Alves do Prado, Renato Grillo

Characterization of β TiNbZrTa Alloy Powder Produced by Ultrasonic Atomization for Additive Manufacturing 38
Renan A. F. Dias, Mariana L. Lourenço, Conrado R. M. Afonso

Characterization of Ni-superalloy MAR-M247 modified with Nb Powder Produced by Ultrasonic Atomization for Additive Manufacturing 39
Isabela Maria da Silva, Renan Dias, Mariana S. Pereira, Carlos A. Nunes, Conrado R. M. Afonso

Characterization of Secondary Precipitation in Modified HP-NbTi Stainless Steels in Aging States II and III at 700–850 °C. 40
Victor Max Barros da Silva de Lima, Taissa Zangerolami Lopes Rodrigues, Rebecca Mederos da Silveira, Fabio dos Santos Queiroz, Luiz Henrique de Almeida

Characterization of the β Ti-35Nb-6Ta alloy manufactured by 3D printing with surface modification via Micro-arc Oxidation. 41
Lucas D. Duro, Giovanna E. Santo, Renan A. F. Dias, Bruno M. Casarin, Conrado R. M. Afonso

Cold Plasma Applied to Sustainable Cellulosic Materials: Evaluation of Cell Adhesion 42
Maciel Barbosa, Paula Fernandes, Marina Fontes, Bruno Bruno Caillier, Sandra Cruz, Hernane Barud

Cooling Rate Effects on Microstructure, Hardness and Strength of a Low-Carbon Nb-Microalloyed Steel 43
Lavínia Ayumi Yamautti, Daniel G. S. dos Santos, Renan A. F. Dias, Jitendra Patel, Vinicius Cardoso Ottani, José Britti Bacalhau, Conrado R. M. Afonso

Correlative Electron Microscopy Approach for the Characterization of Nanocarbides in Nb Microalloyed Steels 44
Daniel G. S. dos Santos, Lavínia Ayumi Yamautti, Renan A. F. Dias, Vinicius Cardoso Ottani, José Britti Bacalhau, Jitendra Patel, Conrado R. M. Afonso

Corrosion analysis of a gray cast iron in saline environments 45
Lorena Maria da Silva, Leandra Marques, Vinicius Felippe Elias, Herique Marchezine Mazzer, Francisco Gil Coury

Development of Zr-based Vitreous Alloys and the Study of Quasicrystal Formation During Crystallization 46
Guilherme Araújo Teixeira, Witor Wolf

Early Biological Response to β-Ti, β-TN15, and Microarc-Oxidized β-TN15: A Combined In Vivo and Surface Characterization Approach. 47
Giovanna do Espirito Santo, Breno Rocha dos Santos, Stella Machado Gualti, Karina Nogueira Zambone Pinto Rossi, Conrado Ramos Moreira Afonso

Effect of Adding Recycled Titanium Chips in a Molten Salt Bath on the Production of Ti-rich Coating in AISI 1513 Steel 48
Vitor S. Rolin, José Gedael Fagundes Jr, Vicente A. Ventrella, Juno Gallego

Effect of Alloying Elements on the Microstructure and Oxidation Resistance at 800 °C of Ni-15Nb-M Ternary Alloys 49
Mariana S. Pereira, Gabriel M. de Camargo, Mariana C. Rossi, Conrado R. M. Afonso

Effect of Hydrogen on the Microstructure of C14-Type Laves Phase Multicomponent Alloys 50
O. A. Pedroso, W. J. Botta, G. Zepon

Effect of Ni Addition on the 3D Morphology of Fe-Rich Intermetallics in Directionally Solidified Al–5Cu–1.2Fe Alloys 51
Felipe Escher Saldanha, Jaderson Rodrigo da Silva Leal, Guilherme Lisboa de Gouveia, José Eduardo Spinelli

Effect of Scale Inhibitor Molecules on the Nucleation and Growth of Calcium Carbonate Nanoparticles Revealed by Cryo-TEM and LP-TEM..... 52
Fernanda C. Medeiros, Raquel P. Gonçalves, Vanessa P. Lages, Gisele M. Dalmônico, Rubens Bisatto, Mariana M. Longuinho, Dris Ihiawakrim, Jacques G. J. Werckmann, Marcos Farina, Ovidiu Ersen, Amaro G. B. Junior, André L. Rossi

Effect of SiO_2 addition on Microstructure of 3D Printed β Ti-35Nb-6Ta Alloys 53
Giovanna E. Santo, Lucas D. Duro, Bruno M. Casarin, Renan A. F. Dias, Conrado R. M. Afonso

Effect of Thermal Aging on the Corrosion Resistance of Deformed UNS S39274 54
Iasmin Maciel Vieira da Silva, André Rocha Pimenta

Effect of Yttrium Addition on Carbide Nucleation and Interdendritic Network Fragmentation in modified HP Nb-Ti Centrifugally Cast Stainless Steel..... 55
Gabriel Souza Bento, Taissa Zangerolami Lopes Rodrigues, Fabio dos Santos Queiroz, Leonardo Sales Araujo, Luiz Henrique de Almeida

Effects of Solidification Cooling Rate and Aging Time on the Microstructure of Al-4%Ni-0.07%Nb Alloy..... 56
Marcella Gautê Cavalcante Xavier, José Eduardo Spinelli

Enhancement of zinc nanoparticles to produce supraparticles as a potential agricultural input. 57
Júlia Rodrigues de Freitas, Mariana Monteiro de Lima Honorato Forini, Luiz Aparecido Ferreira Cavalcante, Renato Grillo

Expansão celular diferencial no endosperma de *Coffea arabica* durante a torrefação 58
Vinicius P. M. Xavier, Marta R. Verruma-Bernardi, Patrícia H. Santoro, Lyssa S. Sakanaka, Paulo S. P. Herrmann

Feasibility Study of Niobium Chip Recycling for the Development of Welding Fluxes for Hardfacing..... 59
Letícia K. M. Firmo, José Gedael Fagundes Jr, Vicente A. Ventrella, Juno Gallego

Hierarchical Organization of Hybrid Supraparticles Revealed by Scanning Electron Microscopy 60
Mariana M. L. H. Forini, Luiz A. F. Cavalcante, Júlia R. de Freitas, Débora R. Antunes, Érica R. Biscalchim, Renato Grillo

Hydrogen storage properties of multicomponent alloys produced using Ti6Al4V alloy scrap and commercially pure elemental feedstocks 61
Mariana de Brito Ferraz, Claudia Zlotea, Guilherme Zepon, Walter José Botta

Hysteresis in BCC alloys: EBSD insights into the β↔δ phase transformation..... 62
Gabriela C. Mayer, Walter J. Botta, Guilherme Zepon

Impact of Zn Additions on Sn–40Bi/Cu Interfacial Reactions: A Microstructural Study for Solder Alloy Design 63
Carolina de Siqueira Simioli, Guilherme Lisboa de Gouveia, José Eduardo Spinelli.

Influence of Casting, Hot Rolling, and ECAP on the Elastic Modulus and Mechanical Performance of β Ti–33Nb–33Zr Alloy for Biomedical Applications..... 64
M. L. Lourenço , R. F. M. dos Santos, L. A. R. Leão, P. A. B. Kuroda, A. Plaine, C. R. M. Afonso

Influence of Short-Range Chemical Ordering on the Ductile-to-Brittle Transition in Fe–V Alloy . 65
Leandra Marques, Gabriela Bugni Ribeiro, Francisco Gil Coury

In-situ alloying of Ti-Nb-Sn samples by Laser Additive Manufacturing: phase stability and non-isothermal heat treatment 66
Márcio Sangali, João Felipe Q. Rodrigues, Leticia F. Starck, Gilberto V. Prandi, Matheus Valentim, Josef Stráský, Rodolfo da Silva Teixeira, Leandro S. Silva, Miloš Janeček, Rubens Caram

Interfacial morphology evolution of PLA/PBSA blends during reactive extrusion with phenylene bis(oxazoline) - XII MICROMAT 2026 67
Marcos V. Basaglia, Lucas H. Staffa, Sílvia H. P. Bettini

Microestruturas hierárquicas em chapas Cu/Nb com interfaces não-lineares obtidas por Laminação Acumulada (ARB) 68
João Vitor Barletta Macêdo, Diogo Pedrino Braga, Pedro Henrique Fernandes Oliveira, Andrea Madeira Kliauga, Danielle Cristina Camilo Magalhães

Microstructural analysis of the TiZrSnMnFe HEA for potential use as a biomaterial 69
Thiago Alves de Oliveira, Carlos Eduardo da Silva, Carlos Roberto Grandini, Diego Rafael Nespeque Corrêa

Microstructural and surface characterization of MAO-treated TiZrNbMnFeAl Bio-HEA for biomedical applications 70
Jhuliene E. M. Torrento, Conrado R. M. Afonso, Carlos R. Grandini, Diego R. N. Correa

Microstructural and Topographical Analysis of MAO-treated Ti-30Nb-5Mo Alloy 71
Gustavo da Silva Diniz, Giovanna Cardososo Collombaro, Carlos Roberto Grandini, Diego Rafael Nespeque Correa

Microstructural and topographical analysis of the TiNbFeMnAl high-entropy alloy functionalized by micro-arc oxidation for biomedical applications 72
Luccas Nunes Caetano da Silva, Jhuliene Elen Muro Torrento, Diego Rafael Nespeque Correa, Carlos Roberto Grandini

Microstructural and Wear-Track Characterization of High-Entropy Alloys for Metallic Biomaterial Applications 73
Carlos Eduardo Manreza, Mariana Luno Lourenço, Diego Rafael Nespeque Correa, Carlos Alberto Fonzar Pintão, Carlos Roberto Grandini

Microstructural characterization and identification of quasicrystalline phases in an $Al_{90}Cu_4Fe_2Cr_4$ alloy processed by copper mold casting 74
Marcelo Fabiano Filho, Samuel Lima de Souza, Witor Wolf

Microstructural Characterization of Refractory Nb-based Alloys (C-103 and FS-85) Fabricated by Laser Powder Bed Fusion (LPBF) 75
João Vitor Garcia Lourenço, Mariana Luna Lourenço, Miloslav Béreš, Conrado R. M. Afonso

Microstructural characterization of the solid stated welded joint of Lean duplex stainless steel UNS S2101 76
Pedro Henrique Barletta Macedo, Leonardo Martins Tavares, David Jose Barreto Aviles, João Gabriel da Cruz Passos, Rodrigo de Oliveira França, Diogo Pedrino Braga, Jean Carlos dos Santos, Guilherme dos Santos Vacchi, Carlos Alberto Della Rovere

Microstructural characterization of the Ti-40Nb-xO alloys 77
João Pedro Ferreira Martins, Felype Narciso de Mattos, Pedro Akira Bazaglia Kuroda, Diego Rafael Nespeque Corrêa, Carlos Roberto Grandini

Microstructural characterization of zeolites for application in polymers 78
Lucas Campestrini, Marindia Decol, Marilena Valadares Folgueras, Daniela Becker

Microstructural Evolution and Phase Stability of Ti-Nb-Sn-(Ta-Mn) Multicomponent β-Type Titanium Alloys for Biomedical Applications 79
Victor dos Santos Pena de Araújo, Rafael Formenton Macedo dos Santos, Diego Rafael Nespeque Correa, Carlos Roberto Grandini

Microstructural Evolution of Cu/Cu15Zn Heterostructures Produced by Accumulative Roll Bonding (ARB) 80
Mila Christy de Oliveira, Andrea Kliauga, Diogo Pedrino Braga, Thiago Carvalho da Silva, Danielle Cristina Camilo Magalhães

Microstructural Evolution of Electrochemically Induced Niobium Hydrides 81
Audrey Marie Bedoch, Guilherme Yuuki Koga, Guilherme Zepon

Microstructural Exploration of Multiprincipal Components Ti Alloys for Biomedical Applications 82
Rafael Formenton Macedo dos Santos, Conrado Ramos de Moreira Afonso, Diego Rafael Nespeque Correa, Carlos Roberto Grandini

Microstructural features of a non-equiatomic TiCrCoAlFe HEA for potential use as external prostheses 83
Vinícius Melo Pellegrino, Gustavo Diniz, Carlos Roberto Grandini, Diego Rafael Nespeque Corrêa

Microstructure and crystallographic features of novel TiZrNbMo(Fe, Ta) high-entropy alloys 84
Vitor Meirelles Santos Toschi, Carlos Eduardo Manreza, Diego Rafael Nespeque Correa, Carlos Roberto Grandini

Microstructure and Elastic Modulus of the β Ti-35Nb-6Ta Alloy Produced by Laser Melting and 3D Printing for Implant Applications 85
Bruno M. Casarin, Renan A. F. Dias, Mariana L. Lourenço, Giovanna Santo, Conrado R. M. Afonso

Microstructure and plastic deformation effects on hydrogen generation from recycled Al–Zn chips 86
João G. M. Braghin, Rodrigo A. V. Reyes, Guilherme. L. De Gouveia, Cássia C. De Carvalho, José M. Aquino, Bismarck L. Silva, Carlos A. D. Rovere, José Eduardo Spinelli

Morphological Transition of Grass-Like γ-Alumina Nanostructures during Hydrothermal Treatment 87
Lucas H. M. Paodjuenas, Bernado P. Eduardo, Paula M. Jardim

Multiscale Characterization of Phases in UNS S41426 Supermartensitic Steel: from Optical Microscopy to EBSD 88
Priscila Carvalho Borba Cardoso, Bruno da Silva de Paiva, Vinycius Tavares Heuser, Suzana Bottega Peripolli, José Brant de Campos, André Rocha Pimenta

Multitechnique Characterization of CPV-ARI Portland Cement Hydration: A Microstructural and Chemical Approach 89
Elton Jose de Souza, Marcelo Bortolleto, Jorge Luis Akasaki, José Antonio Malmonge, Alex Otávio Sanches

Nanostructured $NaNbO_3$ Photocatalysts Grown on Nb Plates and Decorated with Gold Nanoparticles 90
Leticia Pinheiro Muniz de Carvalho, Thaís Lima de Paiva, Beatriz Rodrigues Canabarro, Paula Mendes Jardim

Real-Time Observation of Martensitic Reversibility in a Cu-based Shape Memory Alloy Using In Situ TEM 91
Gabriela Bugni Ribeiro, Eric Mazzer, Lucas Otani, Francisco Gil Coury

SEM and nanomechanical AFM Investigation of Recycled PE/PET Blends: Effects of a titanate neoalkoxy compatibilization 92
Marina E. M. Mergulhão, João Paulo Cosas Fernandes, Lucas Henrique Staffa

Structural and Microstructural analysis of the addition of Cu into Zr-25Ta-25Ti alloy 93
Gabriel E. G. P. Aguillera, Fernanda F. Quadros, Vinicius R. M. Gonçalves, Gerson S. Almeida, Willian F. Zambuzzi, Diego R. N. Corrêa, Carlos R. Grandini

Structural Characterization of the TiVNbCr alloy activated by Pulsed Laser Activation (PLA) method 94
Ana Rodrigues Cameirão, Juliana M. P. Almeida, Antônio C. Hernandes, Guilherme Zepon

Study of intermetallic phase formation in AISI H13 steel used in the HPDC process immersed in molten aluminum 95
Geovanne S. Santana, Raul E. de Sousa, Athos H. Plaine

Study of the Topography and Chemical Composition of Coatings Produced on Titanium by Micro-Arc Oxidation 96
Giovana Collombaro Cardoso, Manuel Amado Rodas O'Meany, Angel Vicente Escuder, Carlos Roberto Grandini, Vicente Amigó-Borras

Sunlight-Photoresponsive Nanostructured Lipid Carriers for the Controlled Release of Agrochemicals 97
Beatriz A. Riga-Rocha, Mariana M. L. H. Forini, Luiz A. F. Cavalcante, Rosangela S. Laurentiz, María E. Taverna, Renato Grillo

Surface Modification of Bioabsorbable Mg-8Li-1Y and Mg-1Zn-0.4Ca Alloys by Micro-Arc Oxidation for Temporary Implant Applications 98
Matheus Henry da Silva, Denize Maria S. e Silva , Daniel G. S. dos Santos , Peter Minarik , Danielle C. C. Magalhães, Conrado R. M. Afonso

Surface modification of Ti-25Ta-xNb alloys by micro arc oxidation for biomedical applications: microstructural characterization, bioactivity, and antimicrobial activity 99
Fernanda de Freitas Quadros*, Diego Rafael Nespeque Corrêa,Carlos Roberto Grandini

Synthesis and characterization of mesoporous silica nanoparticles with potential application in agriculture 100
Rafaela de Souza Mendonça, Érica Rennó Biscalchim, Mariana Monteiro de Lima Honorato Forini, Beatriz Aline Riga-Rocha, Renato Grillo

Synthesis and Microstructural Analysis of Ti-Nb Based Composites for Orthopedic Implants .. 101
Carlos Eduardo da Silva, Vinícius Richieri Manso Gonçalves, Carlos Roberto Grandini, Gerson Santos de Almeida, William Fernando Zambuzzi, Sophia Alexandra Tsipas, Paulo Noronha Lisboa-Filho, Diego Rafael Nespeque Corrêa

Tracking Impact and Expanding Access in a Core Microscopy Facility: The LIMicro-IQ Experience 102
Hugo C. Loureiro, Leandro de Abreu, Raquel E. Miller, Rene A. N. Silva, Ana Flávia Nogueira, Camila A. Rezende, Daniela Zanchet

Use of SEM imaging to characterize the effect of adding helium to the welding gas in TIG welding of superduplex stainless steel - XII MICROMAT 2026 103
Diel Silva Botão, Eustáquio de Souza Baêta Junior, Camila Alves Pelicarto da Silva Botão, Frederico Garcia Bindi de Lacerda, Jonas Gabriel Ramos da Silva Ataliba, André Rocha Pimenta

ÍNDICE DE AUTORES 104

REGISTRO FOTOGRÁFICO DO EVENTO 108

INVITED LECTURE

Advanced micro- and nanostructural characterisation methods for investigating the processing of Ni-based superalloys

Cleiton C. Silva[1]

[1] Universidade Federal do Ceará, Laboratório de Pesquisa e Tecnologia em Soldagem. Fortaleza, CE, Brazil.

The application of advanced microscopy and microanalysis techniques in recent decades has revolutionised the development of Ni-based superalloys, establishing these methods as an essential pillar of cutting-edge materials science. These sophisticated methods enable unparalleled resolution for identifying phases, nanoprecipitates, and crystalline defects, and for elucidating the partitioning behaviours of alloying elements influenced by processes such as welding and additive manufacturing. Scanning electron microscopy (SEM) analysis provides secondary electron (SE) and backscattered electron (BSE) images of the structure, revealing details of harmful secondary phases and enabling their quantification and correlation with performance. SEM coupled with energy-dispersive spectroscopy (EDS) provides a general view and semi-quantitative data on macro- and microsegregation and the partitioning of alloying elements. Electron backscatter diffraction (EBSD) enables the determination of grain orientation, texture, and grain size, as well as microstrain and geometrically necessary dislocation density. For more precise or quantitative analysis, electron probe microscopy (EPMA) is an excellent option that filters continuous X-rays using wavelength-dispersive X-ray spectroscopy (WDS). Transmission electron microscopy (TEM) is a powerful technique that not only enables higher-resolution imaging but also allows unequivocal identification of intermetallic precipitates within the matrix through characteristic signatures in the electron diffraction pattern. It also enables the determination of matrix-precipitate crystal orientation relationships, thereby elucidating the nucleation and growth of these phases. Recent breakthroughs in aberration-corrected electron microscopy have dramatically pushed the boundaries of resolution, enabling atomic-scale structural characterisation. High-Resolution Scanning Transmission Electron Microscopy (STEM) using High-Angle Annular Dark-Field (HAADF) detectors enables direct imaging of individual atomic columns, allowing the study of ordered nanometric phases and the identification of defects such as dislocations, stacking faults, antiphase boundaries, and twin boundaries, helping elucidate interactions between crystalline defects and strengthening mechanisms. Recently, atom probe tomography (APT) has provided unprecedented three-dimensional atomic-scale imaging and chemical composition analysis, enabling breakthroughs that have driven critical advancements in Ni metallurgy by revealing nanoscale features such as ordered phase composition and solute segregation at grain boundaries. Correlating these microstructural insights with material properties to gain a deep understanding of the strength-ductility trade-off is crucial for pioneering the next generation of high-performance alloys. This comprehensive review integrates data from diverse microscopy and microanalysis techniques across multiple scales to uncover fundamental structural principles and accelerate innovation in Ni-based alloy design and performance optimisation.
Keywords: Microscopy; microanalysis; advanced techniques; Ni-based alloys.

Experimental, theoretical, MD and ML simulations of glass-forming ability

Edgar Dutra Zanotto[1,2*]

[1] DEMa, Universidade Federal de São Carlos, Brazil; [2] EZ-GLAD, Wuhan University of Technology, China.
*E-mail: dedz@ufscar.br

Vitrification is a temporal race against structural reorganization. From a theoretical standpoint, virtually any liquid can bypass crystallization and enter a glassy state if it is cooled faster than its critical cooling rate, R_c [1]. However, connecting condensed matter physics with the practical demands of industrial feasibility remains a monumental challenge. As George Morey astutely observed in his classic 1938 monograph, The Properties of Glass: "*The controlled avoidance of devitrification is the principal factor that restricts the compositional range of practical glasses; it is a ubiquitous risk in any glassmaking and glass working process*." This timeless adage continues to highlight a challenging hurdle faced by modern materials scientists: how to efficiently identify, screen, and design novel, stable glass compositions that offer a tailored combination of functional properties without falling prey to spontaneous crystallization. This talk deconstructs the twofold nature that rules the supercooled liquid and glassy states. First, we examine the *intrinsic* scenario: a pristine, ideal realm operated entirely by bulk thermodynamics and intrinsic transport kinetics. In this case, the degree of spatial and temporal overlap between homogeneous crystal nucleation rates and subsequent crystal growth kinetics determines both the theoretical R_c and the intrinsic glass-forming ability (GFA) of a given system. The second aspect, however, is the *extrinsic* (practical) scenario, which inevitably governs laboratory synthesis and large-scale industrial processing. In real-world systems, devitrification is a highly accelerated process. It occurs most rapidly when driven by heterogeneous nucleation pathways, which are catalytically assisted by foreign submicron particles, crucible wall roughness, atmospheric interfaces, and localized surface defects. Understanding the energetic barriers of these competing pathways is essential to preventing structural failure during forming. To explain the delicate atomic and macroscopic determinants of these transformation pathways, we provide an extensive comparative analysis spanning the entire spectrum of inorganic glass-formers—from "excellent" vitrifiers to highly unstable, "reluctant" glass-formers. We approach this multi-scale problem by deploying a well-rounded combination of four distinct methodologies: i) Optical and Electron Microscopy (SEM/TEM): Employed to study real-time crystal morphologies both during *in-situ* thermal stages and after rigorous post-treatments [2]. This allows for the precise quantification of spatial distributions, nucleation density, and interfacial growth kinetics; ii) Classical Nucleation Theory (CNT): Utilized to define structural relaxation, thermodynamic driving forces, and the overall crystallization energetics and dynamics across wide temperature ranges; iii) The JeZiCA Model: A theoretical framework previously derived by our research group. This model bridges a thermodynamic (liquidus temperature) and a kinetic parameter (viscosity), offering an analytical tool for evaluating glass stability without relying solely on empirical metrics; iv) Molecular Dynamics (MD) Simulations: Used to probe the supercooled liquid state's short- and medium-range order. By tracking structural precursors, coordination numbers, and fluctuations in network connectivity, MD reveals the precise atomic dynamics that either inhibit or facilitate localized crystalline arrangements. By integrating these experimental and computational pipelines, we explore new data-driven approaches for predicting GFA. Then, moving beyond the traditional, time-consuming Edisonian trial-and-error approach, we integrate thermodynamic and structural descriptors into advanced Machine Learning (ML) workflows. Training ML models on vast compositional datasets empowers us to chart high-dimensional, multi-component phase spaces *in silico*. This allows for the rapid prediction of R_c and kinetic stability parameters before a single batch is ever melted in the laboratory. Such predictive capability is absolutely crucial for extending the compositional limits of novel functional glasses. These materials are heavily idealized for next-generation energy technologies—such as solid-state battery electrolytes, safe nuclear waste immobilization matrices, and high-efficiency advanced solar substrates—as well as for cutting-edge biomedical implants and flexible optoelectronic devices. Lastly, we will focus on the fascinating and extreme example of *albite glass* ($NaAlSi_3O_8$). Albite represents the absolute zenith of extreme GFA, presenting a kinetic barrier to devitrification that is nearly insurmountable by conventional means. We will present striking experimental evidence demonstrating that this unseeded, highly polymerized tectosilicate material completely resists crystallization even after several years of continuous, optimal thermal treatment at temperatures precisely corresponding to its maximum theoretical crystallization rate. Exploring the structural origins of albite's remarkable resilience reveals a mechanism deeply rooted in its fully interconnected three-dimensional network. The exceptionally high glass transition temperature, T_g, and the requirement for slow, highly cooperative spatial diffusion of multiple ionic species make feldspar crystallization, from a supercooled liquid having a widely different structural arrangement, structurally prohibitive. Ultimately, decoding how albite maintains its amorphous state under such prolonged thermal stress demonstrates that nature still holds the ultimate solutions to addressing Morey's "ever-present danger," offering profound design rules for the future of glass science [3].

References

[1] L.R. Rodrigues, E.D. Zanotto, Critical assessment of GFA in oxide systems, Progress Materails Science (2026) under review.

[2] E.D. Zanotto, Crystals in Glass: A Hidden Beauty, Print ISBN:9781118521434 |Online ISBN:9781118559055, Wiley, NY, 2023

[3] This research was supported by Fapesp and CNPq (Brazil)

ORAL

Correlating microscopy, composition, and sensing behavior in Ce-doped anatase TiO_2 nanoparticles

Adriane Hoeldtke[1*], Renan Barbieri[1], José Pedro Mansueto Serbena[1,2], Ney Mattoso[1,2]

[1] Universidade Federal do Paraná – Programa de Pós-graduação em Engenharia e Ciência dos Materiais; [2] Universidade Federal do Paraná – Departamento de Física.
*E-mail: adrianehoeldtke@ufpr.br

Establishing clear relationships between microstructure, composition, and functional performance is essential for the design of advanced metal oxide nanomaterials for sensing applications. In this work, Ce-doped anatase TiO_2 nanomaterials were investigated to understand how cerium incorporation influences the physicochemical characteristics of the material and its humidity-responsive sensing behavior. Ce doping was employed as a strategy to modify the local structure, surface chemistry, and defect-related features of TiO_2, aiming to improve its interaction with water molecules and its electrical response under humid conditions. The materials were characterized by X-ray diffraction (XRD), Fourier transform infrared spectroscopy (FTIR), photoluminescence spectroscopy (PL), and scanning electron microscopy coupled with energy-dispersive X-ray spectroscopy (SEM/EDS). XRD confirmed the preservation of the anatase phase after doping, while FTIR revealed surface hydroxyl groups relevant to water adsorption processes. PL provided information on defect states and band gap-related changes associated with Ce incorporation. In addition, SEM/EDS analyses enabled the evaluation of morphology and elemental distribution, providing important evidence of the compositional and microstructural features of the sensing material. Humidity tests demonstrated that water vapor strongly affects the electrical behavior of the devices, confirming the key role of surface-mediated interactions in the sensing mechanism. The results suggest that Ce incorporation modifies active surface sites and defect-related states, which, together with the observed microstructural and compositional characteristics, contribute to water adsorption and charge transfer during sensing. Overall, by correlating microscopy, compositional analysis, and sensing performance, this study provides insight into the role of Ce in tuning the functional response of anatase TiO_2 and highlights its potential for humidity-responsive gas sensing applications. **Keywords:** Ce-doped TiO_2; anatase; microscopy; elemental composition; humidity-responsive sensing; defect states.

Enamel prisms organization in rodent incisor teeth: comparison between small and large animals

Vilma Lima[1], Carlos A. Menezes[2], Jean Pierre dos Santos[3], Mair M. M. de Oliveira[2], Marcos Farina[2]

[1] Universidade Federal do Ceará; [2] Instituto de Ciências Biomédicas – UFRJ; [3] Centro Nacional de Biologia Estrutural e Bioimagem CENABIO – UFRJ.
*E-mail: mfarina@icb.ufrj.br

Rodents (Order *Rodentia*) are mammals that are characterized by the presence of pairs of constantly growing rootless incisors in upper and lower jaws which are continuously sharpened during the time due to the wearing process. A distinguishing feature of these teeth is that their front regions have a hard enamel layer while inner surfaces show uncovered dentine. Rodents enamel has two parts: "*portio interna*"(PI), the decussation zone, and "*portio externa*"(PE), the radial zone [1]. In this work we analyzed the organization patterns of prisms, from rat, "cotia" (Rodent Dasyprocta) and "paca" (*Cuniculus* paca - CP) lower incisors, in the PI region, by observing oblique contours of prisms, after polishing the samples in a plane tangent to the front surface of the tooth, by Scanning Electron Microscopy (SEM). In rat (Fig 1A), SEM showed that PI region is formed by parallel rows of prisms ("uniserial" organization), while in cotia (Fig. 1B) and CP (Fig. 1C), PI prisms were organized in bands ("multiserial" organization). However, cotia and CP presented a difference in prisms distribution inside bands: in cotia it was observed a group of 6 to 7 prisms inside each band, with small changes in orientation among them, forming sub-rows (see region inside dashed rectangles in Fig. 1B), while in CP, prisms appeared less oriented relatively to neighbors inside the same band (arrows in Fig. 1C). Regions inside dashed ellipsoids show termination of individual rows (Fig. 1A) and bands (Figs. 1B and 1C). The presence of edge-dislocation-like patterns in the form of rows or bands, may represent a scale factor, which means that both small and large animals are subjected to similar constraints when an organ (rodent´s incisor tooth) is growing in a region with limited volume. Iron was found in *portio externa* of CP (Figures 2A and 2B) as in the enamel of other rodents, and is considered to produce an outermost layer of the enamel endowed with superior functionality and self-sharpening natural tools [2]. In conclusion, this work describes aspects of the organization of enamel prisms in the incisors of 3 rodents, and proposes an approach that takes into account scaling factors related to the formation of the same organ in organisms of different sizes. In the specific case of this work, the incomplete rows and bands observed may be compared with "edge-dislocations" (Fig. 1D) [3].

References

[1] L. Alloing-Séguier et al., The Anatomical Record 302:1195-1209 (2019).

[2] V. Srot et al., ACS Nano 2024,18, 11270-11283.

[3] We acknowledge support from the Brazilian agencies CNPq and Faperj and the electron microscopy facilities from CENABIO – UFRJ.

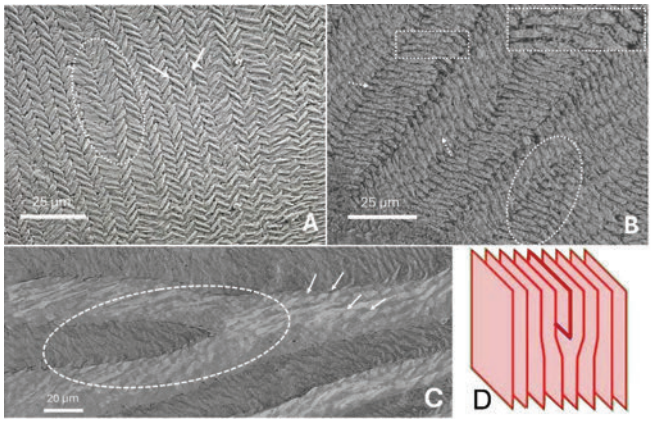


Figure 1. Polished sections parallel to the lower (outer) surface of the incisor tooth, depicting oblique sections of enamel prisms; A) rat enamel; B) Cotia enamel. C) Cuniculus Paca (CP) enamel. Rat enamel is composed by rows of single prisms arranged in parallel in each row, while in cotia and CP, enamel is organized in bands including several prisms in each. Dashed ellipsoidal contours, indicate regions where incomplete rows ("edge dislocations") occurred (in A), or incomplete bands (in B and C). Extremities of enamel prisms (arrows) are seen. In B and C, enamel prisms are organized in parallel bands instead of rows as in rat, with little variation of their orientation inside. Interface between bands (in A, B and C) are characterized by an abrupt change in crystals orientation. Interestingly, "edge dislocation-like defects" also occurs for this type of "supra-organization" (dashed contours in B and C). D) Graphic representation of an edge dislocation. This type of defect is characterized by a half-plane inserted into a periodic lattice.

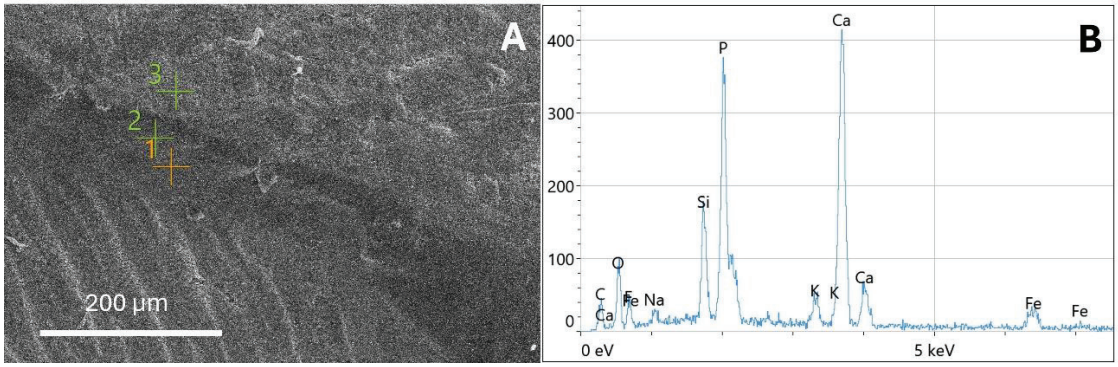


Figure 2. Elemental analysis of CP enamel. A) Fractured enamel showing the internal region (*portio interna*) composed of bands of enamel prisms (lower half), and external layer (*portio externa*), top half in the figure. B) EDS of region 3 in the previous figure. Note the presence of iron besides the expected oxygen, phosphorus and calcium.

Grain refinement of a 316 LV austenitic stainless steel by severe plastic deformation: HPT, ECAP and deep burnishing

Andrea Madeira Kliauga[1*], Danielle Cristina Camilo Magalhães[1], Diogo Pedrino Braga[1], Lucina Montanari[2]

[1] Department of Materials Engineering- Federal University of São Carlos; [2] Department of Mechanical Engineering, University of São Paulo.
*E-mail: kliauga@ufscar.br

The austenitic stainless steel AISI 316 LV is commonly used in nuclear power plants and in biomedical applications [1,2] due to its high corrosion resistance. Nanostructuring, a condition obtained through severe plastic deformation (SPD) processing, can improve the mechanical strength of alloys thanks mainly to grain size refinement [3,4]. SPD can produce nonporous bulk materials with improved fatigue resistance [4]. Grain size reduction impact on the radiation behavior because increasing the grain boundary area per unit volume is expected to hinder the formation of defect clusters and enhance radiation tolerance [1]. The bioactivity of the 316LV alloy has reportedly increased after SPD [2]. Different processes can be applied to produce bulk SPD material such as equal channel angular pressing (ECAP), high pressure torsion (HPT). Deep burnishing is increasingly recognized as SPD process, designed to introduce substantial compressive residual stresses, high hardness, and refined microstructures (often ultrafine grains <1 μm) into the surface layer of metallic materials. Unlike bulk SPD, burnishing creates a gradient microstructure where equivalent strain is highest at the surface and decreases with depth. Whereas for the first two processes the equivalent strains are mathematically well determined by the geometry of the process (number of turns, diameter and height of the disc samples applied pressure in HPT, number of passes and angles of concordance of the ECAP matrix), for the latter the strains will be dependent of process parameters such as feed velocity, penetration depth and number of passes. The grain refinement in SPD is achieved by a dynamic recrystallization imposed by shear strains and dislocation cell rotation at strains higher than 2 and is directly correlated with the dislocation density. Sidor [5] proposed that hardening behavior of a material, which is related to the number of dislocations, can be indirectly quantified by indentation techniques and further correlated to the Kocks Mecking and Esting model. The objective of the present work is to compare the formation of nanostructured microstructure in an AISI 316LV stainless steel through ECAP, HPT and deep burnishing and to correlate applied strain, hardness and grain refinement in order to estimate the strain distribution in gradient microstructure formed by deep burnishing. The HPT was performed at 300 °C applying 6GPa pressure and 5 turns; the equivalent strain was ~ 4.5 at r/2 and ~5.2 at the vicinity of the disk edge. ECAP was performed at the same temperature in a matrix with and internal angle of 120° and a equivalent strain of 0,7 per pass up to a strain of 5,6. Deep burnishing samples were pre-prepared by turning at a cutting speed of Vc = 6 mm/min and a turning feed of ft = 0.01mm/rev the penetration depth of the spheric tool tip was 50 μm per pass Vickers hardness profiles were obtained form all deformed samples and microstructure evolution was observed by transmission electron microscopy (TEM) and electron back-scattered diffraction (EBSD). The grain refinement increased with the amount of applied strain and in the burnished sample the size of recrystallized grains at the surface were of the order of 100 nm (Figure1) At the surface, the equivalent strain per pass was 0,35 and generated a strain gradient of -0,0038 /μm. (Figure 2). The estimated strain distributions were validated using electron back-scattered diffraction-based strain mapping [6,7].

References

[1] Sun C., et al, J. Nucl. Mater., 420, (2012) 235–240

[2] Misraa R.D.K, et al. Acta Biomater. 9 (2013) 6245–6258.

[3] Edalati K. et al.MATER. RES. LETT. 10, (2022), 163–256 https://doi.org/10.1080/21663831.2022.2029779

[4] Valiev, R.Z., *et al.*,*JOM* **58**, (2006) 33–39. https://doi.org/10.1007/s11837-006-0213-7

[5] Sidor, J.J.; et al. *Metals* **2021**, *11*, 1571.

[6] This research was supported by CNPq (Brazil).

[7] This research was supported by FAPESP (Brazil) Grant nr.2024/13959-9.

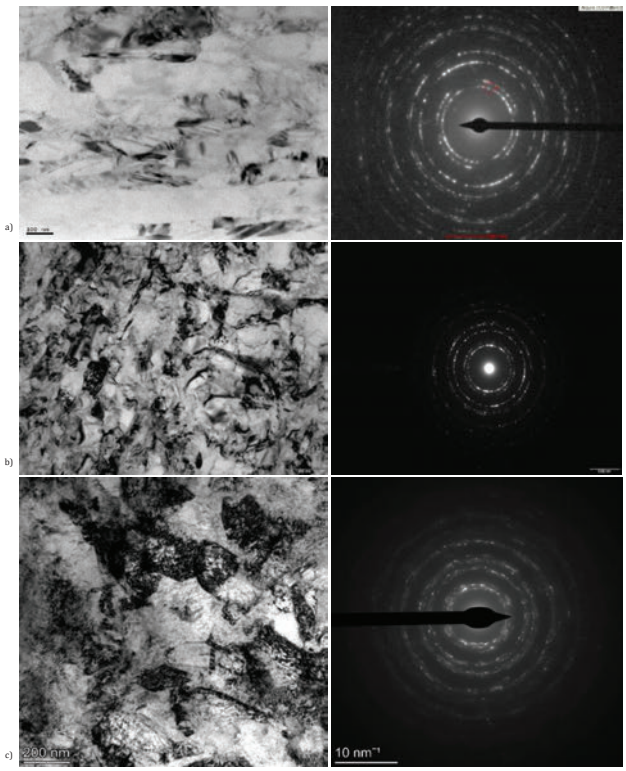


Figure 1. TEM showing grain refinement of the 316LV steel after: 6 ECAP passes, outer diameter of the HPT sample, surface region of the burnished sample.

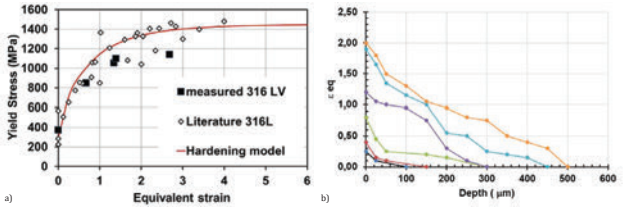


Figure 2. Hardening curve (stress – equivalent strain) obtained measured and SPD data and calculated equivalent strain profiles of the burnished samples.

High-temperature oxidation behavior of multicomponent refractory alloys Al15Nb30Ti25V5Mo25 and Al15Nb30Ti25V5Zr25

João Gabriel da Cruz Passos[1], Carolina Soares[2], Rodrigo de Oliveira França[1], David Jose Aviles[1], Diogo Pedrino Braga[1], Guilherme dos Santos Vacchi[1], Carlos Alberto Della Rovere[1], Artur Mariano de Sousa Malafaia[3], Marcelo Falcão de Oliveira[2]

[1] Universidade Federal de São Carlos; [2] Universidade de São Paulo – Escola de Engenharia de São Carlos; [3] Universidade Federal de São João del Rei.
*E-mail: joaopassos@ufscar.br

Multicomponent refractory alloys (MRAs) are alloys produced with multiple refractory elements in significant concentrations (5 at.% and above). They are derived from equiatomic refractory high-entropy alloys (RHEAs), which were developed in 2010 and gathered significant attention due to their promising mechanical properties, especially at high temperatures [1]. In counterpart, refractory elements and, consequently, refractory alloys in general are highly susceptible to catastrophic oxidation, forming voluminous, spallation-prone, fast-growing and/or volatile oxides [2,3]. Therefore, high-temperature oxidation tests are important to evaluate the behavior of these alloys in such conditions and gather valuable knowledge that could allow future compositional optimizations. In this work, two novel refractory alloys, Al15Nb30Ti25V5Mo25 and Al15Nb30Ti25V5Zr25, discussed in a previous study published by the group [4] were exposed to 600, 800 and 1000 °C for 20 h under still lab air and had their oxidation behavior evaluated. The oxidized samples were characterized through X-ray diffraction (XRD) and scanning electron microscopy with energy dispersive X-ray spectroscopy (SEM-EDX) and the specific mass variation was measured. Samples were placed in crucibles to estimate the gross mass variation (considering spalled oxides). Results show that the alloys behave very similarly at 600 °C. At 800 °C, the alloy with Mo gains more mass and suffers a higher degree of spallation, as indicated by the significant difference between net and gross mass variation values (Figure 1). At 1000 °C, the alloy with Zr gains more mass, but this seems to be caused by a significant degree of volatilization on the alloy with Mo, as the element is known to form volatile oxides [2]. Cross-section characterizations confirm the formation of crack-prone oxide scales in both alloys, with most of the scale being spalled in the alloy with Mo. Both alloys formed a lamellar oxide scale containing a mixed rutile phase (MO_2) with most alloy elements in solid solution, as well as other nonprotective mixed oxides. An example of the formed oxide scales is given in Figure 2. Both alloys could be considered unfit for applications at high temperatures, considering the significant mass variation and formation of nonprotective oxides. Worthy of note, however, is that the alloys did not suffer pesting (complete degradation into powder), possibly as a consequence of the relatively high Al content, as indicated by a previous investigation into Al-containing RHEAs [5]. The microstructure of the alloys close to the oxide scale also changed significantly. Because the alloys are able to dissolve a large amount of oxygen, an oxygen-diffusion zone with significantly increased hardness formed, as shown in Figure 3. This indicates a fragilization of the surface upon exposure, possibly reducing the life under fatigue of the alloy, for example. Practical application of the alloys would require either compositional modifications to increase the content of protective oxide formers (Cr, Al and/or Si) or apply coatings to form protective oxides through, for example, pack aluminization. Considering the high affinity of the alloy for oxygen, a protective layer limiting oxygen ingress is essential to avoid surface fragilization and premature failure, as well as reduce the overall oxidation rate.

References

[1] O.N. Senkov, G.B. Wilks, D.B. Miracle, C.P. Chuang, P.K. Liaw, Refractory high-entropy alloys, Intermetallics 18 (2010) 1758–1765.

[2] B. Gorr, S. Schellert, F. Müller, H.-J. Christ, A. Kauffmann, M. Heilmaier, Current Status of Research on the Oxidation Behavior of Refractory High Entropy Alloys, Advanced Engineering Materials 23 (2021) 2001047. https://doi.org/10.1002/adem.202001047.

[3] R.K. Dehury, R. Kumar, Y.G. Joshi, V. Gupta, Elemental Influence on Oxidation Behaviour of Cantor-Based and Refractory High Entropy Alloys: A Critical Review, Adv Eng Mater 26 (2024) 2302124. https://doi.org/10.1002/adem.202302124.

[4] J.H. Mazo, C. Soares, G.K. Inui, M.F. De Oliveira, J.L.F. Da Silva, Structural and mechanical properties of refractory Nb30X25Ti25Al15V5 (X= Zr, Mo) high-entropy alloys, Materials Science and Engineering: A 929 (2025) 148053. https://doi.org/10.1016/j.msea.2025.148053.

[5] E.A. Anber, D. Beaudry, C. Brandenburg, S. Lech, L. Backman, D.L. Foley, E.L. Wang, M.J. Waters, L. Perriere, J.-P. Couzinie, J.M. Rondinelli, E. Opila, M.L. Taheri, Oxidation resistance of Al-containing refractory high-entropy alloys, Scripta Materialia 244 (2024) 115997. https://doi.org/10.1016/j.scriptamat.2024.115997.

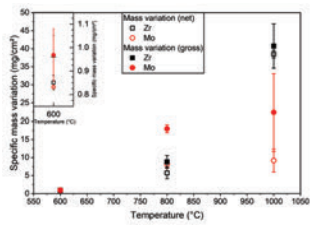


Figure 1. Specific mass variation for both RHEAs upon exposure to the indicated temperatures for 20 h. Inset shows data at 600 °C in detail.

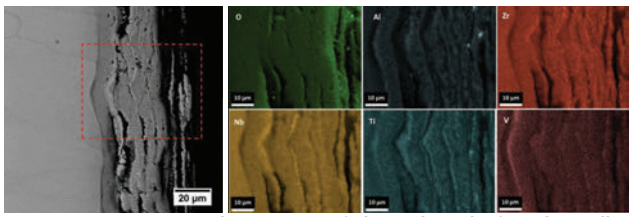


Figure 2. SEM Image and EDX maps of the oxide scale formed on alloy Al15Nb30Ti25V5Zr25 after exposure at 1000 °C for 20 h.

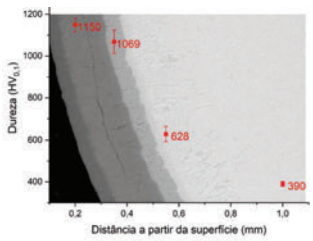


Figure 3. Hardness measurements throughout the oxygen-diffusion layer on alloy Al15Nb30Ti25V5Zr25 after exposure at 1000 °C for 20h.

In situ forming reactions of multicomponent titanium matrix composites produced by arc melting targeted as biomaterials

Carlos Eduardo da Silva[1], Carlos Roberto Grandini[1], Vinícius Richieri Manso Gonçalves[2], Conrado Ramos Moreira Afonso[2], Diego Rafael Nespeque Correa[1*]

[1] Faculdade de Ciências / UNESP – Campus Bauru; [2] Departamento de Engenharia de Materiais/ UFSCar – Campus São Carlos.
*E-mail: diego.correa@unesp.br

Metallic biomaterials are widely used as replacements for hard tissues in the body, including orthopedic and dental load-bearing implants and bone fixation devices. However, conventional materials (e.g., stainless steel, Co-Cr alloys, and Ti alloys) still do not meet current clinical requirements for long-term use, particularly with respect to mechanical, electrochemical, tribological, and biological properties [1]. In this scenario, titanium matrix composites (TMCs) reinforced with ceramic particles can offer a unique combination of properties, tuning their mechanical and tribological performance, as demonstrated in our earlier studies [2]. Furthermore, traditional powder metallurgy processing of TMCs requires optimizing synthesis parameters to enhance matrix-reinforcement bonding. Thus, argon arc melting has been strategically used to form TMCs, as it induces in situ reactions, thereby ensuring advantageous properties [3]. Lastly, the high-entropy alloy (HEA) concept has emerged as a hotspot for the design of novel metallic biomaterials, offering superior mechanical and corrosion properties compared to traditional commercial materials. However, the HEA-based TMCs warrant greater exploitation, given the distinct bonding at the matrix/reinforcement interface [4]. In this study, we produced a novel TMC by arc-melting an HEA ingot (equiatomic TiNbZrTaMo alloy) with B_4C powder. The XRD and SEM results indicated an in situ reaction between B and C atoms and Ti, forming ceramic precipitates (TiC and TiB) embedded in a BCC + HCP microstructure (as shown in Figure 1). The major BCC phase was enriched by the refractory alloying elements (Mo, Nb, and Ta), while the minor HCP phase was located preferentially in the grain boundary and was enriched by light elements (Ti and Zr). TEM analysis revealed a coherent interface between the matrix and TiC with smooth chemical segregation. The resulting microstructure had a significant impact on the selected mechanical, tribological, and biological aspects, opening promising horizons for the development of biomedical implants with functional properties for long-term use [5].

References

[1] Coan, K.S. *et al.* Applied Surface Science 689 (2025) 162557.

[2] Gonçalves. V.R.M. *et al.* Journal of Mat. Research and Technology 30 (2024) 879-889.

[3] Gonçalves, V.R.M. *et al.* Surface & Coatings Technology 506 (2025) 132113.

[4] Maurício, D.C. *et al.* Journal of Mat. Research and Technology 35 (2025) 4009-4019.

[5] FAPESP (Proc. #2024/03148-3) and CNPq (Proc. #404020/2023-2).

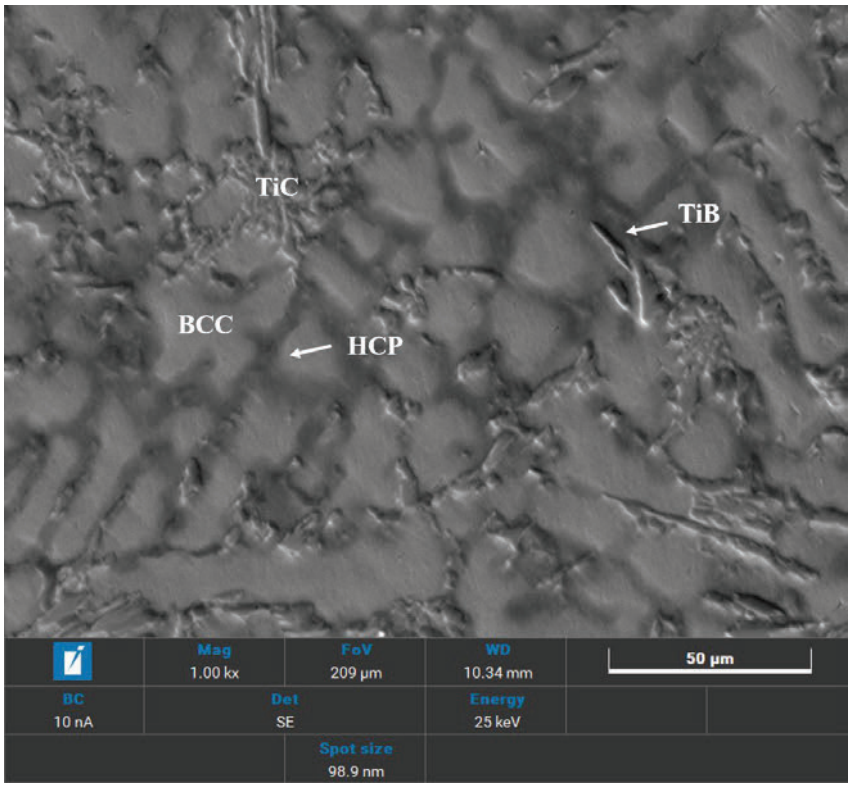


Figure 1. SEM imaging of the TMC sample with the corresponding bulk phases and ceramic precipitates.

Investigation of the microstructure evolution during thermomechanical processing of a Zr-0.6Nb-0.4Mn alloy

Bernardo Pompermayer Eduardo[1*], Paula Mendes Jardim[1], Rafaella Martins Ribeiro[1]

[1] Universidade Federal do Rio de Janeiro – UFRJ /COPPE, Programa de Engenharia Metalúrgica e de Materiais – PEMM.
*E-mail: bernardopeduardo@metalmat.ufrj.br

Zirconium alloys are used as structural materials for nuclear components due to their low neutron absorption and good corrosion resistance. In recent years, Mn additions to Zr–Nb alloys have attracted attention because they improve hydrogen uptake resistance and formability [1,2,3]. Therefore, understanding the microstructural evolution during thermomechanical processing is essential for optimizing these alloys for nuclear applications. In this work, the microstructural evolution of a Zr–0.6Nb–0.4Mn alloy was investigated throughout a thermomechanical processing route using transmission electron microscopy. The alloy was initially hot rolled at 950 °C with 50% thickness reduction, followed by β-solution treatment at 1000 °C for 10 min and water quenching. Subsequently, hot rolling at 850 °C with 13.6% reduction and cold rolling with 81.6% thickness reduction were performed. Final annealing treatments were conducted at 500 °C for 2 h and 4 h. The β-quenched condition exhibited α′ (hcp) laths formed by the martensitic transformation induced by rapid cooling, Figure 1(a), similarly to previous report for quenched Zr–Nb alloys [4]. After hot rolling at 850 °C, the microstructure revealed elongated grains containing cellular dislocation arrangements characteristic of the dynamic recovery process, Figure 1(b). These features are consistent with recovery-dominated mechanisms commonly reported for hot-deformed zirconium alloys [5,6]. After cold rolling with 81.6% thickness reduction, the microstructure exhibited a high density of dislocations arranged as dislocation tangles, Figure 1(c), a typical feature of heavily deformed Zr alloys [4]. After annealing at 500 °C for 2 h, the microstructure exhibited dislocation cells associated with recovery, Figure 1(d), together with recrystallized grains of approximately 200 nm, Figure 1(e), consistent with recovery-dominated mechanisms reported in [52]. In addition, nanosized precipitates sparsely distributed throughout the matrix were observed, Figure 1(f). EDS elemental mapping revealed Nb and Mn rich precipitates with an Nb/Mn ratio close to 2, indicating the formation of Mn_2Nb precipitates. After annealing at 500 °C for 4 h, the microstructure exhibited recrystallized grains coexisting with dislocation tangles, Figures 1(g-h). A bimodal grain size distribution ranging from 300 nm to 2 μm indicated recrystallization progress while maintaining a partially recrystallized microstructure, similarly to annealed Zr–Nb alloys [7]. More pronounced precipitation was observed after 4 h, Figure 1(i). The precipitates were predominantly spherical, randomly distributed throughout the matrix, and ranged from 10 to 40 nm in size. EDS elemental mapping confirmed Nb and Mn enrichment with an Nb/Mn ratio close to 2, while diffraction analysis identified the precipitates as the hcp Mn_2Nb phase [ICSD code 152628]. The results demonstrated that the thermomechanical processing route adopted for the Zr–0.6Nb–0.4Mn alloy promoted a partially recrystallized microstructure associated with fine Mn_2Nb precipitates homogeneously distributed throughout the matrix after annealing at 500 °C for 4 h. This microstructural condition may contribute to improved stability and corrosion resistance, which are important for nuclear applications. Transmission electron microscopy was essential for correlating the evolution of dislocation structures, recrystallized grains, and precipitation during processing. Moreover, the combination of high cold-rolling reduction and low-temperature annealing proved effective in controlling the microstructural evolution of the alloy, highlighting the potential of this processing strategy for zirconium alloys used in nuclear components.

References

[1] R.M. Ribeiro et al., J. Hydrogen Energy. 40 (2015) 17118.
[2] T.B. Pintor et al., Mater. Res. 22 (2019) e20190182.
[3] B.P. Eduardo et al. Metall. Mater. Trans. A. 56A (2025) 3006.
[4] S. Neogy et al., Metall. Mater. Trans. A. 38A (2007) 485.
[5] J. K. Chakravartty et al., J. ASTM Int. 7 (2010) 1.
[6] A Saboori et al., Mater. Sci. Eng. A. 696 (2017) 366.
[7] H. Tian et al., J. Nucl. Mater. 456 (2015) 321.

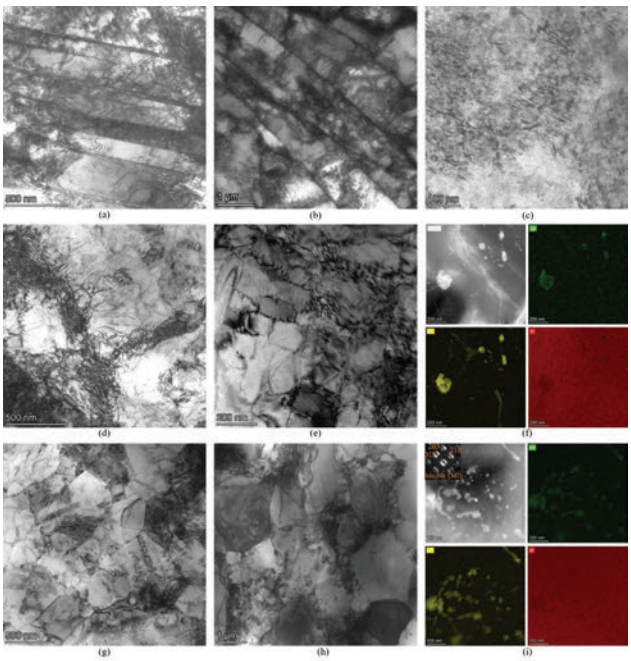


Figure 1. Zr-0.6Nb-0.4Mn alloy: (a) quenched; (b) hot-rolled; (c) cold-rolled; (d-e); annealed at 500°C/2h; (f) STEM-HAADF image and corresponding elemental maps after annealing at 500 °C/2h; (g-h) annealed at 500°C/4h; (i) STEM-HAADF image and corresponding elemental maps after annealing at 500 °C/2h. The inset in Figure 1 (i) corresponds to the convergent beam electron diffraction (CBED) pattern of the Mn_2Nb precipitate along the [362] zone axis

Mapping Local Thermal and Electrical Conductivity in Electronic Ceramics: A Correlative Study via AFM

Danilo Biazon Janes[1,2*], Otavio Berenguel[2], Bruna Sedaca Camargo de Melo[2], Carlos Alberto Rodrigues Costa[2], Tanna Elyn Rodrigues Fiuza[2], Fabiano Emmanuel Montoro[2], Jefferson Bettini, Edson Roberto Leite[1,2]

[1] Federal University of São Carlos (Graduate Program in Materials Science and Engineering), São Carlos, Brazil; [2] Brazilian Center for Research in Energy and Materials, Campinas, Brazil.
*E-mail: djanes@estudante.ufscar.br

Zinc oxide (ZnO) varistors are electronic ceramic devices widely used to protect electrical systems against voltage surges, a function that originates from their highly non-linear current-voltage (I-V) behavior. This response is not an intrinsic property of pure ZnO but rather a consequence of its polycrystalline microstructure, where semiconducting ZnO grains are separated by thin, electrically active intergranular phases. These grain boundary phases are formed from oxide additives, such as Bi_2O_3, which is responsible for creating the potential barriers that dictate non-ohmic properties, and Sb_2O_3, which plays a crucial role in grain size control through the formation of spinel phases [1]. Despite the commercial success of these components, understanding the relationship between the local composition and the device's electrical and thermal performance at the nanoscale remains a challenge [2]. Conventional characterization techniques offer a limited view of local properties, especially concerning thermal management, a critical factor for the varistor's reliability and lifespan. In this context, this work revisits the microstructural analysis of ZnO varistors by employing a set of advanced atomic force microscopy (AFM) techniques: Scanning Thermal Microscopy (SThM), conductive-AFM (c-AFM), and capacitance gradient (dC/dz) measurements. To achieve a comprehensive characterization, a key methodology was developed to track and analyze the exact same microstructural region across different AFM platforms. Furthermore, the sample thickness was progressively reduced while preserving the specific area of interest, allowing for the simultaneous monitoring of property evolution and the identification of local bottlenecks. Complementary dual-beam microscopy (FIB-SEM) was performed for phase identification and 3D reconstruction to evaluate phase percolation. As revealed by the correlative AFM maps (Figure 1), the SThM analyses (Figure 1D) demonstrated that the secondary phases responsible for the device's non-linear electrical behavior act as severe thermal bottlenecks, significantly hindering local thermal conductivity. Concurrently, c-AFM measurements (Figure 1B) demonstrated a persistent electrical contrast between adjacent grains, underscoring the dominance of interfacial barriers over bulk volume. Ultimately, these findings provide critical insights into the nanoscale transport phenomena of ZnO ceramics, establishing a framework for microstructural engineering capable of balancing superior electrical varistor performance with optimized thermal dissipation.

References

[1] CLARKE, D. R. Varistor ceramics, vol. 82, n. 3, p. 485–502, Journal of the American Ceramic Society, 1999.

[2] VAGHEF-KOODEHI, A. Processing–Structure–Property Relationships in Nanostructured ZnO Varistors: Effects of Advanced Sintering and Additive Design. Ceramics International, 2025.

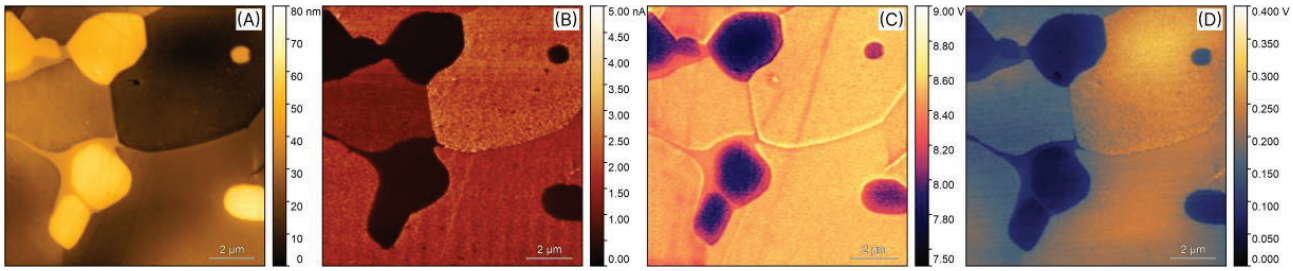


Figure 1. Nanoscale correlative characterization of a ZnO varistor microstructure via AFM modes.
(A) Topography, (B) conductive-AFM (c-AFM), (C) capacitance gradient (dC/dz) map, and (D) Scanning Thermal Microscopy (SThM) signal. All images display the identical spatial region, showing the correlation between local electrical, electrostatic, and thermal transport phenomena.

Microscopia Óptica das Marcas Superficiais Induzidas por Chatter no Torneamento de Aço

Augusto de Souza Graceto[1*], Elvis Soares da Silva[1], Sidney Bruce Shiki[1], Carlos Eiji Hirata Ventura[1], Armando Italo Sette Antonialli[1].

[1] Universidade Federal de São Carlos, São Carlos, Brasil.
*E-mail: augustograceto@estudante.ufscar.br

O torneamento é uma operação fundamental na fabricação mecânica e sua produtividade é frequentemente limitada pelo fenômeno da vibração regenerativa, amplamente conhecido na literatura como chatter. Esta instabilidade dinâmica resulta em oscilações severas entre a ferramenta e a peça, comprometendo a vida útil do ferramental e degradando significativamente a integridade da superfície usinada [1]. A motivação deste estudo reside na necessidade de caracterizar morfologicamente essas marcas por meio de microscopia óptica, correlacionando os parâmetros de corte com os padrões topográficos resultantes. Os procedimentos experimentais foram realizados em um eixo de aço carbono AISI 1045 com diâmetro de 50 mm e dureza média de 239 HB. O sistema de corte utilizou insertos de cermet não revestidos (ISO HT P10), com raio de ponta de 0,2 mm. As condições de ensaio foram executadas sem fluido de corte, mantendo-se o avanço em 0,05 mm e variando-se os demais parâmetros de corte de forma sistemática para explorar os limites de estabilidade do sistema. Foram avaliadas as combinações de velocidade de corte de 80 m/min e profundidade de usinagem de 0,5 mm, 1,0 mm e 1,5 mm, além de um teste adicional com velocidade 160 m/min e profundidade 0,5 mm. Os resultados demonstraram que a estabilidade do processo define diretamente a assinatura microtopográfica da peça fabricada. Em condições de corte estável, obtidas com profundidade de 0,5 mm, a microscopia revelou uma superfície lisa e dominada por marcas de avanço regulares e paralelas (Figura 1), apresentando uma rugosidade condizente com a classe N6 estipulada pela norma ISO 1302 [2].

Em contrapartida, os testes realizados com profundidades mais elevadas ultrapassaram o limite de estabilidade, resultando em vibração dinâmica severa. Nestes casos, a análise microscópica evidenciou o quase desaparecimento das marcas de avanço regulares, dando lugar a um padrão morfológico complexo em formato de "escamas" ou facetas (Figura 2). Esse padrão é decorrente do impacto e do salto cíclico da ferramenta sobre a superfície, consolidando a concepção de texturização induzida por vibração [3]. Essa condição crítica impactou o acabamento, atingindo patamares equivalentes à classe de rugosidade N8. Conclui-se, portanto, que a microscopia óptica constitui uma ferramenta diagnóstica robusta e eficaz para a validação visual do estado do processo. Ela permite diferenciar claramente superfícies com acabamento mais fino daquelas texturizadas por vibrações, servindo como evidência empírica da transição entre regimes estáveis e instáveis de usinagem.

References

[1] Urbikain, G., Olvera, D., López de Lacalle, L. N., Beranoagirre, A., & Elías-Zuñiga, A. (2019). Prediction Methods and Experimental Techniques for Chatter Avoidance in Turning Systems: A Review. *Applied Sciences*, 9, 4718.

[2] International Organization for Standardization. (2002). *ISO 1302:2002 - Geometrical Product Specifications (GPS) - Indication of surface texture in technical product documentation*. 4th ed. Geneva: ISO.

[3] Gibim, T. C. S., Savella, F. B., Trevilato, R., Shiki, S. B., Ventura, C. E. H., & Antonialli, A. I. S. (2025). A Case Study Regarding Vibration-Induced Texturing in Turning. *Materials Research*, 28, e20250235.

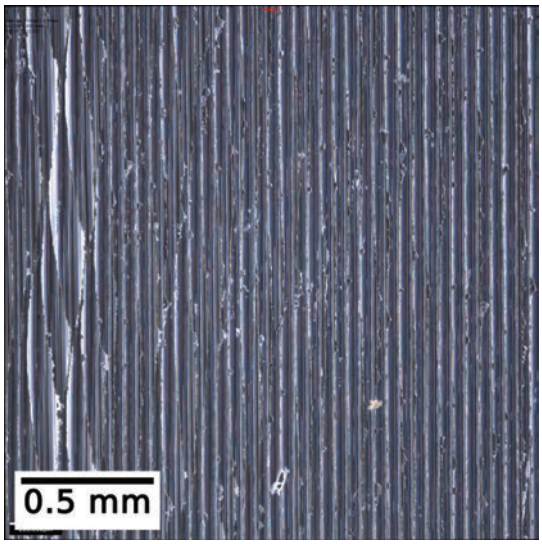


Figure 1. Microscopia óptica da superfície produzida com velocidade de corte 160 m/min e profundidade de usinagem 0,5 mm, exibindo o padrão regular de marcas de avanço gerado em condição de corte estável.

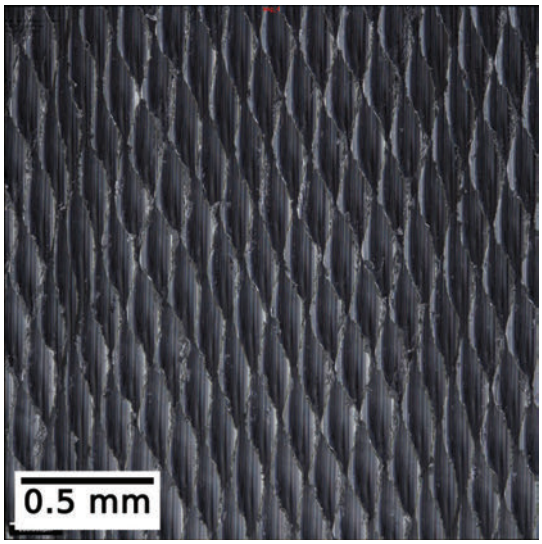


Figure 2. Microscopia óptica da superfície produzida com velocidade de corte 80 m/min e profundidade de usinagem 1,5 mm, ilustrando o padrão escamado derivado da vibração excessiva em condição de usinagem com *chatter*.

Microstructural Analysis of Novel Metastable β-type Titanium Alloys Aiming at Biomedical Applications

Fernanda de Freitas Quadros[1,2], Giovana Collombaro Cardoso[1,2], Pedro Akira Bazaglia Kuroda[3], Conrado Ramos Moreira Afonso[4], Diego Rafael Nespeque Correa[1,2], Carlos Roberto Grandini[1,2*]

[1] UNESP, Laboratório de Anelasticidade e Biomateriais, Bauru, SP; [2] CMDTA – Centro Multidisciplinar para o Desenvolvimento de Tecnologia Assistiva, Bauru, SP; [3] UNILA - Universidade Federal da Integração Latino-Americana, Foz do Iguaçu, PR; [4] UFSCar, Departamento de Engenharia de Materiais, São Carlos, SP.
*E-mail: carlos.r.grandini@unesp.br

Titanium-based alloys containing β-stabilizing elements have attracted significant attention for advanced structural and biomedical applications due to their low elastic modulus, high corrosion resistance, and favorable mechanical performance [1]. In this study, a detailed microstructural investigation of metastable β-type titanium alloys was conducted using complementary microscopy and microanalysis techniques to elucidate phase constitution, morphology, and chemical homogeneity. The alloys were synthesized by arc melting under an inert atmosphere and subsequently subjected to homogenization heat treatment to reduce compositional segregation. Optical microscopy revealed equiaxed prior-β grain structures in both compositions, with notable differences in grain size and intragranular features. Scanning electron microscopy (SEM) combined with backscattered electron (BSE) imaging highlighted compositional contrast associated with elemental partitioning, particularly between Ti and high-atomic-number β-stabilizers. Energy-dispersive X-ray spectroscopy (EDS) mapping confirmed good overall chemical homogeneity. Electron backscatter diffraction (EBSD) analysis revealed a dominant β phase, with local crystallographic heterogeneities indicative of stress-induced or quenched metastable phases. Transmission electron microscopy (TEM) further revealed nanoscale features, including lattice distortions and diffuse diffraction patterns indicative of short-range ordering or incipient phase transformations, as well as the presence of the omega phase. Comparative microstructural analysis highlights the strong influence of alloying chemistry on phase stability and microstructural refinement in β-Ti alloys [2,3]. These findings provide critical insights into structure–property relationships and demonstrate the importance of multi-scale microscopy and microanalysis for guiding the design of next-generation titanium alloys with tailored mechanical and functional properties [4].

References

[1] T. Hanawa, Metallic Biomaterials: Metals for Medical Devices, CRC Press, 2025.

[2] G.C. Cardoso et al., J. Mat. Res. Tech., v. 25, p. 3061-3070, 2023.

[3] F.F. Quadros et al., J. Mat. Res. Tech., v. 28, p. 3699-3706, 2024.

[4] This research was supported by Capes, CNPq, and FAPESP (Brazil).

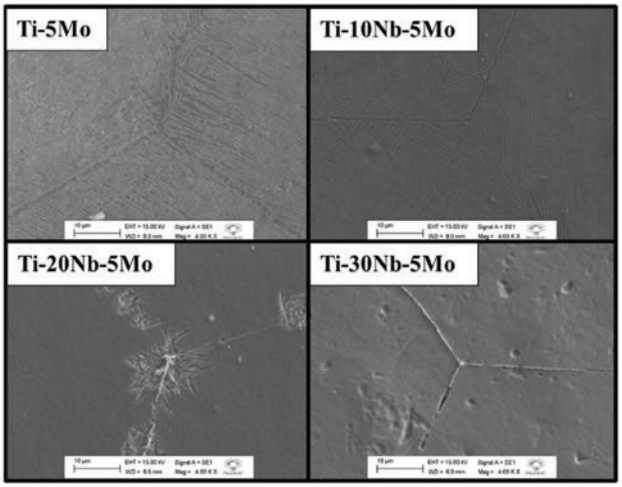


Figure 1. SEM micrographs of the Ti-Nb-5Mo alloys as a function of Nb content [2].

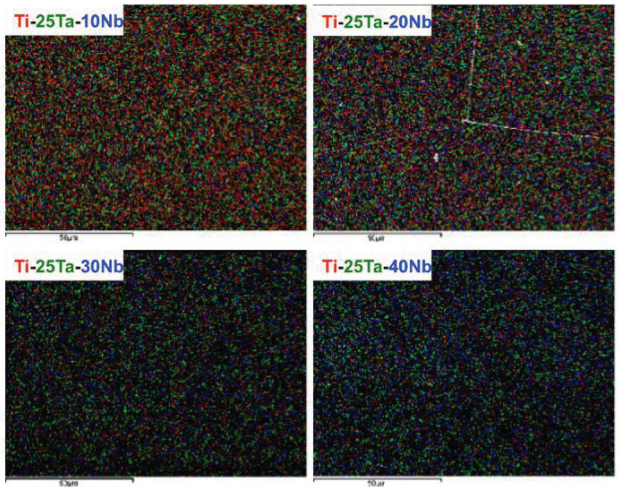


Figure 2. SEM micrographs of the Ti-25Ta-Nb alloys as a function of Nb content [3].

Phase Identification in Multiphase Discontinuous Precipitation Colonies in a Cr-Fe-Ni-N Alloy using EBSD Pattern-Matching Indexing

Julio Spadotto[1,2], Francisco Coury[3], Tristan Manchester[1], Brian Connolly[1], Grace Burke[1,4], Guillermo Solorzano[2]

[1] Department of Materials, The University of Manchester, UK; [2] Chemical and Materials Engineering Department, PUC-Rio, Rio de Janeiro, Brazil; [3] Department of Materials Engineering, UFSCar, Brazil; [4] Idaho National Laboratory, Idaho Falls, ID, USA.

The discontinuous precipitation (DP) reaction is a diffusion-controlled transformation occurring at grain boundaries (GBs), leading to the formation of complex microstructures that can significantly affect the performance of structural alloys [1]. In multicomponent systems containing both substitutional and interstitial elements, such as Alloy 33 (Cr–Fe–Ni–N), the DP reaction becomes particularly complex due to the potential formation of multiple competing phases [2]. Understanding the crystallographic and chemical nature of these phases, as well as their spatial distribution, is essential for establishing reliable structure–property relationships. In this context, advanced electron microscopy techniques play a central role in resolving such complex microstructures. In this study, the microstructural evolution of Alloy 33 aged at 800 °C for 20, 50, and 100 h was investigated using a comprehensive analytical electron microscopy (AEM) approach. The experimental methodology combined scanning electron microscopy (SEM), electron backscatter diffraction (EBSD), transmission electron microscopy (TEM), scanning transmission electron microscopy (STEM), and X-ray energy-dispersive spectroscopy (XEDS), supported by X-ray diffraction (XRD) and CALPHAD thermodynamic calculations. Particular emphasis was placed on EBSD-based phase identification over large areas, complemented by TEM/STEM analyses for local crystallographic and chemical validation. EBSD data were analysed using both conventional Hough transform-based indexing and advanced pattern-matching indexing (MapSweeper, AZtecCrystal Software, Oxford Instruments Nanoanalysis). Pattern matching employed simulated Kikuchi patterns for phase identification and was validated through correlation with SEM-XEDS elemental maps. This combined EBSD–XEDS strategy enabled accurate phase discrimination in regions where conventional Hough indexing approaches are prone to ambiguity. Low-kV SEM-XEDS was additionally used to improve nitrogen detection and support nitride identification. The results reveal that the DP reaction in Alloy 33 leads to the formation of highly heterogeneous microstructures, with up to five different precipitated phases coexisting within a single DP colony, as shown in Figure 1. These include FCC Cr-rich $M_{23}C_6$, diamond-cubic Si-enriched M_6N, BCC α-Cr phase, tetragonal σ-phase, and hexagonal M_2N. The combination of EBSD and TEM analyses confirmed that all precipitated phases exhibit defined orientation relationships with the FCC matrix, indicating strong crystallographic coupling during DP growth. This work demonstrated the limitation of conventional Hough-based EBSD indexing in reliably distinguishing between crystallographically similar phases, particularly the FCC matrix, FCC $M_{23}C_6$, and diamond-cubic M_6N (Figure 2a). These phases can generate nearly indistinguishable Kikuchi patterns due to structural similarities, leading to significant misindexing and incorrect phase fraction estimation when Hough-based indexing was applied. In contrast, pattern-matching indexing significantly improved phase discrimination by exploiting full-pattern information (Figure 2b). This approach enabled accurate identification of $M_{23}C_6$ at GBs and correct localization of M_6N, which was frequently misidentified as FCC matrix using Hough-based methods. Quantitative comparison further showed that Hough-based indexing leads to substantial errors in phase fraction estimation, including overestimation of M_6N and underestimation of α-Cr and M_2N. Pattern matching not only improved spatial phase identification but also provided a more reliable basis for quantitative microstructural analysis. This is particularly important for complex multiphase alloys, where accurate phase quantification is critical for understanding transformation mechanisms and material performance.

References

[1] Williams DB, Butler EP. Grain boundary discontinuous precipitation reactions. Int Mater Rev 1981;26:153–83.

[2] Spadotto JC, Burke MG, Solórzano IG. On the morphology of grain boundary discontinuous reactions and phase identification in an advanced Cr–Fe–Ni alloy. J Mater Sci, 55, 10221–10241, 2020.

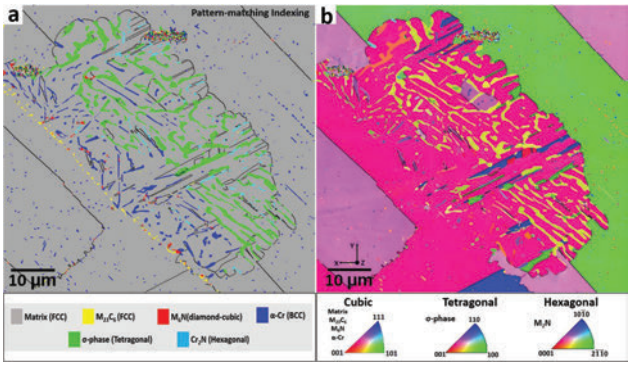


Figure 1 – EBSD maps obtained using pattern-matching indexing of a DP colony at a GB in Alloy 33 aged at 800 °C for 50 h. (a) Phase map and (b) IPF-Z map.

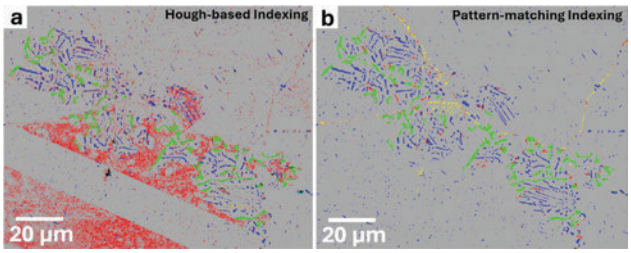


Figure 2. EBSD phase maps of DP colonies at GBs in Alloy 33 aged at 800 °C for 50 hours, obtained with (a) Hough-based indexing and (b) pattern-matching indexing.

PÔSTER

Analysis of long-term contact with sea water impacts into gray iron cast microstructure

Vinícius Felippe Elias[1], Leandra Marques[1], Lorena Maria da Silva[1], Eric Marchezini Mazzer[1], Francisco Gil Coury[1]

[1] Federal University of São Carlos, Department of Materials Engineering.
*E-mail: vinicius.felippe@estudante.ufscar.br

Assuring the long-term survival of metallic alloys in marine environments remains a major engineering challenge. The combined action of dissolved oxygen and chloride ions severely speeds up material degradation. In gray cast irons, this process depends heavily on their internal structure: the network of graphite flakes acts as a cathode within local galvanic couples, driving the fast oxidation of the surrounding iron matrix. This paper studies a gray cast iron specimen taken from a historic cannon that spent about two centuries underwater, focusing on the evaluation of both its surviving microstructure and the resulting corrosion layers. The diagnostic approach integrated Optical Microscopy (OM), Scanning Electron Microscopy (SEM), and X-ray Diffraction (XRD). Structural examinations via OM and SEM confirmed the persistence of a typical gray iron matrix featuring lamellar graphite, illustrating how parts of the original metal withstood the environment. Conversely, XRD data indicated that centuries of underwater exposure induced partial mineralization, converting the outer layers into stable oxide phases, chiefly magnetite (Fe_3O_4) along with maghemite (γFe_2O_3) and hematite (αFe_2O_3). These findings were validated by thermodynamic modeling using a Pourbaix diagram for the Fe-H_2O system tailored to marine parameters, which confirmed the stability of the detected species. Ultimately, this historical case study enhances our understanding of the exceptionally long-term corrosion behavior of cast irons, offering empirical data to refine predictive lifecycle models for metals in severe oceanic environments.

References

[1] ASHKENAZI, D. et al. A method of conserving ancient iron artefacts retrieved from shipwrecks using a combination of silane self-assembled monolayers and wax coating. **Corrosion Science**, v. 123, p. 88–102, Jul. 2017.

[2] MELCHERS, R. E. Long-term corrosion of cast irons and steel in marine and atmospheric environments. **Corrosion Science**, v. 68, p. 186–194, Mar. 2013.

[3] WOOD, R. J. K. Marine wear and tribocorrosion. **Wear**, v. 376-377, p. 893–910, Apr. 2017.

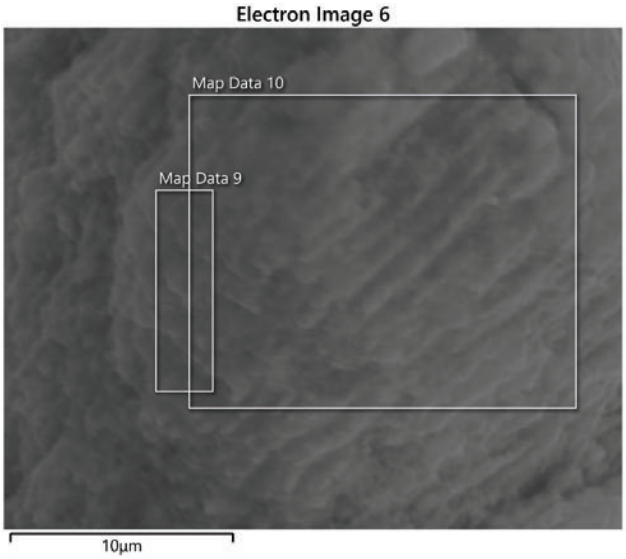


Figure 1. SEM image of the gray cast iron matrix

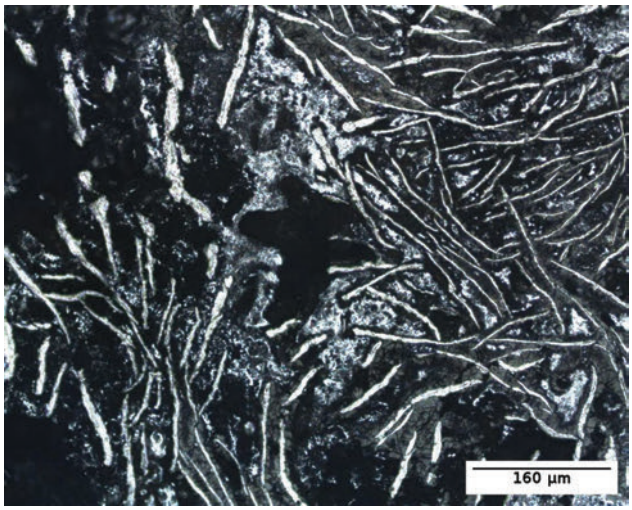


Figure 2. Optical Microscopy of the gray cast iron

Analysis of Pitanga-Like Vanadium Oxide Nanostructures Obtained by the Nanoemulsion Method

Lucas H. M. Paodjuenas[1*], Fernanda T. L. Serrão[1], Marco A. L. Cordeiro[1]

[1] Federal University of São Carlos (UFSCAR),Department of Materials Engineering.
*E-mail: lucas.paodjuenas@estudante.ufscar.br

Nanoemulsions are liquid-liquid colloidal dispersion systems with droplet sizes ranging from 20 to 500 nm, widely explored in the cosmetic and pharmaceutical industries, as well as confinement structures for the synthesis of nanostructures, such as metal oxide nanoparticles [1,2]. Among metal oxides, vanadium oxide exhibits particularly interesting properties, such as multiple oxidation states, making it suitable for catalytic, optical, and electrical applications [3]. Despite the well-documented properties of vanadium oxide, controlling morphology and oxidation state through new synthesis protocols remains an open challenge. In this scenario, nanoemulsion-based routes emerge as a promising alternative, since the confinement provided by the emulsion droplets can direct both nucleation and growth, potentially enabling the formation of unusual. This study reports the synthesis of V_2O_3 nanostructures via a water-in-oil nanoemulsion route and investigates the resulting morphology and crystal structure. Ammonium metavanadate (NH_4VO_3) was dissolved in distilled water and added dropwise to oleic acid under vigorous stirring. The resulting mixture was further processed using a homogenizer at 8000 rpm for 3 minutes to promote the emulsion formation. The emulsion was then transferred to an autoclave and treated at 280 °C for 12 hours. X-ray diffraction (XRD) and scanning electron microscopy (SEM) analysis confirmed the formation of phase-pure rhombohedral V_2O_3, while SEM images revealed pitanga-like nanostructures (PL) with an average diameter of approximately 400 nm as shown in Figure 1. The transmission electron microscopy (TEM) analysis enabled a more detailed evaluation of the formation of these nanostructures. V_2O_3 nanoparticles (NPs) with an average size of approximately 7 nm were observed. In addition to these nanoparticles, star-like nanostructures with diameters of approximately 250 nm were identified, as demonstrated in Figure 2. High-resolution transmission electron microscopy (HRTEM), Figure 3, confirmed the interplanar distance of 0.27 nm associated with the crystallographic plane (104) of the rhombohedral structure of V_2O_3, in agreement with the results obtained from the XRD analysis. The proposed hypothesis for the formation of these nanostructures is that the NPs initially assemble into the star-like morphology. As the reaction progresses, this star-like structure gradually evolves into the denser "pitanga-like" morphology through the continuous incorporation of additional nanoparticles into the structure. The multi-scale characterization allowed us to identify intermediate star-like structures and primary nanoparticles in the vicinity of the PL, supporting a sequential growth mechanism in which NPs progressively assemble into increasingly dense architectures. To the best of our knowledge, this is the first report of this morphology obtained via a nanoemulsion-templated route. Ongoing studies varying the reaction time aim to map the formation stages and consolidate the proposed mechanism [4].

References

[1] A. Gupta et al.,Soft Matter, 12 (2016) 2826.

[2] H. Liu et al., Colloids and Surfaces A: Physicochemical and Engineering Aspects, 356 (2010) 21.

[3] P. Hu et al.,Chemical Reviews, 123 (2023) 4353.

[4] This research was supported by Conselho Nacional de Desenvolvimento Científico e Tecnológico (CNPq) - Process Number 141816/2025-2. This study was financed in part by the Coordenação de Aperfeiçoamento de Pessoal de Nível Superior - Brasil (CAPES) - Finance Code 001.

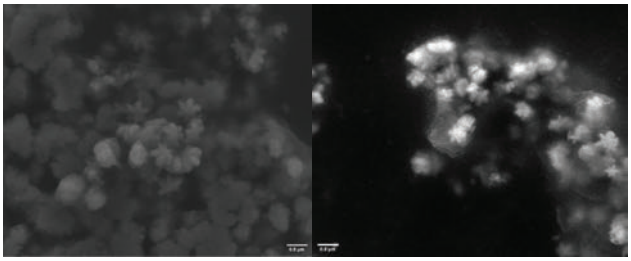


Figure 1. SEM images of the pitanga-like structure in an agglomerated region (right) and in a dispersed region (left).

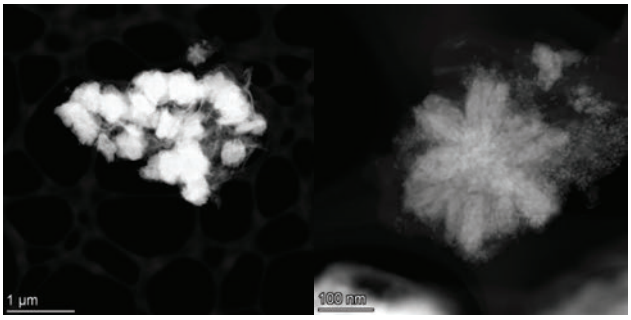


Figure 2. STEM images of the star-like structure located near the pitanga-like structures (left) and of the nanoparticles observed in the vicinity of the star-like structure (right).

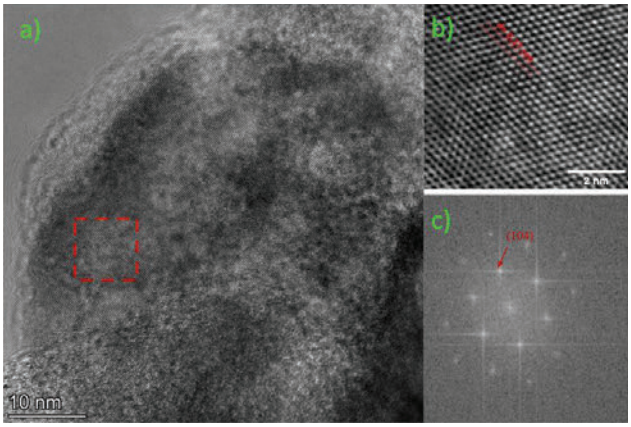


Figure 3. HRTEM images of one extremity of the pitanga-like structure (a), together with the selected area for crystallographic plane analysis (b) and the FFT analysis of this region (c).

Analysis using microscopy techniques of oxide layers formed on the Nb-25Ta-35Ti alloy obtained by micro-arc oxidation

Gabriel Cardoso Rôa[1*], Fernanda de Freitas Quadros[1], Diego Rafael Nespeque Corrêa[1], Carlos Roberto Grandini[1].

[1] São Paulo State University (UNESP).
*E-mail: gc.roa@unesp.br

Nb–Ti-based alloys have attracted significant interest in the biomedical field due to their advantageous mechanical properties, particularly a lower elastic modulus compared to conventional Ti alloys such as Ti-6Al-4V, in addition to their good biocompatibility and high corrosion resistance [1]. However, failures and rejections of internal implants are still reported, highlighting the need for surface engineering strategies to improve osseointegration and long-term biological performance. In this context, the modification of the Nb-35Ti-25Ta alloy by Micro-Arc Oxidation (MAO) emerges as a promising approach, combining favorable bulk properties with the formation of a porous and bioactive oxide coating that can enhance implant performance and durability [2]. The experimental procedures included alloy processing followed by hot rolling and solution treatment, and subsequent MAO treatment at 200, 250, and 300 V under a constant current of 2.5 A for 1 minute, to evaluate the effect of voltage on coating characteristics. The coatings were characterized by Scanning Electron Microscopy (SEM), including surface and cross-sectional analyses, Energy Dispersive Spectroscopy (EDS) with elemental mapping, confocal microscopy, porosity analysis, adhesion testing, and wettability measurements. The results indicate that increasing the applied voltage leads to higher porosity and a more homogeneous pore distribution, while EDS mapping revealed uniform incorporation of electrolyte-derived elements into the oxide layer. Adhesion tests showed a decrease in coating adhesion with increasing voltage, consistent with the formation of thicker and more porous layers, and confocal microscopy indicated an increase in surface roughness as a function of voltage due to more intense micro-arc discharges. Wettability results showed that the sample treated at 250V exhibited the highest hydrophilicity, which favors protein adsorption and may enhance osseointegration. Overall, the Nb-25Ta-35Ti alloy treated by MAO presents promising characteristics for biomedical implant applications, although further analyses are required to better understand the oxide phases and their influence on bioactivity and long-term performance [2,3][4].

References

[1] Correa, D. R. N. et al. Surface and Coatings Technology, v. 344, p. 373-382, 2018.

[2] Gebert, A. et al. Surface and Coatings Technology, v. 302, p. 88-99, 2016.

[3] Quadros, F. F. et al. Journal of Materials Research and Technology, v. 28, p. 3699-3706, 2024.

[4] The authors would like to thank the followingthe Brazilian agencies for their financial support: CNPq, grant #314.810/2021-8, and FAPESP grants #2024/01.132-2 and #2024/22.415-2.

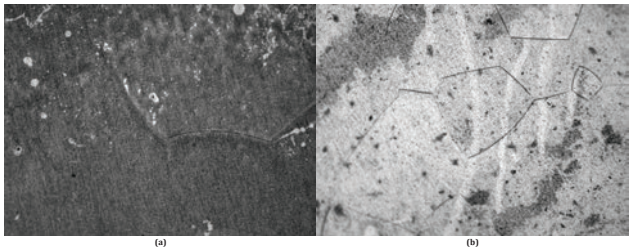


Figure 1. Optical microscopy images of the raw (a) and treated (b) samples.

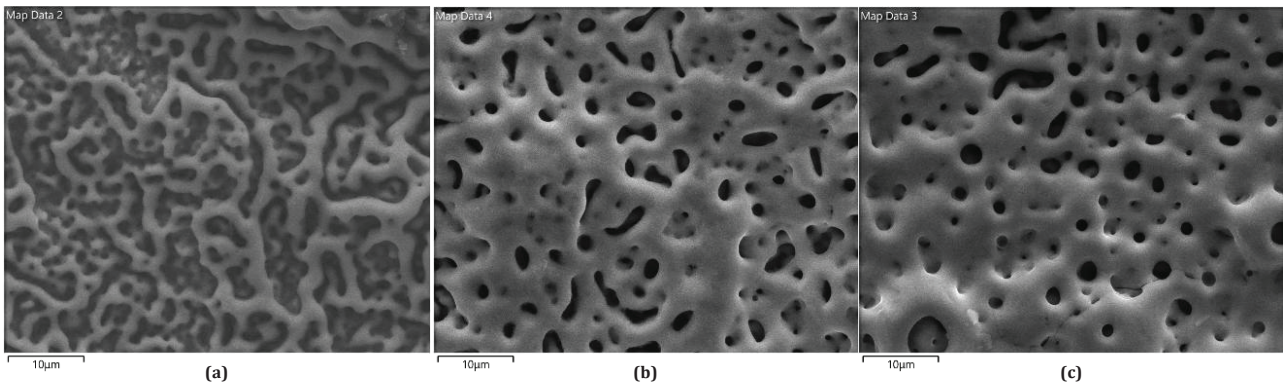


Figure 2. SEM images of the coatings obtained at 200V (a), 250V (b), and 300V (c).

Table 1. Surface roughness parameters and contact angle measurements of the coatings obtained at different voltages.

Contact angles (°)				
Sample	**Voltage (V)**	**Roughness (µm)**	**Deionized Water**	**Glycerol**
Nb-25Ta-35Ti	200	1,3 ± 0,2	103,3 ± 3,0	108,6 ± 2,5
	250	1,6 ± 0,4	84,1 ± 2,7	100,9 ± 3,8
	300	2,1 ± 0,1	135,9 ± 0,8	115,0 ± 6,2

Biotechnological system based on hybrid hydrogel spheres for the release of Zn and plant growth-promoting bacteria

Débora Ribeiro Antunes[1*], Mariana M. L. H. Forini [1], Heloiza F. Alves do Prado[2], Renato Grillo[1*]

[1] São Paulo State University (UNESP), Faculty of Engineering, Ilha Solteira, SP, Brazil; [2] Institute of Biosciences, Rio Claro, SP, Brazil.
*E-mail: debora.antunes@unesp.br, renato.grillo@unesp.br

With population growth and climate change, agriculture faces the challenge of increasing food production sustainably. In this context, zinc (Zn) deficiency stands out, being the most limiting micronutrient for agricultural crops on a global scale, exacerbated by dependence on fertilizers and pesticides that can cause environmental impacts [1]. In this context, nanotechnology has contributed to the development of nanofertilizers capable of increasing Zn efficiency, reducing leaching losses, and promoting controlled release. Simultaneously, the use of microorganisms in agriculture has grown, especially plant growth-promoting bacteria (PGPB), such as *Azospirillum brasilense*, which favor biological nitrogen fixation and plant development. The combination of BPCP and Zn has also been investigated due to the synergy between nanoparticles and bacteria, which can increase the bioavailability and absorption of Zn by plants. However, the efficiency of these compounds can be limited by interactions with abiotic factors in the environment. Therefore, controlled-release systems based on hydrogels have been developed to increase their stability and efficiency in the field, notably polysaccharide hydrogel spheres, which encapsulate and protect the active ingredients, in addition to exhibiting biocompatibility and biodegradability. Hybrid systems of organic and inorganic materials show potential for more sustainable agriculture, although their effectiveness is not yet complete. In this context, the present study aimed to develop a biotechnological system based on hybrid hydrogel spheres, consisting of a pure alginate matrix and an alginate/xylan matrix, for the co-encapsulation of zinc oxide nanoparticles (ZnONPs) and the bacterium *A. brasilense*, aiming at the simultaneous release of micronutrients and microorganisms. ZnONPs were synthesized by precipitation [2], followed by the preparation of spheres by ionic gelation. Physicochemical analyses confirmed the formation of ZnONPs. UV-Vis spectroscopy showed a band at 359 nm (Fig. 1A), characteristic of ZnO, while FTIR revealed bands associated with the Zn–O interaction (Fig. 1B). XRD results (Fig. 1C) indicated a hexagonal wurtzite-type structure, characteristic of ZnO, and an average crystallite size of ~19.8 nm. The SEM/EDS analyses (Fig. 1D–E) showed clusters of nanoparticles and the presence of Zn, as well as a zeta potential of −15.19 ± 1.97 mV. The TEM revealed a faceted polyhedral morphology (Fig. 1F) and well-defined lattice fringes (Fig. 1G), and the diffractogram (Fig. 1H) indicated the polycrystalline nature of the nanoparticles. The SEM micrographs of the hybrid systems consisting of pure alginate and alginate/xylan matrices (Figs. 2 and 3) showed a spherical morphology, with alterations in the surface and cross-section due to the polysaccharide blend. The presence of ZnONPs and *A. brasilense* was also observed in both systems. DSC analyses indicated alterations in thermal properties, while the release kinetics were associated with different transport mechanisms. Thus, the developed system shows potential for applications in sustainable agriculture, by modifying matrix properties and allowing the simultaneous release of assets, favoring plant development and reducing environmental impacts [3].

References

[1] D.R. Antunes et al., *Int. J. Biol. Macromol*, (2026): 151216.

[2] A. Aditya et al., *ACS applied materials & interfaces* 10.18 (2018): 15401-15411.

[3] This research was supported by FAPESP (#2022/03219-2;#2023/00541-3;# 2023/09217-4).This study was financed in part by the Coordenação de Aperfeiçoamento de Pessoal de Nível Superior - Brasil (CAPES) - Finance Code 001. The authors acknowledge Embrapa Soja, Londrina, Brazil, for providing the bacterial strains of *Azospirillum brasilense.*

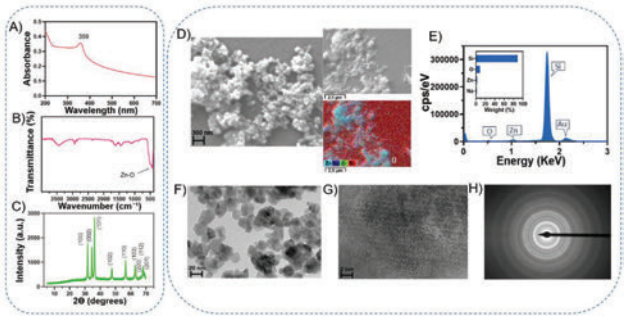


Figure 1. Characterization of ZnO nanoparticles: A) UV-Vis spectrum; B) FTIR spectra; C) X-ray diffractogram; D) SEM/EDS micrograph; E) EDS mapping summary; F) TEM micrograph; G) High-resolution TEM (HRTEM); H) Micrograph with the inset showing the Fast Fourier Transform (FFT) diffraction pattern.

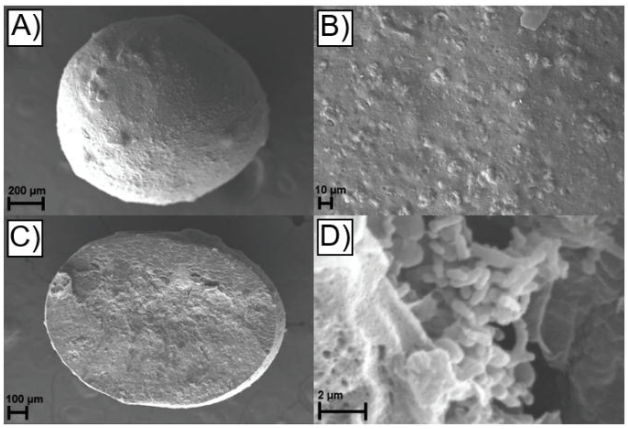


Figure 2. Micrograph of the hybrid alginate sphere: A) Morphology; B) Surface; C) Cross-section; D) Pores of the sphere exhibiting ZnONPs and *A. brasilense.*

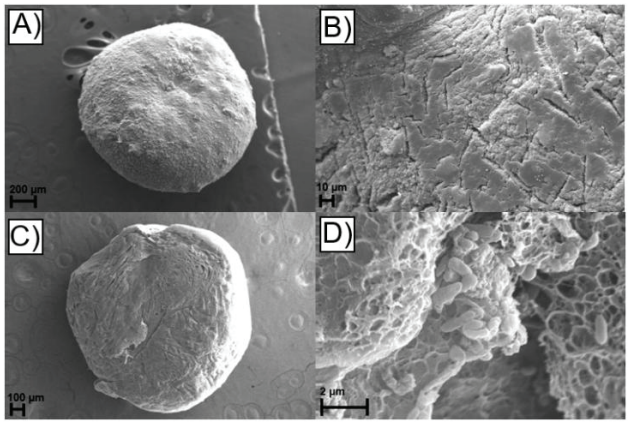


Figure 3. SEM micrograph of the hybrid Alginate/Xylan sphere: A) Morphology; B) Surface; C) Cross-section; D) Pores of the sphere exhibiting ZnONPs and *A. brasilense*.

Characterization of β TiNbZrTa Alloy Powder Produced by Ultrasonic Atomization for Additive Manufacturing

Renan A. F. Dias[1*], Mariana L. Lourenço[1], Conrado R. M. Afonso[1]

[1] BioMet-CAM, Department of Materials Engineering (DEMa), Universidade Federal de São Carlos (UFSCar).
*E-mail: rafdias@ufscar.br

Over the years, β-type titanium (Ti) alloys have become some of the most attractive biomaterials due to their low elastic modulus, which reduces stress-shielding effects, and the absence of toxic elements such as aluminum and vanadium in their composition. In parallel, additive manufacturing (AM) techniques, like laser powder bed fusion (LPBF), have enabled the production of customized implants for specific patients. However, the high cost of β-phase stabilizing elements, such as Mo, Ta, and Nb, together with the elevated production costs, limits the availability and diversity of β-type titanium powders on the market. The aim of this study was to produce micrometric powders and characterize a β-type Ti powder obtained by ultrasonic atomization (UA) for laser powder bed fusion (LPBF). Three ingots of a quaternary equimassic and multiprincipal Ti-25Nb-25Ta-25Zr alloy (wt%) produced by arc melting were atomized using an ATO Lab+ US35 machine at the BioMet-CAM laboratory, currently one of the few operational ultrasonic atomization facilities in Latin America. Powder characterization was conducted by Optical Microscopy (OM), Scanning Electron Microscopy (SEM) coupled with Energy Dispersive Spectroscopy (EDS), Laser Diffraction (LD) and X-ray Diffraction (XRD). Approximately 80% of the obtained powder was within the optimal particle size range for additive manufacturing, between 32 and 75 µm, presenting high sphericity, absence of satellite particles and a fully β-phase microstructure. These results demonstrate the potential of ultrasonic atomization for the production of β Ti powders suitable for additive manufacturing of biomedical implants [4].

References

[1] F. De Mattos et al., Mater. Lett. 358 (2024) 135776.

[2] C.R.M. Afonso et al., J. Mater. Res. Technol. 40 (2026) 1869–1881.

[3] M.L. Lourenço et al., submitted for publication in J. Mater. Res. Technol.

[4] This research was supported by FAPESP PAIP 2023/16836-2 and partially supported by CAPES, Finance Code 001 (Brazil).

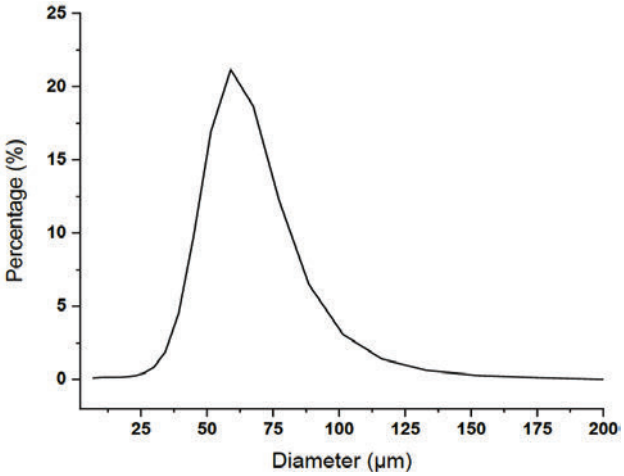


Figure 1. Powder size distribution.

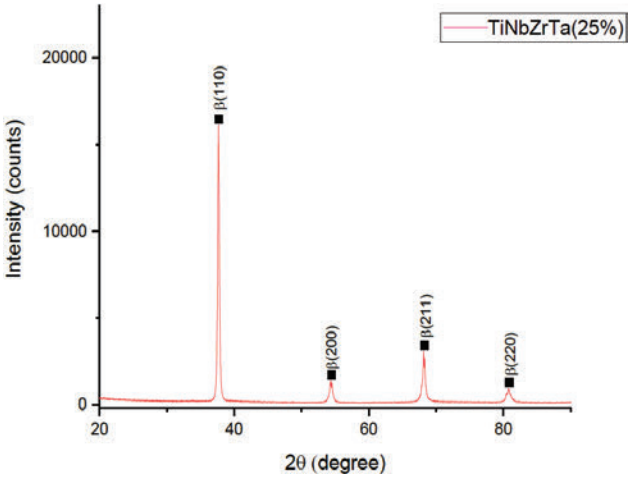


Figure 2. XRD of the powder

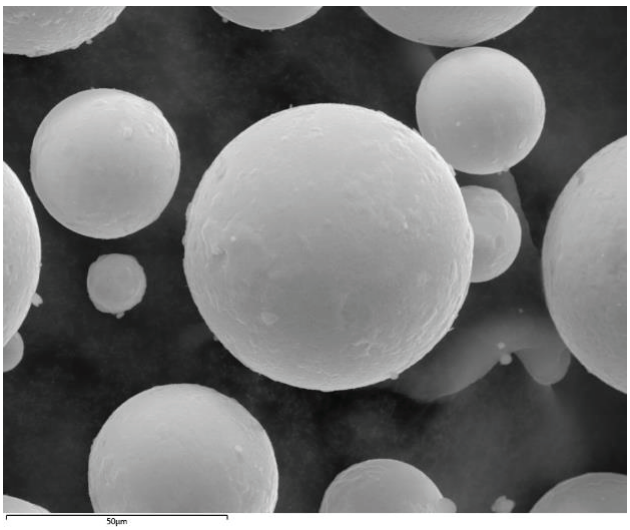


Figure 3. Powder morphology

Characterization of Ni-superalloy MAR-M247 modified with Nb Powder Produced by Ultrasonic Atomization for Additive Manufacturing

Isabela Maria da Silva[1*], Renan Dias[1], Mariana S. Pereira[2], Carlos A. Nunes[3], Conrado R. M. Afonso[1]

[1] BioMet-CAM, Department of Materials Engineering (DEMa), Universidade Federal de São Carlos (UFSCar); [2] PPG-CEM/UFSCar; [3] Escola de Engenharia de Lorena (EEL)/Universidade de São Paulo (USP).
*E-mail: isabela.silva@estudante.ufscar.br

The nickel-based superalloy Mar-M247 is an industrial reference material in the aerospace sector for high-performance components due to its high mechanical strength and chemical stability at elevated temperatures. Currently, research seeks the strategic substitution of Tantalum (Ta) by Niobium (Nb) aiming at cost optimization and density reduction. The study of these Ni-Nb systems is fundamental for conventional metallurgy and for the development of new processing routes and customized alloys. The motivation of this study is based on the need to understand how the replacement of Ta by Nb and different cooling rates impact phase formation, seeking to compare the Mar-M247(Nb) alloy in the as-cast state (slow solidification) with the atomized powder (rapid solidification). The objective is to evaluate the suppression of deleterious phases, such as the Laves phase, and to promote the refinement of gamma-prime (γ′) precipitates and MC carbides, ensuring material quality for metal 3D printing processes. To achieve this, the Mar-M247(Nb) superalloy was melted in a vacuum induction melting (VIM) furnace, while powder production was carried out via ultrasonic atomization using the ATO Lab+ US35 machine at the BioMet-CAM laboratory. Microstructural characterization involved metallographic preparation, Optical Microscopy, Scanning Electron Microscopy (SEM/EDS), X-Ray Diffraction (XRD), and Vickers microhardness tests (500 g for 15 s). The characterization of the niobium-modified MAR-M247 alloy revealed that the fusion morphology is predominantly dendritic, characteristic of a solidification process controlled by this regime. After the ultrasonic atomization process, particle size analysis demonstrated that approximately 80% of the mass of the atomized material is concentrated in the range of 32 to 75 µm. Scanning electron microscopy (SEM) analysis revealed that the particles obtained were completely spherical, without significant deformations. Furthermore, the internal microstructure of the particles exhibited a refined cellular morphology, characteristic of the rapid solidification inherent to the ultrasonic atomization process. This result is fundamental, as it confirms that the ultrasonic atomization technique is effective in obtaining powders with particle size and morphological characteristics suitable for the LPBF (Laser Powder Bed Fusion) process. Finally, EDS analysis demonstrated that the chemical composition of the powder is compatible with the Niobium-modified MAR-M247 alloy available in the literature, validating the chemical stability of the material after processing [4].

References

[1] COSTA, A. M. S. et al. Microstructural and Mechanical Characterization of Directionally Solidified Conventional and Nb-Modified Mar-M247 Superalloy. *Journal of Materials Engineering and Performance*, v. 28, p. 2427-2438, 2019.

[2] SILVA, I. M. Microstructural Characterization of Ni-Nb-M Based Superalloy Metallic Powders Produced by Ultrasonic Atomization. Scientific Initiation Project (CNPq-PIBIC), UFSCar, 2025.

[3] REED, R. C. *The Superalloys: Fundamentals and Applications*. Cambridge University Press, 2006.

[4] This research was supported by FAPESP PAIP 2023/16836-2 and Grant 2025/27069-8 and This study was partially supported by CAPES. Finance Code 001.

Table 1. Particle Size Distribution of the MAR-M247 Alloy

< 20	0.4	0.2%	0.2%
20 - 32	3.1	1.9%	2.1%
32 - 53	30.7	18.4%	20.5%
53 - 75	102.9	61.8%	82.3%
> 75	29.5	17.7%	100.0%
TOTAL	**166.5**	**100.0%**	-

Source: Prepared by the authors (2026)

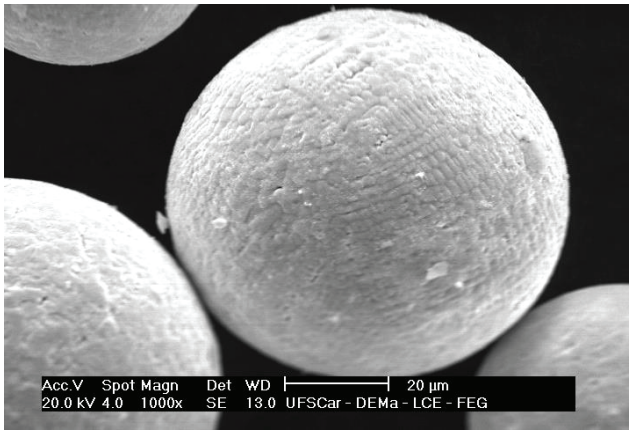


Figure 1. SEM micrograph of the atomized MAR-M247(Nb) superalloy

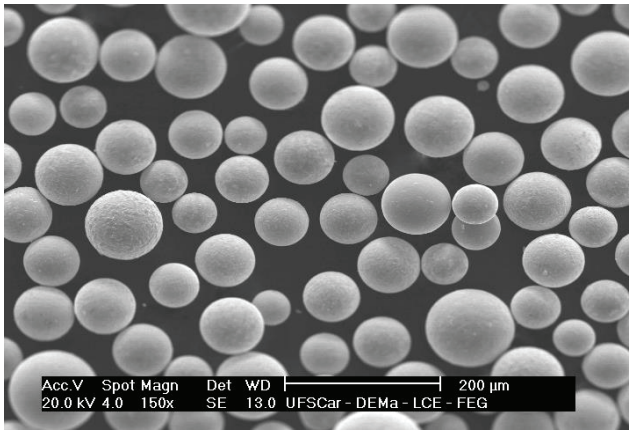


Figure 2. SEM micrograph of MAR-M247(Nb) powder particles obtained via ultrasonic atomization.

Characterization of Secondary Precipitation in Modified HP-NbTi Stainless Steels in Aging States II and III at 700–850 °C.

Victor Max Barros da Silva de Lima[1], Taissa Zangerolami Lopes Rodrigues[1*], Rebecca Mederos da Silveira[1], Fabio dos Santos Queiroz[1], Luiz Henrique de Almeida[1]

[1] Metallurgical and Materials Engineering Program/Department – COPPE/UFRJ.
*E-mail: taissazl@metalmat.ufrj.br

Steam reformer furnace tubes used for hydrogen production in the petrochemical industry are commonly manufactured from centrifugally cast modified HP-NbTi heat-resistant stainless steels due to their excellent high-temperature creep resistance. During long-term service at temperatures approaching 1000 °C, these alloys undergo significant microstructural evolution associated with aging phenomena [1]. The main transformations involve the precipitation and coarsening of secondary carbides within the austenitic matrix, the coalescence of primary interdendritic carbides, and the progressive transformation of Nb-rich carbides into Si-rich phases such as G-phase and η-phase [2]. Previous studies demonstrated that these microstructural changes are strongly dependent on service temperature and can be classified according to six characteristic "Aging States" established for Nb-modified and Nb-Ti-modified HP alloys, which are widely used for residual life assessment of reformer tubes. [3]. Among these conditions, Aging State II, associated with temperatures between 600 and 700 °C, is characterized by the beginning of primary carbide coalescence and by the development of a high density of extremely fine secondary precipitates dispersed within the austenitic matrix, forming particle clouds barely detectable by optical microscopy. In Aging State III, corresponding to temperatures between 700 and 800 °C, these secondary precipitates increase in size and evolve into distinguishable individual particles, while the coalescence of primary precipitates continues. However, due to the extremely fine scale of secondary precipitation in these intermediate aging conditions, their detailed characterization is limited by conventional optical microscopy (OM) and even scanning electron microscopy techniques. In this context, advanced transmission electron microscopy (TEM) associated with EDS chemical mapping becomes essential for understanding the evolution of secondary precipitation and phase transformations in centrifugally cast HP steels subjected to intermediate aging temperatures. Therefore, the present work investigates the microstructural characterization of secondary precipitation in modified HP-Nb stainless steels corresponding to Aging States II and III, associated with exposure temperatures between 600 and 800 °C, using scanning and transmission electron microscopy techniques. Emphasis is given to the identification of finely dispersed secondary precipitates within the austenitic matrix and to the correlation between precipitate chemistry and the microstructural evolution of the alloy in service thermal aging. A steam reformer furnace tube was removed from service after 107,000 h of operation, with the following chemical composition (wt.%): 26.1%Cr, 34%Ni, 0.92%Nb, 1.34%Si, 0.44%C. The microstructure was characterized along the entire tube length, and samples corresponding to Aging States II and III were selected for the present study. Figures 1 and 2 show the microstructures observed by optical microscopy (OM), characteristic of Aging States II and III, respectively. The regions selected for TEM analysis and EDS mapping are highlighted. The results indicate that the "cloud" of secondary precipitates within the matrix, particularly near the primary interdendritic precipitates, is mainly composed of $M_{23}C_6$ carbides and, to a lesser extent, NbC precipitates, which appear more coalesced in Aging State III [4].

References

[1] C. Fuyang et al., Int. J. Pressure Vessels Piping, 192 (2021) 104391.
[2] E.A. Kenik et al., Scripta Mater., 49(2) (2003) 117–122.
[3] F.S. Queiroz et al., J Mater Eng Perf. (2026).
[4] This research was supported by CNPq, Petrobras, and FAPERJ

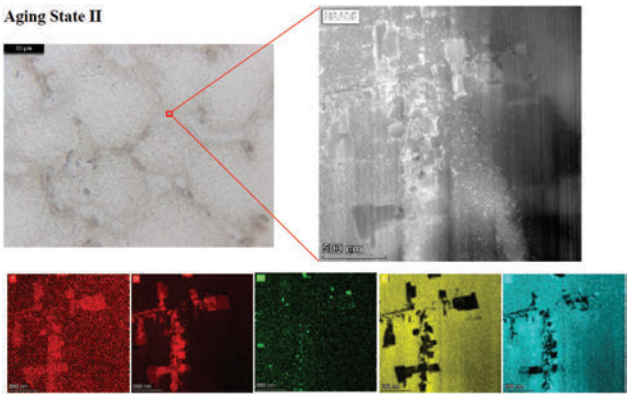


Figure 1. Optical micrograph of modified HP-NbTi steel in Aging State II, showing fine secondary precipitate clouds within the austenitic matrix. The highlighted region indicates the area selected for TEM/EDS analysis.

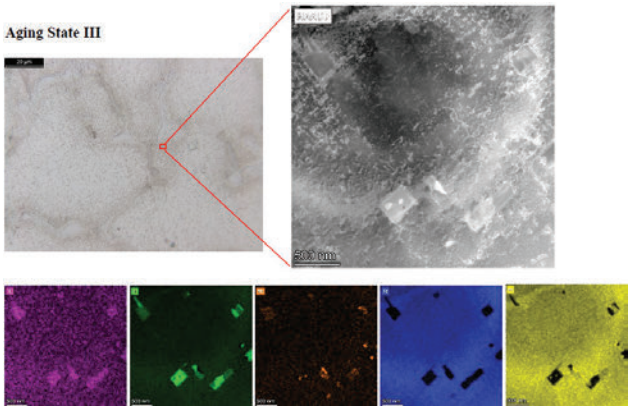


Figure 2. Optical micrograph of modified HP-NbTi steel in Aging State III, showing larger secondary precipitates and continued coalescence of primary carbides. The highlighted region indicates the area selected for TEM/EDS analysis.

Characterization of the β Ti-35Nb-6Ta alloy manufactured by 3D printing with surface modification via Micro-arc Oxidation

Lucas D. Duro[1*], Giovanna E. Santo[1], Renan A. F. Dias[1], Bruno M. Casarin[1], Conrado R. M. Afonso[1]

[1] Department of Materials Engineering (DEMa), Federal University of São Carlos (UFSCar), 13565-905, São Carlos/SP, Brazil.
*E-mail: lucasduro@estudante.ufscar.br

The β-Ti-35Nb-6Ta alloy have emerged as promising materials for biomedical applications due to their low modulus of elasticity, high mechanical strength, and wide microstructural adjustment possibilities. Among structural metallic biomaterials, there is a need to combine high mechanical strength with a modulus of elasticity closer to that of bone tissue, minimizing the stress shielding effect. In this context, body-centered cubic (BCC) titanium β alloys containing multiple β-stabilizing elements emerge as promising alternatives for the development of advanced biomaterials. This project proposes the use of the β-Ti-35Nb-6Ta alloy with xSiO_2 addition for the fabrication of samples by additive manufacturing via Laser Powder Bed Fusion (LPBF). LPBF is a 3D printing method in metals that starts with a thin layer of powder of a given alloy, forming a bed of material, which is then fused using a direct laser beam, forming each layer of the part to be manufactured. Excess powder is removed until the desired shape, according to Computer-Aided Design (CAD) data, is achieved. The process was performed on the OmniTek OMNISINT-160-2 equipment, with a Raycus RFL-C500 Yb:YAG fiber laser (λ = 1700 nm; 80 µm beam), under an argon atmosphere. The study aimed to evaluate the influence of additive manufacturing and surface modifications by Microarc Oxidation (MAO) on the microstructure and composition of Ti-35Nb-6Ta alloys produced by LPBF, as well as to investigate the effect of incorporating different silica concentrations (0.5% and 1.0%) into the alloy. The MAO treatment was performed using a DC power supply (Keysight, N5751A) at 2.5A and 300V, at room temperature for 60s. The electrolyte consisted of 0.35 M calcium acetate monohydrate ($(CH_3COO)2Ca{\cdot}H_2O$), 0.02 M sodium β-glycerophosphate pentahydrate ($C_3H_7Na_2O_6P{\cdot}5H_2O$), and 0.1 M magnesium acetate tetrahydrate ($(CH_3COO)2Mg{\cdot}4H_2O$). After MAO, XRD and SEM were performed on these samples. XRD results indicated the typical β-Ti (BCC) peaks and the formation of oxide phases after MAO treatment, suggesting the development of a bioactive ceramic layer. SEM analyses revealed the formation of porous oxide coatings with typical volcano-like morphology after MAO. The samples containing 0.5% SiO_2 exhibited larger and more heterogeneous pores, with estimated diameters ranging from approximately 10 to 25 µm. In contrast, the 1.0% SiO_2 condition showed a more homogeneous porous surface with smaller pores, predominantly between 5 and 15 µm. These morphological differences suggest that the SiO_2 concentration influenced the plasma discharge behavior and coating growth during MAO processing. Thus, this study aims to promote bioactive surfaces that are potentially favorable to osseointegration, contributing to the development of the β-Ti-35Nb-6Ta alloy processed by additive manufacturing and surface-modified for structural biomedical applications [4].

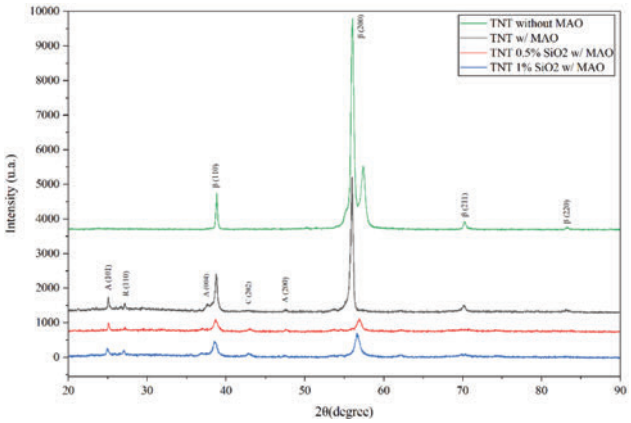


Figure 1. X-ray diffraction (XRD) patterns of Ti-35Nb-6Ta alloys produced by LPBF before and after Microarc Oxidation (MAO), with and without SiO_2 incorporation. The untreated sample (TNT without MAO) exhibited characteristic peaks of the β phase with body-centered cubic (BCC) structure. After MAO treatment, the formation of oxide phases associated with the anodic layer was observed, including peaks attributed to anatase TiO_2 (A), rutile TiO_2 (R), and $CaCO_3$ in the calcite crystalline phase (C). The oxide-related peaks were more evident in the samples containing 0.5% and 1.0% SiO_2.

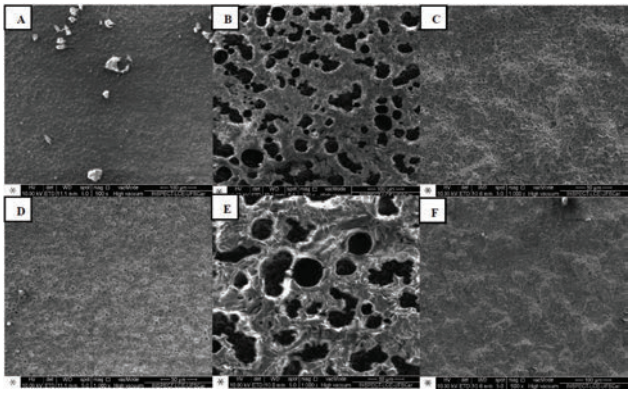


Figure 2. Scanning Electron Microscopy (SEM) of Ti-35Nb-6Ta alloys produced by LPBF, where A, B and C are at 50 µm scale (A with no SiO2 addition to the alloy, B with 0.5% addition and C with 1.0% addition) and D, E and F are at a 100 µm scale (maintaining the respective previous SiO2 additions).

References

[1] Kuroda, P. A. B.; Rossi, Mariana Correa; Grandini, C.R.; Afonso, C. R. M.. Assessment of applied voltage on the structure, pore size, hardness, elastic modulus, and adhesion of anodic coatings in Ca-, P-, and Mg-rich produced by MAO in Ti-25Ta-Zr alloys. Journal of Materials Research and Technology-JMR&T. v.26, p.4656 - 4669, 2023

[2] C.R.M. Afonso et al., J. Mater. Res. Technol. 40 (2026) 1869–1881.

[3] Dos Santos, R. F. M.; Kuroda, P. A. B.; De Almeida, G. S.; Zambuzzi, W. F.; Grandini, C.R.; Afonso, C. R. M. New MAO coatings on Multiprincipal Equimassic Beta TiNbTaZr and TiNbTaZrMo Alloys. Biomedical Engineering Advances. v.9, p.100139, 2025

[4] This research was supported by FAPESP PAIP 2023/16836-2 and partially supported by CAPES, Finance Code 001 (Brazil)

Cold Plasma Applied to Sustainable Cellulosic Materials: Evaluation of Cell Adhesion

Maciel Barbosa[1], Paula Fernandes[2], Marina Fontes[2], Bruno Bruno Caillier[3], Sandra Cruz[1], Hernane Barud[2*]

[1] Federal University of São Carlos,São Carlos, São Paulo, Brasil; [2] University of Araraquara, Uniara, Araraquara, São Paulo, Brazil; [3] University of Toulouse, INU Champollion, DPHE, Albi.
*E-mail: hernane.barud@gmail.com

Cellulose-based materials have attracted increasing interest for biomedical and technological applications due to their renewable origin, cytocompatibility, and potential production through sustainable routes[1]. In this context, bacterial nanocellulose (BNC), films derived from orange agro-industrial coproducts, and onion-based film-forming matrices represent promising systems for the development of functional materials with reduced environmental impact. However, despite their relevant structural properties, these materials may present limitations associated with surface chemistry, particularly regarding wettability, cell adhesion, and interaction with biological systems[2]. In this regard, oxygen plasma technology may constitute an effective alternative, since it can modify the nanoroughness and surface energy of the material, thereby improving adhesive properties and stimulating cell proliferation[3]. Therefore, cold plasma treatment strategies were applied according to the specific characteristics of each matrix. Bacterial nanocellulose and films obtained from orange coproducts were treated with atmospheric-pressure plasma using a dielectric barrier discharge (DBD) configuration, with exposure times of 0, 0.5, 10, and 20s. In turn, onion-based films were subjected to radiofrequency (RF) plasma treatment, with exposure times of 0, 2.5, and 15 min. In both cases, untreated samples were used as controls. After treatment, cell adhesion assays were performed using murine fibroblasts (L929) and human osteoblast-like cells (SaOS-2), followed by evaluation by scanning electron microscopy (SEM), aiming to assess cell interaction with the material surfaces before and after plasma treatment. This analysis enabled the investigation of the influence of surface modifications on the initial cellular response, particularly regarding cell adhesion and spreading on the cellulosic matrices. The micrographs showed that DBD plasma treatment altered the interaction of SaOS-2 and L929 cells with the BNC surface. Although untreated BNC allowed cell adhesion, the treated surfaces exhibited differences in cell morphology and spreading as a function of exposure time (Figure 1). For BNC, DBD treatment for 20 s favored greater cell spreading and the formation of cytoplasmic extensions in both cell lines, indicating improved anchorage to the matrix. At 10 s, increased aggregate formation was observed, suggesting predominant cell–cell adhesion. For the films obtained from orange coproducts (Figure 2), SaOS-2 cells adhered to both control and DBD-treated surfaces, with a response dependent on exposure time. Although the control showed initial adhesion, treatment for 0.5 s enhanced cell–surface interaction, whereas 10 and 20 s favored greater cell aggregation. For onion-based films (Figure 3), cell adhesion was observed in all samples, with increased cell–material interaction after RF plasma treatment, especially after 15 min, a condition associated with greater adhesion and cell spreading. Therefore, oxygen plasma-treated cellulose-based films represent a promising alternative for improving cell adhesion on sustainable polymeric matrices.

Keywords: Agro-industrial coproducts, Bacterial nanocellulose, Cold Plasma

References

[1] W. Cheng *et al.*, Prog. Mater. Sci. 138 (2023) 101152.

[2] A.H. Behroozi, T.H. Mekonnen, EcoMat 8 (2026) e70063.

[3] J. Rondøn, A. Gonzalez-Lizardo, arXiv:2504.03883 (2025).

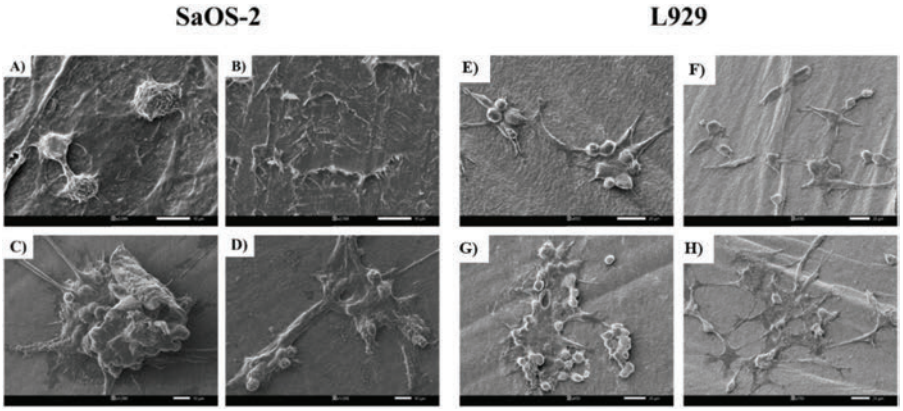


Figure 1. SEM micrographs of plasma-treated and untreated samples showing the growth of SaOS-2 osteoblast-like cells: A) BNC 0 s, B) BNC 0.5 s, C) BNC 10 s, and D) BNC 15 s; and L929 fibroblast cells: E) BNC 0 s, F) BNC 0.5 s, G) BNC 10 s, and H) BNC 15 s.

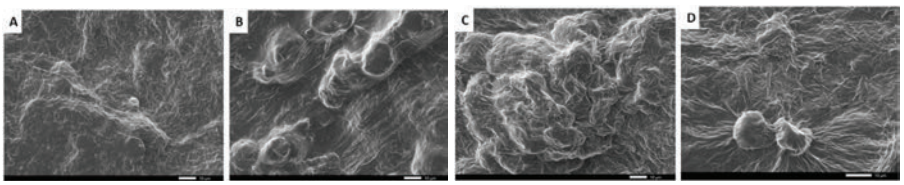


Figure 2. SEM micrographs of plasma-treated and untreated samples showing the growth of SaOS-2 osteoblast-like cells: A) Orange 0 s, B) Orange 0.5 s, C) Orange 10 s, and D) Orange 15 s.

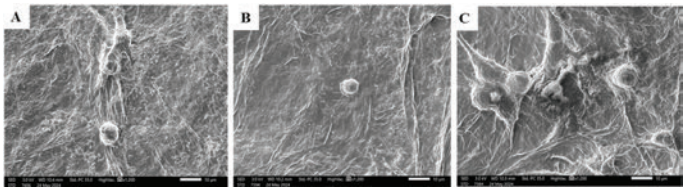


Figure 3. SEM micrographs of plasma-treated and untreated samples showing the growth of L929 fibroblast cells: A) Onion 0 min, B) Onion 2.5 min, C) Onion 15 min.

Cooling Rate Effects on Microstructure, Hardness and Strength of a Low-Carbon Nb-Microalloyed Steel

Lavínia Ayumi Yamautti[1*], Daniel G. S. dos Santos[2], Renan A. F. Dias[1], Jitendra Patel[3], Vinicius Cardoso Ottani[3], José Britti Bacalhau[3], Conrado R. M. Afonso[1]

[1] BioMet-CAM, Department of Materials Engineering (DEMa), Federal University of São Carlos (UFSCar), Brazil; [2] Graduate Program in Materials Science and Engineering (PPGCEM), Federal University of São Carlos (UFSCar), São Carlos- SP, Brazil; [3] Companhia Brasileira de Metalurgia e Mineração (CBMM), São Paulo-SP, Brazil
*E-mail: lavinia.ayumi@estudante.ufscar.br

The cooling rate plays a fundamental role in the microstructural evolution and mechanical properties of hot-rolled structural steels, influencing phase formation and strengthening mechanisms. Microalloyed steels have been widely used due to the possibility of achieving high mechanical properties (or performance) through the combination of chemical composition and thermomechanically controlled processing (TMCP). Elements such as Nb, V, and Mn can act on grain refinement, precipitation strengthening, and solid-solution strengthening, significantly increasing mechanical strength. Among these elements, niobium plays a major role in austenite grain refinement. The enhancement of the mechanical properties of the steel occurs through the undissolved niobium carbides or niobium carbonitrides during hot rolling that precipitate at austenite grain boundaries, promoting grain boundary pinning and inhibiting austenite recrystallization and grain growth processes [1]. To predict the impact of these microstructural changes on the macroscopic behavior, the relationship between hardness and ultimate tensile strength (UTS) can be estimated using Equation (1) [2]: UTS = -99.8 + 3.734 HV. The present work evaluated the influence of different cooling rates on the microstructure and hardness of a low-carbon steel microalloyed with 80 ppm of Nb. To this end, three samples subjected to different cooling conditions were characterized by optical microscopy (figure 1), scanning electron microscopy (SEM) (figure 2), pearlite fraction analysis, and Vickers microhardness tests. Additionally, the correlation between hardness and ultimate tensile strength will be investigated through the empirical relationship presented in Equation (1), allowing the estimation of mechanical properties from the obtained hardness values. Experimental results indicated that increasing the cooling rate led to significant refinement of the grain size and an increase in the pearlite volume fraction. The grain size measurements, obtained from Figures 1 and 2, confirm that this microstructural refinement correlates with the increase in mechanical strength. Consequently, the Vickers microhardness increased from 136 HV under the slowest cooling condition to 152 HV, the estimated UTS followed a similar trend, increasing from 408 MPa to 468 MPa (Table 1). In conclusion, the study demonstrates that varying the cooling rate is an effective route to tailor the microstructural parameters and optimize the mechanical strength of TMCP microalloyed steels without modifying the chemical composition [3].

References

[1] Patel, J., "Ultra-low niobium (ULNb) alloying design solution for commodity grade structural steels", Materials Today: Proceedings, v. 67, p. 523–530, 2022.

[2] Pavlina, E. J.; Van Tyne, C. J, "Correlation of Yield Strength and Tensile Strength with Hardness for Steels", *Journal of Materials Engineering and Performance*, v. 17, n. 6, p. 888–893, 2008.

[3] This research was supported by FAPESP PAIP 2023/16836-2. This study was financed in part by the Coordenação de Aperfeiçoamento de Pessoal de Nível Superior - Brasil (CAPES) - Finance Code 001. The authors thank the Laboratory of Structural Characterization (LCE/DEMa/UFSCar) for the general facilities and CBMM for supplying the samples and financially supporting this study.

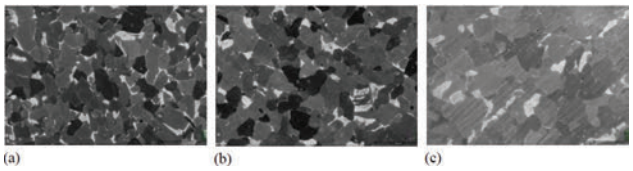


Figure 1. SEM Micrographs of Samples Subjected to Different Cooling Rates (a) 1 °C/s, (b) 0,5 °C/s e (c) 0,1 °C/s. (Source: Prepared by the author, 2026).

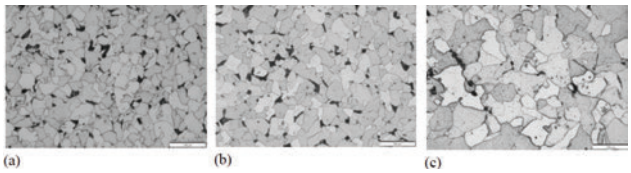


Figure 2. Optical Microscopy of Samples Cooled at Different Rates (a) 1 °C/s, (b) 0,5°C/s e (c) 0,1 °C/s. (Source: Prepared by the author, 2026).

Table 1. Cooling rate, pearlite fraction, grain size, Vickers hardness, and estimated UTS of the analyzed samples.

Sample	Cooling rate	Vickers Hardness	Pearlite fraction	UTS (MPa)	Grain size (µm)
	(ºC/s)	(HV)	(%)		
1	0.1	136	7.5	408	22
2	0.5	137	3.1	413	21
3	1	152	3.6	468	19

Source: Prepared by the author (2026).

Correlative Electron Microscopy Approach for the Characterization of Nanocarbides in Nb Microalloyed Steels

Daniel G. S. dos Santos[1], Lavínia Ayumi Yamautti[2], Renan A. F. Dias[2], Vinicius Cardoso Ottani[3], José Britti Bacalhau[3], Jitendra Patel[3], Conrado R. M. Afonso[2]

[1] Graduate Program in Materials Science and Engineering (PPGCEM), Universidade Federal de São Carlos (UFSCar), São Carlos/SP, Brazil; [2] BioMet-CAM, Department of Materials Engineering (DEMa), Universidade Federal de São Carlos (UFSCar), São Carlos/SP, Brazil; [3] Companhia Brasileira de Metalurgia e Mineração (CBMM), São Paulo/SP, Brazil.
*E-mail: dgssantos@estudante.ufscar.br

Nb- and V-microalloyed steels present high technological relevance due to precipitation strengthening promoted by the formation of nanosized carbides and carbonitrides dispersed within the ferritic matrix [1]. The presence of these precipitates significantly contributes to the increase in mechanical strength through dislocation pinning and retardation of ferritic grain growth during thermomechanical processing [1]. Studies using transmission electron microscopy (TEM) and atom probe tomography (APT) have demonstrated an association between local Nb concentrations and regions containing high dislocation density, reinforcing the importance of nanoscale characterization of these precipitates and their interfaces with the ferritic matrix [2]. However, the crystallographic identification of these precipitates still represents an experimental challenge due to their size ranging from 2 to 10 nm, low volume fraction, and the influence of the crystallographic orientation of the ferrite matrix (α-Fe) during TEM analysis [3]. In addition, Nb- and V-rich carbides exhibit specific orientation relationships with ferrite, such as the Baker–Nutting orientation relationship typically reported for MC-type carbides in microalloyed steels [1,3]. Correlative analysis involving multiple electron microscopy techniques has been used to increase the reliability of microstructural characterization in complex metallic materials, and in the present work a correlative and multiscale approach was employed for the characterization of MC precipitates in Nb- and V-microalloyed steels with partial Mn replacement (composition shown in Table 1). Initially, the sample was subjected to metallographic preparation and characterized by scanning electron microscopy (SEM) (Figure 1(a)) and Electron Backscatter Diffraction (EBSD) (Figure 1(b)) to select a region of interest with favorable crystallographic orientation (Figure 1(c)) for obtaining selected area electron diffraction (SAED) patterns during TEM analysis. From this region, a site-specific lamella was extracted by Focused Ion Beam (FIB) (Figure 2(a)) and subsequently analyzed by TEM using bright field (BF) (Figure 2(b)) and dark field (DF) (Figure 2(c)) modes for precipitate localization (Figure 3(a)). Subsequently, high-resolution TEM (HRTEM) (Figure 3(b)) and fast Fourier transform (FFT) analyses (Figure 3(c)) were performed to measure interplanar spacings (d_{hkl}) associated with Nb- and V-rich precipitates [3]. Nanocarbides (NbC and VC) ranging from 2 to 5 nm were identified by TEM and HRTEM, as well as consistent with precipitate–matrix orientation relationships compatible with Baker–Nutting. The results confirm that the integration of SEM, EBSD, FIB, and TEM significantly increases the reliability of region selection and favors the acquisition of crystallographic information required for the characterization of nanosized MC carbides in microalloyed steels [4].

References

[1] T. Gladman, The Physical Metallurgy of Microalloyed Steels, The Institute of Materials, London, 1997.

[2] J. Takahashi et al., Direct observation of Nb distribution associated with dislocations in microalloyed steels by atom probe tomography and TEM, Scr. Mater. 63 (2010) 261–264.

[3] Y. Wang et al., The formation mechanism of complex carbides in Nb-V microalloyed steel, Mater. Charact. 184 (2022) 111657.

[4] This research was supported by FAPESP PAIP 2023/16836-2. This study was financed in part by the Coordenação de Aperfeiçoamento de Pessoal de Nível Superior - Brasil (CAPES) - Finance Code 001. The authors thank the Laboratory of Structural Characterization (LCE/DEMa/UFSCar) for the general facilities and CBMM for supplying the samples and financially supporting this study.

Table 1. Chemical composition of the steel sample

C	Mn	Nb	V
0.18 %	0.97 %	80 ppm	230 ppm

Source: Prepared by the author (2026).

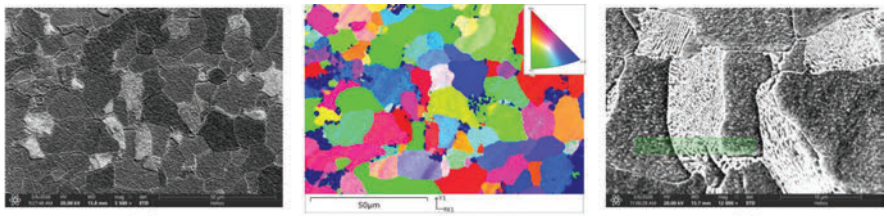


Figure 1. SEM images and EBSD result: (a) Secondary Electrons micrograph of the general region of interest; (b) EBSD IPF Y of the general region of interest; (c) Lamella extraction area highlighted on secondary electrons micrograph.
Source: Prepared by the author (2026).

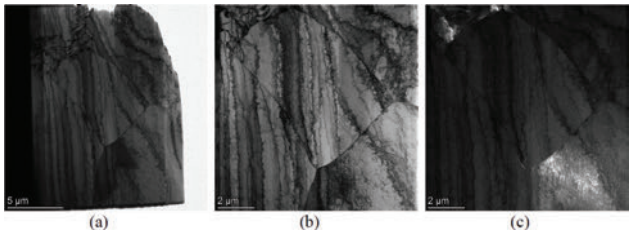


Figure 2. TEM micrographs: (a) BF low magnification view of the entire lamella; (b) BF image showing diffracting regions; (c) DF image of grains and a region rich in precipitates.
Source: Prepared by the author (2026).

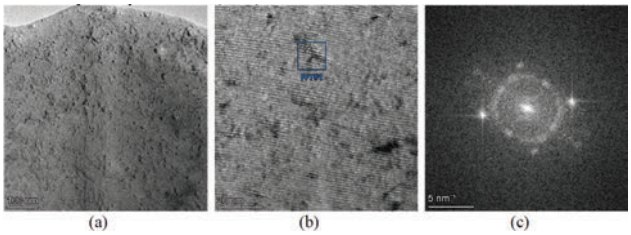


Figure 3. TEM micrographs: (a) Bright Field image of a region rich in precipitates; (b) HRTEM with a highlighted precipitate; (c) FFT showing a simulated diffraction pattern of a NbC precipitate in the [1 0 0] zone axis.
Source: Prepared by the author (2026).

Corrosion analysis of a gray cast iron in saline environments

Lorena Maria da Silva[1*], Leandra Marques[1], Vinicius Felippe Elias[1], Herique Marchezine Mazzer[1], Francisco Gil Coury[1]

[1] Federal University of São Carlos, Department of Materials Engineering.
*E-mail: lorenasilva@estudante.ufscar.br

The durability of metal alloys, especially in marine environments, represents a major challenge for engineering, since corrosion is intensified by the presence of chloride ions and dissolved oxygen. In gray cast irons, the behavior in graphite galvanic cells is the formation of a cathodic region, accelerating the oxidation of the material. This process results in the formation of different corrosion products and progressive degradation of the material over time. This work focuses on the analysis of corrosion in gray cast iron exposed to a saline medium, using as a sample a fragment of a French cannon that remained submerged in seawater for approximately 200 years. The main objective is to identify the oxides formed during long exposure to the marine environment and to understand the degradation mechanisms associated with the interaction between the metal and the saline electrolyte. Characterization was performed by optical microscopy (OM), energy dispersive spectroscopy (EDS) and Raman spectroscopy. OM analyses showed the presence of typical lamellar graphite of gray cast iron, in addition to regions strongly degraded by corrosion. The EDS spectrum (Figure 1) confirmed the elemental composition of the analyzed region, while the EDS elemental distribution map (Figure 2) revealed the distribution of oxygen and chlorine throughout the oxidized layer, indicating the incorporation of species from seawater. Raman spectroscopy will be used to identify the oxidation state of the compounds present in the corroded layer, investigating the possible presence of phases such as magnetite (Fe_3O_4) and hematite/maghemite (Fe_2O_3), typical of corrosive processes in saline environments. These observations are consistent with previous studies on the corrosion behavior of gray cast iron in marine environments. The results obtained contribute to the understanding of corrosion mechanisms in cast irons subjected to prolonged marine exposure, collaborating in the understanding of the oxidation process of a gray cast iron exposed to a marine saline environment.

References

[1] MELCHERS, R. E. Long-term corrosion of cast irons and steel in marine and atmospheric environments. **Corrosion Science**, v. 68, p. 186–194, mar. 2013.

[2] SILVA, J. et al. Oxidation in gray cast iron. **Revista Técnico-Científica do IFSC**, [S. l.], 2023.

[3] WOOD, R. J. K. Marine wear and tribocorrosion. **Wear**, v. 376-377, p. 893–910, abr. 2017.

[4] ABYAZI, A.; FAKHERI, F. Deposition of magnetite nano-particles on gray cast iron via hot alkaline and hydrothermal conversion methods: with regarding corrosion behaviour. **Results in Materials**, v. 28, p. 100828, dez. 2025.

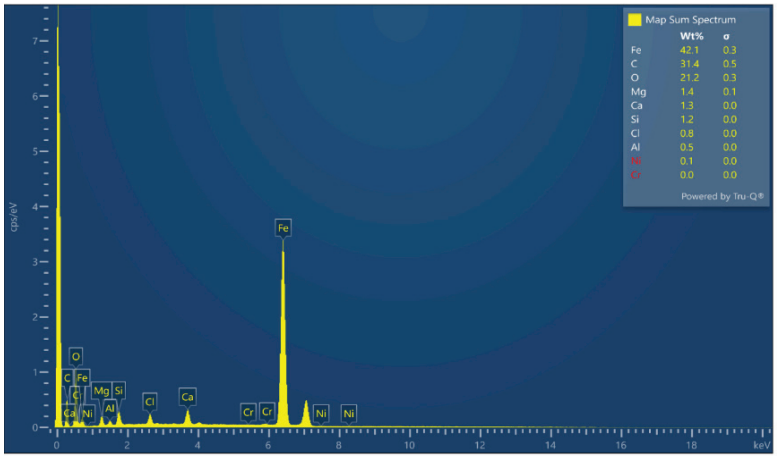


Figure 1. Chemical analysis by EDS

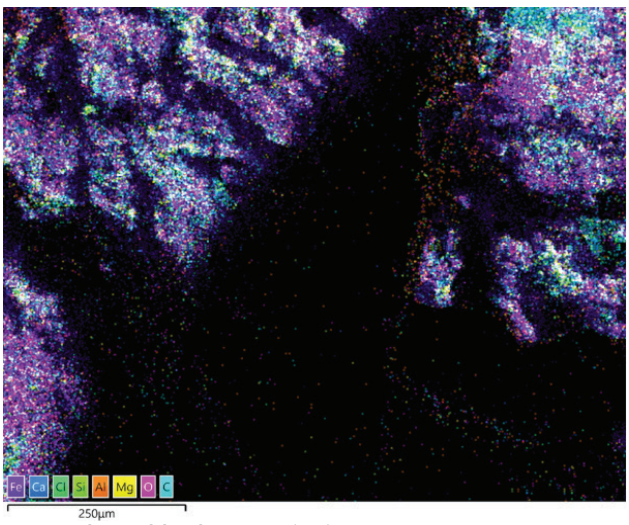


Figure 2. Elemental distribution map (EDS)

Development of Zr-based Vitreous Alloys and the Study of Quasicrystal Formation During Crystallization

Guilherme Araújo Teixeira[1*], Witor Wolf[1]

[1] Department of Materials Engineering (SMM), São Carlos School of Engineering, University of São Paulo (EESC-USP).
*E-mail: guilhermearaujo1102@usp.br

Zr-based Bulk Metallic Glasses (BMGs) are distinguished by their exceptional Glass Forming Abil-ity (GFA) and superior mechanical properties, such as high yield strength and toughness [1]. How-ever, demanding tribological applications require further enhancements in hardness and a reduction in the coefficient of friction, which can be achieved through the controlled nucleation of nanomet-ric quasicrystals (QCs) during the devitrification process [2,3], owing to their high hardness and intrinsically low-friction response. The present study investigates the development of amorphous alloys within Zr-based systems and the structural competition between metastable phases, aiming to identify compositions that combine high Glass Forming Ability with a tendency toward quasicrys-talline phase formation. This approach seeks to mitigate the inherent brittleness of quasicrystals by embedding them within a tough amorphous matrix, thereby enhancing the alloy's tribological per-formance. The studied alloys, including the Vitreloy 105 ($Zr_{52.5}Cu_{17.9}Ni_{14.6}Al_{10}Ti_5$) composition, were processed via arc-melting under an inert argon atmosphere, followed by suction casting into water-cooled copper molds, which ensures the high cooling rates necessary to promote the formation of a glassy metallic structure. X-ray Diffraction (XRD) characterization confirmed the successful synthesis of almost fully amorphous structures, and Differential Scanning Calorimetry (DSC) anal-ysis revealed a distinct two-step crystallization behavior, suggesting the precipitation of metastable icosahedral phases during the early stages of devitrification [4]. This thermal response indicates the existence of a processing window for controlled partial crystallization, in which nanometric precipitates may be introduced without fully compromising the amorphous character of the matrix. Vickers microhardness tests yielded results consistent with literature benchmarks [5], establishing a robust mechanical baseline for the monolithic glassy matrix. Further Scanning Electron Microscopy (SEM) and Transmission Electron Microscopy (TEM) analyses revealed a complex nanometric pre-cipitation structure within the amorphous matrix, including precipitates associated with devitrifica-tion and crystalline features formed during solidification. In particular, SEM imaging highlights the interface between crystalline and amorphous regions, as shown in Figure 1, whereas TEM imaging reveals a crystalline inclusion embedded in the glassy matrix, as shown in Figure 2. The integration of these quasicrystalline phases into tough amorphous matrices represents a promising route for developing composites with high wear resistance and low friction [6].

References

[1] J. Schroers, Phys. Today 66, 32 (2013).

[2] X. Zhao, S. Pang, C. Ma and T. Zhang, Mater. Trans. 50, 1838 (2009).

[3] C. Fan and A. Inoue, Scr. Mater. 45, 115 (2001).

[4] E. Pekarskaya et al., Acta Mater. 51, 4045 (2003).

[5] M. Mohr, R. K. Wunderlich, D. C. Hofmann and H. J. Fecht, Npj Microgravity 5, 1 (2019).

[6] The authors acknowledge the financial support from the São Paulo Research Foundation (FAPESP) under grants #2025/24052-7 and #2025/08661-3. We also thank EESC-USP for the infrastructure and technical support.

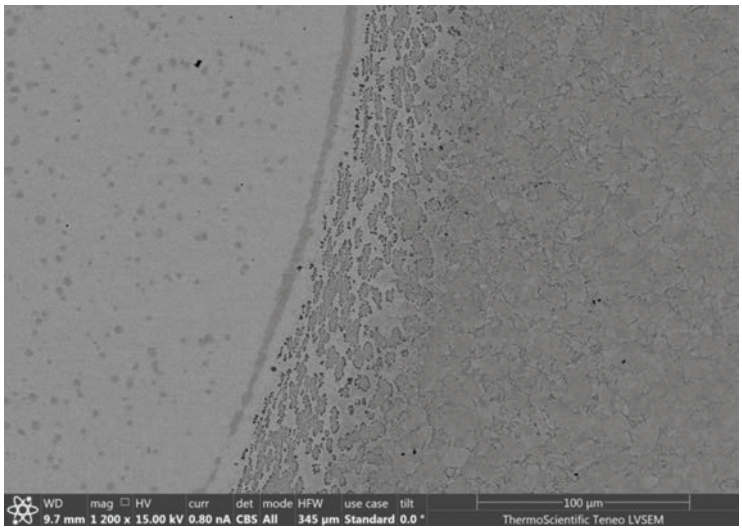


Figure 1. SEM image of the interface between crys-talline and amorphous regions in the Vitreloy 105 sample.

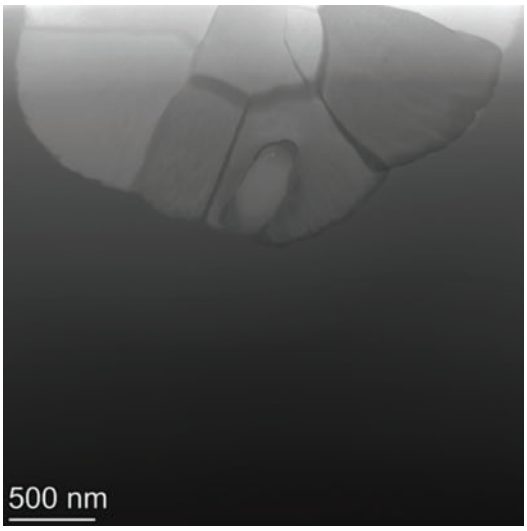


Figure 2. TEM image of crystalline inclusion in the glassy matrix of the Vitreloy 105 sample.

Early Biological Response to β-Ti, β-TN15, and Microarc-Oxidized β-TN15: A Combined In Vivo and Surface Characterization Approach

Giovanna do Espirito Santo[1], Breno Rocha dos Santos[2*], Stella Machado Gualti[2], Karina Nogueira Zambone Pinto Rossi[2], Conrado Ramos Moreira Afonso[1].

[1] Department of Materials Engineering (DEMa), Universidade Federal de São Carlos (UFSCar), São Carlos, SP, Brazil; [2] Department of Morphology and Pathology (DMP), Universidade Federal de São Carlos (UFSCar), São Carlos, SP, Brazil.
*E-mail: brenorocha@estudante.ufscar.br

β-type titanium alloys have been widely investigated for biomedical applications due to their low elastic modulus, excellent corrosion resistance, and favorable biocompatibility compared with conventional titanium alloys. Among these materials, Ti-15Nb alloys are considered promising candidates for orthopedic and dental implants because niobium acts as a non-toxic β-phase stabilizer capable of improving the mechanical compatibility between implant and bone tissue. In addition to alloy composition, surface characteristics such as morphology and roughness play an important role in biomaterial–tissue interactions, directly influencing early biological responses after implantation. In this context, Microarc Oxidation (MAO) has emerged as an effective surface modification technique capable of producing porous oxide layers strongly adhered to titanium substrates. In the present study, commercially pure titanium (Ti), untreated Ti-15Nb alloy (TN15), and microarc-oxidized Ti-15Nb (TN15 + MAO) were investigated in order to evaluate the influence of MAO treatment on surface morphology, roughness, and early tissue response. Surface characterization was performed by scanning electron microscopy (SEM) and atomic force microscopy (AFM), while biological response was evaluated through histological analyses after subcutaneous implantation in mice for 7 and 14 days. SEM analyses demonstrated significant morphological differences between untreated and MAO-treated samples. Ti and TN15 groups presented smoother and more homogeneous surfaces, whereas the TN15 + MAO group exhibited a porous oxide layer with irregular microstructures distributed throughout the surface, characteristic of the MAO process. AFM topographical images and roughness measurements revealed increased surface roughness for the TN15 + MAO group compared with untreated Ti and TN15 samples, indicating the formation of micro- and nanoscale features after surface treatment. The roughness parameters remained higher for the MAO-treated surfaces during both experimental periods. Histological evaluation demonstrated satisfactory tissue compatibility for all groups after 7 and 14 days of implantation. The Ti and TN15 groups showed preserved tissue organization with mild inflammatory infiltrate, while the TN15 + MAO surfaces exhibited tissue integration associated with the porous morphology produced by MAO treatment. Differences in inflammatory cell distribution and connective tissue organization were observed among the groups during the healing period. The obtained results indicate that MAO treatment significantly modifies the surface morphology and roughness of Ti-15Nb alloys, promoting the formation of porous topographies that may contribute to favorable early biological responses. These findings support the potential application of MAO-treated Ti-15Nb alloys as advanced biomaterials for implantable devices [4].

References

[1] M. Geetha et al., Prog. Mater. Sci. 54 (2009) 397.
[2] M. Niinomi, J. Mech. Behav. Biomed. Mater. 1 (2008) 30.
[3] R.O. Hussein et al., J. Mater. Process. Technol. 213 (2013) 201.
[4] This research was supported by FAPESP and CNPq (Brazil).

Table 1. Experimental groups

Sample code	Material	Surface condition
Ti	Commercially pure titanium	Polished
TN15	Ti-15Nb alloy	Polished
TN15 + MAO	Ti-15Nb alloy	Polished + MAO

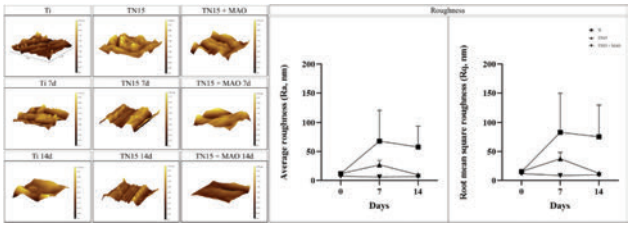


Figure 1. Three-dimensional AFM topographical images and roughness parameters of Ti, TN15, and TN15 + MAO surfaces before implantation and after 7 and 14 days of in vivo evaluation. The graphs represent the average roughness (Ra) and root mean square roughness (Rq) values obtained from AFM analyses. The TN15 + MAO group presented higher roughness values compared with untreated Ti and TN15 surfaces, indicating the formation of micro- and nanoscale topographical features promoted by the MAO treatment.

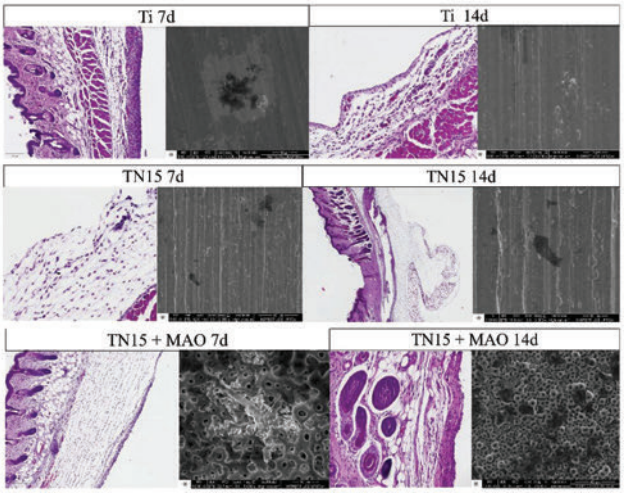


Figure 2. Representative histological (H&E staining) and SEM images of Ti, TN15, and TN15 + MAO after 7 and 14 days of subcutaneous implantation in mice. Histological analyses were performed to evaluate tissue organization and inflammatory response surrounding the implanted materials, while SEM images were used to investigate the surface morphology of the samples before implantation. The TN15 + MAO group exhibited a porous oxide layer characteristic of the MAO treatment, whereas Ti and TN15 presented smoother surface morphologies.

Effect of Adding Recycled Titanium Chips in a Molten Salt Bath on the Production of Ti-rich Coating in AISI 1513 Steel

Vitor S. Rolin[1], José Gedael Fagundes Jr[2], Vicente A. Ventrella[1,2], Juno Gallego[1,2*]

[1] Post-Graduate Program in Mechanical Engineering at UNESP – Ilha Solteira; [2] Department of Mechanical Engineering, São Paulo State University – UNESP, Ilha Solteira, São Paulo, Brazil.
*E-mail: juno.gallego@unesp.br

Wear and corrosion are frequently related to failures that shortened life of mechanical parts. A possible solution to reduce these drawbacks is the strengthening of surfaces by thermochemical treatments, such as thermo-reactive diffusion (TRD) [1-2]. A new sustainable processing for that treatment is recycling of titanium chips, generated after machining of titanium ASTM F67 bars for dental implant production, to be applied for TRD. In this work pieces with 20 x 15 x 3mm size of AISI 1513 C-Mn steel with composition 0.14C, 1.35Mn, 0.25Si (%wt) were submitted to TRD treatments, using 2.5kW electric furnace. Ti-rich molten salt baths were prepared with 2.5, 5 and 10g of Ti chips plus KCl-NaCl eutectic mixture to complete 100g of total charge inside 150ml porcelain crucible. TRD treatments were performed in molten salt bath at 1000 °C during 4h, following air cooling to room temperature. After that samples were investigated by scanning electron microscopy (SEM), EDS microanalysis and X-ray diffraction (XRD). In all analyzed specimens was formed a titanium-rich coating on the surface of AISI 1513 steel, which thickness have increased with higher content of titanium in molten salt bath. So, mean thickness of coatings have changed from 1.1 (2.5g Ti) to 5.7mm (10g Ti). The BSE contrast applied in the SEM micrographs presented in the Fig.1 shows that typical coating is composed by 2 distinctive layers, being visible in the outer layer heterogeneous grooving. The lack of homogeneity of the outer layer is possibly caused by the rapid growth and/or by the redissolution of Ti into the bath. The BSE contrast of coatings could be associated to chemical partition during diffusion of the titanium from molten bath with the iron and carbon from the steel, according EDS results presented in Fig.2. X-ray diffraction results showed in Fig.3 confirms that layer is mainly composed by Ti-α, TiC and Fe-α after Rietveld refinement performed with PROFEX 5 software [3]. When adding 2.5g Ti to the bath, there was a considerable formation of TiC related to free Ti, probably due to the low concentration of the metal in the bath. However, adding up to 10g Ti increased the amount of free Ti with decreasing of TiC concentration in coatings. The obtained results are consistent with earlier reports [4] and confirm that TRD treatment performed using titanium chips is a reliable, sustainable e quite promising metallurgical process to improve surface properties of the non-alloyed steels. The authors are grateful for supporters [5].

References

[1] A. Günen et al. Surface and Coatings Technology, 437 (2022) 128280.

[2] N. Lin et al. Journal of Physics and Chemistry of Solids, 129 (2019) 387-400.

[3] N. Döbelin, R. Kleeberg. Journal of Applied Crystallography, 48 (2015) 1573-1580.

[4] B. Kurt et al. Surface and Coatings Technology, 385, (2020) 125332.

[5] This research was supported by CAPES, CNPq and Implalife Biotecnologia (Brazil).

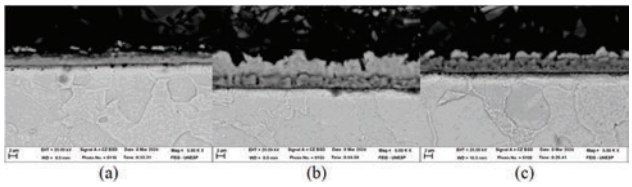


Figure 1. SEM micrographs showing obtained coating after TRD treatment at 1000°C/4h using with 2.5g (a), 5g (b) and 10g (c) of titanium in molten salt.

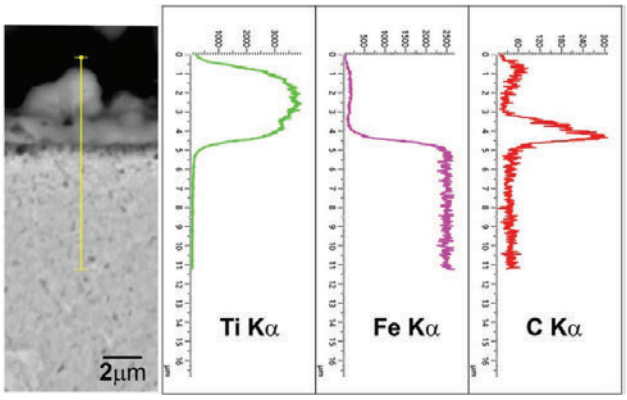


Figure 2. Typical EDS elemental line-scan with compositional variation of Ti, Fe and C on the TRD coating obtained with 5g of titanium in molten salt.

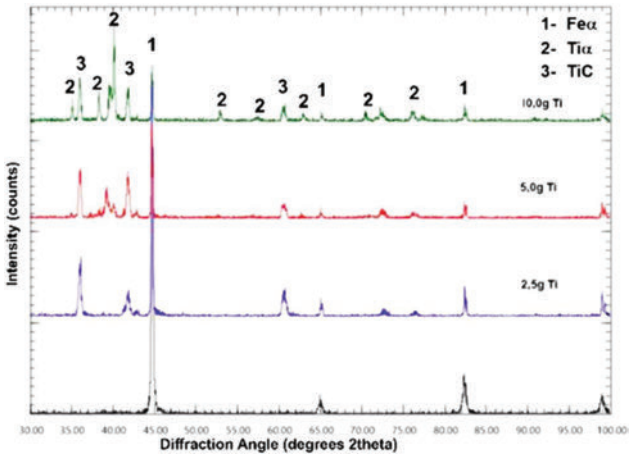


Figure 3. X-ray diffraction patterns of the coatings obtained after TRD treatments.

Effect of Alloying Elements on the Microstructure and Oxidation Resistance at 800 °C of Ni-15Nb-M Ternary Alloys

Mariana S. Pereira[1*], Gabriel M. de Camargo[2], Mariana C. Rossi[2], Conrado R. M. Afonso[2]

[1] Graduate Program in Materials Science and Engineering (PPGCEM), Federal University of São Carlos (UFSCar), São Carlos/SP, Brazil;
[2] BioMet-CAM, Department of Materials Engineering (DEMa), Federal University of São Carlos (UFSCar), São Carlos/SP, Brazil.
*E-mail: pereiramariana@estudante.ufscar.br

Nickel-based superalloys are designed to withstand extreme conditions through a combination of mechanical and chemical properties, and are therefore widely used in the aerospace, energy generation, and petrochemical industries. High-temperature oxidation resistance is a critical property that can extend the service life of various components [1,2]. The microstructure of these alloys can be highly complex, comprising the γ (Ni-fcc), γ' (ordered $Ni_3(Al,Ti)$), γ" (bct-ordered Ni_3Nb), δ (orthorhombic Ni_3Nb), η (ordered Ni_3Ti), as well as carbides and TCP phases considered detrimental, such as μ and Laves phases [3]. The addition of alloying elements such as niobium, aluminum, titanium, chromium, and iron is of paramount importance for precipitate formation in the matrix, and also directly influences the oxidation kinetics and the stability of oxide layers formed in these alloys at high temperatures [4]. Thus, the present study aimed to systematically evaluate the effect of different alloying elements on the microstructure and oxidation resistance of Ni-15Nb-M ternary alloys (M = Al, Ti, Cr, or Fe). To this end, 100 g ingots were produced in a tungsten-electrode arc furnace under argon atmosphere with rapid cooling; 10 × 10 × 0.5 mm specimens were obtained by electrical discharge machining and subsequently subjected to oxidation tests in a resistance furnace at 800 °C for 1 h, 3 h, 10 h, 30 h, and 100 h. Sample characterization involved calculation of the mass gain per unit area to determine oxidation reaction kinetics, X-ray diffraction, optical microscopy, scanning electron microscopy coupled with energy-dispersive X-ray spectroscopy, and Vickers microhardness. As main results, it was observed that the addition of Al, Ti, or Fe, in the studied proportions, to the Ni-15Nb system did not significantly alter the oxidation resistance of the alloys, since they exhibited common characteristics in terms of oxidation rate, oxide layer thickness, and internal oxidation by diffusion through the scale. However, the morphology of the oxide layers in each of these alloys underwent changes, favoring either the oxide associated with the alloying element or Ni-rich oxide only, resulting in porosity in certain cases. Furthermore, within the ternary Al and Cr systems, increasing the alloying element content led to a decrease in the oxidation rate. The main conclusion drawn was that the alloying element conferring the highest oxidation resistance under these conditions was chromium [5].

References

[1] R.C. Reed, The superalloys: fundamentals and applications. Camb. Uni. Press (2008).

[2] D.J. Young, High temperature oxidation and corrosion of metals. Elsevier (2008).

[3] J. Belan, GCP and TCP phases presented in nickel-base superalloys. Mater. Today Proc. (2016).

[4] A.K. Jena et al., The role of alloying elements in the design of nickel-base superalloys. Journal of Mat. Sci. (1984).

[5] This research was supported by FAPESP PAIP 2023/16836-2 and Grants 2022/00030-6 and 2025/27069-8. This study was partially supported by CAPES. Finance Code 001.

Table 1. Rounded parabolic mass gain constants K_p per alloy.

Alloy	K_p [mg^2/mm^{4h-1}]
Ni-15Nb	2.6×10^5
Ni-15Nb-0.5Al	2.3×10^5
Ni-15Nb-2Al	1.5×10^5
Ni-15Nb-1Ti	1.9×10^5
Ni-15Nb-4Ti	2.8×10^5
Ni-15Nb-5Cr	1.5×10^4
Ni-15Nb-15Cr	1.2×10^2
Ni-15Nb-5Fe	2.0×10^5
Ni-15Nb-15Fe	2.3×10^5
Own authorship.	

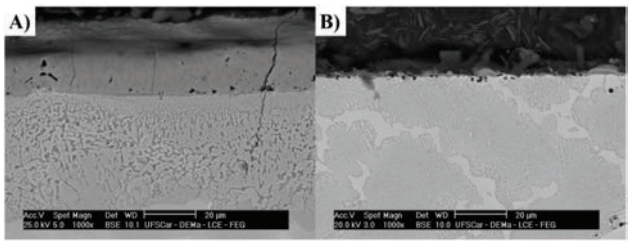


Figure 1. Cross-sectional micrograph of alloys A) 2Al and B) 15Cr, after 100 h at 800 °C.

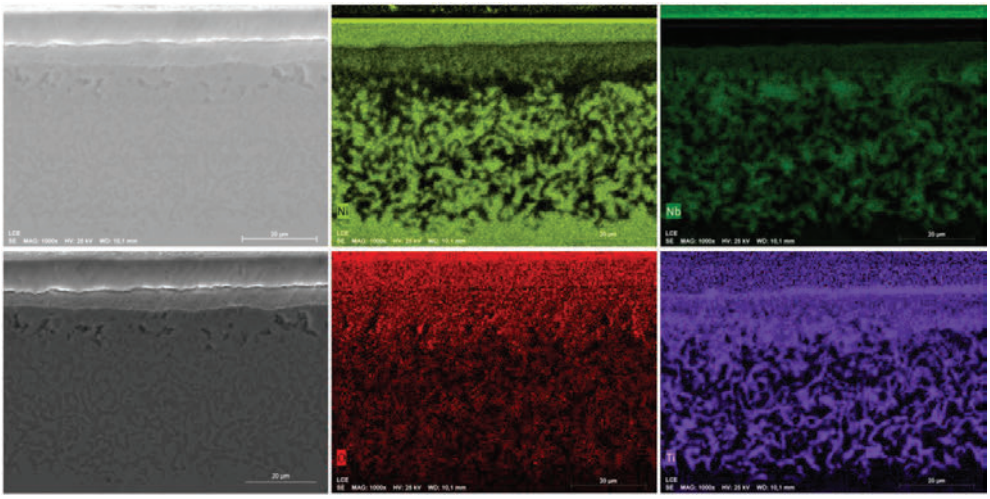


Figure 2. SEM-EDS color map of the Ni-15Nb-4Ti alloy oxidized at 800 °C for 100 h.

Effect of Hydrogen on the Microstructure of C14-Type Laves Phase Multicomponent Alloys

O. A. Pedroso[1], W. J. Botta[1], G. Zepon[1]

[1] Federal University of São Carlos, DEMa, São Paulo, Brasil.
*E-mail: otavioap@df.ufscar.br

The thermodynamic behavior of metal–hydride systems is strongly influenced by both alloy composition and crystal structure. Multicomponent alloys have therefore attracted significant attention for solid-state hydrogen storage due to their huge compositional space, which enables fine tuning of hydrogen-related properties. Among these materials, intermetallic multicomponent alloys, particularly C14-type Laves phases, stand out as promising candidates because of their ability to reversibly absorb substantial amounts of hydrogen under moderate temperature and pressure conditions. Despite these advantages, the hysteresis observed in pressure–composition-isotherms for certain alloy compositions remain insufficiently understood [1]. To better understand this hysteresis, the effects of microstructure and chemical composition on hydrogen behavior were investigated in the $(Ti_{0.2}Zr_{0.8})_1(MnCr)_2$ alloy under three conditions: as-cast, partially hydrogenated, and fully hydrogenated. A combination of advanced characterization techniques was employed. Scanning electron microscopy (SEM) and transmission electron microscopy (TEM), coupled with energy-dispersive X-ray spectroscopy (EDX), were used to analyze the alloy composition. Structural and microstructural changes induced by hydrogen were examined using X-ray diffraction (XRD), electron backscatter diffraction (EBSD), and automatic crystallographic orientation mapping (ACOM). The results indicate that hydrogen incorporation leads to lattice expansion without altering the phase. Although the microstructure does not exhibit significant changes and small-angle rotations, figure 1, could be observed in the crystal structure [2].

References

[1] S. Oian, D.O. Northwood, HYSTERESIS IN METAL - HYDROGEN SYSTEMS: A CRITICAL REVIEW OF THE EXPERIMENTAL OBSERVATIONS AND THEORETICAL MODELS, 13 (1988) 25–35.

[2] This research was supported by FAPESP (Brazil).

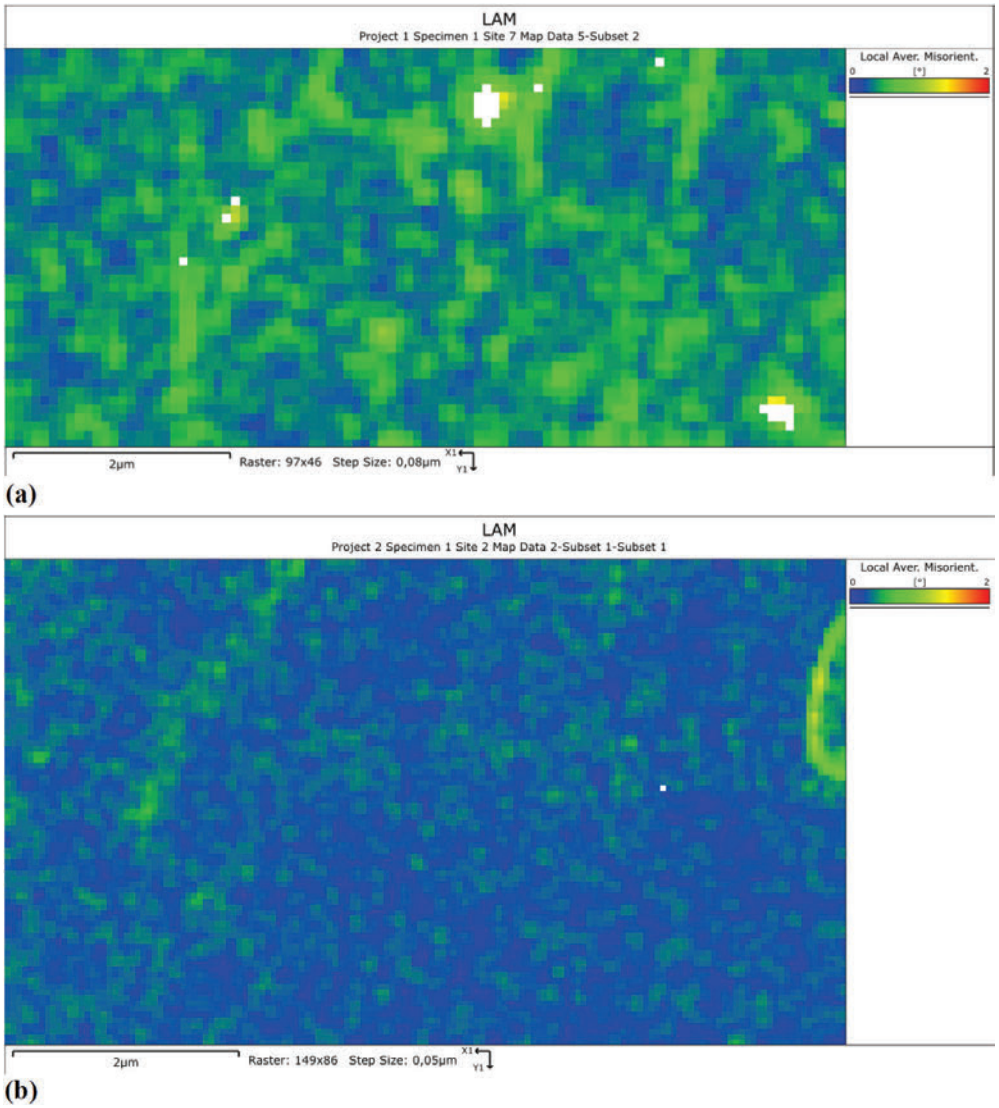


Figure 1. Local average misorientation maps showing the domains in which small angle rotations could be seen in the different hydrogen concentrations: a) partially hydronated, and b) fully hydrogenated

Effect of Ni Addition on the 3D Morphology of Fe-Rich Intermetallics in Directionally Solidified Al–5Cu–1.2Fe Alloys

Felipe Escher Saldanha[1], Jaderson Rodrigo da Silva Leal[1], Guilherme Lisboa de Gouveia[1,2], José Eduardo Spinelli[1,2*]

[1] Department of Materials Engineering, Federal University of São Carlos; [2] Federal University of São Carlos, Graduate Program in Materials Science and Engineering.
*E-mail: spinelli@ufscar.com

The increasing demand for lightweight and sustainable structural materials has intensified interest in recycled Al alloys for transportation and engineering applications [1]. However, Fe contamination introduced during recycling promotes the formation of brittle Fe-rich intermetallic compounds (IMCs), whose morphology and spatial distribution strongly affect mechanical performance. In Al–Cu alloys, coarse needle-like or plate-like IMCs reduce ductility and fracture resistance, making the control of intermetallic evolution essential for improving alloy reliability [2,3]. Although Ni additions have been proposed as an effective strategy to modify Fe-rich phases, their influence on the tensile behavior and fracture mechanisms of Al–Cu–Fe alloys remains insufficiently understood, particularly from a three-dimensional (3D) microstructural perspective. This work investigates the effect of 1 wt.% Ni addition on the solidification behavior, microstructure, tensile response, and fracture mechanisms of directionally solidified Al–5Cu–1.2Fe alloys. Special emphasis is given to the evolution, morphology, and interconnectivity of IMCs through X-ray computed microtomography (micro-CT), combined with conventional microstructural characterization techniques. CALPHAD-based thermodynamic calculations were employed to predict phase formation and solidification sequence, while optical microscopy and scanning electron microscopy were used to support phase identification and microstructural analysis. The ternary Al–5Cu–1.2Fe alloy exhibited the formation of $Al_{13}Fe_4$ intermetallics, whereas the addition of Ni promoted the formation of Al_9FeNi phases. Tensile tests (Figure 1) showed that, at high cooling rates (~13 K/s), the ternary alloy achieved superior tensile strength (>265 MPa) and elongation (>15%) compared with the Ni-containing alloy (~230 MPa and ~9%, respectively). Despite partially refining the intermetallics, Ni addition reduced both strength and ductility, while exerting limited influence on yield strength and microhardness. Three-dimensional micro-CT analyses (Figure 2) revealed bulky and highly interconnected $Al_{13}Fe_4$ networks in the ternary alloy, whereas the Al_9FeNi particles formed in the quaternary alloy were comparatively refined but still exhibited branched morphologies aligned with the solidification direction. Quantitative 3D analysis demonstrated higher surface area-to-volume ratios for the ternary alloy, suggesting more effective stress transfer during tensile loading. The results demonstrate the importance of combining 3D microstructural characterization with mechanical analysis to understand the role of alloying additions on IMC evolution and fracture behavior in recycled Al alloys.

References

[1] Y. Sun, Structures 57 (2023) 105290. https://doi.org/10.1016/j.istruc.2023.105290.

[2] B.J.M. Freitas, et al., The International Journal of Advanced Manufacturing Technology 102 (2019) 3879–3894. https://doi.org/10.1007/s00170-019-03449-z.

[3] P. Mikolajczak, Materials 16 (2023) 3304. https://doi.org/10.3390/ma16093304.

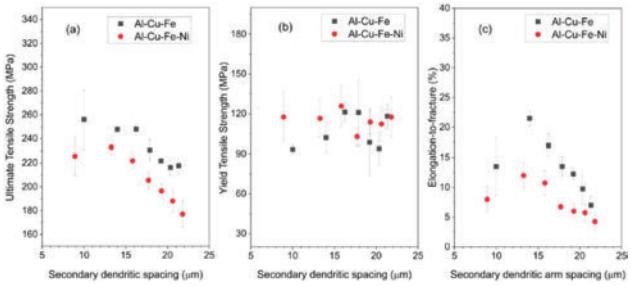


Figure 1. Tensile test results with data converted to true values: (a) ultimate tensile strength, (b) yield strength, (c) elongation at fracture and (d) microhardness of the Al–5Cu–1.2Fe and Al–5Cu–1.2Fe–1Ni alloys.

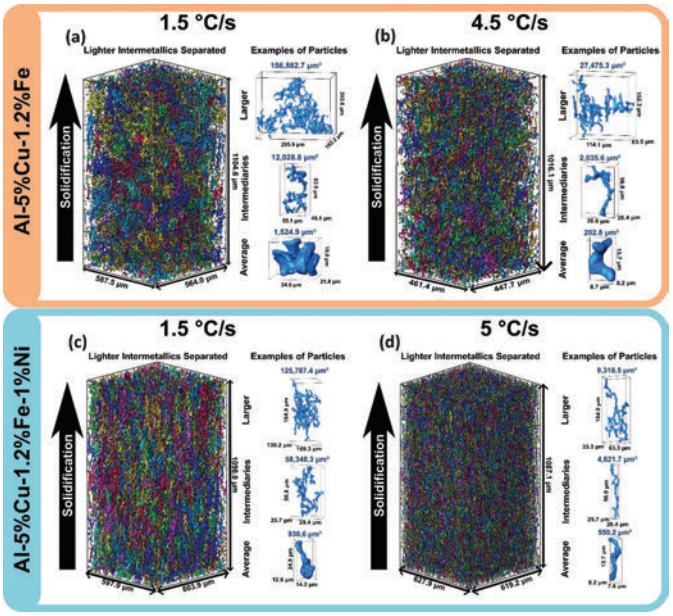


Figure 2. Micro-CT analysis of Fe-rich intermetallics in Al–5Cu–1.2Fe and Al–5Cu–1.2Fe–1Ni alloys solidified at different cooling rates: (a,b) Al–5Cu–1.2Fe at 1.5 and 4.5 °C/s; (c,d) Al–5Cu–1.2Fe–1Ni at 1.5 and 5.0 °C/s.

Effect of Scale Inhibitor Molecules on the Nucleation and Growth of Calcium Carbonate Nanoparticles Revealed by Cryo-TEM and LP-TEM

Fernanda C. Medeiros[1], Raquel P. Gonçalves[2], Vanessa P. Lages[2], Gisele M. Dalmônico[1], Rubens Bisatto[3], Mariana M. Longuinho[4], Dris Ihiawakrim[4], Jacques G. J. Werckmann[4], Marcos Farina[2], Ovidiu Ersen[3], Amaro G. B. Junior[1], André L. Rossi[1]

[1] Brazilian Center for Physics Research, CBPF, Rio de Janeiro, RJ, Brazil; [2] Federal University of Rio de Janeiro, UFRJ, Rio de Janeiro, RJ, Brazil; [3] Federal University of Rio Grande do Sul, UFRGS, Porto Alegre, RS, Brazil; [4] Institute de Physique et Chimie des Materiaux de Strasbourg, IPCMS, Strasbourg, France.

Calcium carbonate ($CaCO_3$) scale formation is a recurring problem in industrial systems such as heat exchangers, water treatment plants, and oil and gas extraction units [1]. Although the literature highlights the role of organic additives in regulating these precursors, understanding the inhibition kinetics at the atomic scale is still an expanding field [2][3]. This work investigates the influence of scale inhibitors (DTPMP, HEMPA, and Vs-Co) on the stabilization of transient $CaCO_3$ phases using advanced electron microscopy techniques. The synthesis was carried out by coprecipitation in aqueous solution, with simultaneous monitoring of pH and calcium concentration. The results obtained by Cryogenic Transmission Electron Microscopy (Cryo-TEM) revealed that, while the control system (without additives) rapidly progresses from 2 nm nanoclusters to crystalline nanoparticles (vaterite and calcite) (Figure 1), the presence of inhibitors promotes the formation and maintenance of pre-nucleation clusters (PNCs) and amorphous clouds (Figure 2). Specifically, the use of Liquid Phase Transmission Electron Microscopy (LP-TEM) allowed real-time visualization of the dynamics of these species. In the case of the DTPMP inhibitor, the evolution of individual nanoclusters into dense aggregates was observed over 284 s, demonstrating a significant extension of the lifespan of the precursor species (Figure 3). The results showed that all inhibitors significantly delayed calcium uptake and initial nucleation compared to the control (not shown). Quantitative analysis of Ca/C by EDS indicated a progressive increase in the stoichiometric ratio as the nanoparticle formation stages progressed in the control group. Cryo Scanning Transmission Electron Microscopy (Cryo-STEM) revealed distinct morphologies according to the inhibitor, with inhD exhibiting elongated morphologies, which differed most significantly from the others (Figure 2). Cryo-STEM-EELS analysis confirmed the chemical composition of the particles, showing spatial correlation between calcium and carbon and characteristic spectra of calcite (not shown). Comparison with the behavior of biopolymers suggests that industrial inhibitors operate through analogous mechanisms, stabilizing ion pairs and preventing binodal phase separation. This study reinforces the effectiveness of in situ monitoring to elucidate the inhibition mechanisms and the relative stability of transient phases, which are fundamental for controlling mineral deposition in industrial systems.

References

[1] CRABTREE, M., et al., Oilfield Review. 11 (1999).

[2] Yan Ji, et al, Desalination, 422 (2017).

[3] Heng Wang, et al., Petroleum, 2021.

[4] This research was supported by CNPq (Brazil)

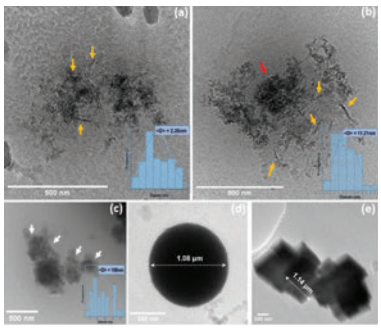


Figure 1. Cryo-TEM images obtained from a 2 min synthesis of (a) agglomeration of 2.3 nm clusters, (b) dense agglomeration (red arrow) with larger nanoclusters (11 nm), (c) (c) 168 nm nanoparticles, many of which contain facets (white arrows), indicating crystallization, (d) d) Spherical vaterite particle measuring ~1 µm. (e) Aggregate of faceted particles with rhombohedral morphology. The details in (a), (b), and (c) show the distribution of the average particle size.

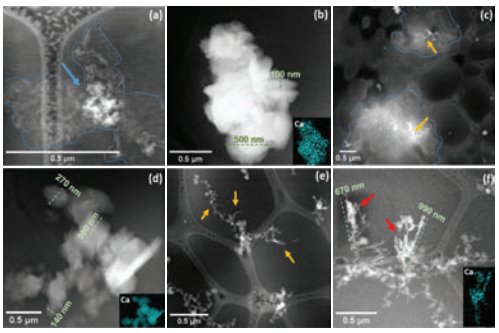


Figure 2. Cryo-STEM and elemental mapping (STEM-EDS) of the nucleation and formation of $CaCO_3$ nanoparticles under the influence of inhibitors. As Figures 2(a,c,e) illustrate initial stages of formation: (a) $CaCO_3$+inhV shows amorphous pre-nucleation clouds (blue dashed line) and a dense core (blue arrow); (c) $CaCO_3$+inhH suggests coalescence of amorphous pre-nucleation clouds (blue dashed line) and nanoclusters forming collars (yellow arrows); (e) $CaCO_3$+inhD presents delayed calcium-rich nanodomains (yellow arrows) and in (d) red arrows. Figures 2(b,d,f) show the morphology of the nanoparticles in advanced stages, with the colored details of the calcium elemental mapping (STEM-EDS) confirming the composition of the structures formed by each inhibitor.

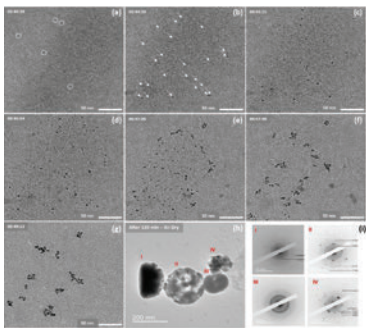


Figure 3. In situ transformation of individual $CaCO_3$ nanoclusters into denser nanoclusters aggregates in the presence of the inhibitor DTPMP. The image sequence (a-g) was acquired by LP-TEM over a time interval of 284 s. (h) TEM image obtained after air drying of the cell used in the experiment (after 120 min of experiment). (i) SAED patterns obtained from 4 different regions of the particle cluster in image (h).

Effect of SiO_2 addition on Microstructure of 3D Printed β Ti-35Nb-6Ta Alloys

Giovanna E. Santo[1*], Lucas D. Duro[1], Bruno M. Casarin[1], Renan A. F. Dias[1], Conrado R. M. Afonso[1]

[1] Department of Materials Engineering (DEMa), Federal University of São Carlos (UFSCar), São Carlos/SP, Brazil.
*E-mail: giovanna.santo@estudante.ufscar.br

β-type titanium alloys have attracted significant attention for biomedical applications due to their low elastic modulus, high corrosion resistance, and excellent biocompatibility. Among these materials, Ti-35Nb-6Ta alloy is considered a promising candidate for orthopedic and dental implants because of the presence of non-toxic β-stabilizing elements such as Nb and Ta. In addition, the incorporation of ceramic particles such as SiO_2 may influence the microstructural characteristics and performance of titanium alloys processed by additive manufacturing techniques. In the present study, β Ti-35Nb-6Ta alloy containing 0.5 wt.% and 1.0 wt.% SiO_2 were manufactured by Laser Powder Bed Fusion (LPBF). Different laser scanning speeds were investigated to evaluate their influence on the microstructure and properties of the alloys. The processing parameters consisted of scanning speeds (and energy density, VED) of 500 mm/s (167 J/mm^3), 750 mm/s (111 J/mm^3), and 1000 mm/s (83 J/mm^3). Due to the rapid melting and solidification associated with LPBF processing, variations in scanning speed can directly affect thermal gradients, cooling rates, and microstructural refinement, leading to differences in phase distribution and morphological characteristics. The structural and morphological characterization of all processing conditions was performed by X-ray diffraction (XRD), optical microscopy (OM), and scanning electron microscopy (SEM). XRD analyses revealed the predominance of the β-Ti phase in all experimental conditions, confirming the stabilization of the β structure promoted by the Nb and Ta additions. No clear formation of Ti_5Si_3 secondary phases neither related to SiO_2 were identified, suggesting nanoscale homogeneous dispersion of the ceramic particles into the alloy β-Ti matrix. For β Ti-35Nb-6Ta alloy + 0.5% SiO_2, variations in peak intensity among the samples suggested a crystallographic texture in [200] plane associated with the different energy densities employed during LPBF processing. These differences are likely related to changes in thermal gradients and directional solidification behavior, which may influence grain orientation and microstructural anisotropy. OM was used to investigate the general microstructural characteristics, while SEM analyses provided detailed information regarding melt pool morphology, surface integrity, and microstructural heterogeneity. SEM observations revealed that the alloys processed with 0.5 wt.% SiO_2 exhibited distinct surface morphologies depending on scanning speed, including smoother and more homogeneous regions at lower speeds (higher VED) and the presence of microcracks and elongated solidification features at higher scanning speeds (higher cooling rates). For the Ti-35Nb-6Ta + 1.0 wt.% SiO_2, irregular surface features, cracks and dispersed particles were observed, suggesting modifications in melt pool stability and consolidation behavior associated with the higher ceramic content. In addition, variations in surface texture and defect distribution indicated a strong influence of laser scanning speed on the solidification behavior and microstructural organization of the LPBF-processed alloys [4].

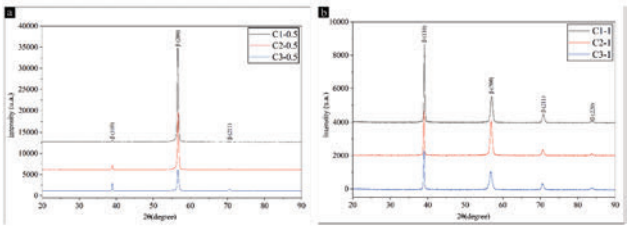


Figure 1. X-ray diffraction (XRD) patterns of Ti-35Nb-6Ta alloys produced by LPBF and treated by Microarc Oxidation (MAO) with different silica concentrations: (a) samples containing 0.5% SiO_2 (C1-0.5, C2-0.5, and C3-0.5) and (b) samples containing 1.0% SiO_2 (C1-1, C2-1, and C3-1). The diffraction peaks indexed to the β phase with body-centered cubic (BCC) structure correspond to the crystallographic planes (110), (200), (211), and (220).

References

[1] F. De Mattos et al., Mater. Lett. 358 (2024) 135776.

[2] C.R.M. Afonso et al., J. Mater. Res. Technol. 40 (2026) 1869–1881.

[3] M.L. Lourenço et al., submitted for publication in J. Mater. Res. Technol.

[4] This research was supported by FAPESP PAIP 2023/16836-2 and partially supported by CAPES, Finance Code 001 (Brazil).

Table 1. Experimental groups according to SiO_2 concentration and laser scanning speed.

Ti35Nb6Ta alloy + SiO_2 (wt.%)	500 mm/s	750 mm/s	1000 mm/s
0.5	C1-0.5	C2-0.5	C3-0.5
1	C1-1	C2-1	C3-1

OmniTek, model OMNISINT-160 with fiber laser Yb:YAG, raycus RFL-C500, and wavelenght λ=1070 nm, spot size of ∅ = 80 µm, Power = 200 W.

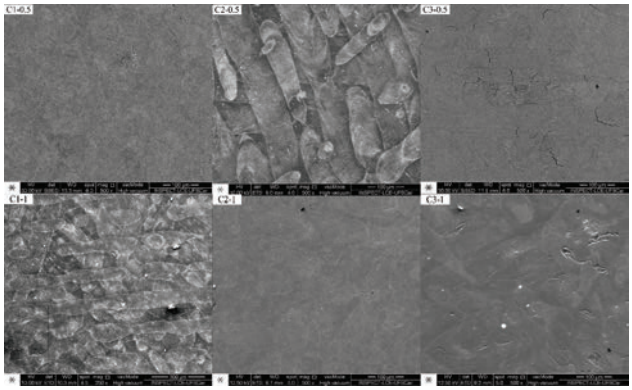


Figure 2. Scanning Electron Microscopy (SEM) of Ti-35Nb-6Ta alloys produced by LPBF with different silica concentrations: samples containing 0.5% (C1-0.5, C2-0.5 and C3-0.5) and samples containing 1.0% SiO_2 (C1-1, C2-1 and C3-1).

Effect of Thermal Aging on the Corrosion Resistance of Deformed UNS S39274

Iasmin Maciel Vieira da Silva[1*], André Rocha Pimenta[1,2]

[1] Programa de Pós-Graduação em Engenharia Mecância PPG-EM, Universidade do Estado do Rio de Janeiro UERJ, Rio de Janeiro, RJ, Brasil; [2] Laboratório de Instrumentação e Simulação Computacional LISCOMP, Campus Paracambi, Instituto Federal do Rio de Janeiro IFRJ, Paracambi, RJ, Brasil.
*E-mail: iasmin.macielvs@gmail.com

Super duplex stainless steels (SDSS) are alloys characterized by a two-phase microstructure composed of ferrite and austenite, ideally in a 1:1 ratio. The chemical composition of the alloy with high contents of chromium, nickel, and molybdenum confers high mechanical strength and corrosion resistance, making them applicable in highly corrosive environments such as those found in the petrochemical industry. However, SDSS may be susceptible to the precipitation of deleterious phases when exposed to temperatures between 600 and 1000°C, including chi and sigma phases and chromium nitrides. Those phases form in the ferrite phase, preferentially at grain boundaries, with their volume fraction tending to increase proportionally with exposure time. These phases consume alloying elements in neighboring regions, causing chromium depletion in the ferrite and leading to localized corrosion (sensitization)[1]. Therefore, evaluating corrosion as a function of aging heat treatment is relevant for establishing safe time and temperature limits for the processing and operation of these alloys. This work investigates the microstructure and corrosion behavior of UNS S39274 rolled steel under three conditions: as-received (AR), aged at 600°C for 2 hours, and aged at 800°C for 15 minutes. It was employed the double-loop electrochemical potentiodynamic reactivation (DL-EPR) test for corrosion analysis, with results assessed through the reactivation-to-activation current ratio (Ir/Ia), where values closer to 0 indicate lower sensitization [2]. The DL-EPR tests were conducted with 3M of HCl solution. In addition, the investigation was complemented by scanning electron microscopy (SEM) on only polished samples, for examination of the microstructure, and on the surface after the DL-EPR test, for examination of the corroded area. The digital image processing (DIP) was used to determine the volume fractions of deleterious phases and the corroded area. The DL-EPR results are shown in Fig 1. This study showed that the AR sample has the greatest corrosion resistance, with a corroded area of 0.71% ± 0,18 evaluated by DIP. The corrosion in the AR sample was restricted to grain boundary regions with no deleterious phases, as shown in Fig 2 a-b. This condition has an Ir/Ia ratio of 0.00015. Aging at 600°C for 2 hours caused limited deterioration, with a 2.48% ± 0,64 corroded area and a sensitization degree of 0.046, the results are consistent with the 1,3% ± 0,8 fraction of chi phase in the ferrite boundaries, evaluated by DIP. The 800°C/15-minute treatment produced the highest corrosion index and highest fraction of deleterious phases, with 7.04% ± 2,52 corroded area and an Ir/Ia ratio of 0.737, demonstrating sensitization associated with a greater extent of deleterious phases, as shown in Fig 3 a-b, and 3,9% ± 2,4 of deleterious phase chi. The progressive increase in both DIP consumed-area fractions and Ir/Ia values indicates a growing susceptibility to corrosion with advancing heat treatment and increasing chi and sigma phase fractions in the microstructure (Fig 4 a-b). This work does not observe nitrides as cause of corrosion in the DL-EPR test. No formation of sigma phase was observed in the conditions tested.

References

[1] ASM International, Properties and Selection: Irons, Steels, and High-Performance Alloys, (1). Ohio: ASM, 1990.

[2] M. Bassiouni, "Evaluation of the microstructure and localized corrosion behaviour of AISI 2507 super duplex stainless steel welds", RMIT University, 2024.

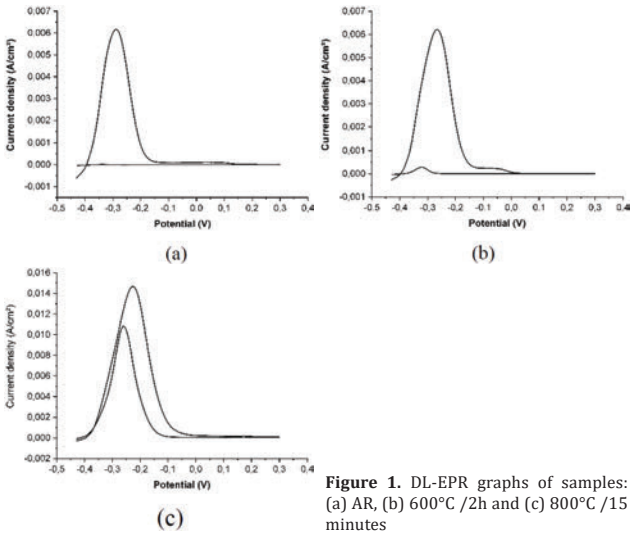


Figure 1. DL-EPR graphs of samples: (a) AR, (b) 600°C /2h and (c) 800°C /15 minutes

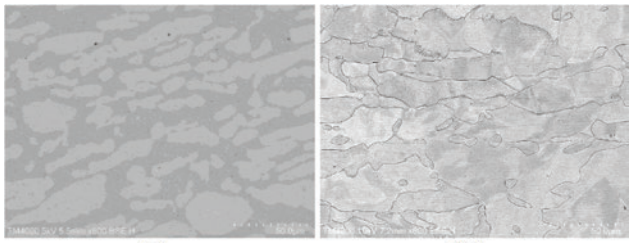


Figure 2. SEM images of AR sample: (a) before DL-EPR, (b) after DL-EPR

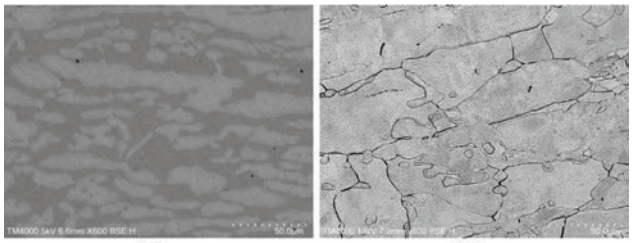


Figure 3. SEM of 600°C for 2 hours sample: (a) before DL-EPR, (b) after DL-EPR.

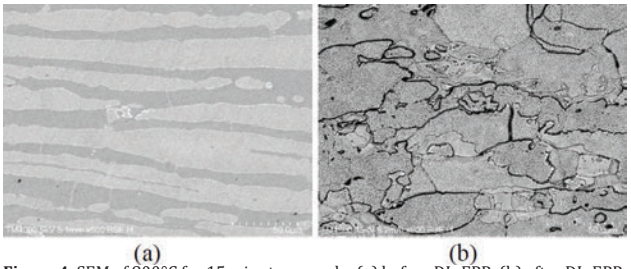


Figure 4. SEM of 800°C for 15 minutes sample: (a) before DL-EPR, (b) after DL-EPR.

Effect of Yttrium Addition on Carbide Nucleation and Interdendritic Network Fragmentation in modified HP Nb-Ti Centrifugally Cast Stainless Steel

Gabriel Souza Bento[1], Taissa Zangerolami Lopes Rodrigues[1*], Fabio dos Santos Queiroz[1], Leonardo Sales Araujo[1], Luiz Henrique de Almeida[1]

[1] Metallurgical and Materials Engineering Program/Department – COPPE/UFRJ.
*E-mail: taissazl@metalmat.ufrj.br

Cast austenitic stainless steels of the HP class are widely used in steam reforming furnaces due to their high-temperature strength and corrosion resistance. During service, these components are exposed to severe creep conditions. The microstructure of HP steel consists of an austenitic matrix containing interdendritic carbides, M23C6 and NbC, whose morphology, distribution, and stability strongly influence the creep resistance and high-temperature performance of the alloy. Also, the addition of titanium acts on the microstructure by transforming Nb carbides into Nb-Ti carbides and improving the creep properties of the material and reducing the formation of the G phase [1]. In recent years, the addition of rare earths elements has attracted considerable attention due to their ability to modify solidification behavior and refine the microstructure of centrifugally cast alloys. Among elements, yttrium (Y) has shown promising effects as a microstructural refining element, acting as a nucleation site for Nb-Ti carbides and promoting the fragmentation of the chromium carbide network. Previous studies suggest that Y addition may promote chromium carbide fragmentation and improve the mechanical behavior of HP steels by reducing crack propagation [2]. Therefore, this work investigates the influence of yttrium addition on the microstructure of HP Nb-Ti stainless steel using Optical Microscopy (OM) and Scanning Electron Microscopy (SEM). One conventional HP Nb-Ti alloy was used as a reference and compared with two modified alloys containing different yttrium contents: Y6 (0.028%) and Y3 (0.070%). Special emphasis is given to the refined microstructure observed near the outer wall of the tube, where a higher local concentration of Y appears to be associated with the fragmentation of Cr-rich carbides and the formation of Y-rich precipitates. The results contribute to a better understanding of the role of yttrium in precipitate distribution and microstructural stability, aiming at improving the high-temperature performance and creep resistance of HP-class reformer alloys.

References

[1] L.H. Almeida et al., Mater. Charact, 49(3) (2003) 219–229.

[2] F.C. Nunes et al., Mater. Charact. 58 (2007) 132–142.

[3] This research was supported by CNPq and Petrobras (Brazil).

Y3 Sample

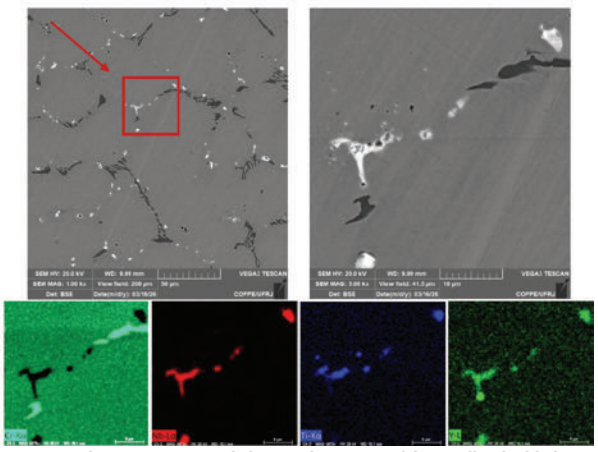


Figure 1. SEM characterization and elemental mapping of the Y3 alloy, highlighting Y-rich particles acting as nucleation sites for Nb-Ti carbides.

Y6 Sample

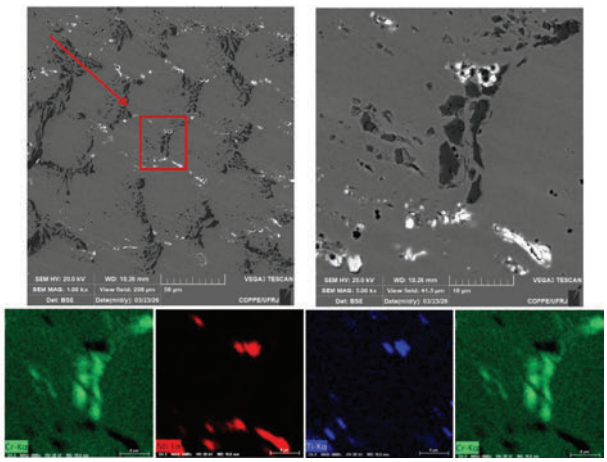


Figure 2. SEM characterization and elemental mapping of the Y6 alloy, showing fragmentation of the Cr-rich carbide network and the presence of Nb-Ti carbides associated with yttrium addition.

Effects of Solidification Cooling Rate and Aging Time on the Microstructure of Al-4%Ni-0.07%Nb Alloy

Marcella Gautê Cavalcante Xavier[1*], José Eduardo Spinelli[1]

[1] Univerdade Federal de São Carlos (Graduate Program in Materials Science and Engineering).
*E-mail: marcella.xavier@estudante.ufscar.br

The growing demand for high-performance aluminum alloys for elevated-temperature applications (200-400°C) drives strategies to enhance microstructural stability. Al-Ni alloys are promising due to the Al_3Ni intermetallic phase, but their morphology is strongly dependent on processing conditions [1]. The microaddition of Nb emerges as an effective strategy to refine the microstructure and retard phase coalescence through grain boundary pinning. In this context, the present study investigates, with emphasis on scanning electron microscopy (SEM/EDS), the microstructural evolution of the Al-4%Ni-0.07%Nb alloy processed under five different cooling rates, comparing as-cast conditions with those subjected to aging heat treatments at three selected solidification cooling rates. The alloy was produced in an induction furnace from high-purity raw materials (99.83% Al, 99.85% Ni, 99.95% Nb), and its nominal composition was confirmed by ICP-OES and EDS. The theoretical solidification path was determined by CALPHAD/TCAL 7.1, and the eutectic temperature was identified by DSC. The upward directional solidification process, monitored by type K thermocouples along the ingot, enabled the determination of five distinct cooling rates ($\dot{T}_E$), along with the simultaneous determination of solid-liquid interface growth rates (V_E) and thermal gradients (G_E). Samples extracted exactly at the thermocouple positions were metallographically prepared (Keller's reagent for microstructure and Poulton's reagent for macrostructure) and analyzed by OM and SEM/EDS (Figure 1). For each of the five cooling conditions in the as-cast state, measurements of average primary dendritic spacings, as well as eutectic spacings (differentiating between fibrous and lamellar morphologies), were performed using ImageJ software with 40 measurements per sample. For comparative analysis with aging, three out of the five cooling rates (specific positions along the ingot) were selected. From each of these three positions, samples were subjected to aging at 300 °C in an EDG furnace, with holding times of 4 h, 24 h, and 50 h. The temperature of 300 °C is considered severe for Al alloys, and evaluating material behavior under such an extreme condition is often feasible within relatively short exposure times [2,3]. All aged samples were characterized following exactly the same microstructural quantification methodology employed for the as-cast samples, including the same metallographic preparation, the same SEM/EDS image acquisition protocol, and the same 40 measurements per sample in ImageJ for dendritic and eutectic spacings. In the as-cast condition, increasing the cooling rate promoted significant refinement, with average dendritic spacings ranging from 9.1 µm to 11.8 µm and submicrometric eutectic spacings from 0.40 µm to 0.50 µm. The effectiveness of Nb as a refining agent is evidenced by comparison with binary alloys: while the Al-1%Ni alloy exhibits coarse fibers (1-3 µm), the Nb-containing alloy reaches a scale of 0.40 µm, approaching the limit of 0.30 µm observed only in the eutectic Al-6.3%Ni alloy under rapid cooling [1]. For aging at 300 °C, three cooling rates (2.1 K/s, 4.6 K/s and 5.6 K/s) were selected. For the highest cooling rate condition, the eutectic spacing evolved progressively with aging time: 0.40 µm (4 h), 0.51 µm (24 h), and 2.32 µm (50 h). Samples solidified under high cooling rates maintained a refined microstructure even after 50 h at 300 °C (Figure 2). In contrast, those solidified under low cooling rates exhibited pronounced coalescence and spheroidization of the eutectic phases during aging. The results demonstrate that the interaction between cooling rate and aging time produces distinct microstructural changes. The systematic quantification methodology proved essential for comparability across different processing conditions. These findings contribute to the development of thermally stable Al-Ni-based alloys for high-temperature applications [4].

References

[1] R. Kakitani et al., J. Alloys Compd., 733, 59, 2018.

[2] S.Y. Kwon et al., J. Alloys Compd., 997, 174810, 2024.

[3] J. Smalc et al., J. Mater. Res. Technol., 32, 1928, 2024.

[4] This research was supported by CAPES (Brazil) - Process No. 88887.103473/2025-00.

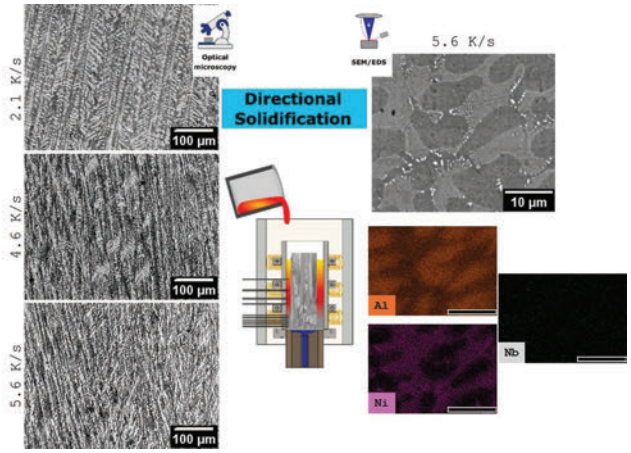


Figure 1. As-cast characterization of the Al-4%Ni-0.07%Nb alloy (OM and SEM/EDS). The microstructural refinement as a function of the cooling rate ($\dot{T}_E$) is highlighted, alongside the elemental distribution of Al, Ni, and Nb via chemical mapping.

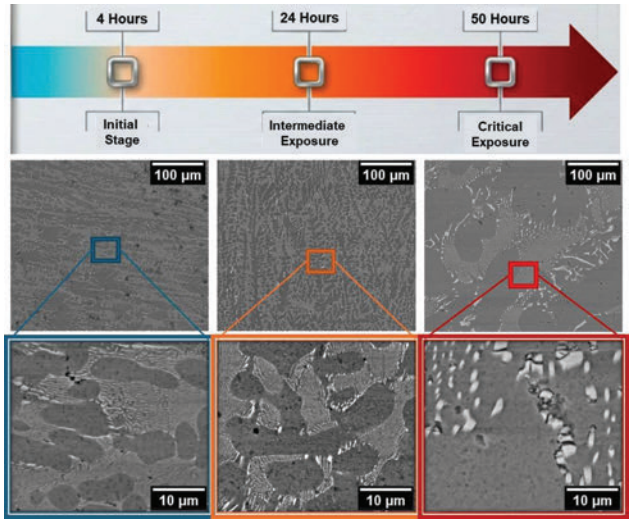


Figure 2. Thermal stability evolution of the Al-4%Ni-0.07%Nb alloy at 300 °C during the initial stage (4 h), intermediate exposure (24 h), and critical exposure (50 h). For $\dot{T}_E$ = 5.6 K/s, coalescence and spheroidization of the intermetallic phases are observed, with the eutectic spacing evolving from 0.40 µm (4 h) to 2.32 µm (50 h).

Enhancement of zinc nanoparticles to produce supraparticles as a potential agricultural input

Júlia Rodrigues de Freitas[1], Mariana Monteiro de Lima Honorato Forini[1], Luiz Aparecido Ferreira Cavalcante[1], Renato Grillo[1*]

[1] São Paulo State University (UNESP), Faculty of Engineering, Department of Physics and Chemistry, Ilha Solteira, SP, Brazil.
*E-mail: renato.grillo@unesp.br

Nanotechnology has been widely used to develop and improve agricultural inputs for the controlled release of nanoagrochemicals[1]. In this context, the use of supraparticles, complex structures formed by colloidal particles of nano- or micrometer dimensions, can reduce problems associated with conventional agriculture, such as bioaccumulation and leaching in the soil [2]. Thus, this work aimed to prepare and characterize zinc oxide nanoparticles (ZnO NPs) for the fabrication and characterization of zinc oxide supraparticles (ZnO SPs), and to evaluate the *in vitro* release profiles of the NPs and SPs, as well as their mobility in soil. The NPs were synthesized using the co-precipitation method [3] with some modifications, and characterized by Transmission Electron Microscopy (TEM), Dynamic Light Scattering (DLS), and Fourier Transform Infrared Spectroscopy (FTIR) (Figures 1A, B and C); the SPs were produced via self-assembly induced by evaporation on a hydrophobic surface and characterized by Scanning Electron Microscopy coupled with Energy Dispersive Spectroscopy (SEM-EDS) and FTIR (Figures 1E-1L). *In vitro* release kinetics of the NPs and SPs were evaluated to assess their release profiles, and mobility tests in soil columns were conducted for the NPs, SPs, and zinc sulfate ($ZnSO_4$) compared with a control. The NPs had sizes less than 50 nm, with a polydispersity index (PDI) of 0.177, and a zeta potential of +23.74 mV. The SPs exhibited spherical morphology, showing affinity among the constituent NPs (Figures 1D and E). The *in vitro* release kinetics evaluation revealed a higher release profile (around 7%) for the NPs compared to the SPs (around 6%), indicating that SPs provide a slower ion-release profile relative to the NPs (Figure 2E). Soil mobility experiments showed that the conventional $ZnSO_4$ treatment leached rapidly along the soil column, whereas the NP treatment exhibited some leaching but was slower than sulfate, indicating that zinc ions were distributed throughout the soil column, whereas the supraparticles remained contained in the upper soil layer. This indicates that SPs are retained in the soil surface layer near the rhizosphere, where plants can absorb the micronutrients made available by the SPs; consequently, ions are not leached into deeper soil layers. Therefore, this work provided insights into enhancing nanoparticles within complex supraparticles, which allow for slower release of agricultural inputs into the environment and exhibit lower leaching rates, thereby preventing bioaccumulation in soils [4].

References

[1] R. Grillo et al., Nano Today, 37, 2021.

[2] W. Liu; M. Kappl; H-J. Butt. ACS Nano, v. 13, n 12, 2019.

[3] A. Aditya et al. ACS Applied Materials & interfaces, v. 10, n. 18, 2018.

[4] This research was supported by FAPESP (2026/05427-2; 2024/20135-2; 2022/03219-2; 2023/00541-3; 2023/09217-4] and CNPq (#310846/2022-6).

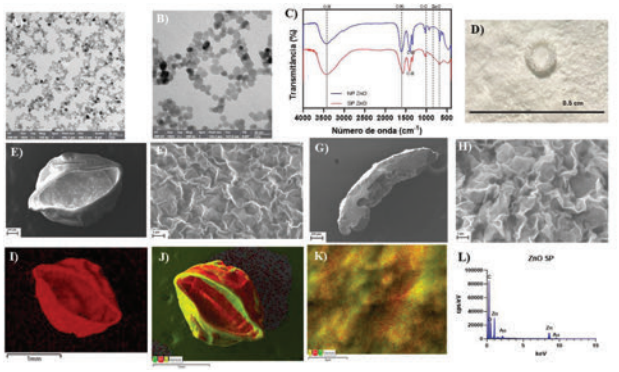


Figure 1. Characterization of the ZnO nanoparticles (ZnO NPs) and ZnO supraparticles (ZnO). A-B) Transmission Electron Microscopy (MET) of the ZnO NPs; C) Fourier Transform Infrared Spectroscopy of the ZnO NPs and SPs; D) Stereoscopic Microscopy of the SPs; E-F) Scanning Electron Microscopy of the SP and its external surface, respectively; G-H) Scanning Electron Microscopy of the SPs section and its internal surface; I-K) Scanning Electron Microscopy coupled with Energy Dispersive Spectroscopy (SEM-EDS) of the SPs and its external surface, respectively; L) Diffractogram of the ZnO SP.

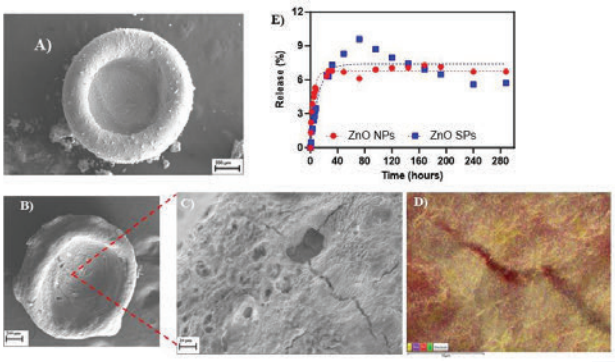


Figure 2. *In vitro* release kinetics experiment. A) Scanning Electron Microscopy of the ZnO SP before the experiment; B) Scanning Electron Microscopy of the ZnO SP after the experiment; C) Scanning Electron Microscopy of the surface of the ZnO SP, showing fractures; D) Scanning Electron Microscopy coupled with Energy Dispersive Spectroscopy (SEM-EDS) of the SP showing the elements Zn and O; E) Evaluation of the *in vitro* release kinetics of nanoparticles and supraparticles.

Expansão celular diferencial no endosperma de *Coffea arabica* durante a torrefação

Vinicius P. M. Xavier[1*], Marta R. Verruma-Bernardi[2], Patrícia H. Santoro[3], Lyssa S. Sakanaka[1], Paulo S. P. Herrmann[4]

[1] Universidade Tecnológica Federal do Paraná (UTFPR), Londrina, PR, Brasil; [2] Universidade Federal de São Carlos (UFSCar), Araras, SP – Brasil; [3] Instituto de Desenvolvimento Rural do Paraná (IDR), Londrina, Paraná – Brasil; [4] Embrapa Instrumentação, São Carlos, SP, Brasil.
*E-mail: viniciuspariser@alunos.utfpr.edu.br

O processo de torrefação do café promove transformações físicas e químicas na estrutura dos grãos. Contudo, as respostas estruturais das diferentes regiões do endosperma ao aquecimento ainda são pouco compreendidas. O endosperma de *Coffea arabica* possui organização heterogênea, dividindo-se em porções mais compactas e rígidas (endosperma duro) e menos compactas (endosperma macio) [1,2] e algumas das células mais internas do endosperma possuem paredes primárias mucilaginosas [3]. Essa variação na composição e organização da parede celular pode influenciar diretamente a expansão térmica e a formação de poros durante a torra [4,5]. O objetivo deste estudo foi avaliar, por microscopia eletrônica de varredura (MEV), as alterações da estrutura celular do endosperma de grãos de *C. arábica submetidos* a diferentes tempos de torrefação. As amostras foram torradas nos tempos de 0, 5, 10 e 12 min, submetidas à criofratura por meio de imersão em nitrogênio líquido e seccionadas transversalmente com lâmina cortante, assegurando a preservação das estruturas celulares originais. Posteriormente foram fixadas em *stubs* de alumínio e recobertas com ouro (20 nm) utilizando um *Sputter Coater* SCD 050 LEICA. As imagens foram obtidas em MEV JSM-6510/JEOL, com tensão de aceleração de 5 kV e distância de trabalho de 20 mm, com foco na avaliação da expansão do lúmen celular e da evolução da porosidade nas diferentes zonas do endosperma. As imagens apresentadas na Figura 1 indicaram que o grão cru apresentou estrutura celular compacta, com lúmens reduzidos e paredes celulares bem delimitadas. Com o avanço da torrefação, observou-se aumento progressivo dos espaços celulares, deformação da matriz do endosperma e desenvolvimento de porosidade. Entretanto, as alterações não ocorreram de forma homogênea entre as regiões avaliadas. A zona correspondente ao endosperma macio (A) apresentou maior expansão celular que endosperma duro (B), caracterizada pelo aumento mais evidente do lúmen e pela ampliação dos espaços internos entre as paredes celulares. Em contraste, na zona do endosperma duro observou-se estrutura mais compacta ao longo do processo, com menor expansão relativa das células e maior preservação da organização celular. Esse comportamento heterogêneo sugere que a evolução da porosidade interna do café durante a torra depende da região do endosperma. Estudos prévios demonstram que as condições de torra alteram substancialmente a microestrutura do café, promovendo aumento do volume do grão, do volume de poros e dos microporos nas paredes celulares [6]. Assim, os resultados deste estudo indicam que essa expansão celular não ocorre de maneira uniforme, mas é influenciada pela heterogeneidade estrutural do endosperma [7].

Referências

[1] R. D. de Castro; P., Marraccini. Braz. J. Plant Physiol. 18 (2006). 175.
[2] M. T. S. Eira et al., Braz. J. Plant Physiol. 18 (2006). 149.
[3] D. M. Dedecca. Bragantia. 16 (1957). 315.
[4] P.W. Sutherland et al., Protoplasma, 223 (2004). 203.
[5] Z. Li et al., Food Qual. Saf. 5 (2021).
[6] S. Schenker et al., Food Sci, 65 (2000). 452.
[7] Embrapa Instrumentação, São Carlos, SP, Brasil.

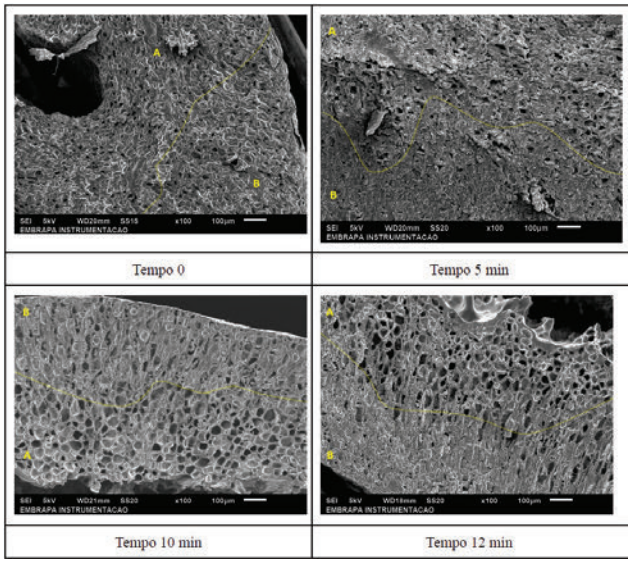


Figura 1 – Efeito do tempo de torra na microestrutura do endosperma macio (A) e duro (B) grãos de café observado por MEV. Linha amarela demarcando a região de transição entre os dois endospermas.

Feasibility Study of Niobium Chip Recycling for the Development of Welding Fluxes for Hardfacing

Letícia K. M. Firmo[1], José Gedael Fagundes Jr[2], Vicente A. Ventrella[1,2], Juno Gallego[1,2*]

[1] Post-Graduate Program in Mechanical Engineering at UNESP – Ilha Solteira; [2] Department of Mechanical Engineering, São Paulo State University – UNESP, Ilha Solteira, São Paulo, Brazil.
*E-mail: juno.gallego@unesp.br

Abrasive wear stands as one of the primary failure mechanisms in mechanical components within the steel, mining, and agricultural sectors. Consequently, mitigating this process is necessary to optimize operational costs and extend equipment service life [1]. In light of this, the present study proposed a sustainable and low-cost alternative for mitigation. Given the high commercial cost of pure niobium, the research investigated the reuse of niobium chips, machining waste frequently discarded, as a raw material for developing welding fluxes intended for hardfacing. The methodology consisted of embrittling the chips in a microwave oven using coal powder, followed by milling to a particle size of 0.42 mm. This powder was combined with alloying elements (C, Si, Mn) and sodium silicate to compose a flux, which was preliminarily validated via the Gas Tungsten Arc Welding (GTAW) process on a SAE 1020 steel substrate. Scanning electron microscopy (SEM) analyses and energy-dispersive X-ray spectroscopy (EDS) mapping (Figures 1 and 2) confirmed the effective formation of a metallic matrix reinforced by niobium carbides (NbC) originated from the recycled waste. A overlapping concentration of niobium and carbon was observed in the dendritic regions [2], in addition to a microstructural refinement toward the fusion line. Although the observed dilution rate (42.42%) exceeded the values recommended in the literature between 10% and 25% for hardfacing applications [3], the flux composition ensured a significant volume fraction of hard phases (60.96%). This microstructural condition reflected positively on the Vickers microhardness profile (Figure 3) of the fusion zone, which presented values between 450 HV and 800 HV, with peaks up to 1000 HV in the NbC clusters, values significantly higher than the hardness of the base metal (150–180 HV). The results validate the effectiveness of the coating and prove that recycling niobium waste is technically viable for producing wear-resistant surfaces, offering a solid foundation for the future development of flux-cored wires (FCAW). The authors acknowledge the support received [4].

References

[1] B. Swain et al. Tribology in Materials and Manufacturing - Wear, Friction and Lubrication (2021).

[2] T. Oliveira, A. Costa, Revista Materia 24 (2019).

[3] D. Tandon et al. Metals (Basel). 13 (2023).

[4] This research was supported by CAPES and FAPESP.

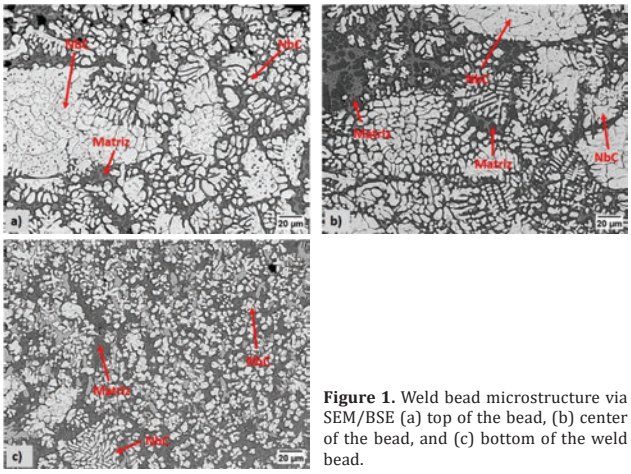


Figure 1. Weld bead microstructure via SEM/BSE (a) top of the bead, (b) center of the bead, and (c) bottom of the weld bead.

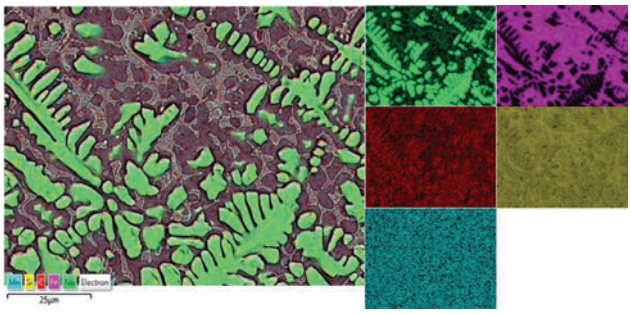


Figure 2. Chemical area mapping via EDS.

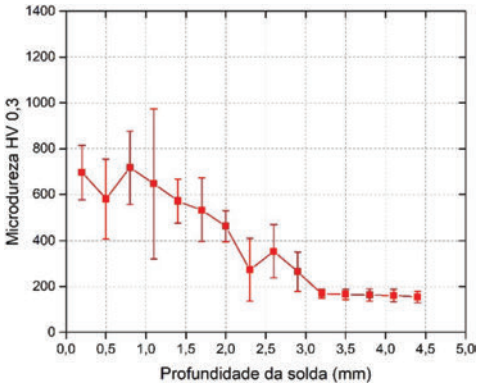


Figure 3. Microhardness (HV 0.3) as a function of weld depth.

Hierarchical Organization of Hybrid Supraparticles Revealed by Scanning Electron Microscopy

Mariana M. L. H. Forini[1], Luiz A. F. Cavalcante[1], Júlia R. de Freitas[1], Débora R. Antunes[1], Érica R. Biscalchim[1], Renato Grillo[1*]

[1] São Paulo State University (UNESP), Faculty of Engineering, Department of Physics and Chemistry, Ilha Solteira, SP, Brazil.
*E-mail: renato.grillo@unesp.br

It is estimated that the world population will reach 10.4 billion people by 2100, implying an increase in global food production. However, conventional agriculture will not be able to meet the population's need for food. Given this scenario, agrochemicals are used excessively, potentially bioaccumulating in the soil and groundwater, and exhibiting low efficiency. Nanotechnology is emerging as a promising area in the agricultural sector, enabling the design and manipulation of nanoparticulate systems for the preparation of larger structural blocks from the self-assembly of colloidal nanoparticle clusters, called supraparticles (SPs) [1]. Supraparticles exhibit unique functionalities that differentiate them from individual nanoparticles, such as coupling, synergism, and co-localization, in addition to enabling the controlled release of agrochemicals and exhibiting reduced mobility in the soil [2]. In this study, hybrid supraparticles were fabricated from magnetic nanoparticles coated with sodium citrate (Fe_3O_4@Sodium Citrate NPs), lipid nanocarriers containing the herbicide Atrazine (CLN:ATZ), and microcrystalline cellulose using the self-assembly method induced by evaporation on a superhydrophobic surface. The synthesized NPs were characterized by scanning electron microscopy and transmission electron microscopy and showed the spherical morphology of the NPs (Figure 1). Furthermore, the morphology and hierarchical organization of the SP were characterized by Scanning Electron Microscopy coupled with Energy Dispersive Spectroscopy (SEM-EDS), making it possible to observe the spherical morphology of the SP (Figure 2-B, D) and the presence of NPs in the internal structure of the SP (Figure 2-C). Stereoscopic microscopy analyses demonstrated the evaporation process of the hybrid SP over time until its formation (Figure 2-A). *In vitro* release kinetics analyses of the herbicide Atrazine showed a slower release of the herbicide associated with SPs compared to nanoagrochemicals (Figure 2-F). After the release kinetics test, the SPs were analyzed by Scanning Electron Microscopy (Figure 2-G), and it was possible to observe the presence of pores and changes in the roughness of the SP, indicating morphological alteration. In this way, this hybrid system demonstrates potential as an agrochemical delivery system, in addition to contributing to agricultural sustainability [3].

References

[1] Wintzheimer, S., Reichstein, J., Groppe, P., Wolf, A., Fett, B., Zhou, H., Pujales-Paradela, R., Miller, F., Müssig, S., Wenderoth, S., & Mandel, K. Advanced Functional Materials. 2021.

[2] Forini, M. M. L. H., Cavalcante, L. A. F., Antunes, D. R., Freitas, J. R., Lima, P. H. C., Biscalchim, E. R., Mattos, B. D., Filho, M. C. M. T., Grillo, R. Advanced Sustainable Systems. 2026.

[3] This research was supported by (#2022/03219-2, #2023/09217-4, #2023/00541-3, #2025/02896-9, #2026/05427-2), CNPq (#310846/2022-6) and CAPES.

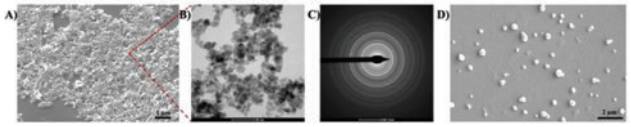


Figure 1. Fe_3O_4@Sodium Citrate NPs. A) Scanning Electron Microscopy. B) Transmission Electron Microscopy. C) X-ray Diffraction. D) Scanning Electron Microscopy of the lipid nanocarrier containing the herbicide Atrazine.

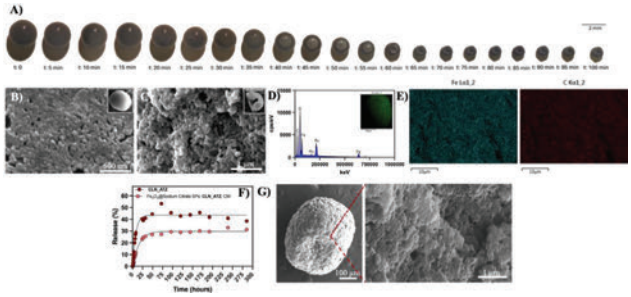


Figure 2. A) Micrographs of the self-assembly process of colloidal particles on a superhydrophobic surface. B e C) SEM of the surface and the internal region of the supraparticle, respectively. D) SEM-EDS of the SP surface. E) SEM-EDS of the internal region of SP. F) *In vitro* release kinetics profile of the herbicide. G) SEM of SP after *in vitro* release kinetics assay.

Hydrogen storage properties of multicomponent alloys produced using Ti6Al4V alloy scrap and commercially pure elemental feedstocks

Mariana de Brito Ferraz[1*], Claudia Zlotea[2], Guilherme Zepon[1], Walter José Botta[1]

[1] Federal University of São Carlos; [2] Univ Paris Est Créteil, CNRS, ICMPE.
*E-mail: marianadebritoferraz@gmail.com

The generation of energy from clean and renewable sources is essential for sustainable development. Hydrogen is a promising energy carrier, and improving its storage capacity, particularly by increasing volumetric density, remains a major challenge [1]. Among the different classes of hydrogen storage materials, multicomponent alloys based on the Ti-V-Nb-Cr system have attracted considerable attention because their hydrogen storage properties can be tailored through compositional design. Nevertheless, most reported multicomponent hydrides are produced using high-purity primary metallic elements, which require energy-intensive processing routes and are associated with significant environmental impacts. In this context, the use of metallic scraps and commercially available feedstock materials emerges as a promising strategy to reduce the environmental footprint of hydrogen storage alloys while maintaining competitive performance. In this work, sustainable alloys were explored through the production of multicomponent alloys using Ti_6Al_4V alloy scraps from the biomedical industry combined with elemental feedstock materials of different purity levels. Two alloys were investigated: $Ti_{18}Nb_{23}V_{24}Cr_{33}Al_2$, produced from Ti6Al4V scraps combined with high purity elements, and $Ti_{32}Al_2V_1Nb_{37}Cr_{28}$, produced using Ti6Al4V-ELI scraps alloy together with commercially available Nb and Cr while minimizing the use of primary vanadium, a high-carbon-emission element. The alloys were synthesized by arc melting and characterized by X-ray diffraction (XRD) and scanning electron microscopy (SEM) coupled with EDS. Both alloys exhibited predominantly body-centered cubic (BCC) microstructures, with minor microsegregation features, as shown in SEM analysis in Figure 1 for $Ti_{18}Nb_{23}V_{24}Cr_{33}Al_2$ and Figure 2 for $Ti_{32}Al_2V_1Nb_{37}Cr_{28}$. Hydrogen storage measurements demonstrated that $Ti_{18}Nb_{23}V_{24}Cr_{33}Al_2$ reached a maximum hydrogen storage capacity of 2.75 wt.% H_2 with room-temperature reversibility, showing performance comparable to conventional alloys produced exclusively from high-purity elements. The $Ti_{32}Al_2V_1Nb_{37}Cr_{28}$ alloy exhibited a hydrogen storage capacity of 2.50 wt.% H, with approximately 1 wt.% H reversibly absorbed and desorbed at room temperature. These results demonstrate that recycled materials and commercially available elements can be used to produce multicomponent hydrogen storage alloys without compromising reversible hydrogen storage performance, providing a viable pathway toward more sustainable metal hydride systems [2].

References

[1] A. Züttel, Materials for hydrogen storage, 2003.

[2] This work was financed in part by the Serrapilheira Institute (grant number Serra-1709–17362) and in part by the Brazilian National Council for Scientific and Technological Development – CNPq (Grant number: 309467/2021-7 and 407906/2022-3). This study was also financed in part by the Coordenação de Aperfeiçoamento de Pessoal de Nível Superior - Brasil (CAPES) - Finance Code 001, Federal University of Sao Carlos, Graduate Program in Materials Science and Engineerin

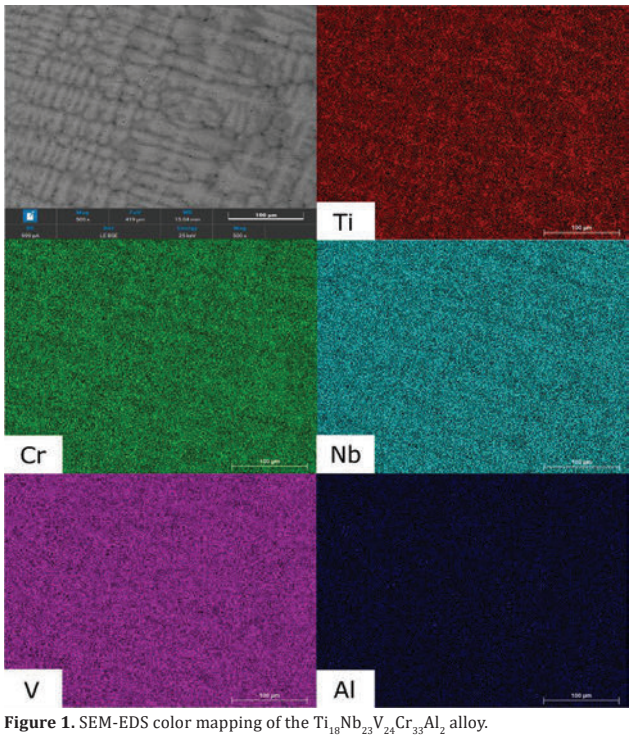


Figure 1. SEM-EDS color mapping of the $Ti_{18}Nb_{23}V_{24}Cr_{33}Al_2$ alloy.

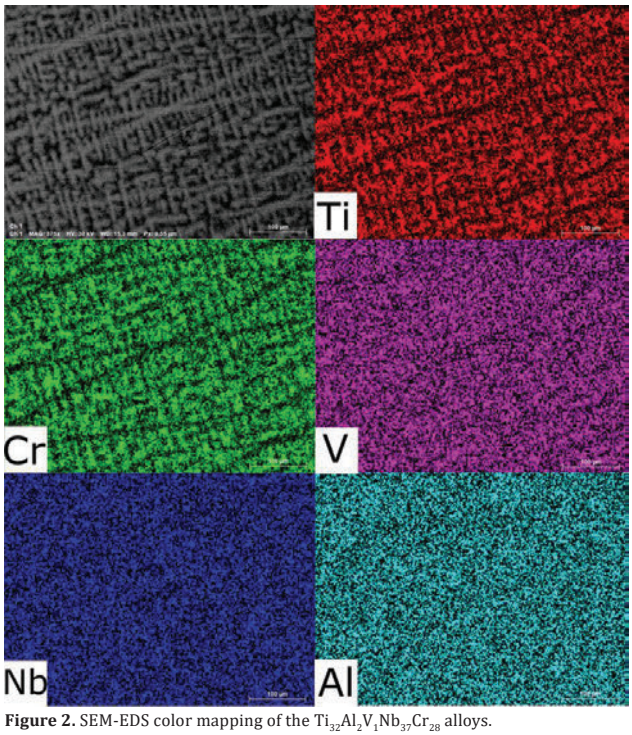


Figure 2. SEM-EDS color mapping of the $Ti_{32}Al_2V_1Nb_{37}Cr_{28}$ alloys.

Hysteresis in BCC alloys: EBSD insights into the β↔δ phase transformation

Gabriela C. Mayer[1*], Walter J. Botta[1,2], Guilherme Zepon[1,2].

[1] Graduate Program in Materials Science and Engineering (PPGCEM/UFSCar) - Rodovia Washington Luiz, km 235, Federal University of São Carlos, São Carlos, São Paulo, Brazil; [2] Department of Materials Engineering (DEMa/UFSCar), Federal University of São Carlos, São Carlos, Brazil.
*E-mail: gabrielamayer@estudante.ufscar.br

Metal hydrides are promising materials for diverse applications, including solid-state hydrogen storage tanks, rechargeable batteries, hydrogen compressors, and heat pump systems. In this context, body-centered cubic (BCC) multicomponent alloys stand out due to their compositional tunability, enabling fine control of their properties. During hydrogenation, these alloys undergo sequential phase transformations: from a BCC solid solution (α-phase) to an intermediate hydride (β-phase, BCC or BCT structure), and from the β-phase to a face-centered cubic (FCC) hydride (δ-phase) [1]. The pressure-composition-isotherm (PCI) curves show the equilibrium pressure as a function of the hydrogen content. While the β and δ phases coexist, a pressure plateau is seen in the isotherm. As the β-phase is highly stable, the α–β plateau is usually below the equipment detection limit. In the β–δ plateau, however, hysteresis is typically observed for BCC alloys: the plateau pressure during absorption is higher than during desorption, reducing energy efficiency and limiting the overall performance in practical applications. Although this phenomenon has been investigated since the 1930s, its causes are still unclear. Therefore, this work proposes a new approach to understanding hysteresis, based on a detailed analysis of the phase transformation mechanisms between the β-phase and the δ-phase. Samples of the TiVNbCr BCC alloy were hydrogenated and/or dehydrogenated to selected points along both branches of the PCI curve and subsequently analyzed by Electron Backscatter Diffraction (EBSD), which provided phase maps, band contrast maps, and inverse pole figure (IPF) maps. The phase maps (Fig. 1) show the microstructural evolution during absorption and desorption and reveal that β↔δ transformations proceed via a displacive mechanism in both directions, similar to Widmanstätten ferrite formation in steels [2], with the new phase growing as lenticular plates following predominantly the Nishiyama-Wassermann (NW) orientation relationship. The observed phase transformations involve features such as interface formation, volumetric expansion/contraction, and plastic deformation in both absorption and desorption, which are expected to contribute to hysteresis in BCC alloys [3].

References

[1] Zepon et al., Thermodynamic modelling of hydrogen-multicomponent alloy systems: Calculating pressure-composition-temperature diagrams, Acta Materialia 215 (2021).

[2] H.K.D.H. Bhadeshia, Theory of transformations in steels, CRC Press, Boca Raton, 2021.

[3] This work was supported in part by the São Paulo Research Foundation, FAPESP (grant number: 2024/16147-5) and in part by the Coordenação de Aperfeiçoamento de Pessoal de Nível Superior-Brasil (CAPES)-Finance Code 001, Federal University of São Carlos, Graduate Program in Materials Science and Engineering. The authors also acknowledge the Laboratory of Structural Characterization (LCE-DEMa/UFSCar) for providing access to the structural characterization facilities.

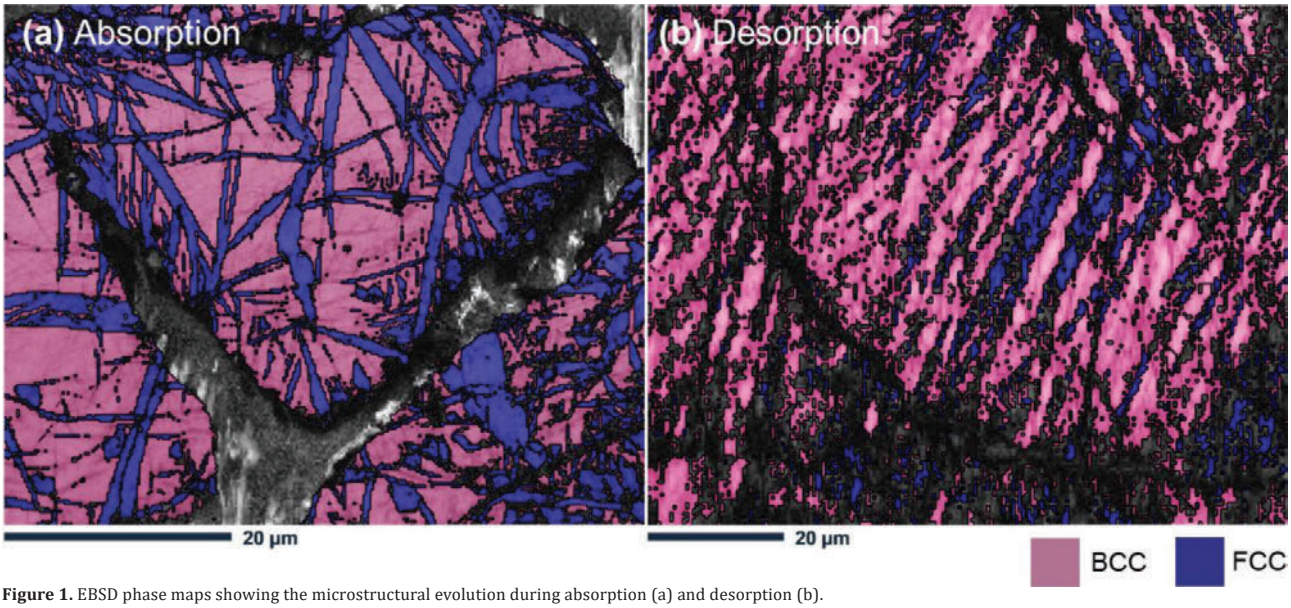


Figure 1. EBSD phase maps showing the microstructural evolution during absorption (a) and desorption (b).

Impact of Zn Additions on Sn–40Bi/Cu Interfacial Reactions: A Microstructural Study for Solder Alloy Design

Carolina de Siqueira Simioli[1], Guilherme Lisboa de Gouveia[1,2], José Eduardo Spinelli[2*].

[1] Department of Materials Engineering, Federal University of São Carlos; [2] Federal University of São Carlos, Graduate Program in Materials Science and Engineering.
*E-mail: spinelli@ufscar.com

The continuous miniaturization of electronic devices has increased the demand for reliable low-temperature solder alloys capable of maintaining structural integrity during service. Among lead-free systems, Sn–Bi alloys have attracted considerable attention due to their low melting temperature, good wettability, competitive cost, and compatibility with temperature-sensitive electronic components and polymer-based substrates. In particular, hypoeutectic Sn–40Bi alloys exhibit improved ductility compared with near-eutectic compositions while preserving the advantages of low-temperature processing. However, the reliability of Sn–Bi/Cu solder joints is strongly dependent on the microstructural evolution of the solder/substrate interface during thermal exposure [1]. The interaction between Sn-based solders and Cu substrates promotes the formation of intermetallic compounds (IMCs), especially Cu_6Sn_5. Although a thin IMC layer is necessary to ensure metallurgical bonding, excessive growth and morphological instability may compromise joint reliability by promoting interfacial embrittlement and reducing adhesion. Additionally, Bi segregation at the interfacial region during thermal aging has been associated with crack initiation and degradation of joint integrity. Therefore, controlling interfacial reactions is essential for the development of reliable low-temperature solder systems [2]. Recent studies indicate that Zn additions can improve the microstructural stability of Sn–Bi alloys by refining the Bi-rich phase and suppressing the growth kinetics of interfacial IMCs. Zn incorporation has also been associated with reduced Bi segregation at the Sn–Bi/Cu interface, contributing to a more homogeneous reaction layer during thermal exposure [3]. Nevertheless, the influence of Zn concentration on the interfacial microstructure evolution of Sn–Bi/Cu joints under high-temperature conditions remains insufficiently understood. In this context, the present study investigates the effect of Zn additions on the interfacial reactions between Sn–40Bi–xZn alloys (x = 0, 2, and 10 wt.%) and Cu substrates subjected to thermal exposure. Optical microscopy (OM) and scanning electron microscopy (SEM), combined with energy-dispersive X-ray spectroscopy (EDS), are employed to characterize the morphology and growth behavior of interfacial IMCs as a function of alloy composition, temperature, and exposure time. The results demonstrated that Zn addition significantly modified the interfacial reaction layer, promoting the formation of a CuZn layer at the solder/substrate interface. This layer acted as a diffusion barrier and suppressed the formation of Cu–Sn IMCs.

References

[1] M.G.C. Xavier, B.L. Silva, J.E. Spinelli, MetalMat (2025). https://doi.org/10.1002/metm.70015.

[2] J.R. da S. Lealet al., Metals (Basel). 14 (2024) 963. https://doi.org/10.3390/met14090963.

[3] O. Mokhtari, et al., Mater. Trans. 57 (2016) 1272–1276. https://doi.org/10.2320/matertrans.MD201515.

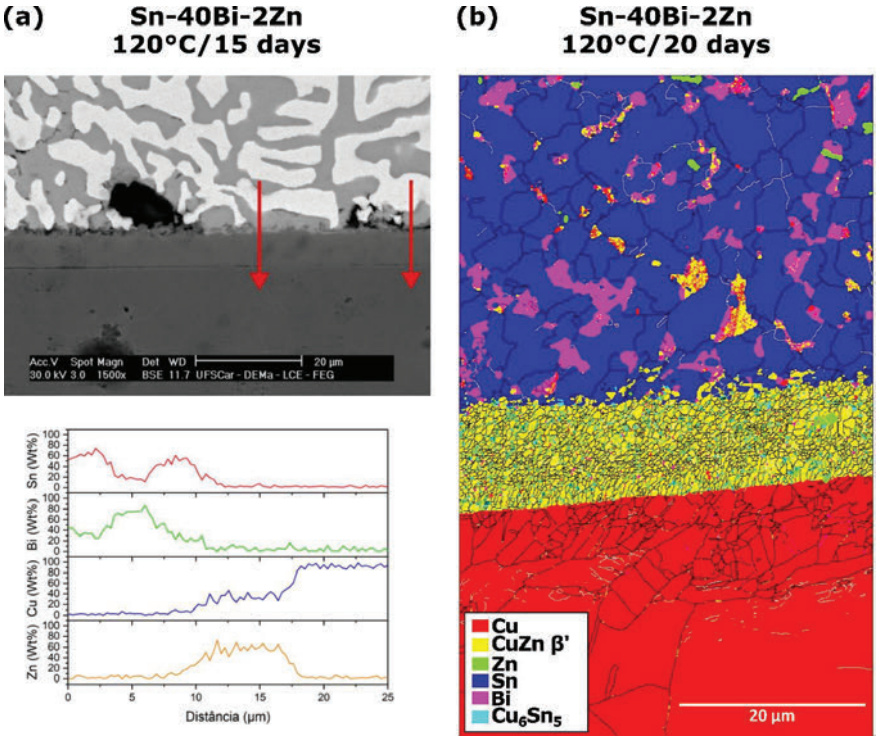


Figure 1. Interfacial microstructure between the Sn–40Bi–2Zn solder alloy and the Cu substrate after heat treatment at 120 °C, characterized by SEM–EDS analysis (a) and EBSD mapping (b).

Influence of Casting, Hot Rolling, and ECAP on the Elastic Modulus and Mechanical Performance of β Ti–33Nb–33Zr Alloy for Biomedical Applications

M. L. Lourenço [1*], R. F. M. dos Santos[1], L. A. R. Leão[2], P. A. B. Kuroda[3], A. Plaine[4], C. R. M. Afonso[1]

[1] BioMet-CAM Laboratory, Department of Materials Engineering (DEMa), Universidade Federal de São Carlos (UFSCar), São Carlos, SP, Brazil; [2] Faculdade de Engenharia Mecânica da Universidade Estadual de Campinas, FEM, Unicamp; [3] UNILA – Universidade Federal da Integração Latino-Americana, Foz do Iguaçu, PR, Brazil; [4] Department of Mechanical Engineering, State University of Santa Catarina (UDESC), Paulo Malschitzki, Joinville, SC, Brazil.
*E-mail: mariana.lourenco@ufscar.br

β-type titanium alloys are considered promising materials for biomedical applications due to their unique combination of low elastic modulus, high mechanical strength, corrosion resistance, and excellent biocompatibility with bone tissue and physiological environments. Compared with conventional titanium alloys, β-Ti alloys exhibit lower elastic modulus values, typically between 50 and 80 GPa, which are closer to those of human bone and therefore help reduce stress shielding effects in implants. In addition, these alloys can achieve mechanical strengths of 500-1000 MPa, making them attractive for orthopedic and dental applications. However, despite these advantages, achieving an ideal balance between mechanical resistance and elastic compatibility through thermomechanical processing remains a significant challenge. In particular, the influence of severe plastic deformation techniques on the microstructural evolution and mechanical behavior of multicomponent β-Ti alloys remains incompletely understood. In this context, the present study investigates the effects of melting, hot rolling, and Equal Channel Angular Pressing (ECAP) on the microstructure and mechanical properties of the β–Ti–33Nb–33Zr alloy. The alloy was initially produced by arc melting, followed by hot rolling, and subsequently processed by ECAP at temperatures of 25 °C and 350 °C using different numbers of passes. Microstructural characterization was carried out using Optical Microscopy (OM), Scanning Electron Microscopy (SEM), Transmission Electron Microscopy (TEM), Electron Backscatter Diffraction (EBSD), and ASTAR analyses. The results demonstrated that hot rolling promoted dynamic recrystallization and improved microstructural homogeneity. ECAP processing produced significant grain refinement, particularly after two passes, resulting in a more refined and heterogeneous structure. Samples processed at 25 °C showed high dislocation densities and subgrain formation, while processing at 350 °C favored dynamic recovery mechanisms and stress relaxation. Microhardness increased after rolling and remained relatively stable after ECAP, indicating a balance between grain-refinement strengthening and recovery effects. The elastic modulus remained close to 80 GPa across all conditions, owing to the stability of the β phase and the unchanged alloy composition. Overall, the results demonstrate that ECAP combined with controlled processing temperature is an effective approach to improve the mechanical performance of β-Ti alloys while preserving their elastic compatibility with bone for biomedical implant applications [5].

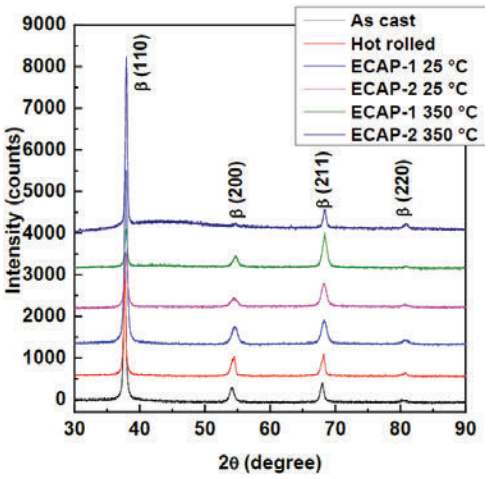


Figure 1 - X-ray diffraction (XRD) patterns for the alloys showing: in black (as cast), red (hot rolled), blue (ECAP-1 25 ºC), pink (ECAP-2 25 ºC), green (ECAP-1 350 ºC), and dark blue (ECAP-2 350 ºC). All conditions exhibit diffraction peaks corresponding exclusively to the β-Ti body-centered cubic (BCC) phase, indicating phase stability throughout thermomechanical processing.

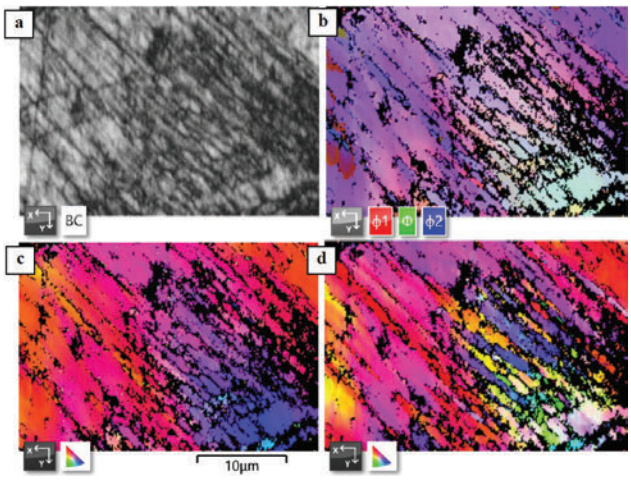


Figure 2. EBSD characterization of the Ti–33Nb–33Zr alloy after ECAP processing (2 passes at 25 °C). **(a)** Band contrast map showing a highly deformed microstructure with elongated grains and regions of high dislocation density. **(b–c)** Orientation maps indicating significant crystallographic fragmentation and intragranular orientation gradients. **(d)** Phase map confirming the predominance of the single β-Ti (BCC) phase.

References

[1] M.L. Lourenço et al., Thermo, (2025) v. 5, p. 46.

[2] C.R.M. Afonso et al., J. Mater. Res. Technol. 40 (2026) 1869–1881.

[3] M.L. Lourenço et al., submitted for publication in J. Mater. Res. Technol.

[4] F. De Mattos et al., Mater. Lett. 358 (2024) 135776.

[5] This research was supported by FAPESP PAIP 2023/16836-2 and partially supported by CAPES, Finance Code 001 (Brazil).

Influence of Short-Range Chemical Ordering on the Ductile-to-Brittle Transition in Fe–V Alloy

Leandra Marques[1], Gabriela Bugni Ribeiro[1], Francisco Gil Coury[1]

[1] Federal University of São Carlos (Department of Materials Engineering).
*E-mail: leandramarques@estudante.ufscar.br

The mechanical behavior of body-centered cubic (BCC) alloys is characterized by a strong temperature dependence, making the ductile-to-brittle transition (DBTT) a decisive parameter for their structural applications. Deciphering the mechanisms that govern this transition requires a detailed understanding at the atomic and microstructural levels. In this context, chemical short-range order (CSRO) has emerged as a significant factor capable of altering local slip modes and modifying strength and ductility. Given that the Fe–V system shows a strong thermodynamic tendency toward local chemical ordering within BCC matrices, mapping the spatial and morphological evolution of CSRO in these alloys is highly pertinent [1]. Consequently, this study aims to evaluate the impact of CSRO on the ductility of Fe–V alloys across various compositions, utilizing advanced electron microscopy and microstructural analysis as central characterization pillars. Such local ordering phenomena have been shown to play a decisive role in shifting plastic deformation mechanisms, directly influencing the homogeneity of dislocation flow observed through structural characterization [2]. The experimental procedure involved synthesizing the alloys in an arc furnace, followed by a homogenization treatment at 1200 °C for 8 hours. To induce distinct levels of CSRO, the samples underwent cold rolling and were subjected to aging treatments at 525 °C, 475 °C, and 425 °C for 24 hours. Characterization was designed to correlate the macrometallurgical scale with microscopic phenomena using scanning electron microscopy (SEM)—focusing on backscattered electron (BSE) imaging for compositional contrast and electron backscatter diffraction (EBSD) for grain mapping, crystallographic texture, and geometrically necessary dislocation (GND) density determination. Complementarily, synchrotron X-ray diffraction (SXRD) was used to identify phases and lattice parameter fluctuations associated with ordering, alongside Vickers microhardness testing and differential scanning calorimetry (DSC) for thermomechanical support. Initial SXRD results confirmed a single-phase BCC structure in all specimens. Moving forward, SEM/EBSD analysis and high-resolution electron fractography after mechanical testing will be instrumental in establishing a direct correlation between the degree of short-range ordering and dislocation mobility, as core structures and associated lattice barriers are heavily modulated by the presence of CSRO [3]. This microscopy-driven approach is expected to elucidate the micromechanical processes governing the DBTT in BCC alloys, providing valuable insights for designing materials with optimized microstructures.

References

[1] TURCHI, P. E. A. et al. Comparative study of short-range order in Fe–Cr and Fe–V alloys. MRS Online Proceedings Library (OPL), v. 1043, p. 1-6, 2007.

[2] TANG, Y. T. et al. Effect of short-range order on the deformation mechanisms of a high-strength refractory high-entropy alloy. Scripta Materialia, v. 202, p. 114002, 2021.

[3] GIBSON, J. B. et al. The effect of short range order on dislocation core structures and mobility in refractory high entropy alloys. Acta Materialia, v. 244, p. 118570, 2023.

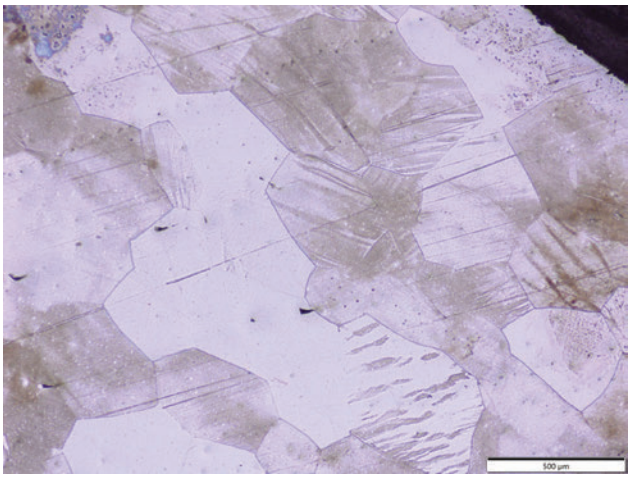


Figure 1. Optical micrograph of the homogenized $Fe_{90}V_{10}$ alloy etched with aqua regia.

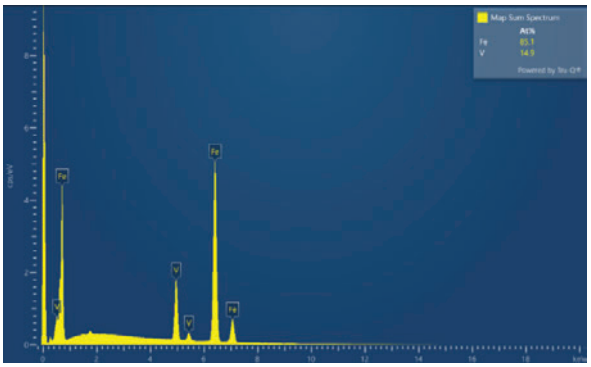


Figure 2. EDS sum spectrum of the Fe–V alloy, displaying the characteristic X-ray peaks for Iron (Fe) and Vanadium (V).

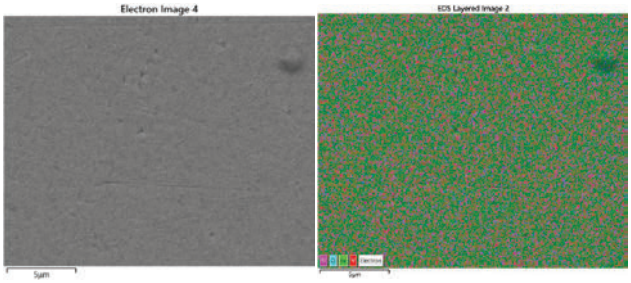


Figure 3. SEM microstructural and chemical mapping of the Fe–V alloy: (a) Secondary electron (SE) micrograph highlighting the surface morphology of the analyzed region, and (b) corresponding EDS layered elemental map displaying a highly homogeneous distribution of Iron (Fe, green) and Vanadium (V, red) across the matrix.

In-situ alloying of Ti-Nb-Sn samples by Laser Additive Manufacturing: phase stability and non-isothermal heat treatment

Márcio Sangali[1], João Felipe Q. Rodrigues[2], Leticia F. Starck[2], Gilberto V. Prandi[2], Matheus Valentim[2], Josef Stráský[3], Rodolfo da Silva Teixeira[2], Leandro S. Silva[4], Miloš Janeček[3], Rubens Caram[2]

[1] Federal Institute of Education, Science and Technology of São Paulo (IFSP), São João da Boa Vista, SP, Brazil; [2] Faculdade de Engenharia Mecânica, Universidade Estadual de Campinas (UNICAMP), Campinas, 13083-860, São Paulo, Brazil; [3] Department of Physics of Materials, Faculty of Mathematics and Physics, Charles University, Prague, Czech Republic; [4] Instituto de Ciências Ambientais, Químicas e Farmacêuticas, Universidade Federal de São Paulo (UNIFESP), Diadema, SP, Brazil.

Powder bed fusion-laser beam (PBF-LB) enables the production of titanium alloys with complex geometries, but relies on costly pre-alloyed powders. In-situ alloying, synthesizing the alloy from elemental powder blends during deposition, offers a cost-effective alternative for non-commercial compositions such as Ti-Nb-Sn, relevant for orthopedic implants due to low elastic modulus and biocompatibility [1–4]. A Ti-30Nb-2.5Sn (wt.%) alloy was fabricated under two PBF-LB conditions: Condition I (100 W, 300 mm/s) and Condition II (200 W, 100 mm/s) [5]. As-built and DSC-cycled samples (up to 1000 °C) were characterized by SEM-EDS, EBSD, XRD, TEM, and compression testing, supported by Thermo-Calc, DICTRA, and TC-PRISMA simulations. Condition I produced a heterogeneous microstructure with unmelted Nb particles that stabilized the β phase locally, promoting α′, α′′, and ω-phase formation (the latter confirmed by TEM-SAED along [113]β). Condition II yielded homogeneous columnar prior-β grains with predominantly α′′ martensite and suppressed ω-phase. Compressive strength of Condition II (1303 ± 117 MPa) exceeded both Condition I (1142 ± 22 MPa) and cast counterparts (~1000 MPa). DSC revealed overlapping events between 325-615 °C consistent with $\beta \rightarrow \omega_{iso} \rightarrow \beta_0 \rightarrow \alpha$; after two cycles, only α and β were detected. TC-PRISMA predicted α onset at ~530 °C. In Condition II, differential oxygen uptake produced a systematic α-plate thickness gradient along the sample height, suppressed in Condition I by Nb-driven β-stabilization. These findings highlight the role of processing parameters on phase stability and microstructural uniformity, and identify oxygen-driven α-plate gradients as a route for spatially tailoring mechanical properties in PBF-LB components.

References

[1] Abd-Elaziem, W. et al., Mater. Des., (2024) 112850.
[2] Banerjee, D., Williams, J.C., Acta Mater., 61 (3) (2013) 844–879.
[3] Xue, R. et al., J. Mater. Res. Technol., 36 (2025) 2532–2543.
[4] Masahashi, N. et al., Thin Solid Films, 820 (2025) 140674.
[5] Rodrigues, J.F.Q. et al., Mater. Chem. Phys., (2025) 131497.

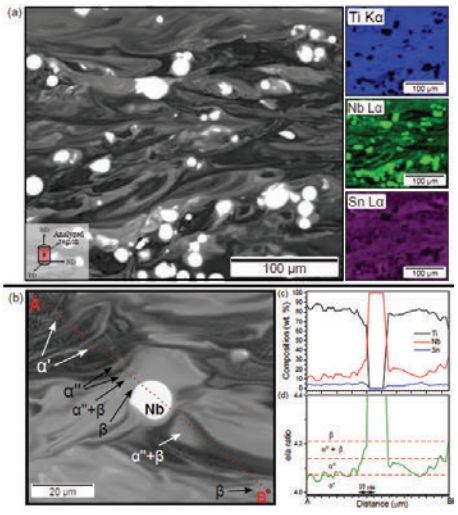


Figure 1. (a) SEM-BSE image and EDS composition maps of the in-situ alloyed AM sample I; and (b) SEM-BSE image and EDS line scan showing the composition variation near a Nb particle.

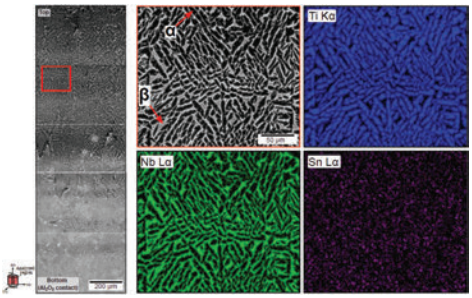


Figure 3. SEM-BSE micrograph and EDS composition maps of an DSC heat-treated Ti-30Nb-2.5Sn sample that was built at condition II.

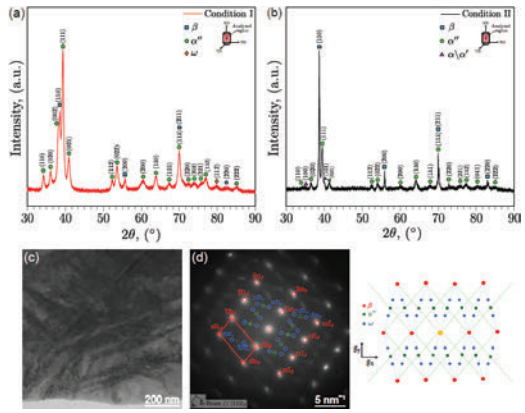


Figure 2. XRD patterns from samples at conditions I and II showing the retained metastable β phase, α′ and α′′ martensitic phases, as illustrated in Fig. 2a-b and Fig. 2cb-c. TEM analysis of condition I: (c) BF and (d) SAED pattern confirming the ω phase, and a schematic diagram illustrating the distribution of the distinct phases in the diffraction pattern is also provided.

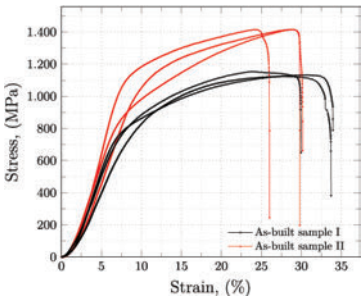


Figure 4. Engineering stress-strain curves of compression tests for as-built sample I and sample II.

Interfacial morphology evolution of PLA/PBSA blends during reactive extrusion with phenylene bis(oxazoline) - XII MICROMAT 2026

Marcos V. Basaglia[1*], Lucas H. Staffa[1,2], Sílvia H. P. Bettini[1,2]

[1] Graduate Program in Materials Science and Engineering (PPGCEM), Federal University of São Carlos (UFSCar), São Carlos, SP, Brazil; [2] Department of Materials Engineering (DEMa), Federal University of São Carlos (UFSCar), São Carlos, SP, Brazil.
*E-mail: marcosbasaglia@estudante.ufscar.br

Poly(lactic acid) (PLA) and poly(butylene succinate-co-adipate) (PBSA) blends have attracted increasing attention due to their potential to tailor mechanical performance through improved toughness and flexibility compared to neat PLA. However, the immiscibility between these polymers results in poor interfacial adhesion, which limits stress transfer across the phases and compromises the expected improvements in mechanical performance [1]. In this context, reactive compatibilization emerges as an effective strategy to improve interfacial interactions and control blend morphology. Therefore, PLA/PBSA blends with different compositions (80/20, 60/40, 40/60, and 20/80 wt.%) were initially prepared by melt mixing and analyzed by Scanning Electron Microscopy (SEM) on cryo-fractured cross-sectional surfaces to identify a suitable composition for subsequent reactive compatibilization. The images revealed a droplet–matrix morphology for compositions rich in one of the polymers, whereas co-continuous structures were observed for the intermediate compositions, indicating that the phase inversion transition occurs between PLA contents of 40 and 60 wt.%. Based on the results, the 80/20 PLA/PBSA composition was selected for reactive compatibilization using 2,2'-(1,4-phenylene)-bis(2-oxazoline) (p-PBO), a chain extender capable of reacting with carboxyl end groups, generating in situ copolymers at the interface [2]. Blends containing 0, 0.5 and 2 wt.% p-PBO were investigated, and SEM analyses were performed to evaluate the morphological evolution. The uncompatibilized blends exhibited poor interfacial adhesion and pronounced domain pull-out. The addition of 0.5 wt.% compatibilizer promoted significant interfacial improvement, reducing pull-out, leading to a more homogeneous morphology, and favoring transparticle fracture mechanisms. Furthermore, the average dispersed phase size decreased from 0.60 µm to 0.32 µm compared to the uncompatibilized blend. On the other hand, blends containing 2 wt.% compatibilizer exhibited indications of interfacial saturation, with the reappearance of pull-out features. Nevertheless, the average dispersed phase size was still reduced compared to the uncompatibilized blend, reaching 0.45 µm. The partial loss of compatibilization efficiency at higher p-PBO contents may be associated not only with interfacial saturation effects, but also with possible self-interactions of the additive and changes in the viscosity ratio between the polymer phases caused by the chain extension mechanism promoted by p-PBO. Overall, these results demonstrate that p-PBO was able to promote effective compatibilization between PLA and PBSA, although an optimal concentration appears to exist between 0.5 and 2 wt.%, above which the compatibilization efficiency decreases [3].

References

[1] V. Ojijo, S.S. Ray, E.R. Sadiku, ACS Appl. Mater. Interfaces 4 (2012) 6690–6701.

[2] C.Q. Huang et al., J. Appl. Polym. Sci. 115 (2009) 1555–1565.

[3] This study was financed in part by the Coordenação de Aperfeiçoamento de Pessoal de Nível Superior - Brasil (CAPES) - Finance Code 001. The present work was carried out with the support of the National Council for Scientific and Technological Development – Brazil (CNPq) (Process 140069/2024-0).

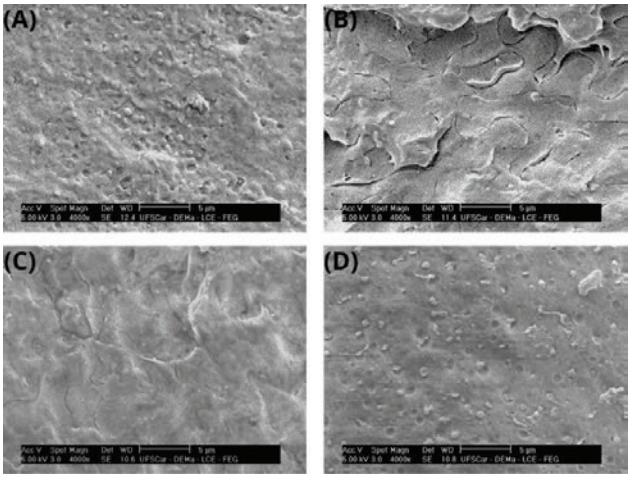


Figure 1. SEM micrographs showing the morphological evolution of PLA/PBSA blends with composition variation: (A) 80/20, (B) 60/40, (C) 40/60, and (D) 20/80 wt.%.

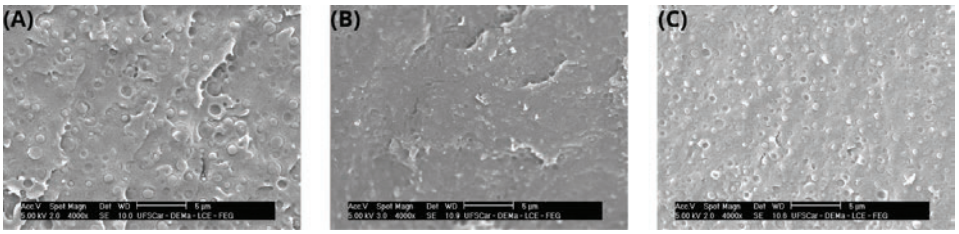


Figure 2. SEM micrographs of PLA/PBSA blends (80/20 wt.%) processed with different concentrations of 2,2'-(1,4-phenylene)-bis(2-oxazoline) (p-PBO): (A) 80/20_0%p-PBO, (B) 80/20_0,5%p-PBO, (C) 80/20_2%p-PBO.

Microestruturas hierárquicas em chapas Cu/Nb com interfaces não-lineares obtidas por Laminação Acumulada (ARB)

João Vitor Barletta Macêdo[1*], Diogo Pedrino Braga[1], Pedro Henrique Fernandes Oliveira[1], Andrea Madeira Kliauga[1], Danielle Cristina Camilo Magalhães[1]

[1] Universidade Federal de São Carlos, Departamento de Engenharia de Materiais.
*E-mail: jvbmacedo@estudante.ufscar.br

Neste trabalho, laminados heterostruturados de Cu/Nb foram produzidos por Laminação Acumulada (ARB), com ênfase na engenharia de interfaces não lineares e gradientes de espessura de camadas [1,2]. Duas rotas de processamento foram investigadas: uma convencional (razão Cu:Nb de 4:1, amostras 6X e 6X+1) e uma modificada, com inserção de novas chapas de Nb em etapas intermediárias do processo (razão Cu:Nb de 1,5:1, amostras 6X+Nb e 6X+Nb+1). As microestruturas foram caracterizadas por microscopia eletrônica de varredura (MEV), difração de elétrons retroespalhados (EBSD) e difração de raios X (DRX). As imagens de MEV revelaram estruturas alternadas de camadas de Cu e Nb com interfaces bem definidas e boa adesão, porém com distintas morfologias: enquanto as camadas de Cu permanecem contínuas, as camadas de Nb apresentam estricção localizada, ondulações e fragmentação progressiva ao longo do processamento. A condição 6X+Nb exibe uma distribuição bimodal de espessuras de camadas de Nb, camadas espessas e contínuas (recém-inseridas) coexistindo com camadas mais delgadas e fragmentadas (previamente deformadas), amplificando o caráter heteroestruturado do material [1,3]. A aplicação do passe extra (+1) intensifica o refinamento microestrutural e aumenta a densidade de ilhas de Nb fragmentadas em todas as condições. Os resultados de EBSD revelaram que, na condição 6X, as camadas de Cu apresentam grãos recristalizados com tamanho médio de ~22 µm e maclas de recozimento, enquanto as camadas de Nb exibem grãos fortemente alongados na direção de laminação (Figura 1). O passe extra (6X+1) promove refinamento significativo do Cu (~14 µm) e maior fragmentação das camadas, com nucleação de grãos refinados nas interfaces Cu/Nb. Na condição 6X+Nb, as camadas de Nb apresentam estados de deformação distintos, refletindo as diferentes históricos termomecânicos impostos pelo processamento modificado [3]. A análise por DRX (Tabela 2) confirmou ausência de fases secundárias ou compostos intermetálicos em todas as condições, com os padrões de difração compatíveis com as estruturas CFC (Cu) e CCC (Nb). A condição 6X+1 apresentou as maiores densidades de discordâncias e microdeformações, especialmente no Nb (~6,14 × 10^{14} m/m^3), enquanto a condição 6X+Nb exibiu valores comparativamente menores devido à contribuição das camadas de Nb menos deformadas, evidenciando que a inserção de novas camadas é uma estratégia eficaz para modular o estado de deformação armazenada e a heterogeneidade microestrutural do laminado [4].

References

[1] Y. Zhu et al., Mater. Res. Lett. 9 (2021) 1–31.
[2] U. Saito et al., Acta Mater. 47 (1999) 579–583.
[3] D.P. Braga et al., J. Alloys Compd. 184967 (2025).
[4] Este trabalho foi apoiado pela FAPESP Proc. 2023/03242-7.

Tabela 2 – Resumo das características microestruturais determinadas por DRX.

Amostra	Camada	Densidade de discordâncias [× 10^{14} m/m^3]	Tamanho de cristalito [nm]	Microdeformação [× 10^{-3}]
6X	Cu	0.77 ± 0.22	118 ± 19	3.9 ± 0.7
	Nb	1.95 ± 0.14	98 ± 21	5.6 ± 1.1
6x+1	Cu	1.58 ± 0.42	81 ± 12	5.6 ± 0.5
	Nb	6.14 ± 0.31	45 ± 12	11.0 ± 0.3
6X+Nb	Cu	1.49 ± 0.19	82 ± 6	5.7 ± 1.4
	Nb	1.15 ± 0.57	104 ± 27	5.4 ± 1.7
6X+Nb+1	Cu	2.64 ± 0.34	62 ± 4	7.6 ± 1.8
	Nb	1.75 ± 0.98	83 ± 21	6.5 ± 2.2

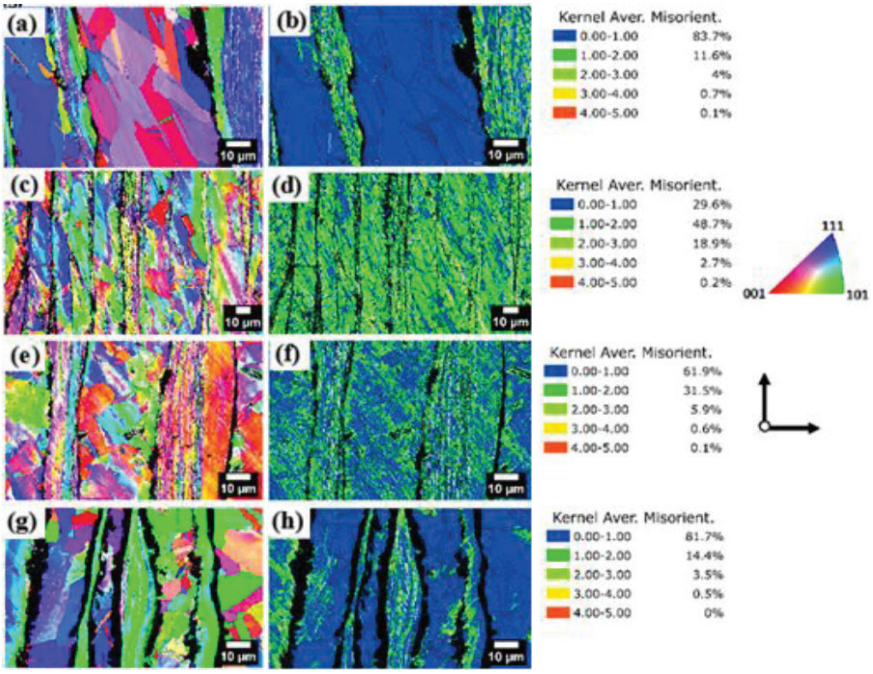


Figura 1 – Figura de polo inversa (IPF) e mapas de "Kernel Average Misorientation" (KAM) das chapas heteroestruturados de Cu/Nb sob diferentes condições de processamento: (a, b) 6X, (c, d) 6X+1, (e, f) 6X+Nb, and (g, h) 6X+Nb+1.

Microstructural analysis of the TiZrSnMnFe HEA for potential use as a biomaterial

Thiago Alves de Oliveira[1], Carlos Eduardo da Silva[1], Carlos Roberto Grandini[1], Diego Rafael Nespeque Corrêa[1]

[1] São Paulo State University (UNESP), School of Sciences, Laboratory of Anelasticity and Biomaterials, Bauru (SP), Brazil.
*E-mail: thiago-alves.oliveira@unesp.br

High-entropy alloys (HEAs) are emerging solutions for the global market, potentially contributing to both medicine and engineering. These materials exhibit unique microstructures and phases that depend on the elements' stoichiometry, configurational system entropy, and the process method [1]. Microstructural analysis allows characterization of essential alloy properties, including chemical stability, biological response, and mechanical properties such as Young's modulus, as well as the phases that confer these properties in this material [2]. In this context, this study aims to investigate the microstructural aspects of a novel HEA, TiZrSnMnFe, developed for biomedical implants, with a non-equivalent composition and using non-toxic elements with low melting points, such as Sn and Mn. The experimental procedure comprises the theoretical design of the alloy using its phase diagram generated with Thermocalc, the production of the sample in an arc-melting furnace, and structural characterization by optical microscopy (OM), as shown in Figure 1. Scanning Electron Microscopy (SEM) to investigate the microstructural characteristics of the alloy. Energy Dispersive Spectroscopy (EDS) to analyze the elemental chemical composition of the sample, the intermetallic compounds [3], and the dendritic phase formed in the sample. In summary, the results indicated that the microstructure consisted of a typical dendritic structure composed of distinct alloying elements, in the form of BCC and Laves phases. Further mechanical, electrochemical, and biological evaluations can provide additional information on the potential biomedical applications of the produced material [4].

References

[1] Zhu, D. et al. J. Mater. Sci. 59, 1153-1183 (2024).

[2] X. Zhou, H.Y. Fang, T.C. Yuan, R. Li, J. Alloys Compd. 892 (2022) 162164.

[3] P. Lia, L. Yang, F. Zhang, P. Hao, Z. Zhu, H. Qi, F. Qunbo, X. Cheng, Acta Mater. (2026) 122310.

[4] The authors acknowledge the São Paulo Research Foundation (FAPESP) for the financial support. Process no. 2026/00029-9.

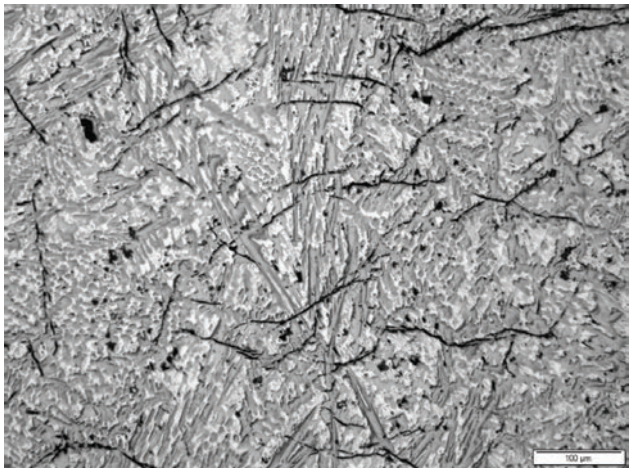


Figure 1. Optical microscopy of the alloy TiZrFeMnSn.
The image shows the morphological characteristics of the alloy resulting from arc-furnace melting, with emphasis on dendritic phases and intermetallic compounds. Scale of 100 µm.

Microstructural and surface characterization of MAO-treated TiZrNbMnFeAl Bio-HEA for biomedical applications

Jhuliene E. M. Torrento[1*], Conrado R. M. Afonso[2], Carlos R. Grandini[1], Diego R. N. Correa[1]

[1] São Paulo State University (UNESP), Laboratory of Anelasticity and Biomaterials, Bauru, SP, Brazil; [2] Federal University of São Carlos (UFSCar), Department of Materials Engineering, São Carlos, SP, Brazil.
*E-mail: jhuliene.torrento@unesp.br

Biomedical high-entropy alloys (Bio-HEAs) have attracted increasing attention for implant applications due to their combination of low elastic modulus, high mechanical strength, good corrosion resistance, and compositional versatility [1]. In addition, these alloys offer promise for overcoming some limitations of conventional metallic biomaterials, such as insufficient long-term mechanical and electrochemical stability. However, despite the excellent bulk properties of HEAs, the surface characteristics of metallic biomaterials still require optimization to improve their interaction with the biological environment, promote cell adhesion and proliferation, and enhance long-term performance and bone regeneration [2]. In this context, the present study investigated the effect of micro-arc oxidation (MAO) treatment time on the surface characteristics and microstructural features of a Ti-30Zr-28Nb-5Fe-5Mn-1.5Al (Wt %) Bio-HEA. The alloy was produced by arc melting under a controlled argon atmosphere, followed by homogenization heat treatment. The MAO process was carried out at 300 V and 2.5 A for 1-9 min in a Ca-, P-, and Mg-rich electrolyte. The coated surfaces were characterized by optical microscopy, scanning electron microscopy, energy-dispersive spectroscopy, X-ray diffraction, Fourier-transform infrared spectroscopy, X-ray photoelectron spectroscopy, confocal microscopy, wettability, corrosion, and tribocorrosion analyses. The MAO-treated samples exhibited porous oxide layers (see micrographs in Figure 1) with micrometric porous and increased thickness, incorporating bioactive elements from the electrolyte. The coatings were mainly composed of substrate elements, especially Ti, Zr, Nb, and Mn, together with electrolyte-derived elements such as Ca, P, Mg, O, and C, forming amorphous and nanocrystalline regions favorable for corrosion resistance and bioactivity. The oxide layer also exhibited morphological features, including interconnected pores and rough surfaces, which are considered beneficial for bone tissue anchorage and osseointegration. In addition, the treated surfaces exhibited enhanced hydrophilicity and increased roughness compared with the untreated substrate. Corrosion and tribocorrosion analyses revealed improved performance after MAO treatment, demonstrating that the incorporation of the oxide layer significantly enhanced these surface properties by acting as a protective and bioactive barrier. Furthermore, the treatment time was directly related to oxide layer growth, elemental incorporation, porosity, roughness, and surface morphology. These findings demonstrate that MAO is an effective strategy to functionalize TiZrNbMnFeAl Bio-HEAs and suggest their strong potential for future biomedical applications [3].

References

[1] J.E. Torrento, et al. APL Materials, 10, 081113, 2022.

[2] J.E. Torrento, et al. Materials Characterization, 208, 113678, 2024.

[3] This research was supported by FAPESP grants #2023/15812-2 and #2021/13921-3.

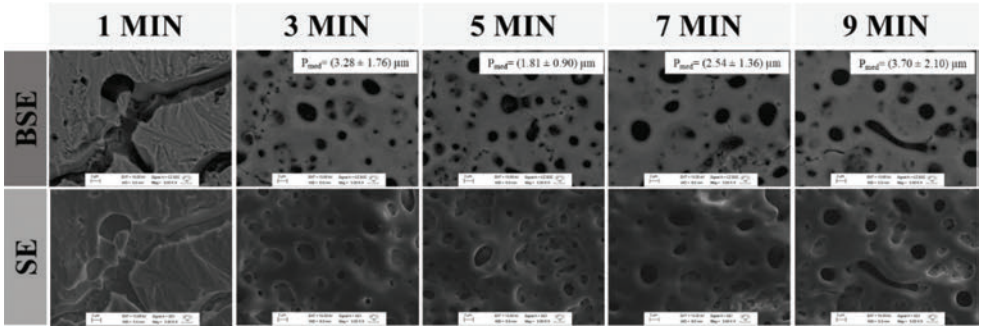


Figure 1. Micrographs of the MAO-coated samples and their respective average pore sizes.

Microstructural and Topographical Analysis of MAO-treated Ti-30Nb-5Mo Alloy

Gustavo da Silva Diniz[1*], Giovanna Cardososo Collombaro[2], Carlos Roberto Grandini[3], Diego Rafael Nespeque Correa[4].

[1] UNESP "Júlio de Mesquita Filho", Faculdade De Ciências, Campus de Bauru – Brasil; [2] Universitat Politècnica de València, Laboratório de Tecnologia em Materiais, Valência - Espanha.
*E-mail: gustavo.s.diniz@unesp.br

Despite their remarkable properties, titanium alloys exhibit low surface bioactivity [1]. To overcome this limitation, several surface modification techniques have been explored, with micro-arc oxidation (MAO) standing out as a direct and versatile method [1]. This process promotes the formation of a porous oxide layer capable of enhancing corrosion and wear resistance, reducing the release of potentially harmful ions, and improving cell adhesion, osseointegration, and antimicrobial activity [2]. In this context, the present study investigates the effect of current density on the MAO process, aiming to incorporate copper into the Ti-30Nb-5Mo alloy to improve osseointegration and provide antibacterial properties. The choice of copper is associated with its well-known antimicrobial properties, which can help reduce the risk of implant-related infections. The main objective is to characterize the TiO_2 coating formed on the surface of the samples using the MAO technique, analyzing its physical, chemical, and structural properties [3]. Special attention is given to the relationship between processing parameters and coating performance. The results show that the coatings comprise two crystalline phases of TiO_2: anatase and rutile, which are commonly reported in MAO-treated titanium alloys and are known to influence biological responses. Scanning electron microscopy (SEM) images reveal low porosity and reduced pore density (Figure 2), with increasing current contributing to further reductions in these parameters. Furthermore, the MAO treatment resulted in a porous surface morphology, which favors mechanical interlocking with bone tissue and enhances osseointegration. The oxide coating showed higher wear resistance than the control sample, as confirmed by SEM (Figure 1) 4 observations. Mechanical tests, such as Vickers microhardness, indicated an increase in surface hardness after treatment, which is directly related to the formation of the ceramic oxide layer. Additionally, morphological and chemical characterization of the coating was carried out using techniques such as X-ray photoelectron spectroscopy (XPS), energy-dispersive spectroscopy (EDS), and wettability analysis. These results confirmed the presence of incorporated elements and changes in surface energy, both of which are important factors in biological interactions. Cross-sectional analyses were also conducted to evaluate the thickness and uniformity of the coatings, demonstrating that higher current densities tend to produce thicker oxide layers [4].

References

[1] G. C. Cardoso *et al.*, "Antimicrobial Cu-Doped TiO2 Coatings on the β Ti-30Nb-5Mo Alloy by Micro-Arc Oxidation," *Materials*, vol. 17, no. 1, Jan. 2024, doi: 10.3390/ma17010156.

[2] G. Mortazavi, J. Jiang, and E. I. Meletis, "Investigation of the plasma electrolytic oxidation mechanism of titanium," *Appl. Surf. Sci.*, vol. 488, pp. 370–382, Sep. 2019, doi: 10.1016/j.apsusc.2019.05.250.

[3] G. C. Cardoso, C. R. Grandini, and J. V. Rau, "Comprehensive review of PEO coatings on titanium alloys for biomedical implants," *Journal of Materials Research and Technology*, vol. 31, pp. 311–328, Jul. 2024, doi: 10.1016/j.jmrt.2024.06.068.

[4] Financial Support: CNPq grant #314.810/2021-8 and FAPESP grants #2021/15.018-9, 2024/08094-9, 2025/05867-0 e 2024/01/132-2.

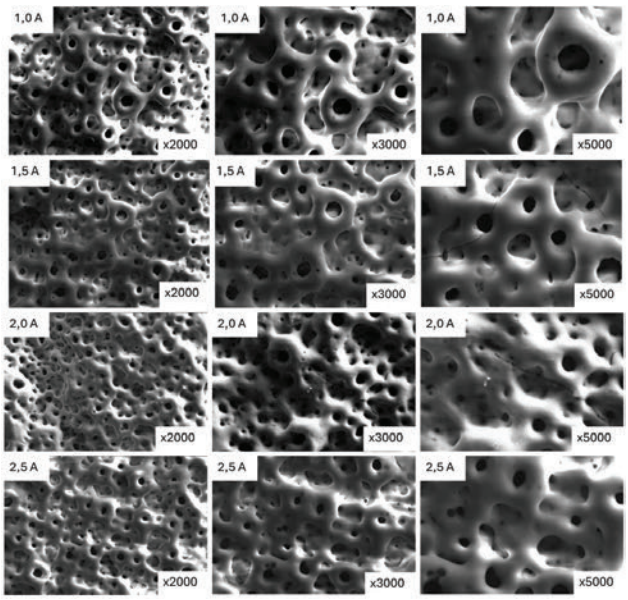


Figure 1. SEM images of the porous surface for each sample parameter.

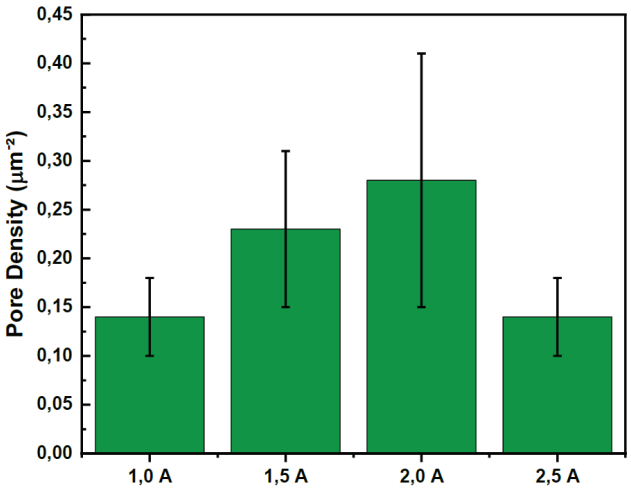


Figure 2. Analysis of pore density related to micro-arc oxidation (MAO).

Microstructural and topographical analysis of the TiNbFeMnAl high-entropy alloy functionalized by micro-arc oxidation for biomedical applications

Luccas Nunes Caetano da Silva[1*], Jhuliene Elen Muro Torrento[1], Diego Rafael Nespeque Correa[1], Carlos Roberto Grandini[1]

[1] Universidade Estadual Paulista (UNESP) – Laboratório de Anelasticidade e Biomateriais, Bauru, SP, Brazil.
*E-mail: luccas.nunes@unesp.br

High-entropy alloys (HEAs) are an emerging class of metallic materials composed of five or more principal elements, exhibiting remarkable physical, chemical, and mechanical properties. Due to their excellent corrosion and wear resistance, reduced cytotoxicity, and potential antibacterial behavior, HEAs have attracted increasing attention for biomedical applications [1]. In this context, surface functionalization techniques such as micro-arc oxidation (MAO) have been widely explored to improve the biological and tribological performance of metallic biomaterials by forming porous oxide coatings with predominantly circular morphology [2]. This work aims to present the microstructural and topographical characterization of a novel 30Ti–30Nb–5Fe–30Mn–5Al (at.%) alloy system, evaluating both the as-cast and homogenized conditions, as well as the functionalized surface. The alloy was synthesized by arc melting using commercially pure metals, followed by ten remelting cycles under an argon atmosphere. Subsequently, a homogenization heat treatment was performed at 1273 K for 43200 s under vacuum. Afterward, the homogenized samples were subjected to micro-arc oxidation (MAO) under a constant voltage of 300 V for 540 s. The microstructural and topographical evolution was thoroughly investigated using Optical Microscopy (OM) and Scanning Electron Microscopy (SEM) in secondary electron (SE) and backscattered electron (BSE) modes. In the homogenized alloy, BSE images revealed significant chemical segregation, as evidenced by atomic number (Z) contrast. Two major phases were identified: a bright region corresponding to a TiNb-rich BCC phase and a darker region associated with the FeMn-rich C14 Laves intermetallic phase. The aluminum exhibited a nearly homogeneous distribution throughout both phases. The micrographs showed that the heat treatment produced a more regular, rounded grain morphology compared with the as-cast condition (Figure 1). After MAO functionalization, the topographical analysis revealed the formation of a porous oxide coating (Figure 2). The combined application of microscopy and chemical microanalysis proved essential for understanding the phase crystallization mechanisms in the TiNbFeMnAl alloy. Furthermore, the porous surface morphology produced by MAO suggests promising potential for favorable bone interactions, reinforcing the applicability of this material for biomedical implants [3].

References

[1] N. Ma, et al., Frontiers in Bioengineering and Biotechnology, 8 (2020) 1-18.

[2] G. Li, et al., Journal of Alloys and Compounds, 948 (2023) 169773.

[3] This research was funded by CNPq (Brazil), grant number 14390.

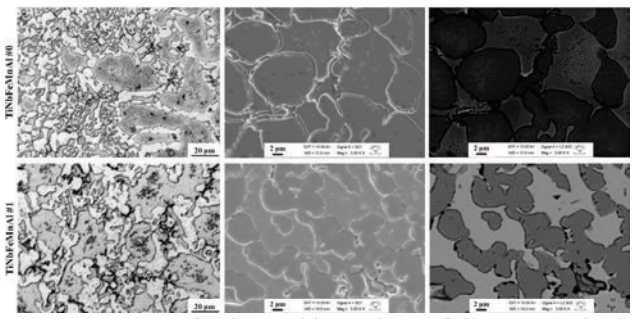


Figure 1. Microstructural evaluation of the samples: OM (left), SE-SEM (medium), and BSE-SEM (right) imaging.

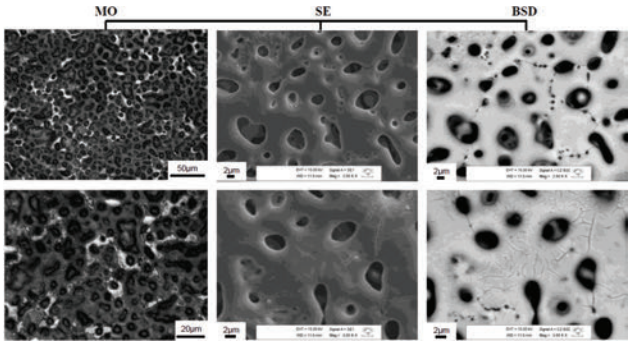


Figure 2. Microstructural evaluation of the MAO-treated surface: OM (left), SE-SEM (middle), and BSE-SEM (right) imaging.

Microstructural and Wear-Track Characterization of High-Entropy Alloys for Metallic Biomaterial Applications

Carlos Eduardo Manreza[1*], Mariana Luno Lourenço[2], Diego Rafael Nespeque Correa[3], Carlos Alberto Fonzar Pintão[4], Carlos Roberto Grandini[5]

[1] UNESP, School of Sciences, Campus Bauru, Laboratory of Anelasticity and Biomaterials; [2] UNESP, Institute of Biosciences, Botucatu, Department of Chemistry and Biochemistry.
*E-mail: carlos.manreza@unesp.br

High-entropy alloys (HEAs) are promising metallic biomaterials due to their ability to combine phase stability, mechanical strength, corrosion resistance and biological response through multicomponent alloy design [1–3]. In this work, microscopy and microanalysis were used to correlate microstructure, chemical distribution and surface degradation of four HEAs: CoCrFeMnNi, FeCoCrMnNi, TiNbTaZrMo and TaNbHfZrTi, evaluated in the as-cast and thermally homogenized conditions. Optical microscopy (OM), scanning electron microscopy (SEM), energy-dispersive X-ray spectroscopy (EDS), chemical mapping, X-ray diffraction (XRD), Vickers microhardness, corrosion, tribocorrosion and preliminary cell assays were performed. OM and SEM revealed dendritic/interdendritic morphologies in all alloys, typical of multicomponent cast systems. The Fe/Co-based alloys showed predominantly FCC-related microstructures, with local contrast variations attributed to solidification microsegregation. In contrast, the Ti-based refractory alloys exhibited biphasic dendritic microstructures associated with BCC phases rich in refractory elements. After thermal treatment, smoother interfaces and reduced visible heterogeneity suggested partial microstructural homogenization. EDS spectra confirmed the expected alloying elements, while chemical maps revealed micrometric compositional variations related to dendritic solidification [4]. Post-tribocorrosion OM/SEM analysis revealed distinct surface damage mechanisms. The Fe/Co-based alloys exhibited more continuous and shallower wear tracks, indicating better resistance to mechanical wear under sliding conditions. Conversely, TiNbTaZrMo and TaNbHfZrTi showed more localized deformation and evidence of tribochemical oxide formation. Electrochemical tests in Hanks' solution indicated that the Ti-based refractory alloys presented lower current densities, wider passive regions and improved repassivation behavior [2,5]. These results show that microscopy and microanalysis were essential to connect dendritic morphology, elemental partitioning, phase constitution and wear-track features with functional performance. Overall, CoCrFeMnNi and FeCoCrMnNi showed better wear-track morphology, whereas TiNbTaZrMo and TaNbHfZrTi exhibited superior electrochemical stability and favorable preliminary cell response, with viability above 80% relative to the control. Therefore, Ti-based refractory HEAs appear more promising for prolonged contact with physiological media, while Fe/Co-based HEAs may be considered for external or temporary components where mechanical wear resistance is critical [6].

References

[1] D. Castro et al., *Metals* 11 (2021) 648.
[2] N. Hua et al., *J. Alloys Compd.* 861 (2021) 157997.
[3] J. Feng et al., *Front. Bioeng. Biotechnol.* 10 (2022) 977282.
[4] J.I. Goldstein et al., *Scanning Electron Microscopy and X-Ray Microanalysis*, Springer, 2018.
[5] M.T. Mathew et al., *Adv. Tribol.* 2010 (2010) 578760.
[6] This work was supported by PIBIC/CNPq (Brazil).

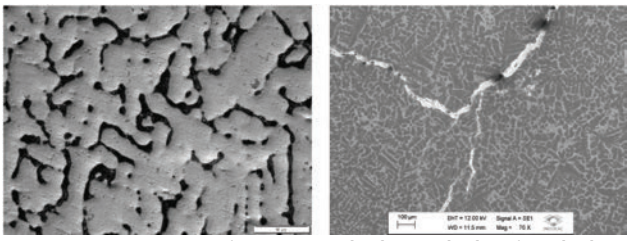


Figure 1. Representative OM/SEM micrographs showing dendritic/interdendritic microstructures in the investigated HEAs.

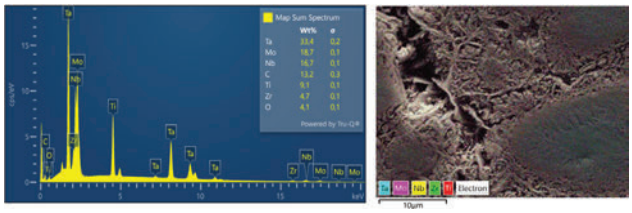


Figure 2. EDS spectrum and elemental chemical mapping of a representative HEA sample.

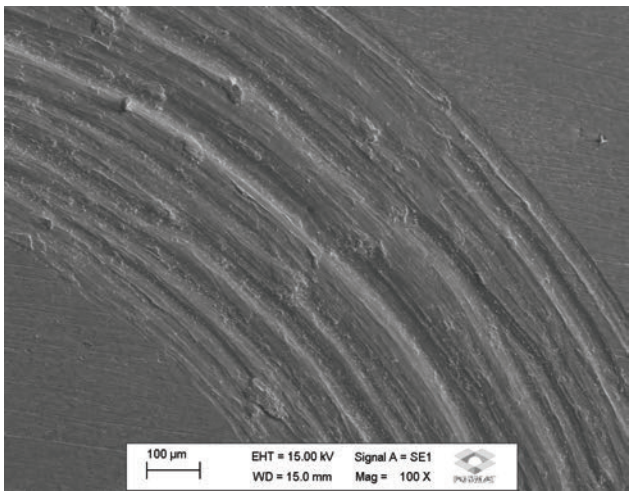


Figure 3. SEM image of the wear track after tribocorrosion testing, showing surface damage morphology under sliding in Hanks' solution.

Microstructural characterization and identification of quasicrystalline phases in an $Al_{90}Cu_4Fe_2Cr_4$ alloy processed by copper mold casting.

Marcelo Fabiano Filho[1], Samuel Lima de Souza[2], Witor Wolf[2]

[1] Graduate Program in Materials Science and Engineering, São Carlos School of Engineering, University of São Paulo (EESC-USP), São Carlos, SP, Brazil; [2] Department of Materials Engineering, São Carlos School of Engineering, University of São Paulo (EESC-USP), São Carlos, SP, Brazil.
*E-mail: marcelofabianofilho@usp.br

Since their discovery by Dan Shechtman in 1982, quasicrystals (QCs) have emerged as a significant field of research [1]. Their surface properties, particularly their tribological behavior, stand out due to high hardness and low friction coefficients [2]. The Al-Cu-Fe-Cr system is particularly promising in this context [3]. However, achieving a suitable microstructure for mechanical applications remains a challenge. This study investigates the microstructural and mechanical characteristics of a rapidly solidified $Al_{90}Cu_4Fe_2Cr_4$ (at.%) alloy processed by copper mold casting, aiming to evaluate the formation and dispersion of metastable quasicrystalline phases within an α-Al matrix. The alloy was synthesized in an electric arc melting furnace from commercially pure elements (>99%). The pre-alloy was subsequently remelted and cast into a wedge-shaped copper mold to investigate the effect of varying cooling rates on the formation, morphology, and distribution of the quasicrystalline phases. Microstructural characterization was carried out using Scanning Electron Microscopy (SEM), X-ray Diffraction (XRD) and Transmission Electron Microscopy (TEM). The thermal stability of the quasicrystalline phase was evaluated via Differential Scanning Calorimetry (DSC). Additionally, Vickers microhardness testing was performed across different sections of the wedge to correlate the mechanical properties with the local microstructure obtained at varying cooling rates. Characterization of the $Al_{90}Cu_4Fe_2Cr_4$ alloy revealed a microstructure composed of quasicrystalline particles embedded in an α-Al matrix. In the thinner sections of the wedge samples, the higher cooling rates promoted a refined and more globular morphology of the quasicrystals. Conversely, the thicker sections exhibited a transition toward coarser dendritic structures, alongside the formation of secondary intermetallic phases (θ-Al_2Cu included). DSC curves exhibited exothermic peaks attributed to the transformation of quasicrystals into stable phases. Accordingly, the Vickers microhardness increased in regions associated with higher cooling rates, where a greater volume fraction of quasicrystals is expected. These data confirm that microstructural refinement and the successful retention of the quasicrystalline particles are strongly dependent on the cooling rate applied during processing [4].

Table 1. Hardness properties of the $Al_{90}Cu_4Fe_2Cr_4$ alloy.

Sample	Microhardness (HV)	Indentation diagonal (μm)
Wedge I	197 ± 16	69.2 ± 5.4
Wedge II	185 ± 12	70.9 ± 4.3
Wedge III	165 ± 16	72.9 ± 6.9
Wedge II after heating up to 520°C	186 ± 11	70.6 ± 3.1

Hardness measurements were performed using a Buehler 1600-6300 microhardness tester with an applied load of 500 gf.

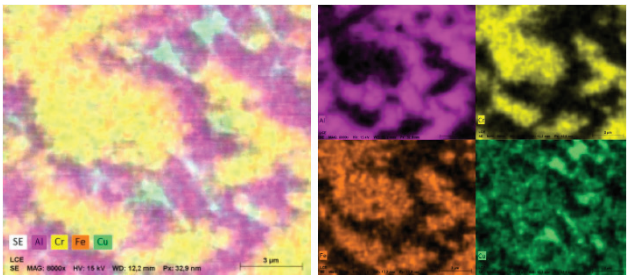


Figure 2. BSE-SEM image and corresponding EDS elemental maps of wedge II.

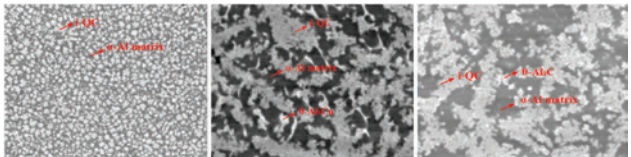


Figure 1. BSE-SEM micrographs of the $Al_{90}Cu_4Fe_2Cr_4$ alloy: **a)** wedge I at 4000X magnification; **b)** wedge II at 8000X magnification; and **c)** wedge II after heating up to 520°C at 8000X magnification.

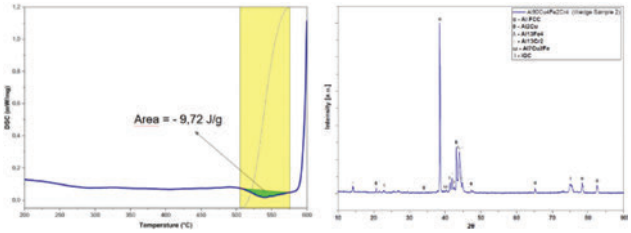


Figure 3. DSC curve and XRD pattern of wedge II.

References

[1] SHECHTMAN, D.; BLECH, I. Metallic Phase with Long-Range Orientational Order and No Translational Symmetry. Physical Review Letters, v. 53, p. 1951-1953, 1984.

[2] DUBOIS, J. M. Properties and applications of quasicrystals and complex metallic alloys. Chemical Society Reviews, v. 41, n. 21, p. 6760-6777, 2021.

[3] WOLF, W. et al. Assessment of phase constitution on the Al-rich region of rapidly solidified Al-Cu-Fe-Cr alloys. Materials Characterization, v. 122, p. 76-82, 2016

[4] This research was supported by the National Council for Scientific and Technological Development (CNPq - Brazil), grant nº 352288/2025-6. Additional financial support for materials and analyses was provided by the São Paulo Research Foundation (FAPESP), grant nº 2025/08661-3.

Microstructural Characterization of Refractory Nb-based Alloys (C-103 and FS-85) Fabricated by Laser Powder Bed Fusion (LPBF)

João Vitor Garcia Lourenço[1*], Mariana Luna Lourenço[1], Miloslav Béreš[2], Conrado R. M. Afonso[1]

[1] BioMet-CAM, Department of Materials Engineering (DEMa), Federal University of São Carlos (UFSCar), São Carlo/SP, Brazil;
[2] Department of Metallurgical and Materials Engineering, Federal University of Ceará, Fortaleza, CE, Brazil.
*E-mail: joaolourenco@estudante.ufscar.br

Niobium alloys are strategic materials for aerospace applications due to their high melting point, excellent thermal stability, and corrosion resistance. However, processing these alloys via Laser Powder Bed Fusion (LPBF) presents significant challenges due to the extreme thermal gradients and high melting temperatures (~2477 °C). The present study aims to evaluate the feasibility of producing high-integrity components of C-103 (Nb-Hf-Ti) and FS-85 alloys through advanced LPBF processing. The objective was to characterize the effect of rapid solidification on phase formation and grain morphology. Niobium alloys are strategic materials for aerospace applications due to their high melting point, excellent thermal stability, and corrosion resistance. However, processing these alloys via Laser Powder Bed Fusion (LPBF) presents significant challenges due to the extreme thermal gradients and high melting temperatures (~2477 °C). The present study aims to evaluate the feasibility of producing high-integrity components of C-103 (Nb-10Hf-1Ti) and FS-85 (Nb-28Ta-10W-1Zr) alloys through advanced LPBF processing. The objective was to characterize the effect of rapid solidification on phase formation and grain morphology. The alloys were processed using an OmniTek OMNISINT-160 system with a fiber laser (Yb:YAG, 1070 nm). Crystallographic characterization was performed via X-ray Diffraction (XRD) using Cu-Kα radiation (1.5406 Å). Microstructural analysis was carried out using Optical Microscopy (OM) and High-Resolution Scanning Electron Microscopy (SEM). XRD analysis confirmed a fully Body-Centered Cubic (BCC) solid solution for both alloys, with no evidence of secondary phases or oxidation. The calculated lattice parameters were 3.3176 ± 0.003 Å for C-103 and 3.2999 ± 0.003 Å for FS-85. The slight lattice expansion in C-103 is attributed to the Hf and Ti solutes in the Nb matrix. Using the Scherer equation on the (110) peak, crystallite sizes were determined as 46.5 nm and 43.9 nm for C-103 and FS-85, respectively. OM and SEM micrographs revealed well-defined melt pool tracks and significant epitaxial grain growth along the building direction. High-magnification SEM revealed a refined cellular-dendritic sub-structure, typical of the high cooling rates in LPBF, with high densification and minimal porosity. These results demonstrate that LPBF is a viable technique for manufacturing high-integrity Niobium alloy components with controlled microstructural features and chemical homogeneity [3].

References

[1] Callister, W. D., Jr., & Rethwisch, D. G. (2014). Materials science and engineering: An introduction (9th ed.). Wiley.

[2] J.I. Goldstein et al., Scanning Electron Microscopy and X-ray Microanalysis, Plenum, New York, 1992.

[3] This research was supported by FAPESP PAIP 2023/16836-2 and partially supported by CAPES, Finance Code 001 (Brazil).

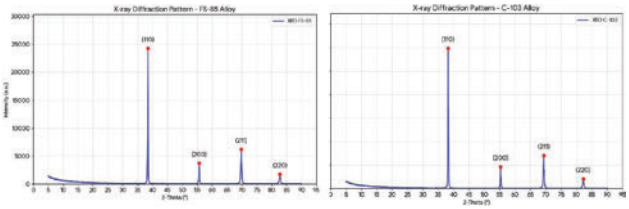


Figure 1. FS-85 X-ray Diffraction (XRD) pattern and C-103 X-ray

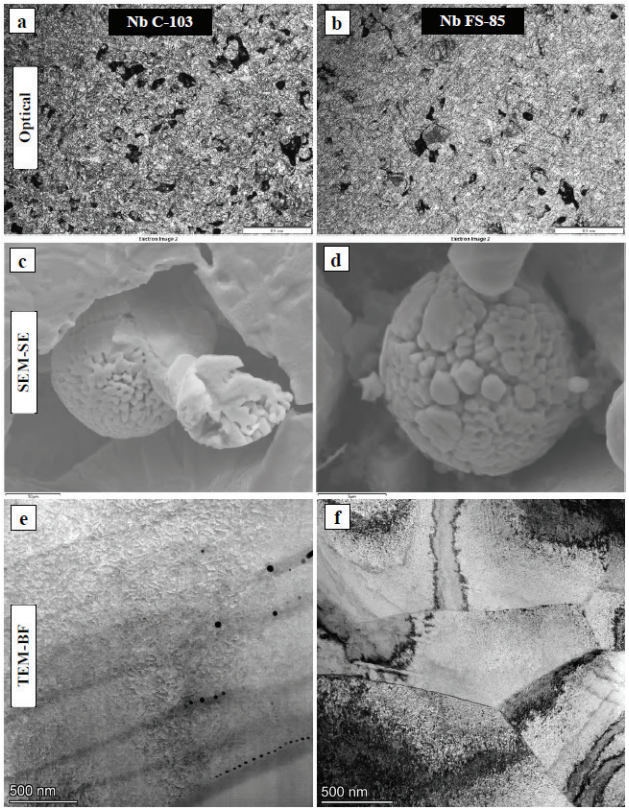


Figure 2. Optical a) and b), SEM c) and d) and TEM e) and f) micrographs of Nb-based C-103 and FS-85 alloys, respectively showing microstructure of LPBF process.

Microstructural characterization of the solid stated welded joint of Lean duplex stainless steel UNS S2101

Pedro Henrique Barletta Macedo[1*], Leonardo Martins Tavares[1], David Jose Barreto Aviles[1], João Gabriel da Cruz Passos[1], Rodrigo de Oliveira França[1], Diogo Pedrino Braga[1], Jean Carlos dos Santos[1], Guilherme dos Santos Vacchi[1], Carlos Alberto Della Rovere[1]

[1] Universidade Federal de São Carlos, Departamento de Engenharia de Materiais, São Carlos - SP, Brazil.
*E-mail: phbmacedo@estudante.ufscar.br

Lean duplex stainless steel UNS S2101 has attracted increasing attention as a cost-effective alternative for structural and industrial applications requiring a combination of high mechanical strength, good weldability, and satisfactory corrosion resistance. Due to its duplex microstructure, composed of ferrite and austenite, the performance of this alloy is strongly governed by phase balance and microstructural stability, both of which may be significantly affected by welding thermal cycles [1,2]. In this context, friction stir welding (FSW) has emerged as a promising joining route for stainless steels, since it is performed in the solid state and can mitigate many of the problems typically associated with conventional fusion welding, such as solidification defects, segregation, and excessive microstructural degradation [3,4]. This study investigates the effect of frictionless pin welding on the joint microstructure of lean duplex stainless steel UNS S2101. The welded joints were characterized by hardness mapping, optical microscopy, and ferrite volumetric fraction measurements in different welded regions. The base metal (BM), thermomechanically affected zone (TMAZ), and stir zone (SZ) were identified and subdivided into advancing side (AS) and retreating side (RS). In the stir zone, both the central region and the areas closer to the TMAZ were analyzed. The hardness results showed an increase in hardness in the welded regions, which was attributed to the grain refinement observed in these areas as shown in Figure 1. In addition, measurable changes in the ferrite/austenite balance were observed, indicating that the thermomechanical cycle imposed by FSW has a direct effect on phase stability in UNS S2101, with the ferrite volumetric fractions of the different welded regions summarized in Table 1. Optical microscopy showed the occurrence of chromium-rich precipitates in the TMAZ-RS and SZ regions, as presented in Figure 2. Taken together, the results indicate that FSW is a feasible route for joining lean duplex stainless steel UNS S2101, producing joints with good metallurgical integrity while also promoting significant microstructural changes. However, the formation of chromium-rich precipitates and the variations in phase balance highlight the need for careful control of processing conditions, since these features may influence the corrosion behavior of the welded regions. The present study therefore contributes to a better understanding of the relationship between welding, microstructural evolution, and performance in friction stir welded lean duplex stainless steels [5].

References

[1] R.N. Gunn, Duplex Stainless Steels: Microstructures, Properties and Applications, Abington Publishing, 1997.

[2] I. Alvarez-armas, S. Degallaix-moreuil, Duplex Stainless Steels, John Wiley & Sons, 2009.

[3] J.C. Lippold; D.J. Kotecki, Welding metallurgy and weldability of stainless steels, John Wiley & Sons, New Jersey, 2005.

[4] A.L.V. Costa e Silva; P.R. Mei, Aços e ligas especiais. Blücher, São Paulo, 2021.

[5] This research was supported by CNPq (Brazil).

Table 1. Ferrite phase volumetric fraction in different welded regions.

Region	Volumetric fraction
BM	49.8 ± 1.7
SZ	52.6 ± 1.2
TMAZ-RS	54.7 ± 2.1
SZ-RS	59.0 ± 1.6
TMAZ-AS	50.7 ± 1.5
SZ-AS	51.0 ± 0.4

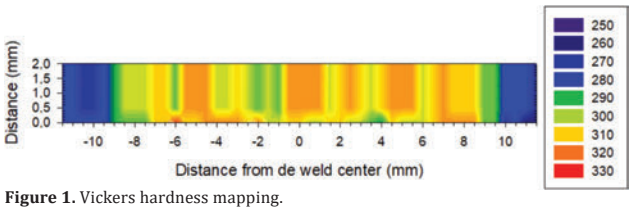


Figure 1. Vickers hardness mapping.

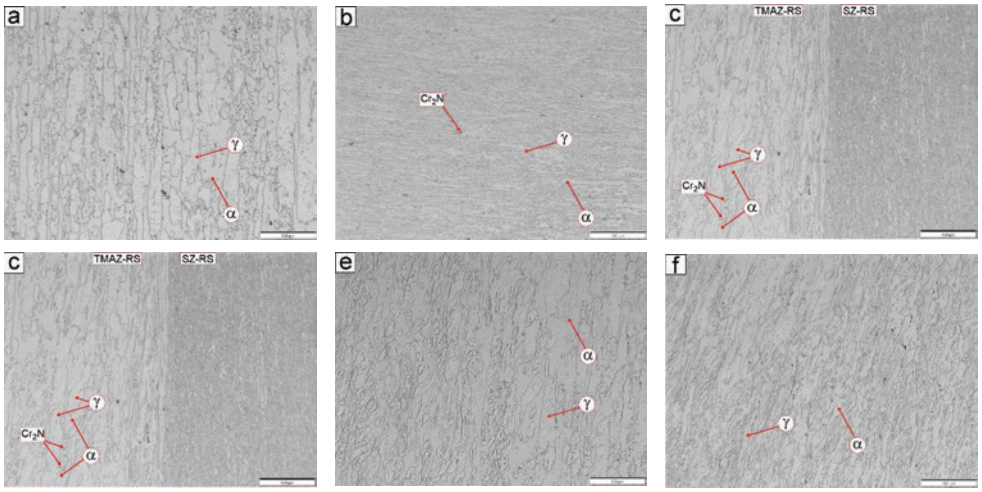


Figure 2. Optical microscopy after electrolytic etching in oxalic acid of the different welded regions: (a) BM, (b) SZ, (c) TMAZ-RS, (d) SZ-RS, (e) TMAZ-AS, and (f) SZ-AS.

Microstructural characterization of the Ti-40Nb-xO alloys

João Pedro Ferreira Martins[1*], Felype Narciso de Mattos[1], Pedro Akira Bazaglia Kuroda[2], Diego Rafael Nespeque Corrêa[1], Carlos Roberto Grandini[1]

[1] Universidade Estadual Paulista Júlio Mesquita Filho - UNESP, Bauru, SP, Brazil; [2] UNILA, Foz do Iguaçu, PR, Brazil.
*E-mail: jpf.martins@unesp.br

Titanium-based alloys stand out in the field of biomaterials due to their combination of high biocompatibility, excellent corrosion resistance, and ability to promote osseointegration [1]. In addition, they exhibit low density and favorable mechanical properties, making them promising materials for biomedical applications. From a microstructural perspective, titanium may present mainly two crystalline phases: the β phase, with a hexagonal close-packed (HCP) structure, and the β phase, characterized by a body-centered cubic (BCC) structure [2]. The control of these phases through the addition of alloying elements allows the adjustment of properties such as elastic modulus, mechanical strength, and ductility. In this context, the addition of oxygen (O) and niobium (Nb) plays an important role in the microstructural development of these materials. Interstitial oxygen is known to promote solid-solution strengthening and induce anelastic effects, while niobium acts as an efficient β-phase stabilizer [3], contributing to lower elastic modulus values, which are desirable for biomedical applications. Ti–40Nb–xO alloys (x = 0.2, 0.4, 0.6, 0.8, 1.0 and 1.2 wt%) were produced by arc melting. Phase identification was performed by X-ray diffraction (XRD), while the microstructural evolution associated with the incorporation of oxygen and niobium was investigated using optical microscopy (OM). In addition, the elastic modulus was measured using the impulse excitation technique under flexural vibration, and hardness was measured using the Vickers method. The results demonstrated that increasing oxygen content increases hardness, indicating a strengthening effect due to interstitial oxygen atoms. Furthermore, OM (showed in Fig 1 and 2) and XRD analyses revealed the predominance of the β phase in all investigated compositions, suggesting that oxygen addition does not significantly modify the phase constitution of the Ti–40Nb alloy system [4].

References

[1] MARIN, E. et al., *Materials*, v. 17, n. 1, p. 114, 2023.

[2] REN, Y. et al., *Crystals*, v. 15, n. 7, id. 618, 2025.

[3] DE MATTOS, F. N. et al., *Materials Research*, v. 27, e20230494, 2024

[4] This research was supported by Fapesp (grants #2024/01132-2, #2025/11920-0 and #2026/00049-0)

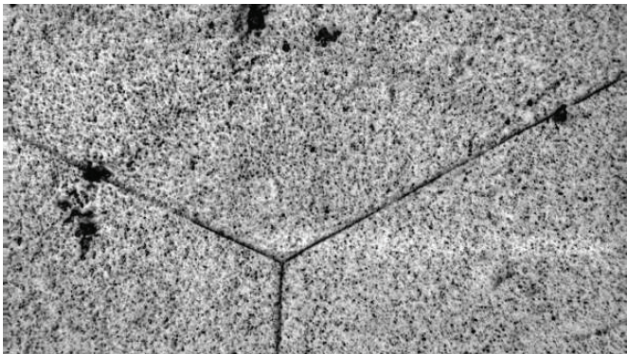


Figure 1. Optical microscopy image of Ti-40Nb-0.2O alloy magnified 1000x.

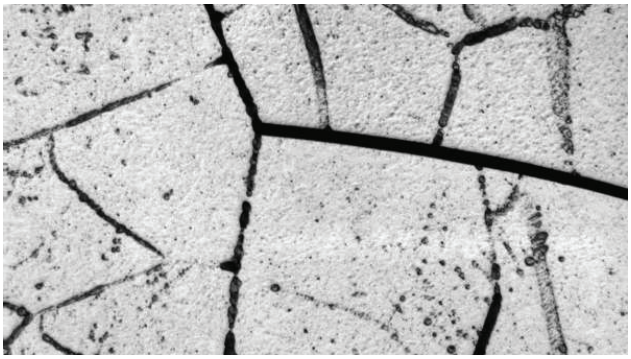


Figure 2. Optical microscopy image of Ti-40Nb-1.2O alloy magnified 1000x

Microstructural characterization of zeolites for application in polymers

Lucas Campestrini[1*], Marindia Decol[1], Marilena Valadares Folgueras[1], Daniela Becker[1]

[1] Universidade do Estado de Santa Catarina - UDESC
*E-mail: lucas.campestrini21@gmail.com

Polymer nanocomposites are emerging as a promising alternative to conventional multilayer packaging, whose structural complexity hinders recycling processes. By integrating nanoparticles into a single polymer matrix, it is possible to confer optimized barriers, mechanical, and thermal properties, enabling the development of high-performance and sustainable solutions [1]. The largest market share in packaging materials belongs to thermoplastic polymers, especially polyolefins, such as low-density polyethylene (LDPE), a polymer with excellent chemical resistance, high toughness, good thermal sealing, and low moisture absorption. However, LDPE has a high oxygen transmission rate (OTR), which is detrimental to the packaging of perishable items such as raw foods, cosmetics, and pharmaceuticals, providing inadequate barrier properties unless they are treated with additives [1,2]. Therefore, this work focuses on the use of zeolites as additives for improving oxygen barrier properties in LDPE. Zeolites are microporous crystalline aluminosilicates, with a three-dimensional structure formed by interconnecting tetrahedral units of silica (SiO4) and alumina (AlO4), linked by shared oxygen atoms, forming channels and cavities with dimensions on the order of molecular magnitude [2,3]. Due to their structure, zeolites are widely used as catalysts in various industrial processes, as well as adsorbent materials, molecular sieves, and promising inorganic additives for plastic packaging applications [3,4]. In this context, microstructural characterization is essential to understand and correlate their properties with performance in polymer matrices. Parameters such as pore volume and distribution, pore size, network connectivity, and specific surface area directly influence adsorption capacity, diffusion, and catalytic activity, being key factors for the efficiency of these materials in industrial applications. The combined use of scanning electron microscopy (SEM) equipped with an energy-dispersive X-ray spectroscopy (EDS) detector and transmission electron microscopy (TEM) is essential to establish these correlations. These techniques allow evaluation of composition, morphology, crystal size, particle size distribution, degree of agglomeration, and surface characteristics, as well as enabling the investigation of the internal structure of zeolites with high resolution. In this study, four types of zeolites synthesized using controlled chemical routes (Z1,Z3,Z4,Z5) and one commercial zeolite (Z2) were characterized by X-ray diffraction (XRD), differential thermal analysis (DTA), specific surface area measurements, and porosimetry. The results were correlated with scanning electron microscopy (SEM), and transmission electron microscopy (TEM) analyses, aiming to establish correlations that support the definition of functionalization procedures to maximize the performance of these materials when dispersed in polymer matrices. The results demonstrated that, although electron microscopy techniques do not allow direct visualization of micropores (with dimensions below 2 nm), it is possible to establish relationships between the obtained images and the experimentally determined surface area and particle size. Furthermore, the observed particle morphology enables correlation with the type of crystalline structure formed [5].

References

[1] Sarfraz, J. et al. Nanomater. 11(2020) 1.

[2] Fornaro, M. et al. Polymer. 16 (2024) 3399.

[3] Kordala, N. et al. Molecules. 29 (2024) 1069.

[4] Hosseinnia, M. et al. J Vinyl Addit Technol. 30 (2024) 363.

[5] This research was supported by 35/2025 FAPESC. The authors are thankful for the Multi-User Facility infrastructure from Santa Catarina State University's Technological Sciences Center. The authors are thankful to Meiry Gláucia Freire Rodrigues UFCA.

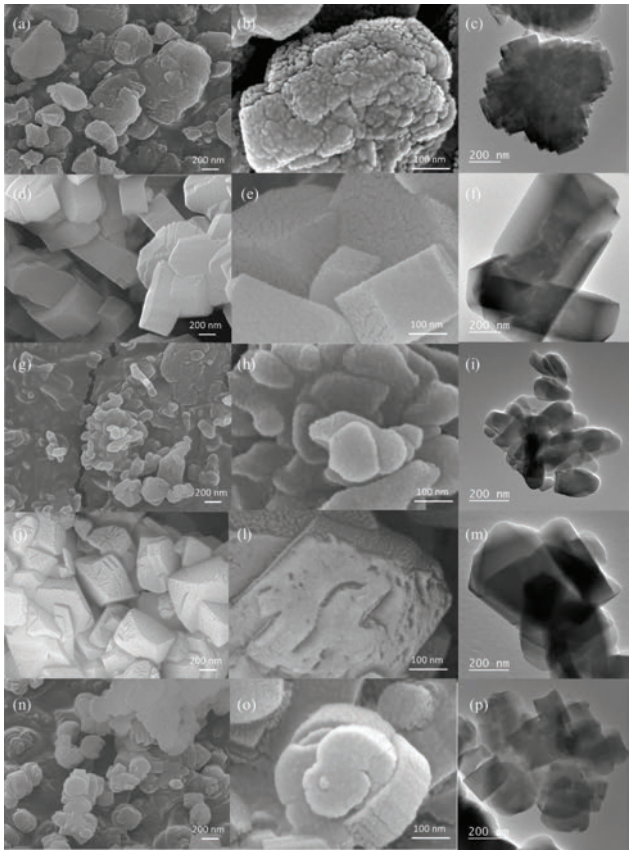


Figure 1. SEM and TEM images of the five types of zeolites studied. (a,b,c) Z1;(d,e,f) Z2; (g,h,i) Z3; (j,l,m) Z4; (n,o,p) Z5

Table 1. Results of XRD, DTA, surface area measurements, and EDS analyses for the zeolites

Ref.	XRD	Code IZA	Area (m^2/g)			DTA - Weight (%)		Si/Al
			Total	Microp.	Surface	≤ 150 °C	150–300 °C	
Z 01	ZSM 5	MFI	439.95	262.36	177.6	7.77	0.87	37±4
Z 02	ZSM 5	MFI	405.5	297.78	107.72	37.65	1.65	16±2
Z 03	Mordenite	MOR	444.13	402.06	42.06	8.45	2.4	10±0.5
Z 04	Zeolite Y	FAU	808.79	766.17	42.63	12.56	13.22	2.74±0.07
Z 05	Zeolite L	LTL	324.6	307.01	17.59	7.63	3.86	3.25±0.05

Microstructural Evolution and Phase Stability of Ti-Nb-Sn-(Ta-Mn) Multicomponent β-Type Titanium Alloys for Biomedical Applications

Victor dos Santos Pena de Araújo[1*], Rafael Formenton Macedo dos Santos[1], Diego Rafael Nespeque Correa[1], Carlos Roberto Grandini[1]

[1] Laboratório de Anelasticidade e Biomateriais, UNESP—Universidade Estadual Paulista, Bauru SP, Brazil.
*E-mail: victor.s.araujo@unesp.br

The increasing global demand for orthopedic treatments associated with bioengineering has stimulated substantial investments in the development of biomaterials and medical devices, highlighting the importance of designing materials capable of combining mechanical performance, long-term durability, and improved patient quality of life at economically viable costs [1–2]. In this context, β-type titanium alloys (β-Ti) have attracted considerable attention because of their excellent biocompatibility, high corrosion resistance, and elastic modulus closer to that of human bone when compared to conventional titanium alloys, thereby minimizing stress shielding effects [1,2]. Consequently, multicomponent systems free from potentially toxic elements, such as Ti-Nb-Sn-(Ta-Mn), have been extensively investigated for advanced biomedical applications. Equimassic systems based on Ti-Nb-Zr and the quaternary alloys Ti-Nb-Zr-Ta and Ti-Nb-Zr-Ta-Mo has demonstrate strong potential to achieve high mechanical strength while maintaining the low elastic modulus characteristic of β-Ti alloys, which is essential for biomedical applications [3]. In the search for lighter, more cost-effective, and sustainable alternatives, the present work proposes the replacement of molybdenum (Mo), a high-density and expensive transition metal, with manganese (Mn), which is lighter, more abundant, and exhibits proven biocompatibility. Similarly, zirconium (Zr) is replaced by tin (Sn), another element recognized for its excellent biocompatibility. In this study, the alloys were produced by arc melting under a protective argon atmosphere using high-purity metallic elements (>99%). The investigation aims to correlate chemical composition, phase stability, and microstructural evolution in titanium-based multicomponent systems. X-ray diffraction (XRD), scanning electron microscopy (SEM), and optical microscopy (OM) analyses are currently in progress to identify the phases formed, evaluate microstructural homogeneity, and understand the transformation mechanisms present in the developed alloys. Preliminary thermodynamic simulations indicate an increase in both microstructural complexity and the number of phases as the number of alloying elements increases, a behavior consistent with Gibbs' phase rule, which predicts a greater possibility of multiphase equilibrium in multicomponent systems. Therefore, this work is expected to provide important insights into phase stability and transformation mechanisms, contributing to the development of new β-Ti alloys with optimized mechanical and biological properties for orthopedic and dental applications [4].

References

[1] M. Geetha et al, Progress in Materials Science 54 (3) (2009) 397–425.

[2] S. Liang, Advanced Engineering Materials 22 (11) (2020) 2000555.

[3] R.F.M. dos Santos et al, J. Alloy. Compd. Commun. 4 (2024) 100040.

[4] FAPESP (projetc #2024/01132-2 and grants #2026/00061-0, #2025/11856-0) for their financial support.

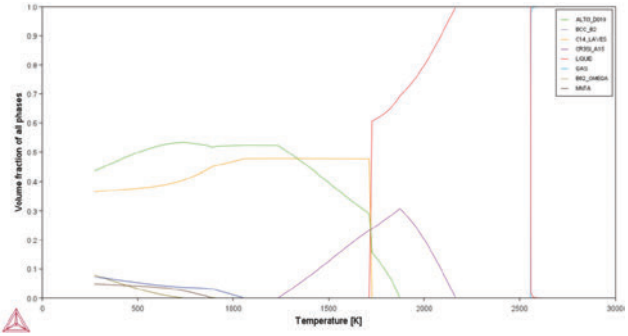


Figure 1. Evolution of the volume fraction of phases as a function of temperature for the quinary alloy: thermodynamic simulation (Thermo-Calc) –

Table 1. Chemical composition of the alloys proposed in the present study

Liga (% peso)	Liga (% at.)	
Ti-33Nb-33Sn	$Ti_{52,87}Nb_{26,44}Sn_{20,69}$	TNS-33
Ti-25Nb-25Sn-25Ta	$Ti_{30,16}Nb_{36,26}Sn_{20,27}Ta_{13,30}$	TNST-25
Ti-20Nb-20Sn-20Ta-20Mn	$Ti_{32,74}Nb_{16,87}Sn_{13,20}Ta_{8,66}Mn_{28,53}$	TNSTM-20

Microstructural Evolution of Cu/Cu15Zn Heterostructures Produced by Accumulative Roll Bonding (ARB)

Mila Christy de Oliveira[1*], Andrea Kliauga[2], Diogo Pedrino Braga[2], Thiago Carvalho da Silva[3], Danielle Cristina Camilo Magalhães

[1] Graduate Student in Materials Science and Engineering, Federal University of São Carlos; [2] Department of Materials Engineering, Federal University of São Carlos, [3] Undergraduate Student in Materials Engineering, Federal University of São Carlos.
*E-mail: mila.oliveira@estudante.ufscar.br

Heterostructured materials (HM) are a promising class of materials because they combine different compositions and microstructures, resulting in mechanical properties better than those predicted by the rule of mixtures [1]. Among the different HM architectures, multilayer structures are important because they can combine high strength and good ductility. In this work, Cu/Cu15Zn heterostructured sheets were produced by solid-state bonding using the accumulative roll bonding (ARB) process, with alternating layers of pure copper (stacking fault energy, SFE = 78 mJ/m^2) and Cu15Zn brass (SFE = 20 mJ/m^2) [2]. The difference in stacking fault energy between the materials promotes different plastic deformation mechanisms and affects the microstructural evolution. The process used successive rolling cycles with 50% thickness reduction, including six cycles (6X) and eight cycles (8X), as well as conditions with one additional rolling step (6X+1 and 8X+1). The objective of this study was to investigate the microstructural evolution of the samples by analyzing grain size, layer thickness, interfacial bonding, and grain morphology. The samples were characterized in the as-received and homogenized conditions (Figure 1). Optical microscopy was used to analyze grain size, while scanning electron microscopy (SEM) with EDS and electron backscatter diffraction (EBSD) were used to analyze the interfaces between layers (Figure 2). The preliminary results showed that the average grain size decreased as the number of ARB cycles increased, reaching about 20 µm for 6X and 13 µm for 8X. The average layer thickness was about 25 µm for 6X and 10 µm for 8X. Sheets processed with an extra rolling step (6X+1 and 8X+1) showed better interfacial bonding. EBSD maps showed grain elongation along the rolling direction, indicating the formation of crystallographic texture related to shear and plane strain deformation. EDS analyses confirmed strong Zn interdiffusion from the brass layers into the copper layers, with about 4 µm for 6X sheets and 5 µm for 8X sheets. Overall, the results show that the ARB process can control the microstructural architecture of Cu/Cu15Zn sheets and may help optimize mechanical properties by changing the number of cycles and layer geometry [4].

References

[1] H. Zhou, X. Wu, D. Srolovitz, and Y.D. Zhu, Nature Materials 25, 366-372 (2026).

[2] D.C.C. Magalhães, et al., Journal of Materials Science 52, 7466–7478 (2017).

[3] U.F. Kocks, and H. Mecking, Progress in Materials Science 48, 171-273 (2003).

[4] This research was supported by FAPESP (Grant No. 2026/02621-2) and by the CNPq (Grant No. 112450/2025-3).

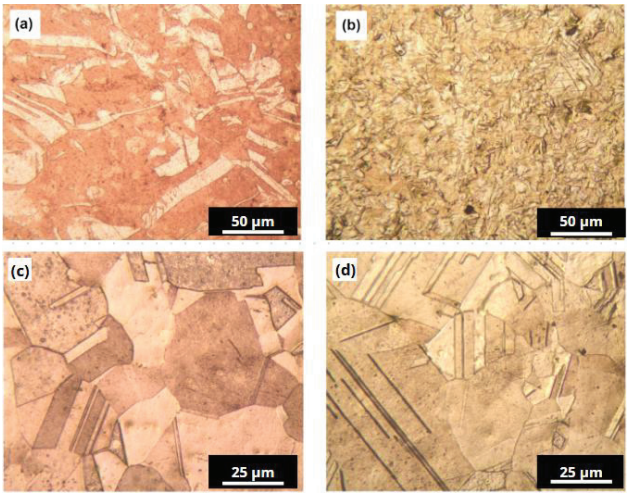


Figure 1. Micrographs of the materials in the as-received condition: (a) Cu, (b) Cu15Zn brass; (c) Cu and (d) Cu15Zn microstructures after annealing at 700 °C for 1 h, respectively.

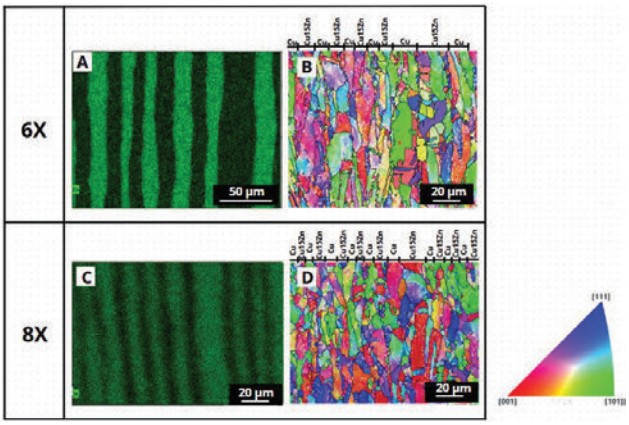


Figura 2. Zinc element mapping (in green) in the layers by EDS and corresponding EBSD analysis showing the inverse pole figure (111) of Cu/Cu15Zn sheets processed by ARB with different numbers of cycles: (a) and (b) 6X; and (c) and (d) 8X.

Microstructural Evolution of Electrochemically Induced Niobium Hydrides

Audrey Marie Bedoch[1*], Guilherme Yuuki Koga[1], Guilherme Zepon[1]

[1] Federal University of São Carlos, Department of Materials Engineering.
*E-mail: audrey.bedoch@estudante.ufscar.br

Energy storage remains one of the main scientific challenges for the large-scale implementation of renewable energy sources such as solar and wind power. In this context, metal hydrides have attracted considerable attention as safe solid-state hydrogen storage materials. Among them, niobium is particularly interesting because it is a body-centered cubic (BCC) metal capable of forming different hydride phases during hydrogen absorption. Therefore, understanding the mechanisms governing hydride formation in BCC systems is essential for the development of advanced hydrogen storage materials. In this work, the microstructural evolution of niobium during electrochemical hydrogenation was investigated using X-ray diffraction (XRD), scanning electron microscopy (SEM), and electron backscatter diffraction (EBSD). The results reveal the sequential formation of β-$NbH_{0.89}$ and δ-NbH_2 hydrides. Both the β- and δ-phases exhibit plate-like growth morphologies similar to martensitic [1] or Widmanstätten ferrite structures, suggesting displacive transformation mechanisms assisted by rapid hydrogen diffusion. Since one of the transformations occurs between the BCC β-phase and the FCC δ-phase, an analogy can be established with phase transformations in steels between austenite (FCC) and martensite (BCC), exhibiting orientation relationships similar to Kurdjumov–Sachs (KS) and Nishiyama–Wassermann (NW). These findings provide important insights into the mechanisms controlling hydride formation and stability in BCC systems [2].

References

[1] A.M. Bedoch, G.Y. Koga, V. Roche, G. Zepon, Electrochemical Hydrogenation of Nb: Unraveling Structural and Surface Dynamics of Hydride Formation, J. Phys. Chem. C. 129 (2025) 8509–8520. https://doi.org/10.1021/acs.jpcc.5c00570.

[2] This research was financially supported by the Instituto Serrapilheira (grant number Serra-1709-17362) and the CNPq - National Council for Scientific and Technological Development (grant numbers 140179/2021-6 and 309467/2021-7). This study was also supported by the Coordination for the Improvement of Higher Education Personnel - Brazil (CAPES) - Finance Code 001. The authors thank the Laboratory of Structural Characterization (LCE/DEMA/UFSCar) for the general facilities and support to this research.

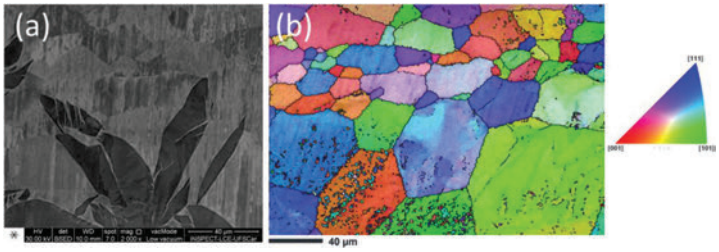


Figure 1. (a) BSE images of the electrode containing both α and β phases (darker regions). **(b)** EBSD maps along the Z direction of the electrode containing both α and β phases.

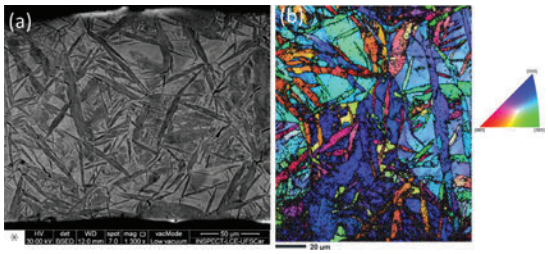


Figure 2. (a) BSE image after electrochemical hydrogenation, showing the presence of both β and δ (darker regions) phases. **(b)** EBSD maps along the Z direction of the same sample, containing both β and δ phases.

Microstructural Exploration of Multiprincipal Components Ti Alloys for Biomedical Applications

Rafael Formenton Macedo dos Santos[1*], Conrado Ramos de Moreira Afonso[2], Diego Rafael Nespeque Correa[1], Carlos Roberto Grandini[1].

[1] Laboratório de Anelasticidade e Biomateriais, UNESP—Universidade Estadual Paulista, Bauru SP, Brazil; [2] BioMet-CAM Laboratory, Department of Materials Engineering (DEMa), Universidade Federal de São Carlos (UFSCar), São Carlos, SP, Brazil.
*E-mail: rafael.formenton@unesp.br

The development of novel β-titanium (β-Ti) alloys has emerged as a promising strategy to overcome the intrinsic limitations of conventional biomaterials, such as Ti-6Al-4V and 316L Stainless Steel, particularly regarding stress shielding and limited biocompatibility [1,2]. In recent years, significant efforts have been directed toward developing materials with elastic moduli closer to those of human bone (10–30 GPa) while avoiding potentially toxic alloying elements [1,3]. Nevertheless, suitable biomaterials must also satisfy additional requirements, including high corrosion resistance in physiological environments, adequate mechanical strength, and sufficient fatigue resistance for long-term cyclic loading conditions. In this study, equimassic β-Ti multiprincipal-component alloys were designed, processed, and characterized with the aim of achieving an optimal balance between a low elastic modulus and high mechanical strength [4,5]. The microstructure was characterized by optical microscopy, scanning electron microscopy (SEM), and transmission electron microscopy (TEM). Microstructural characterization revealed a predominant β phase, while both thermodynamic simulations and experimental results indicated β-transus temperatures below 500 °C. In addition to the β phase, the ω phase was also observed, although this phase is generally not expected in alloys containing high concentrations of β-stabilizing elements. These observations indicate that the ω phase may remain stable in β alloys even under conditions where it is traditionally assumed to disappear, possibly persisting in very small volume fractions that are difficult to detect by conventional techniques. Furthermore, electron diffraction analysis revealed the presence of β and β′ phases, representing a novel result that has not yet been reported for multiprincipal component alloys. The microstructural analysis revealed unexpected phase features in the multiprincipal-component β-Ti alloys, including the presence of the ω phase and the coexistence of the β and β′ phases. These findings provide new insights into the phase stability and transformation mechanisms of complex β-Ti alloys, advancing the understanding and development of advanced biomedical materials [6].

References

[1] L.-Y. Chen et al, Metals (Basel). 10 (9) (2020) 1139.
[2] P.A.B. Kuroda et al, Vacuum 217 (2023) 112541.
[3] R.F.M. dos Santos et al, J. Alloy. Compd. Commun. 4 (2024) 100040.
[4] S. Bahl et al, Int. Mater. Rev. 66 (2) (2021) 114–139.
[5] J. Takadoum, Corros. Mater. Degrad. 4 (4) (2023) 644–658.
[6] CAPES financial code 001, and FAPESP (project PAIP EMU-PMP #2023/16836-2 and grants #2018/18293-8, #2019/26517-6, #2025/11856-0) for their financial support.

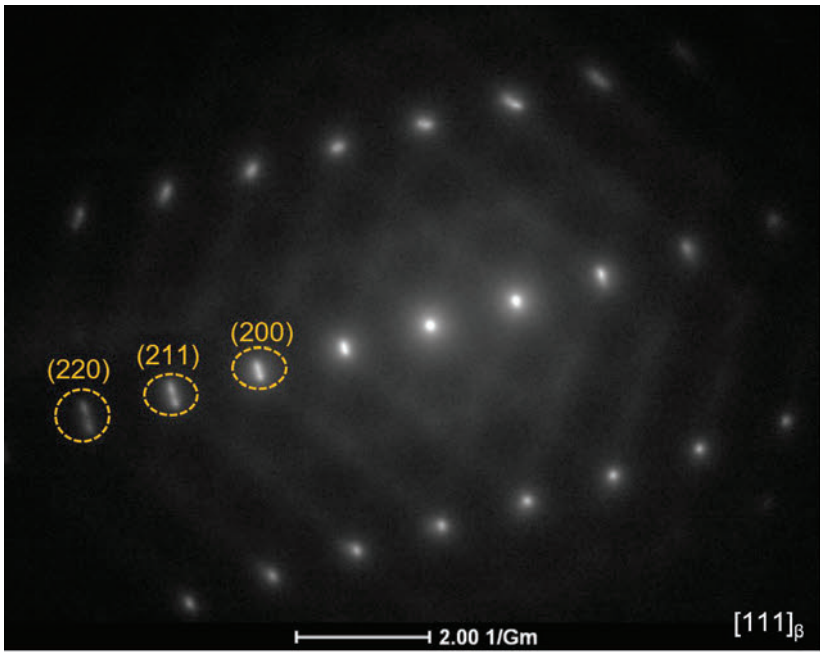


Figure 2. Selected area electron diffraction (SAD) patterns for a TiNbZrTa multiprincipal component alloy.

Microstructural features of a non-equiatomic TiCrCoAlFe HEA for potential use as external prostheses

Vinícius Melo Pellegrino[1*], Gustavo Diniz[1], Carlos Roberto Grandini[1], Diego Rafael Nespeque Corrêa[1]

[1] São Paulo State University (UNESP), School of Sciences, Laboratory of Anelasticity and Biomaterials, Bauru (SP), Brazil.
*E-mail: vm.pellegrino@unesp.br

High-entropy alloys (HEAs) are a very important innovative technology across several areas, especially in health, and their microstructural analysis contributes to their characterization because, in addition to their high melting point and good microstructural stability, combined with optimal mechanical properties at elevated temperatures, these alloys have limitations. [1]. These materials exhibit unique microstructures and phases that depend on the stoichiometry of the elements, the configurational entropy, and the processing method. since they have unique microstructures that vary according to their stoichiometry and the entropy of the entire system [2]. The microscopic study of alloys like this allows us to determine their properties, such as chemical stability, mechanical properties, and biological response [3]. The analyses performed are for a new non-equiatomic alloy, TiCrCoAlFe, produced and characterized for external prostheses. To produce such an alloy, experimental procedures were carried out, starting with a phase diagram generated with Thermocalc to determine the theoretical design, followed by melting in an arc melting furnace. The metallographic procedures evolved optical microscopy (OM), Scanning Electron Microscopy (SEM), and energy-dispersive spectroscopy (EDS) to analyze its microstructural characteristics and chemical composition. The results indicated a multiphase microstructure, consistent with design criteria for HEA processing and the predictive phase diagram. Finally, it is expected to yield good results in mechanical properties, as it has a beneficial use in the medical field [4].

References

[1] Torrento, J.E.M. et al. Mater. Charact. 208 (2024) 113678.

[2] Zhu, D. et al. J. Mater. Sci. 59 (2024) 1153-1183.

[3] X. Zhou, H.Y. Fang, T.C. Yuan, R. Li, J. Alloys Compd. 892 (2022) 162164.

[4] The authors acknowledge the São Paulo Research Foundation (FAPESP) for the financial support. Process no. 2026/00029-9.

Microstructure and crystallographic features of novel TiZrNbMo(Fe, Ta) high-entropy alloys

Vitor Meirelles Santos Toschi[1*], Carlos Eduardo Manreza[1], Diego Rafael Nespeque Correa[1], Carlos Roberto Grandini[1]

[1] São Paulo State University (UNESP), School of Sciences, Laboratory of Anelasticity and Biomaterials, Bauru, SP, Brazil.
*E-mail: vitor.toschi@unesp.br

The development of novel metallic biomaterials has been strongly driven by the exploration of High Entropy Alloys (HEAs). Despite having complex chemical compositions, HEAs often exhibit superior mechanical strength, ductility, and corrosion and wear resistance compared to conventional alloys. In this scenario, the previously developed HEAs have attracted attention for biomedical applications, particularly for hard-tissue replacements and surgical instruments [1]. However, a comprehensive understanding of phase stability and microstructure, combining X-ray diffraction (XRD) with microscopy, is essential to fully elucidate the structure-property relationships in these materials [2]. In this context, the current study investigated the microstructures and crystalline structures of newly developed non-equiatomic TiZrNbMoTa (TaMo), TiZrNbMoFe (MoFe), and TiZrNbTaMn (TaMn) HEAs in the as-cast condition for biomedical applications. The study correlated *in situ* XRD results at varying temperatures with microscopy analyses conducted at room temperature, using the corresponding phase diagrams predicted by CALPHAD. The complementary microstructural characterization was performed by combining optical microscopy with phase identification from X-ray diffraction, allowing a direct comparison between experimental observations and thermodynamic predictions. This integrated approach provides a more comprehensive understanding of phase formation, elemental partitioning, and the influence of refractory alloying elements on the evolution of dendritic morphologies during solidification, thereby supporting the interpretation of the crystallographic behavior observed during thermal analysis. By evaluating the shift of the diffracted peak as a function of temperature, the lattice parameters, the unit-cell volume, and the thermal expansion coefficients were calculated. These crystallographic findings provide the fundamental macroscopic basis for the local microstructural analysis, which primarily revealed dendritic structures in the BCC and C14 Laves phases (as shown in Figure 1). The additional comparison between our theoretical values, XRD structural data, and microstructural observations allowed us to evaluate the role of the alloying elements in crystalline anisotropy and defect dynamics under thermal stress, a phenomenon also reported in complex refractory systems [3]. Furthermore, the combined experimental and theoretical analyses establish a framework for correlating phase stability, thermal expansion behavior, and microstructural evolution in complex high-entropy alloys. Such correlations are essential for optimizing alloy composition and processing parameters to improve long-term structural reliability and performance under service conditions. The findings show that advancing the complementary understanding of the microstructural and crystallographic features of these HEAs directly contributes to the development of high-performance biomaterials aligned with priority areas in health and advanced materials technologies [4].

References

[1] N. Schlegel et al., Chemistry of Materials, 37 (2025) 939-953.
[2] B. O. Pinto et al., Materials Today Communications, 41 (2024) 110885.
[3] M. Behera et al., Journal of Alloys and Compounds, 892 (2021) 162154.
[4] This research was supported by CNPq (Brazil).

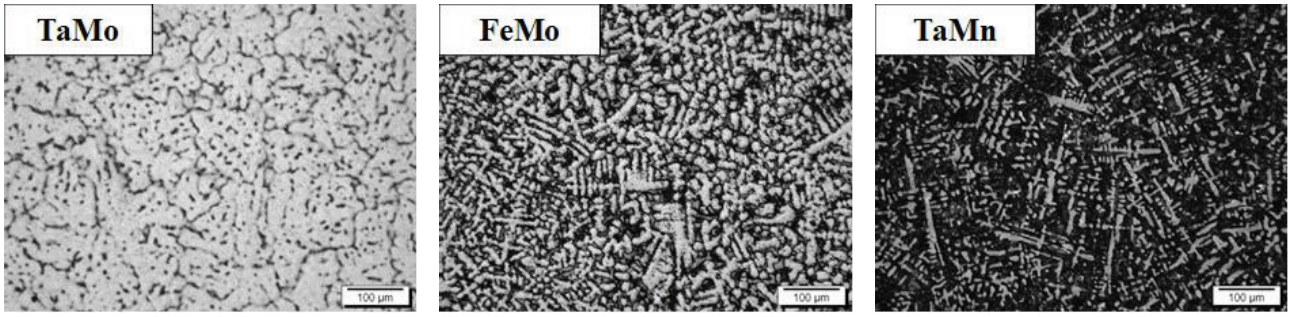


Figure 1. Optical microscopy of the as-cast samples.

Microstructure and Elastic Modulus of the β Ti-35Nb-6Ta Alloy Produced by Laser Melting and 3D Printing for Implant Applications

Bruno M. Casarin[1*], Renan A. F. Dias[1], Mariana L. Lourenço[1], Giovanna Santo[2], Conrado R. M. Afonso[1]

[1] BioMet-CAM, Department of Materials Engineering (DEMa), Universidade Federal de São Carlos (UFSCar); [2] PPG-CEM/UFSCar.
*E-mail: brunomc@estudante.ufscar.br

Among biomaterials, metals play a significant role in structural applications, where high load-bearing capacity and resistance to different mechanical stresses are required. The first metallic biomaterials used were relatively inert materials, such as stainless steels, Co-Cr-Mo alloys, and the Ti-6Al-4V alloy. However, these materials exhibit elastic moduli much higher than that of human bone (E ≈ 30 GPa), which may lead to problems related to the *stress shielding* effect. In this context, β-Ti alloys with a body-centered cubic (bcc) structure stand out due to their reduced elastic modulus, ranging from 42 to 80 GPa, while multi-principal element bcc alloys open new perspectives for the development of low elastic modulus biomaterials. Furthermore, surface treatments have been employed to improve the interaction between the implant and the surrounding biological tissue. Therefore, the present project aims to perform the microstructural and mechanical characterization of the β Ti-35Nb-6Ta alloy produced by arc melting and laser additive manufacturing, comparing the changes in the alloy properties under different processing conditions. The first condition corresponds to arc casting ("as-cast" – AC), performed in a water-cooled copper mold under a controlled ultrapure argon atmosphere. The second condition involves additive manufacturing through the *Laser Powder Bed Fusion* (LPBF) process, using a laser power of 200 W and scanning speeds ranging from 500 to 1000 mm/s. This study seeks to overcome the challenges associated with β-Ti alloys applied as implant biomaterials, especially the combination of low elastic modulus and high mechanical strength, promoting greater compatibility with human bone tissue. The microstructural study was initially carried out using optical microscopy (OM), followed by metallographic preparation and analyses by scanning electron microscopy (SEM), Energy-Dispersive X-ray Spectroscopy (EDS), and X-ray diffraction (XRD). As a preliminary result of the XRD analysis, the presence of the β-Ti phase with a BCC crystal structure was identified, and the detected peaks were consistent with the experimental data obtained from EDS analysis [4].

References

[1] De Mattos, F., et al., Unraveling composition graded microstructure of in-situ alloyed Ti-15Nb alloy through laser powder bed fusion. Materials Letters, 2024. 358: p. 135776.

[2] Prandi, G.V., et al., HYbrid Titanium Alloys produced by laser powder bed Fusion using Ti-5553 and Ti–42Nb powder recycling. Journal of Materials Research and Technology, 2023. 27: p. 8281-8291.

[3] Joaõ V. Calazans Neto, Cícero A. S. Celles, Catia S. A. F. de Andrade, Conrado R. M. Afonso, Bruna E. Nagay,* and Valentim A. R. Barão. Recent Advances and Prospects in β-type Titanium Alloys for Dental Implants Applications. ACS Biomater. Sci. Eng. 2024, 10, 6029−6060.

[4] This research was supported by FAPESP PAIP 2023/16836-2 and This study was partially supported by CAPES. Finance Code 001.

Table 1. Laser 3D including laser power of 200 W and scanning speed of 500 to 1000 mm/s using, printing by OmniTek parameters.

Condição	Potência Laser (W)	Velocidade Varredura (mm/s)	Densidade de Energia (J/mm³)
1	200	500	167
2	200	750	111
3	200	1000	83

Table 2. Chemical composition analysis across a wide area using Energy-Dispersive Spectroscopy (EDS).

Element	At No	Mass Norm. [%]	Atom [%]	Abs. Error [%]	Re. Error [%]
Titanium	22,0	60,0	76,0	1,5	2,8
Niobium	41,0	35,0	22,5	1,2	3,9
Tantalum	73,0	5,0	1,5	0,2	3,9

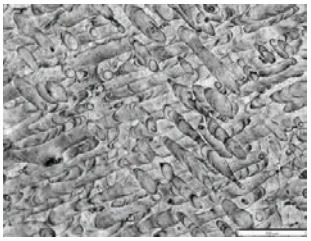


Figure 1. Ti35Nb6Ta - 500mm/s(LPBF)

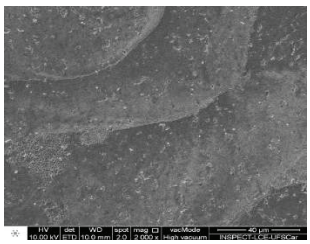


Figure 2. Ti35Nb6Ta - 1000mm/s(LPBF)

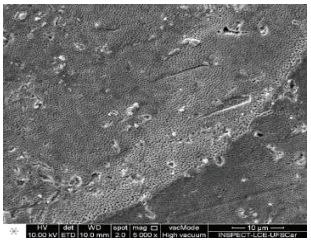


Figure 3. Ti35Nb6Ta - 750mm/s(LPBF)

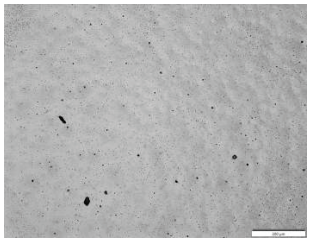


Figure 4. Ti35Nb6Ta - 500mm/s(LPBF)

Microstructure and plastic deformation effects on hydrogen generation from recycled Al–Zn chips

João G. M. Braghin[1], Rodrigo A. V. Reyes[2], Guilherme. L. De Gouveia[2], Cássia C. De Carvalho[3], José M. Aquino[4], Bismarck L. Silva[3], Carlos A. D. Rovere[1], José Eduardo Spinelli[1]

[1] Department of Materials Engineering, Federal University of São Carlos; [2] Federal University of São Carlos, Graduate Program in Materials Science and Engineering; [3] Department of Materials Engineering, Federal University of Rio Grande do Norte; [4] Department of Chemistry, Federal University of São Carlos.

The study of the solidification of electrochemically active alloys, with controlled microstructures and morphologies, is essential in prospecting for a higher volume of hydrogen[1]. Transient solidification has been used to produce Al-10 wt% Zn alloy samples, which have been machined into chips and further compacted into discs. Chips with different dendritic scales have been extracted to produce compacted samples. Both microstructures of the as-directionally-solidified and as-compacted samples have been characterized to evidence the distribution of the Al-rich and Zn phases in both conditions. The samples have been characterized using optical (OM) and scanning electron microscopy (SEM) images and measurements have been taken along the entire ingot length, revealing that the dendritic spacing at the top has increased approximately fivefold compared to the base (Figure 1). Two ingot positions have been selected for the tests, 4 mm and 69 mm. The two as-solidified samples exhibit primary dendritic spacings of 39.6 µm and 215 µm. Correspondingly, the Al/Zn layer spacings in the compacted samples are 9.9 µm and 21 µm, respectively. A simple H_2 generation system was used, with 5M NaOH as the solution. Compacted samples exhibit a significantly higher volume of generated hydrogen at both testing temperatures, furthermore, the generation increases with increasing temperature. At 25°C for a given time interval, the hydrogen volume produced by the compacted samples is four times that of the bulk samples. At 45°C this difference further increases have been observed. This difference is attributed to the larger contact area between metal and solution, as crevices were identified within the green compacted samples. For bulk samples at 25 °C, hydrogen production followed linear kinetics, with higher rates observed for finer microstructures due to micro-galvanic effects. In contrast, the compacted briquettes exhibited two distinct production regimes: Regime I, where originally coarser and harder samples generated more hydrogen due to the compaction structure that facilitates solution penetration; and Regime II, occurring after chip disintegration, which is governed by the formation of ZnxOy that counterbalanced the increase in surface area. Following the hydrogen generation tests, SEM-EDS characterization has been performed to prove the presence of oxides formed during the reaction (Figure 2).

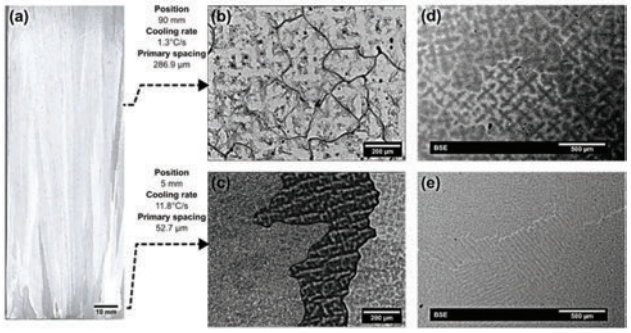


Figure 1. (a) Macrostructure morphology, (b,c) optical and (d,e) SEM micrographs at two representative positions along the directionally solidified casting of the Al-10 wt% Zn alloy, highlighting variations in microstructure associated with the local thermal conditions.

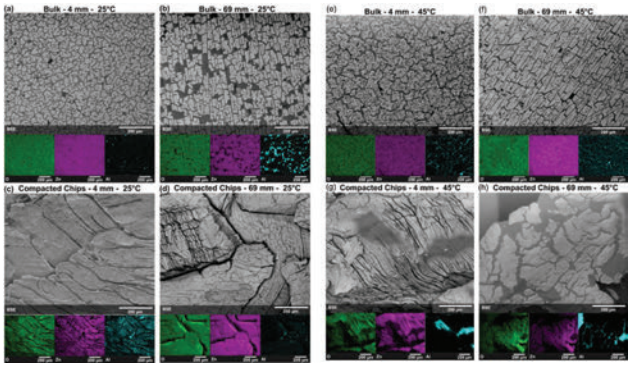


Figure 2. SEM micrographs and corresponding EDS dot-maps (O, Zn, Al) for bulk and compacted Al-10 wt% Zn samples at 25 °C / 45 °C after the experiments of hydrogen generation, comparing positions at 4 mm (a,c,e,g) and 69 mm (b,d,f,h) along the casting length.

References

[1] Xu, S., Zhao, X. & Liu, J. Liquid metal activated aluminum-water reaction for direct hydrogen generation at room temperature. Renew. Sustain. Energy Rev. 92, 17–37 (2018).

Morphological Transition of Grass-Like γ-Alumina Nanostructures during Hydrothermal Treatment

Lucas H. M. Paodjuenas[1,2*], Bernado P. Eduardo[2], Paula M. Jardim[2]

[1] Graduate Program in Materials Science and Engineering - PPGCEM – UFSCar; [2] Metallurgical and Materials Engineering Program – PEMM - COPPE - UFRJ
*E-mail: lucas.paodjuenas@estudante.ufscar.br

The grass-like or flower-like alumina structure is a nanostructure formed during hydrothermal treatments at temperatures close to the boiling point of water. Initially, the grass-like structure was observed in amorphous alumina thin films [1]; however, more recently, its formation has also been reported on aluminum alloy surfaces [2]. Despite its potential applications in optics [1] and catalysis [3], the formation mechanism of the grass-like structure and the effect of using temperatures above the boiling point of water during hydrothermal treatment remain unclear in the literature. In the present study, 6061 aluminum plates were subjected to hydrothermal treatments under different temperatures and immersion times in order to investigate the influence of these parameters on the grass-like structure formation. Prior to the treatments, the plates were cleaned and mechanically polished to avoid contamination. The hydrothermal treatments were then carried out at temperatures of 110, 125, and 140 °C for periods of 4, 6, and 8 hours. The resulting surfaces were analyzed by scanning electron microscopy (SEM) and, after lamella preparation using focused ion beam (FIB) techniques, by transmission electron microscopy (TEM). In all samples, the formation of a dense and amorphous alumina layer was observed in the region closest to the metallic substrate. Furthermore, samples treated at 140 °C exhibited thicker regions of this amorphous layer, with an increase of approximately 350 ± 125 nm. Hydrothermal treatments performed at 140 °C also promoted the formation of thicker and more faceted nanostructures, displaying a distinct rod-like morphology, as shown in Figure 1. Selected-area electron diffraction analyses (Figure 2(a) inset) indicated that for all analyzed conditions the grass-like structure consisted of γ-alumina. Additionally, the convergent beam electron diffraction pattern, Figure 2(c), corresponding to the faceted nanostructures shown in Figure 2(b), confirms the γ-alumina phase [ICSD code 99836]. Regarding the effect of immersion time, samples treated for longer periods exhibited the formation of a transition layer between the amorphous alumina layer and the grass-like structure. This transition region was composed of smaller and thinner "grass" nanostructures formed beneath the larger nanostructures, as demonstrated in Figure 3 [4].

References

[1] K. Tanadaga et al., J. Am. Ceram. Soc., 80 (1997) 1040.

[2] N.S. Saadi et al., Sci. Rep., 7 (2017) 7158.

[3] T.Wang et al., J. CO2 Util., 17 (2017) 162.

[4] This research was supported by Conselho Nacional de Desenvolvimento Científico e Tecnológico (CNPq) - Process Number 141816/2025-2. This study was financed in part by the Coordenação de Aperfeiçoamento de Pessoal de Nível Superior - Brasil (CAPES) - Finance Code 001.

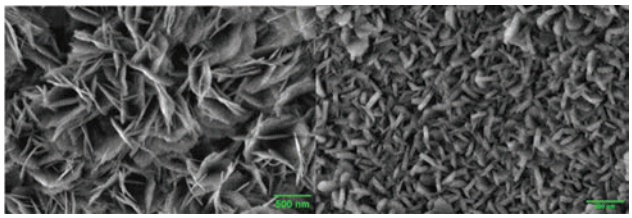


Figure 1. SEM images of the plate surface after hydrothermal treatment at 110 °C for 4 hours (left) and at 140 °C for 4 hours (right).

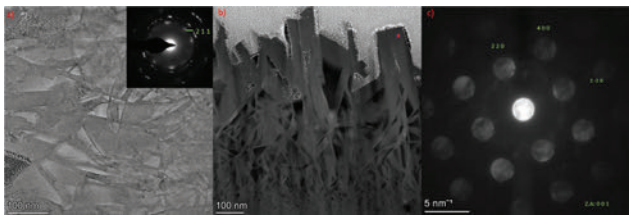


Figure 2. STEM images of the sample after hydrothermal treatment at 140 °C for 4 hours. STEM image of the region where the selected-area electron diffraction was performed, together with the corresponding diffraction pattern (a). STEM image indicating the point where convergent beam electron diffraction (CBED) was carried out (b), along with the corresponding CBED pattern (c), highlighting the crystallographic plane orientations present in the specific rod analyzed.

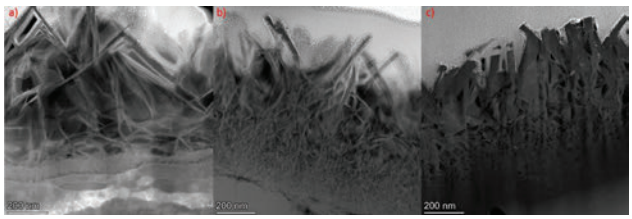


Figure 3. STEM images of the lamellae from samples containing grass-like structures obtained at 110 °C for 4 hours (a), 110 °C for 8 hours (b), and 140 °C for 4 hours (c).

Multiscale Characterization of Phases in UNS S41426 Supermartensitic Steel: from Optical Microscopy to EBSD

Priscila Carvalho Borba Cardoso[1*], Bruno da Silva de Paiva[2], Vinycius Tavares Heuser[2], Suzana Bottega Peripolli[1], José Brant de Campos[1], André Rocha Pimenta[2]

[1] Rio de Janeiro State University; [2] Federal Institute of Rio de Janeiro.
*E-mail: priborbaengenharia@gmail.com

The UNS S41426 supermartensitic stainless steel (SMSS), used in oil country tubular goods (OCTG), requires detailed microstructural characterization due to a complex phase balance (tempered martensite, retained/reversed austenite, delta ferrite, and Ti(C/N) carbonitrides) that dictates its mechanical properties and corrosion resistance [1,2]. Martensitic stainless steel (MSS) were developed to exhibit high mechanical properties with adequate corrosion resistance levels. The SMSS were an evolution of MSS, due to a maximum of 0.05 wt% of C, have also good weldability, and, due to their lower cost, to be an attractive option to substitute duplex stainless steels and Ni-based alloys [1]. This work demonstrates a multi-technique approach to identify and quantify these phases using optical microscopy (OM), scanning electron microscopy (SEM), and electron backscatter diffraction (EBSD). Samples from hot-rolled seamless pipe manufactured in UNS S41426 steel were prepared by standard metallography (grinding to 1200 grit and 1 µm diamond polishing). Different chemical attacks were applied. Figure 1 presents unetched samples: (A) OM and (B) SEM, where TiN particles were identified in the OM image as gold particles; and in the SEM image as dark particles. TiN particles were quantified by digital image processing using ImageJ software [3], with a volume fraction of 0.18%. Figure 2 shows samples etched with Villela's reagent (5 mL HCl + 2 g picric acid + 100 mL ethyl alcohol, immersion): (A) OM and (B) SEM, revealing the martensitic matrix and delta ferrite; while visible in OM, SEM provides more definitive results, principally for delta ferrite identification. Figure 3 displays OM images etched with (A) V2A reagent (100 mL distilled water + 100 mL hydrochloric acid + 10 mL nitric acid, immersion) and (B) ammonium persulfate reagent, highlighting prior austenite grain boundaries with an average size of 17.27 µm measured by the intercept method. Figure 4 presents OM images after selective etchings: (A) Marble's reagent show the martensite grains, but with worst quality than Villela's reagent, and (B) NaOH electrolytic solution (20% NaOH in distilled water, 3 V, for 30 s) reveals delta ferrite grains. Figure 5 shows the EBSD image, with the martensite grain size map, revealing groups of laths with similar crystallographic directions, allowing measurement of the martensite packet size; an average lath width of 6.0 µm was measured from the EBSD phase maps. The combined use of selective etching, OM, SEM, and EBSD provided a robust protocol for phase characterization in SMSS, critical for correlating microstructure with mechanical failures.

References

[1] I.P. Baptista, A.R. Pimenta, M. de A.V. Heringer, G. Perez, S.S.M. Tavares, Microstructure, mechanical properties and corrosion resistance of supermartensitic steel UNS S41426: comparison between forged and hot rolled seamless pipe, The International Journal of Advanced Manufacturing Technology (2022). https://doi.org/10.1007/s00170-022-10290-4.

[2] A.R. Pimenta, I.P. Baptista, I.M.D.S. Breves, J.M. Pardal, S.S.M. Tavares, Effects of post-weld heat treatments in microstructure, mechanical properties, and corrosion resistance of simulated heat-affected zone of supermartensitic steel UNS S41426, Int J Adv Manuf Technol (2024). https://doi.org/10.1007/s00170-024-13448-4.

[3] C.A. Schneider, W.S. Rasband, K.W. Eliceiri, NIH Image to ImageJ: 25 years of image analysis, Nat Methods 9 (2012) 671–675. https://doi.org/10.1038/nmeth.2089.

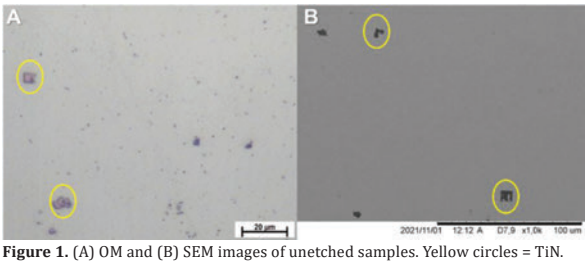


Figure 1. (A) OM and (B) SEM images of unetched samples. Yellow circles = TiN.

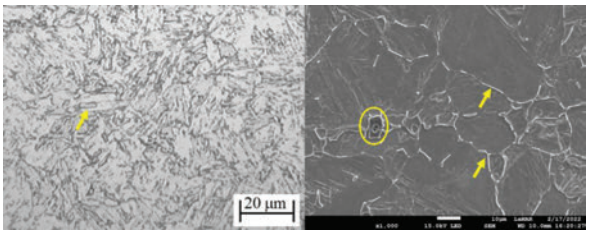


Figure 2. (A) OM and (B) SEM images etched with Villela's reagent. Yellow circle = TiN; Yellow arrows = delta ferrite.

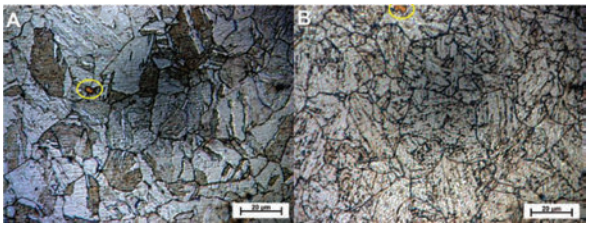


Figure 3. OM images etched with (A) V2A and (B) Ammonium Persulfate's reagents. Yellow circles = TiN.

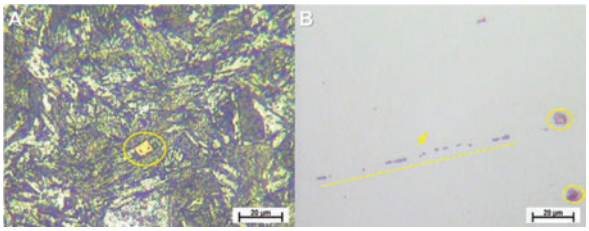


Figure 4. OM images etched with (A) Marble's reagent and (B) NaOH Electrolytic's reagents. Yellow circles = TiN; Yellow arrow and line = delta ferrite.

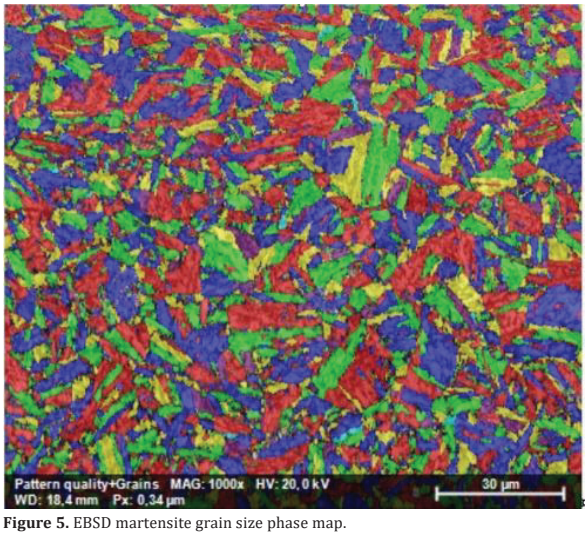


Figure 5. EBSD martensite grain size phase map.

Multitechnique Characterization of CPV-ARI Portland Cement Hydration: A Microstructural and Chemical Approach

Elton Jose de Souza[1*], Marcelo Bortolleto[1], Jorge Luis Akasaki, José Antonio Malmonge, Alex Otávio Sanches[1]

[1] São Paulo State University (UNESP), Faculty of Engineering, Campus of Ilha Solteira, Ilha Solteira, SP, Brazil.
*E-mail: elton.souza@unesp.br

Portland cement is the main binder used in civil construction. Its properties result from complex exothermic hydration reactions, triggered by contact with water [1]. Although widely used in construction, the mechanisms involved in the hydration reactions of Portland cement are not fully known or mapped, and their understanding is fundamental for the development, optimization and control of mixtures and new cementitious compositions. In particular, the in-situ characterization of Portland cement is highly complex, requiring the application of sensitive and complementary techniques capable of monitoring the evolution of the binder's hydration reactions. In this sense, this work aimed to investigate the structural evolution and elemental chemical evolution of this ligand, using the Scanning Electron Microscopy (SEM) technique integrated with Energy Dispersive Microanalysis (EDX), with a special focus on the elementary chemical mapping of the hydrated phases. Combined with the SEM technique, Electrical Impedance Spectroscopy (EI) measurements were also carried out, in order to monitor the hydration of Portland cement, serving as a guide for stopping the reaction at strategic stages for microstructural analysis [2]. To monitor the hydration of Portland cement, Portland cement pastes (CPV-ARI) using a water/binder ratio of 0.4 were produced at room temperature. EI measurements were carried out over 28 days. SEM measurements were carried out in secondary electron mode (SE) based on the inflections of the electrical conductivity derivative curve obtained by EI and at 28 days. In turn, images in backscattered mode (BSE) were performed at 28 days. The images in (SE) mode allowed observing the morphological transition of the cement matrix, from the nucleation of ettringite needles to the precipitation of hexagonal portlandite plates (CH), as well as the nucleation and densification of the C-S-H gel. In the images in BSE mode, through the use of chemical mapping by EDS, they were essential to validate the nature of these hydrated phases, revealing the concentration of elements such as calcium, silicon, aluminum, sulfur and iron in specific microareas. The mapping demonstrated the evolution of the grain-matrix interface, showing the covering of the anhydrous Portland cement particles by the C-S-H gel and the consequent densification of the porous structure [3]. Finally, it was possible to highlight that the SEM images combined with EI allowed a holistic understanding of the hydration of Portland cement over time, as well as analysis of its porous structure

References

[1] M. Jaganmohan, Production volume of cement worldwide from 1995 to 2023, (2024). https://www.statista.com/statistics/1087115/global-cement-production-volume/(accessed May 6, 2026).

[2] M. Bortoletto, A.O. Sanches, J.A. Santos, R.G. da Silva, M.M. Tashima, J. Payá, L. Soriano, M.V. Borrachero, J.A. Malmonge, J.L. Akasaki, New insights on understanding the Portland cement hydration using electrical impedance spectroscopy, Constr. Build. Mater. 407 (2023) 133566.

[3] E. Aprianti, P. Shafigh, S. Bahri, J.N. Farahani, Supplementary cementitious materials origin from agricultural wastes - A review, Constr. Build. Mater. 74 (2015) 176–187. https://doi.org/10.1016/j.conbuildmat.2014.10.010.

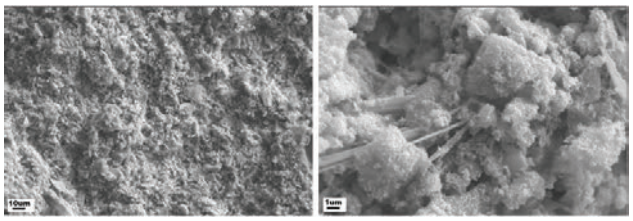


Figure 1. Images of Portland Cement paste with secondary electron detector (SE) after 240 min of hydration with magnification in the same region

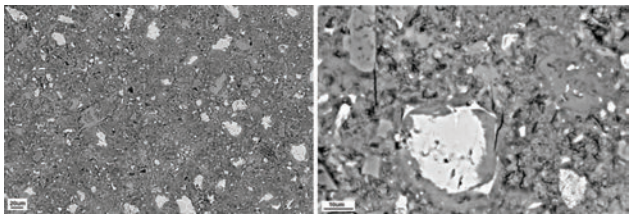


Figure 2. Images of Portland Cement paste with backscattered electron detector (BSE) with 28 days of hydration and magnification in the same region.

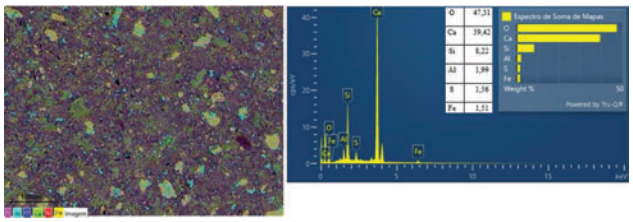


Figure 3. Chemical mapping of Portland cement after 28 days of curing, highlighting the elements Oxygen, Sulphur, Calcium, Aluminum, Silicon and Iron associated with the chemical spectrum of the elements with their respective proportions.

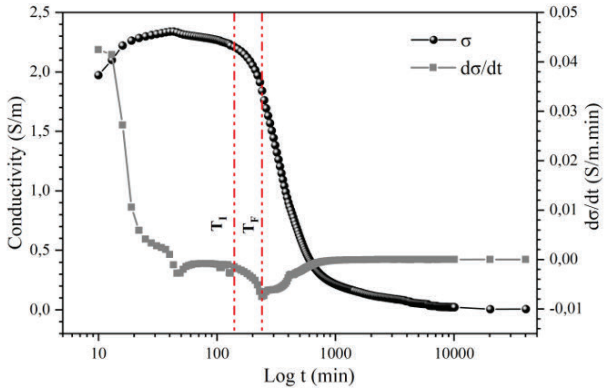


Figure 4. Graph of conductivity and its derivative as a function of time for (CPV-ARI).

Nanostructured $NaNbO_3$ Photocatalysts Grown on Nb Plates and Decorated with Gold Nanoparticles

Leticia Pinheiro Muniz de Carvalho[1*], Thaís Lima de Paiva[1], Beatriz Rodrigues Canabarro[2], Paula Mendes Jardim[1]

[1] PEMM-COPPE/UFRJ; [2] CBPF - Centro Brasileiro de Pesquisas Físicas.
*E-mail: leticia.pinheiro@poli.ufrj.br

Sodium niobate exhibits semiconducting properties that provide it with photocatalytic activity, making it a promising material for applications in hydrogen generation and the degradation of organic pollutants. These applications contribute to strategies aimed at mitigating environmental impacts and producing alternative fuels [1]. Although its photocatalytic efficiency is still limited, the deposition of cocatalysts, particularly noble metal nanoparticles, is among the main strategies used to enhance its performance [2,3]. In this work, a nanostructured $NaNbO_3$ surface was produced from metallic niobium subjected to hydrothermal synthesis in a NaOH solution inside an autoclave, followed by heat treatment. In order to enhance the photocatalytic activity of these nanostructures, gold nanoparticles will be deposited onto the surface by sputtering, to act as cocatalysts. The synthesis conditions were previously studied and optimized, and the following parameters were defined: hydrothermal treatment in an autoclave at 40 °C for 36 hours using a NaOH solution with a concentration of 0.75 $mol \cdot L^{-1}$, followed by heat treatment at 520 °C for 15 minutes under vacuum [4,5]. After synthesis, the surface morphology and phase composition were characterized by scanning electron microscopy (SEM) and grazing-incidence X-ray diffraction (GIXRD). Regarding the deposition of the cocatalyst by sputtering, an experimental design was carried out to evaluate the effect of deposition current and time on the size of the gold nanoparticles. For this purpose, depositions were performed on carbon-coated copper grids under four distinct conditions: 20 mA–5 s, 20 mA–10 s, 10 mA–5 s, and 10 mA–10 s. The samples were analyzed by transmission electron microscopy (TEM), allowing the determination of the particle size distribution and mean particle diameter. SEM images (Fig. 1) of the niobium plate surfaces after hydrothermal treatment followed by heat treatment revealed the formation of a layer of one-dimensional nanostructured $NaNbO_3$. The orthorhombic crystal structure of $NaNbO_3$ was confirmed by grazing-incidence X-ray diffraction. The effect of sputtering parameters on the dimensions of the gold nanoparticles was evaluated through TEM analyses (Fig. 2), which showed that, as expected, both the mean diameter and the most frequent diameter reached maximum values (6.64 nm and 4.26 nm, respectively) under the most severe deposition conditions, and minimum values (2.61 nm and 1.91 nm) under the mildest conditions. In contrast, the particle density per analyzed area showed the opposite behavior, with approximately 160 particles/area for the condition with the highest current and deposition time and 195 particles/area for the mildest condition, indicating a finer and more homogeneous distribution at lower sputtering currents and deposition times. Together, these results establish suitable conditions for the fabrication of Au-decorated $NaNbO_3$ photocatalysts. In the subsequent stage of this research, gold nanoparticles will be deposited directly onto the nanostructured sodium niobate surface using the optimized sputtering parameters identified in this study. The resulting materials will be characterized by TEM analyses of FIB-prepared cross-sectional lamellae to evaluate the distribution of the deposited nanoparticles along the nanoribbons and throughout the thickness of the nanostructured layer. This analysis will contribute to a better understanding of the integration of the cocatalyst within the photocatalytic structure and support the development of more efficient $NaNbO_3$-based photocatalysts [6].

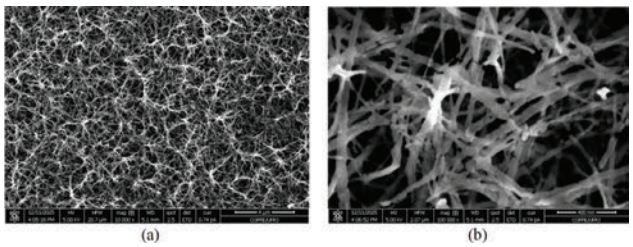


Figure 1. SEM images of the sodium niobate surface showing the nanoribbons in two different magnifications, (a) 10 kx (scale bar: 4 µm) and (b) 100 kx (scale bar: 400 µm).

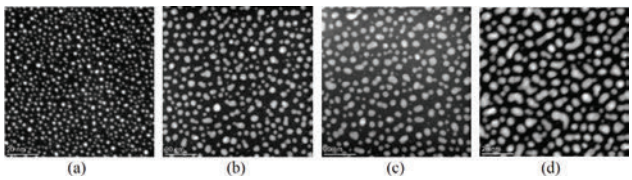


Figure 2. TEM images of the gold nanoparticles deposited on a carbon-coated copper grids with the sputtering conditions of current and time of (a) 20 mA and 5 seconds, (b) 20mA and 10 seconds, (c) 40 mA and 5 seconds and (d) 40 mA and 10 seconds. Scale bars: 20 nm.

References

[1] H. Shi, T. Wang, J. Chen, C. Zhu, J. Ye, Z. Zou, Catal Letters 141 (2011) 525–530.

[2] M. Haruta, Catalysis Today 36 (1997) 153–166.

[3] A. Wolf, F. Schüth, Applied Catalysis A: General 226 (2002) 1–13.

[4] B.R. Canabarro, P.M. Jardim, Advances in Materials Science and Engineering 2018 (2018) 1–9.

[5] Q. Yu, F. Zhang, G. Li, W. Zhang, Applied Catalysis B: Environmental 199 (2016) 166–169.

[6] This research was supported by CNPq (Brazil).

Real-Time Observation of Martensitic Reversibility in a Cu-based Shape Memory Alloy Using In Situ TEM

Gabriela Bugni Ribeiro[1*], Eric Mazzer[1], Lucas Otani[1], Francisco Gil Coury[1]

[1] Federal University of São Carlos (Department of Materials Engineering).
*E-mail: gabrielabugni@estudante.ufscar.br

Shape memory alloys (SMAs) exhibit their functional properties due to a reversible martensitic transformation between martensite, stable at lower temperatures, and austenite, stable at higher temperatures [1]. Although transformation temperatures are usually determined by bulk characterization techniques, direct observation of phase evolution at the microscale is important for understanding the mechanisms involved in transformation reversibility and microstructural stability. In this work, the martensitic–austenitic transformation in a CuAlNiMnNb shape memory alloy was investigated through in situ heating experiments in a transmission electron microscope (TEM). A lamella was prepared by focused ion beam (FIB) milling and welded onto a Protochips heating chip for in situ thermal cycling inside the TEM. Prior to heating, the lamella was extensively characterized by TEM using bright-field (BF) imaging (Fig. 1), energy-dispersive X-ray spectroscopy (EDS), and Automated Crystal Orientation Mapping in TEM (ACOM-TEM, ASTAR). These analyses enabled the identification of the martensitic microstructure and the presence of Cu-rich and Nb-rich precipitates. The sample was then heated up to 475 °C at a rate of 0.25 °C·s^{-1}, with additional ACOM-TEM acquisitions of the same region of interest performed at elevated temperatures, allowing direct comparison of the microstructural evolution throughout the thermal cycle. Cooling was subsequently carried out at 0.75 °C·s^{-1}. Real-time TEM observations showed a gradual reduction of the martensitic lamellae during heating, indicating the occurrence of the martensite-to-austenite transformation. However, the martensitic features did not disappear completely, even at temperatures well above those determined by differential scanning calorimetry (DSC) for the end of the reverse transformation as discussed by Chen and Schuh [2]. This difference suggests that specimen geometry, free-surface effects, and possibly preparation-induced stresses have a significant influence on the transformation behavior of thin TEM samples, leading to a shift in transformation temperatures compared to bulk material. During cooling, martensitic features reappeared, confirming the reversibility of the transformation. In addition, abrupt changes in lamella morphology and apparent orientation were observed, suggesting local accommodation processes during martensite formation. These results demonstrate the usefulness of combining in situ heating TEM and ACOM-TEM to follow phase transformations in shape memory alloys. At the same time, they highlight the difficulties associated with interpreting transformation temperatures obtained from this specimens. The observations also provide insight into the influence of specimen dimensions and surface effects on martensitic transformations studied by advanced electron microscopy techniques [3].

References

[1] Oliveira, J. P., et al. Laser welding of Cu-Al-Be shape memory alloys: Microstructure and mechanical properties. Materials & Design 148 (2018): 145-152.

[2] Chen, Y. and Schuh, C.A., 2011. Size effects in shape memory alloy microwires. Acta Materialia, 59(2), pp.537-553.

[3] This study was financed in part by the Coordenação de Aperfeiçoamento de Pessoal de Nível Superior - Brasil (CAPES) - Finance Code 001

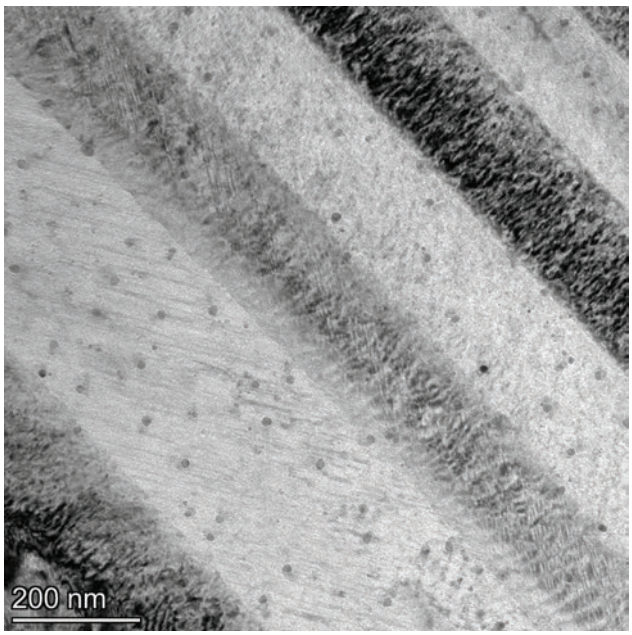


Figure 1. Bright-field TEM image showing martensitic variants and finely dispersed precipitates in the CuAlNiMnNb shape memory alloy.

SEM and nanomechanical AFM Investigation of Recycled PE/PET Blends: Effects of a titanate neoalkoxy compatibilization

Marina E. M. Mergulhão[1*], João Paulo Cosas Fernandes[2], Lucas Henrique Staffa[1,3]

[1] Graduate Program in Materials Science and Engineering, UFSCar, São Carlos, SP, Brazil; [2] Univ. Grenoble Alpes, CNRS, CERMAV, Grenoble, France; [3] Department of Materials Engineering, UFSCar, São Carlos, SP, Brazil.
*E-mail: marina.mergulhao@estudante.ufscar.br

Polyethylene (PE) and polyethylene terephthalate (PET) are widely used in packaging and multilayer films due to their complementary sealability, barrier, and mechanical properties [1]. However, recycling PE/PET mixed waste remains challenging because of their intrinsic immiscibility, leading to phase separation and poor interfacial adhesion. Titanium-based coordination compounds have emerged as promising compatibilizing additives, as they may improve interfacial interactions while also promoting chain re-formation during melt processing, enabling recovery of properties in degraded recycled polymers [2]. In this context, scanning electron microscopy (SEM) and atomic force microscopy (AFM) provide complementary information on morphology and local mechanical behavior. AFM nanomechanical mapping enables phase identification through elastic modulus, adhesion, and deformation contrast, allowing investigation of interphase regions and compatibilization effects [3]. The main objective of this study is to employ SEM and AFM microscopy to investigate the morphology and local nanomechanical properties of post-consumer recycled PE/PET (40/60 wt.%) blends, focusing on the effect of a titanium-based coordination compound on phase dispersion and mechanical response. Post-consumer recycled (PCR) PE and PET blends were processed in a thermokinetic mixer (Drais) for 60s with and without the addition of a neoalkoxy titanate coordination compound (LICA 12). Morphological and nanomechanical characterization were performed using SEM (Philips XL30 FEG) and AFM (Park Systems FX40, PinPoint mode). SEM analysis was conducted on cryogenically fractured samples to evaluate phase morphology and droplet size distribution. For AFM, samples were cryo-ultramicrotomed at −120 °C using a LEICA ultramicrotome. Measurements were performed using AC160TS probes (Park Systems), enabling acquisition of topography, elastic modulus, adhesion, and deformation maps from force-distance curves. Cantilever calibration was performed using a sapphire reference sample, while relative tip radius calibration used PS/LDPE reference samples. Nanomechanical data were processed using MountainsSPIP software, and elastic modulus maps (Fig. 1e, 1f) and histograms (Fig. 1g, 1h) were obtained. SEM results (Fig. 1a, 1b) showed a reduction in droplet size after LICA 12 addition, with average droplet size decreasing from 14.2 ± 10.0 µm to 6.0 ± 3.0 µm. This was accompanied by a narrower droplet size distribution, suggesting a more homogeneous morphology. AFM nanomechanical maps helped to identify the phases and can reveal changes in local mechanical response associated with the compatibilized structure. The SEM/AFM approach linked morphological refinement with nanoscale mechanical response, demonstrating the effect of the coordination compound and its potential for recycling PE/PET blends [4].

References

[1] M. K. Eriksen et al., Waste Manag., 96 (2019) 75.

[2] S. J. Monte, Functional Fillers for Plastics (2010) 91.

[3] J. P. C. Fernandes, et al., Polymer, 146 (2018) 151

[4] This study was financed in part by the Coordenação de Aperfeiçoamento de Pessoal de Nível Superior - Brasil (CAPES) - Finance Code 001. FAPESP grants #2023/05519-6, #2025/04198-7, and #2025/24490-4).

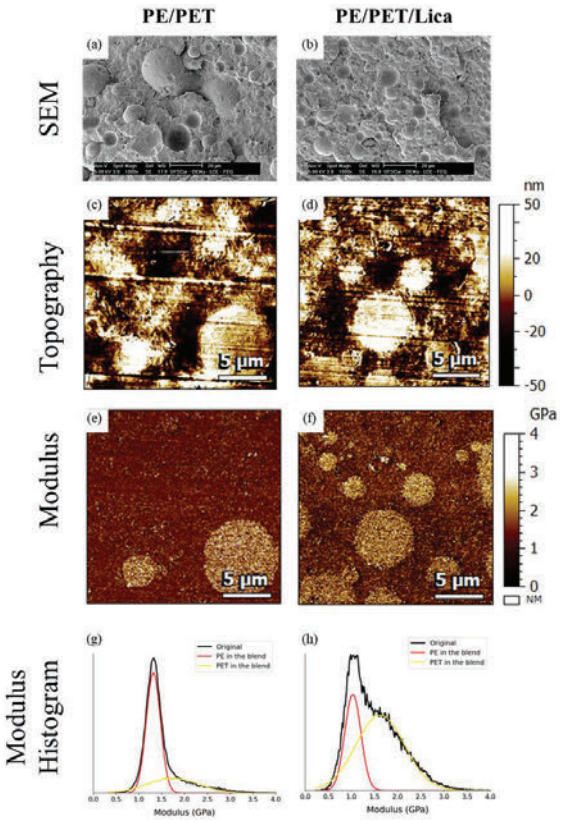


Figure 1. Characterization of post-consumer recycled PE/PET blends without and with titanate-based coordination compound addition, shown on the left and right columns, respectively. (a, b) SEM micrographs of cryogenic fracture surfaces; (c, d) AFM topography images; (e, f) AFM nanomechanical elastic modulus maps; and (g, h) deconvoluted elastic modulus histograms obtained from the corresponding AFM modulus maps.

Structural and Microstructural analysis of the addition of Cu into Zr-25Ta-25Ti alloy

Gabriel E. G. P. Aguillera[1*], Fernanda F. Quadros[1], Vinicius R. M. Gonçalves[2], Gerson S. Almeida[3], Willian F. Zambuzzi[3], Diego R. N. Corrêa[1], Carlos R. Grandini[1]

[1] UNESP - Department of Physics and Meteorology; [2] UFSCar - Department of Material Engineering; [3] UNESP - Institute of Biosciences.
*E-mail: gabriel.aguillera@unesp.br

Titanium and its alloys have been extensively studied in the field of biomaterials due to their high biological and mechanical compatibility in orthopedic and orthodontic applications. Initially, Ti alloys were composed of an α-type crystalline structure, similar to that of commercially pure Ti (Ti Grades 1 to 4). This type of structure presents high ductility and mechanical strength, making it suitable for load-bearing implant applications [1]. Over time, α+β-type alloys gained notoriety due to their higher biocompatibility compared to α-type alloys, with Ti-6Al-4V (Ti Grade 5) being one of the most widely employed orthopedic alloys. However, aluminum and vanadium ions have been detected in the bloodstream of patients with implants and have been associated with a predisposition to Alzheimer's disease and other neurological degenerative conditions [1],[2]. These findings raised significant concerns regarding the long-term safety of such alloys in permanent implant applications. Consequently, new Ti alloys have been developed to improve biocompatibility and mechanical properties while addressing toxic ion release. These alloys, with a β-type crystalline structure, exhibit elastic modulus and hardness values closer to those of cortical bone tissue, thereby reducing the stress shielding effect commonly associated with metallic implants. Additionally, their higher chemical resistance helps prevent the release of potentially harmful ions into the surrounding biological environment. This study analyzes the effect of copper addition on the βZr-25Ta-25Ti alloy system previously developed by P. Kuroda [3]. This system presents well-defined β-type structures (Fig. 1, 3), high biocompatibility and excellent corrosion resistance [3], [4]. The addition of copper, a β-type stabilizer, promoted the formation of CuZr intermetallic compounds (Fig. 2, 4), resulting in a notable increase in both microhardness and elasticity modulus (Table 1), consistent with a second-phase strengthening mechanism. The formation of these intermetallics is driven by the difference in Gibbs free energy between them and compounds within the alloy system [5]. They form both around grain boundaries and within the crystalline matrix, modifying the microstructural arrangement in a manner similar to that observed in low-zirconium Zr-Ta-Ti alloys [3], [4]. These findings suggest that the addition of copper is a promising strategy for tailoring the mechanical and biological properties of β-type Ti alloys for biomedical applications [6].

References

[1] KURODA, D. et al. Mat. Sci. Eng A, v. 243, n. 1-2, p. 244-249, 1998.

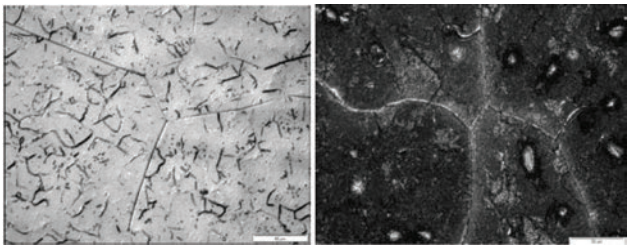
[2] SIDHU, S.S. et al. Materials Science & Engineering C 121 (2021) 111661.

[3] KURODA, P.A.B. et al. J. Mat. Res. Tech., v. 29, p. 4579-4587, 2024.

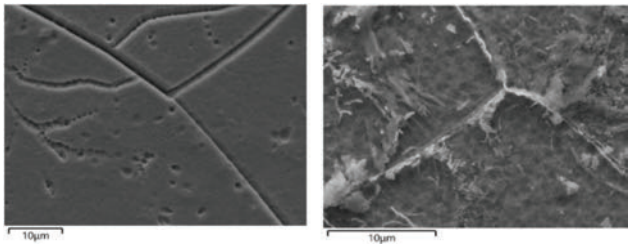
[4] KURODA, P.A.B. et al. Mat. Sci. Forum., 2021. p. 137-144.

[5] TURCHANIN, M.A. et al. Powder Metallurgy and Metal Ceramics, v. 47, n. 7, p. 428-446, 2008.

[6] This research was supported by CNPq and FAPESP (Brazil).



Figures 1 and 2 – Optical Micrographs of Zr-25Ta-25Ti and Zr-25Ta-25Ti-3Cu, respectively.



Figures 3 and 4 – SE Micrographs of Zr-25Ta-25Ti and Zr-25Ta-25Ti-3Cu respectively.

Table 1. Vickers' Microhardness and Young Modulus averages.

Alloy	Assay	Average Values
0% Cu	E-Modulus (GPa)	63,27 ± 9,55
	HV 0,5 (4.903N)	329,1 ± 8,61
3%Cu	E-Modulus (GPa)	96,98 ± 8,55
	HV 0,5 (4.903N)	483,1 ± 9,73

Structural Characterization of the TiVNbCr alloy activated by Pulsed Laser Activation (PLA) method

Ana Rodrigues Cameirão[1*], Juliana M. P. Almeida[1,2], Antônio C. Hernandes[3], Guilherme Zepon[1,2]

[1] Federal University of São Carlos, Graduate Program in Materials Science and Engineering (PPGCEM/UFSCar), São Carlos, SP, Brazil; [2] Federal University of São Carlos, Department of Materials Engineering (DEMa/UFSCar), São Carlos, SP, Brazil; [3] São Carlos Institute of Physics, University of São Paulo, São Carlos, SP, Brazil.
*E-mail: anacameirao@estudante.ufscar.br

Hydrogen storage alloys are promising materials for enabling the energy transition from fossil fuels towards a more sustainable hydrogen-based energy economy. In particular, multicomponent alloys offer a safer and efficient way of storing hydrogen, as they can reversibly react with H_2 to form metal hydrides with tunable hydrogen storage properties. Alloys from the Ti-V-Nb-Cr system, for example, are capable of reversibly storing about 3 wt.% of H under mild pressure and temperature conditions [1]. However, prolonged exposure to air or moisture, due to surface contamination, may prevent hydrogen absorption [2]. In this context, our group was the pioneer in reporting an alternative activation method based on pulsed laser scanning of the alloy surface, named PLA (Pulsed Laser Activation). Although the PLA method proved effective, X-ray photoelectron spectroscopy (XPS) analysis showed an increase of an oxide layer, which is commonly associated with preventing hydrogen dissociation and diffusion into the bulk [1]. Thus, due to this controversial result, the objective of this study was to investigate the PLA process of an equiatomic TiVNbCr alloy for hydrogen storage, advancing the understanding of the mechanisms involved in the PLA method through the surface characterization of powder samples under 5 conditions: i) pristine, ii) aged in water (immersed for 24 h in deionized water), iii) aged in air (30 days exposure to air), iv) after thermal activation (390ºC for 2h under dynamic vacuum), and v) after PLA treatment. These samples were characterized through X-ray Diffraction (XRD), Scanning Electron Microscopy (SEM), Transmission Electron Microscopy (TEM), Energy Dispersive X-ray Spectroscopy (EDX), XPS and hydrogen absorption measurements using a Sieverts-type volumetric apparatus. SEM analysis revealed that the PLA method induces surface modifications such as localized remelting, increased roughness and the formation of holes and cracks, without changing the crystalline structure. To further investigate the surface after PLA, lamellas were prepared by Focused Ion beam (FIB) after carbon sputtering to preserve the surface. Subsequent TEM-EDS analysis of these lamellae (Figure 1) demonstrated that aging in water promoted surface oxidation whereas the PLA process specifically induced the formation of a Ti-rich oxide layer of about 10 nm. This result suggests that this oxide may not act as a barrier for hydrogen absorption, given that the PLA method fully restored the hydrogen storage ability of the TiVNbCr alloy after aging in water, promoting high hydrogen capacity and kinetics, reaching 3 wt.% of H in just one minute. Furthermore, samples subjected to PLA preserved about 70-80% of their hydrogen capacity even after subsequent exposure to water or air, conditions that would normally deactivate the alloy. These results suggest that the Ti oxide may play an active role in the PLA activation mechanism, possibly acting as a catalyst, facilitating hydrogen absorption and dissociation, but also may act as protective barrier against further contamination while remaining permeable to hydrogen, especially in combination with the cracks and defects generated during the PLA method.

References

[1] B.H. Silva et al., Int. Journal of Hydrogen Energy. 31 (2024) 885-890.

[2] A.R. Cameirão et al., Journal of Energy Storage. 161 (2026) 122014.

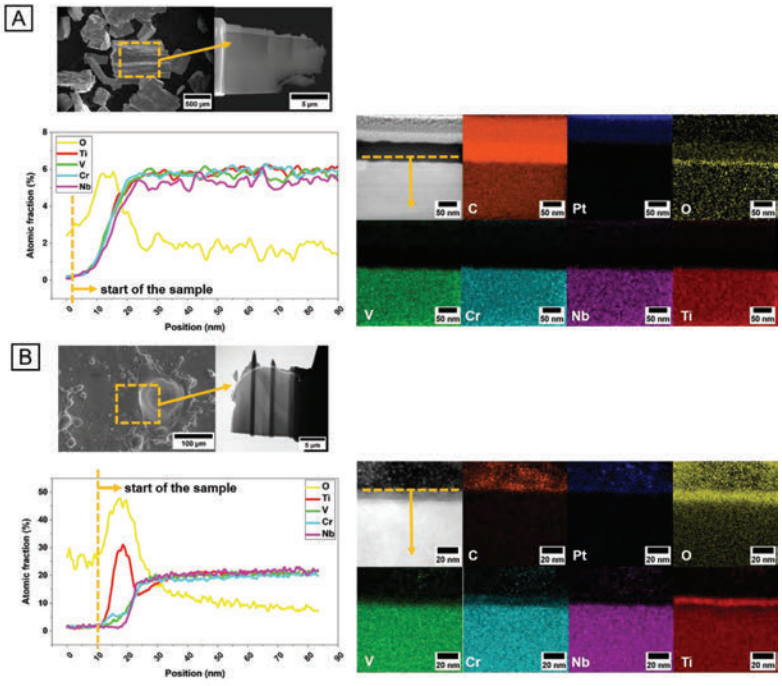


Figure 1. FIB lamellas and TEM-EDS map and quantification of the TiVNbCr alloy (a) aged in water and (b) aged in water + PLA process. The analysis confirm the presence of surface oxides in both conditions and reveal the formation of a distinct 10 nm Ti-rich oxide layer after the PLA method.

Study of intermetallic phase formation in AISI H13 steel used in the HPDC process immersed in molten aluminum

Geovanne S. Santana[1*], Raul E. de Sousa[1], Athos H. Plaine[1]

[1] Universidade do Estado de Santa Catarina – UDESC.
*E-mail: gs3761960@gmail.com

Aluminum and its alloys hold a prominent position in the manufacture of non-ferrous metallic materials, substantially driven by the demands of the automotive sector. The unique properties of aluminum make it an essential material for the modern automotive industry, allowing the creation of lighter, more efficient, safer, and sustainable cars. Currently, among automotive manufacturing processes, High-Pressure Die Casting (HPDC) of aluminum is one of the most prominent technologies, with hypoeutectic alloys of the Al-Si-Cu family being the most used[1,2]. However, the continuous contact between the steel die and the molten aluminum at high pressures and high temperatures triggers what is called die soldering (or mold soldering). This adhesion phenomenon occurs when the aluminum in the alloy reacts with the iron in the matrix, forming layers of brittle intermetallic phases, which are deposited on the mold surface. These intermetallics make it difficult to extract the parts, compromise the surface quality, and drastically reduce the tool life [2,3]. Faced with this challenge, the present work aims to investigate the formation kinetics and morphological evolution of these intermetallic phases formed on the mold surface through an immersion test. H13 steel samples were manufactured in prismatic shapes and immersed in a commercial aluminum alloy bath, maintained at a temperature between 720 °C and 725 °C. The total test time was 16 h, distributed in time intervals for each specimen with exposure times of 1 h, 2 h, 4 h, 8 h, and 16 h. Cooling and metallographic preparation followed the standardized procedure, and Nital 3 % was used for chemical etching; the interface was characterized via Scanning Electron Microscopy (SEM) and Energy Dispersive Spectroscopy (EDS). The results obtained through SEM evidenced the formation of a continuous and heterogeneous intermetallic layer at the mold-aluminum alloy interface at all immersion times. In the initial intervals of 1 h and 2 h, the interface showed the formation of three distinct intermetallic layers, and as time evolved, these layers increased progressively and moved to a five-layer configuration with more complex morphologies. The use of EDS was crucial to perform the chemical mapping of these regions, showing stoichiometric variations between the layers that indicate different concentrations of Fe, Al, and Si. The application of SEM/EDS proved to be fundamental to quantify the growth kinetics and map the stoichiometric variations in the reaction zone. The results obtained allow concluding that the wear of the H13 steel die in the HPDC process is driven by the progressive formation of brittle intermetallic layers [4].

References

[1] HAN, Q. et al., NADCA Transactions, (2015).

[2] SHANKAR, S.; APELIAN, D. Metall. Mater. Trans. B, 33 (2002) 465.

[3] SONG, J. et al., Metall. Mater. Trans. A, 47 (2016) 3163.

[4] The authors acknowledge financial support from CAPES (Coordenação de Aperfeiçoamento de Pessoal de Nível Superior-Brazil) - Finance Code 001; financial support from CNPq (Conselho Nacional de Desenvolvimento Científico e Tecnológico) – RES: N°142084/2024-7; institutional support from UDESC (Universidade do Estado de Santa Catarina) and IFMA (Instituto Federal de Educação, Ciência e Tecnologia do Maranhão); Multi-User Facility infrastructure from Santa Catarina State University's Technological Sciences Center (CMU/CCT/UDESC); and financial support from MOVER Program, Line IV (FUNDEP) – Project 27194*10.

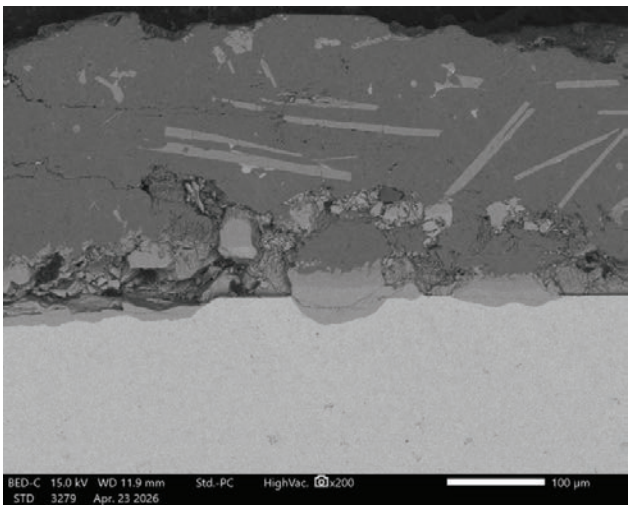


Figure 1. Cross-sectional SEM micrograph (BSE) of the H13 steel interface after 1 h of immersion at 725 °C, highlighting the formation of two distinct intermetallic layers and a third very thin layer adjacent to the substrate.

The BSE-SEM analysis (Fig.1) of the H13 steel after 1 h of immersion revealed an advanced degradation state characterized by a stratified interface. Below the adhered aluminum layer, two distinct intermetallic sublayers were identified, followed by a third very thin layer adjacent to the substrate, evidencing the early stages of atomic diffusion. The reaction zone exhibits a high density of transverse and longitudinal cracks, alongside delamination of the brittle phases. Furthermore, erosive pits were observed on the H13 steel surface, where the chemical attack of the molten alloy disrupted the matrix integrity, marking the onset of tool failure.

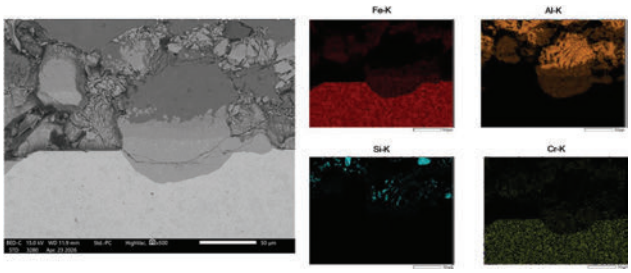


Figure 2. EDS mapping of the cross-sectioned H13 steel sample interface after a 1 h immersion test.

The characteristic X-ray mapping (Fig. 2) identified three main regions within the Fe-Al-Si diffusional layer. The maps for Fe, Al, and Si show distinct concentration plateaus that correlate with the stratified morphology observed in the SEM images. These results corroborate the literature, indicating that the diffusion process at 1 h is already sufficient for the formation of a multiphase zone, in which the solute flux creates favorable conditions for the nucleation of intermetallic phases on the die surface.

Study of the Topography and Chemical Composition of Coatings Produced on Titanium by Micro-Arc Oxidation

Giovana Collombaro Cardoso[1,2*], Manuel Amado Rodas O'Meany[2], Angel Vicente Escuder[2], Carlos Roberto Grandini[1], Vicente Amigó-Borras[2]

[1] UNESP – Univ. Estadual Paulista, Laboratório de Anelasticidade e Biomateriais, Bauru, Brazil; [2] UPV - Universitat Politècnica de València, Materials Technology Institute (ITM), Valencia, Spain.
*E-mail: giovana.collombaro@unesp.br

Titanium is already a well-established biomaterial for implant production [1]. However, numerous studies continue to seek improvements in its surface properties to enhance osseointegration and increase resistance to corrosion and wear [2]. The growing demand for coatings with controlled properties has driven the development and optimization of electrochemical surface modification processes. In this context, several parameters, such as applied voltage and current, as well as deposition time, directly influence the morphology, chemical composition, and thickness of the resulting coatings [3]. Therefore, microscopic characterization is essential to understand the relationship between processing conditions and coating properties. The objective of this study was to investigate how the properties of coatings produced by Micro-Arc Oxidation (MAO) vary as different oxidation parameters are modified. The coatings were produced by varying the applied voltage (200, 250, 300, and 400 V), the electrode spacing (1, 3, 5, and 7 cm), and the oxidation time (1, 2, and 3 minutes). The parameters kept constant in all experiments were the electrolyte solution (composed of calcium acetate, magnesium acetate, and disodium β-glycerophosphate), the current (4 A), and the sample dimensions (commercially pure titanium plates measuring 10 × 15 × 1.5 mm^3).The analyses included evaluation of surface topography and cross-sectional morphology by Scanning Electron Microscopy (SEM) and chemical composition by Energy-Dispersive Spectroscopy (EDS). The results showed that coatings exhibiting the volcano-like morphology typical of most MAO coatings appeared in samples treated at voltages of 250 V and above (Fig. 1b). In contrast, samples produced at 200 V displayed a slightly different morphology (Fig. 1a). Oxidation time influenced the coating thickness and, in some cases, made the coatings more fragile. On the other hand, shorter electrode spacing led to greater coating instability. Overall, the results were important in improving the understanding of the behavior of MAO coatings under the influence of various processing parameters.

References

[1] G.C. Cardoso, P.A.B. Kuroda, C.R. Grandini, Journal of Materials Research and Technology, 25, 3061-3070 (2023).

[2] X.e. Zhang, W. Zhou, W. Xi, Frontiers in Chemistry, 12 (2024).

[3] G. Li, F. Ma, P. Liu, S. Qi, W. Li, K. Zhang, X. Chen, Journal of Alloys and Compounds, 948, 169773 (2023).

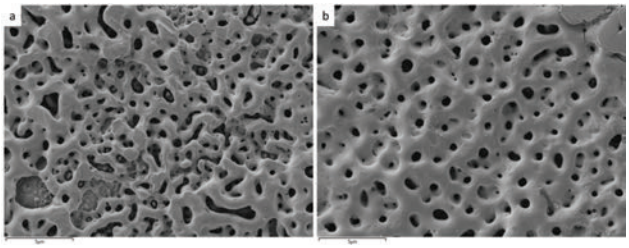


Figure 1. SEM Images of the coatings' topography produced by Micro-Arc Oxidation with 200 V (a) and 250 V (b).

Sunlight-Photoresponsive Nanostructured Lipid Carriers for the Controlled Release of Agrochemicals

Beatriz A. Riga-Rocha[1*], Mariana M. L. H. Forini[1], Luiz A. F. Cavalcante[1], Rosangela S. Laurentiz[1], María E. Taverna[2,3], Renato Grillo[1*]

[1] São Paulo State University (UNESP), Faculty of Engineering, Department of Physics and Chemistry, Ilha Solteira, SP, Brazil; [2] Instituto de Desarrollo Tecnológico para la Industria Química (INTEC), Universidad Nacional del Litoral (UNL), Consejo Nacional de Investigaciones Científicas y Técnicas (CONICET), Santa Fe, Santa Fe, Argentina; [3] Facultad Regional San Francisco, Universidad Tecnológica Nacional (UTN), San Francisco, Córdoba, Argentina.
*E-mail: riga.rocha@unesp.br; renato.grillo@unesp.br

Luminescent radiation, especially ultraviolet light, is among the most widely investigated stimuli for triggering the controlled release of agrochemicals [1]. However, research on photoresponsive release often yields systems that are activatable only at very specific wavelengths [2], hindering their implementation for large-scale cultivation and confining these technologies to greenhouse conditions, where the incident light can be modulated as needed. Against this background, we aimed to develop a photoresponsive nanocarrier that wasn't limited to artificial light sources. Accordingly, our sunlight-photoresponsive nanostructured lipid carrier (p-NLC) was designed. This photoresponsive NLC is composed of tripalmitin, Myritol® 318, and a novel amphiphilic dye (derived from methyl red), which was designed to be the photoactivator for the controlled release of the model agrochemical, atrazine (ATZ). The formation and photoresponsiveness of the lipid nanoparticles (p-NLC:ATZ) were assessed by FTIR and UV-Vis (Figure 1), revealing that the amphiphilic dye was successfully incorporated into the NLC structure and that its presence sensitized p-NLC:ATZ to sunlight. The DLS analysis of p-NLC:ATZ revealed nanoparticles with a hydrodynamic diameter of 324.7 nm (± 8.7) and a PDI of 0.110 (± 0.073), featuring high colloidal stability with a zeta potential value of −15.93 mV (± 0.70). The SEM characterization of the pristine p-NLC:ATZ (Figure 2A) revealed nanocarriers with spherical morphology and slightly irregular surfaces. The ATZ kinetic release study of both pristine and sunlight-exposed p-NLC:ATZ was conducted using a two-compartment device and quantified by UV-Vis analysis. The release process was assessed for approximately 17,000 min. Pristine p-NLC:ATZ reached a maximum ATZ release of 26% (±0.139), whereas the sunlight-exposed p-NLC:ATZ released 36% (±0.01) of its ATZ content. These values indicate that the liberation of ATZ from p-NLC nanocarriers is directly affected by sunlight exposure. This observation is supported by analysis of SEM images of the nanocarriers after the release study (Figures 2B and 2C). The microscopy results indicate that after the release assay, the nanocarrier's structure is more relaxed and less turgid, as a direct consequence of the release process. However, the main structure of the p-NLC:ATZ, which wasn't exposed to the sunlight (Figure 2B), seems more preserved than the irradiated p-NLC:ATZ (Figure 2C), whose aspect is more deteriorated. These observations are pieces of evidence that p-NLC is indeed a photorresponsive nanostructured lipid carrier with an agrochemical liberation process that might be modulated by exposure to the Sun [3].

References

[1] M. Shen et al. **Eco-Environment & Health**, 2 (2023) 161.

[2] N. Fomina et al. **Advanced Drug Delivery Reviews** 64 (2012) 1005.

[3] This research was supported by FAPESP (#2022/03219-2; #2023/00541-3; #2023/17369-9; #2023/09217-4) and CNPq (#310846/2022-6; 150759/2024-0).

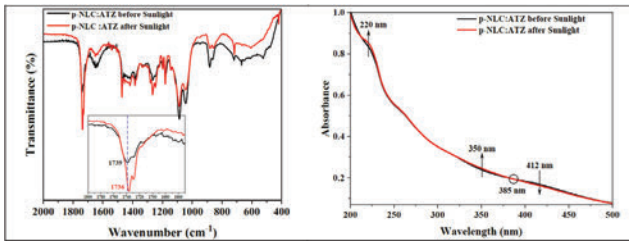


Figure 1. FTIR (left) and UV-Vis (right) spectra of p-NLC:ATZ before and after 6 hours of exposure to sunlight.

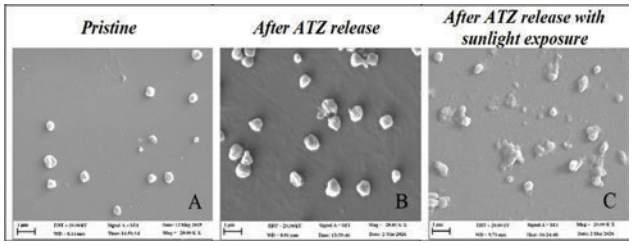


Figure 2. Scanning Electron Microscopy images of p-NLC:ATZ under different conditions.

Surface Modification of Bioabsorbable Mg-8Li-1Y and Mg-1Zn-0.4Ca Alloys by Micro-Arc Oxidation for Temporary Implant Applications

Matheus Henry da Silva[1], Denize Maria S. e Silva [2], Daniel G. S. dos Santos [2], Peter Minarik [3], Danielle C. C. Magalhães[1], Conrado R. M. Afonso[1]

[1] BioMet-CAM, Department of Materials Engineering (DEMa), Universidade Federal de São Carlos (UFSCar), 13.565-905, São Carlos/SP, Brazil; [2] Graduate Program in Materials Science and Engineering (PPGCEM), Federal University of São Carlos (UFSCar), São Carlos/SP, Brazil; [3] Charles University (CUNI), Department of Physics of Materials, Ke Karlovu 5, 12116 Prague, Czechia.
*E-mail: conrado@ufscar.br

Magnesium (Mg)-based alloys have attracted attention due to their high biocompatibility and low Young's modulus (45–60 GPa), which is closer to that of bone tissue (45 GPa) than that of traditional metallic alloys (> 100 GPa) [1]. These characteristics make Mg and its alloys promising candidates for temporary applications in the human body, where the material must function during tissue regeneration and subsequently degrade in a controlled manner. However, the high corrosion rate of these alloys in physiological environments remains an important challenge, as it may compromise the mechanical integrity of the implant before complete tissue recovery. Therefore, this study aimed to evaluate the effect of surface modification by micro-arc oxidation (MAO) [2], an electrochemical process capable of forming adherent, porous, oxide-rich ceramic coatings, on Mg-8Li-1Y (LW81) and Mg-1Zn-0.4Ca (Zx10) alloys. The objective was evaluating MAO coating and effect of bioactive ions, contributing to the reduction and/or modulation of the corrosion rate and to the improvement of the interaction between the material and the biological environment. The Mg alloys were produced by melting pure magnesium (99.96%), Mg-28.1Y, and Mg-20Li master alloys (wt.%) argon atmosphere. They were subsequently processed by severe plastic deformation by ECAP technique. After metallographic preparation, the surfaces were modified by MAO in an aqueous electrolyte based on anhydrous potassium phosphate (K_3PO_4), at a concentration of 12.6 g/L and pH ≈ 12. Figure 1 shows the experimental setup. The electrical power supply was operated in pulsed current mode, with a frequency of 1000 Hz, and a maximum voltage of 300 V. There is an increase in Vickers microhardness after MAO, from 65 to 90 HV for the ZX10 alloy and from 57 to 91 HV for the LW81 alloy. MAO coating showed a reduction in contact angle, with greater surface wettability, which may favor cell adhesion, as shown in Table 1. X-ray diffraction (XRD) showed MAO layer phases, such as MgO, as well as the $Mg_3(PO_4)_2$ phase, confirming the incorporation of bioactive species into the coating. The porous morphology of the MAO layer can be observed in Figs 2.c and 2.e. MAO coating presents random pores, with diameters of a few micrometers. The coating thickness values and pore sizes are shown in Table 2. Fig. 3 shows STEM-HAADF analysis of the interface between the upper layer of the MAO coating, with the oxide and bioactive ions, and the denser lower layer, predominantly of MgO [3][4].

References

[1] Staiger, M. P. et al., "Magnesium and its alloys as orthopedic biomaterials: A review," *Biomaterials*, 27, 1728–1734, 2006

[2] Vertaľ, J. et al., "Improving Biodegradable Mg-Zn(-Ca) Alloys by Surface Treatment via Plasma Electrolytic Oxidation," *Materials*, 18, 747, 2025.

[3] Yue, X. et al., "SLM Magnesium Alloy Micro-Arc Oxidation Coating," *Materials*, 17, 4988, 2024

[4] This research was supported by FAPESP PAIP 2023/16836-2 and partially supported by CAPES, Finance Code 8888.976486/2024-00 (Brazil).

Table 1. Contact angle values of the ZX10 and LW81 Mg alloys before and after MAO treatment.

Alloy	Contact angle	Contact angle -MAO
Zx10	73±5	45±4
LW81	64±2	51±3

Table 2. Coating thickness and pore size of the ZX10 and LW81 Mg alloys after MAO treatment.

Alloy	Thickness (µm)	Pore size (µm)
Zx10	22±6	1.2 ±2.5
LW81	17±3,5	0.7±3.1

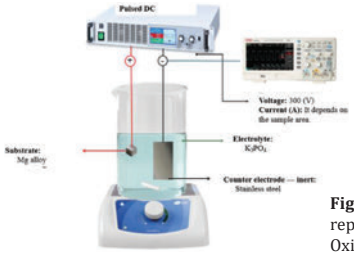


Figure 1. Schematic representation of the Micro-Arc Oxidation (MAO) system.).

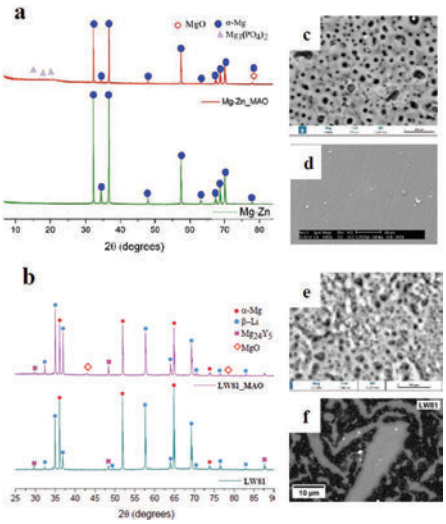


Figure 2. XRD patterns of the ZX10 and LW81 alloys before and after MAO treatment: **(a)** ZX10 alloy in the substrate condition, in green, and after MAO, in red; **(b)** LW81 alloy in the substrate condition, in green, and after MAO, in pink. SEM-BSE images of the substrates before modification: **(d)** ZX10 and **(f)** LW81. SEM-BSE images of the surfaces after MAO: **(c)** ZX10 and **(e)** LW81.

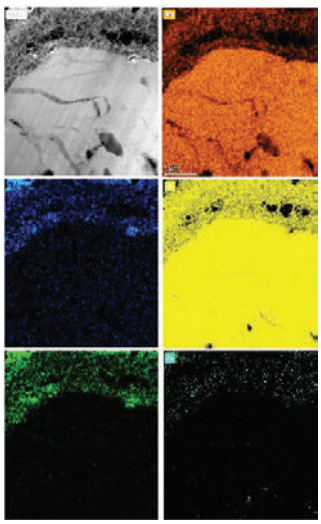


Figure 3. STEM-HAADF micrograph, high-angle annular dark-field, followed by EDS elemental mapping obtained after in situ FIB lift-out lamella preparation of the MAO-treated Mg-1Zn-0.5Ca alloy.

Surface modification of Ti-25Ta-xNb alloys by micro arc oxidation for biomedical applications: microstructural characterization, bioactivity, and antimicrobial activity

Fernanda de Freitas Quadros[1]*, Diego Rafael Nespeque Corrêa[1],Carlos Roberto Grandini[1]

[1] UNESP: São Paulo State University, Laboratory of Anelasticity and Biomaterials, Bauru, SP, Brazil, and CMDTA, Multidisciplinary Center for Assistive Technology, Bauru, SP, Brazil.
*E-mail: ff.quadros@unesp.br

Titanium (Ti) is widely used in the development of metallic alloys due to its good biocompatibility, high corrosion resistance, and excellent strength-to-weight ratio [1]. It is also an allotropic element, which can form different crystalline structures depending on the alloying elements added. Niobium (Nb) and tantalum (Ta), similarly recognized for their biocompatibility and corrosion resistance, act as beta-phase stabilizers when incorporated into Ti alloys, reducing the beta transus temperature and favoring the production of alloys whose elastic modulus is close to that of cortical bone, thereby minimizing the risk of bone resorption [2]. In this context, the micro arc oxidation (MAO) technique stands out as a promising alternative for the surface treatment of such alloys, as it enables the formation of a thin oxide layer incorporating bioactive elements from the electrolyte [3]. The combination of low-elastic-modulus alloys with bioactive coatings supports the development of surfaces that promote osseointegration and exhibit antimicrobial activity. On this basis, the present study aimed to produce biofunctionalized coatings containing Ca, P, Mg, and Ag on alloys of the Ti-25Ta-xNb system (x = 10, 20, and 30 wt.% Nb), assessing the influence of the microstructure and of the applied anodic potential (200, 250, and 300 V) on coating formation. The results showed that increasing the voltage raises the energy of the microdischarges, producing more uniform and porous coatings [3]. Electron microscopy analyses revealed that the alloy with 10 % Nb, in which the α″ phase prevails, exhibited greater porosity than the β alloys (20 % and 30 % Nb), evidencing the direct relationship between the microstructural phase and the morphology of the coating [3]. X-ray diffraction (XRD) analyses identified the anatase and rutile phases of TiO_2, with the rutile fraction increasing as the applied voltage was raised [3]. Biological assays demonstrated that the Ti-25Ta-xNb alloys treated by MAO were non-cytotoxic to stem cells and effective against E. coli, S. aureus, P. aeruginosa and E. faecalis, with the most promising performance observed for the Ti-25Ta-30Nb composition treated at 300 V. The results confirm that surface modification by MAO, combined with the controlled addition of Nb, makes it possible to obtain coatings with good adhesion and biocompatibility, highlighting their potential for biomedical applications [4].

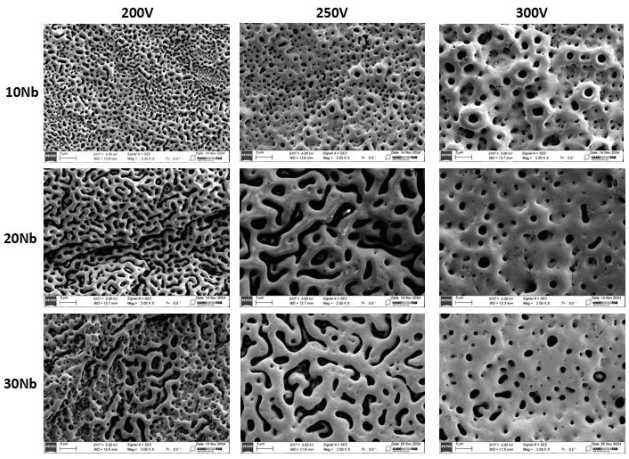


Figure 1. SEM micrographs of the oxide layers obtained by MAO treatment.

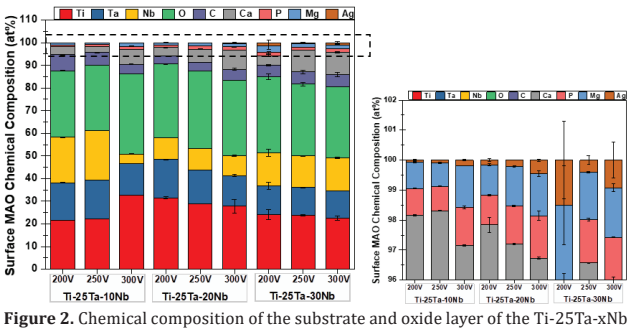


Figure 2. Chemical composition of the substrate and oxide layer of the Ti-25Ta-xNb alloys processed at different anodic potentials.

References

[1] Pesode, P. and S. Barve, *A review—metastable β titanium alloy for biomedical applications.* Journal of Engineering and Applied Science, 2023. **70**(1): p. 1-36.

[2] de Freitas Quadros, F., et al., *Chemical, structural, microstructural, mechanical, and biological characterization of Ti–25Ta-xNb system alloys for biomedical applications.* Journal of Materials Research and Technology, 2024. **28**: p. 3699-3706.

[3] Quadros, F.d.F., et al., *Surface Characteristics of TiO2 Coatings Formed by Micro-Arc Oxidation in Ti-25Ta-x Nb Alloys: The Influence of Microstructure and Applied Voltage.* Coatings, 2025. **15**(6): p. 730.

[4] The authors gratefully acknowledge financial support from the Brazilian funding agencies FAPESP, CAPES, and CNPq.

Synthesis and characterization of mesoporous silica nanoparticles with potential application in agriculture

Rafaela de Souza Mendonça[1], Érica Rennó Biscalchim[1], Mariana Monteiro de Lima Honorato Forini[1], Beatriz Aline Riga-Rocha[1], Renato Grillo[1*]

[1] São Paulo State University (UNESP), Faculty of Engineering, Department of Physics and Chemistry, Ilha Solteira, SP, Brazil.
*E-mail: renato.grillo@unesp.br

The growing population increase, combined with imminent environmental crises, has driven the search for new approaches and technologies aimed at more efficient and sustainable agricultural production, as well as contributing to the achievement of the Sustainable Development Goals (SDGs) proposed by the United Nations (UN) [1]. Given the current scenario, nanotechnology has gained prominence as a promising alternative for innovative and technological applications that adopt a more sustainable approach to increasing food production [2]. Nanoparticles made from inorganic materials, such as mesoporous silica nanoparticles, can add value to agricultural systems due to their high pore volume, controllable pore diameter, small size, and large surface area. Additionally, they exhibit high synthesis precision and purity, ensuring high physical-chemical and thermal stability [3], which are essential aspects for maintaining the system's viability over time. These nanoparticles are capable of slowly and gradually releasing and delivering active ingredients, such as pesticides and fertilizers [3]. In this work, mesoporous silica nanoparticles were synthesized using the Stöber method [4], with some modifications: initially, a solution containing ethanol, deionized water, CTAB, tetraethyl orthosilicate (TEOS), and ammonium hydroxide was prepared. Then, the solution was stirred for some hours, and after this period, the resulting white precipitate was subjected to centrifugation and washed with deionized water to remove excess reagents. Subsequently, the sample was dried in an oven and calcined in a muffle furnace, resulting in powder nanoparticles. The obtained nanoparticles were characterized by X-ray Diffraction (XRD), Fourier Transform Infrared Spectroscopy (FTIR), Scanning Electron Microscopy (SEM), and Transmission Electron Microscopy (TEM), and the analyzed results demonstrated spherical morphology (Figures 1-A, B, and C), satisfactory features in the XRD and FTIR analyses, where the XRD showed a broad peak around 22º, indicating an amorphous nanoparticle (Figure 1-E), and typical FTIR peaks, compatible with data available in the literature (Figure 1-D). Furthermore, the results obtained by TEM revealed and confirmed the amorphous nature of the nanoparticles (Figure 2. A), their spherical morphology (Figure 2-B), and porosity (Figure 2-C); additionally, they also demonstrated high purity in the synthesis through chemical mapping (Figures 2-D, E, and F) [5].

References

[1] P.H.C. Lima et al. Frontiers in Nanotechnology. 3 (2021) 809329.

[2] N. Thakur, A.N. Yadav. BioNanoScience. 15 (2025) 243.

[3] H.I. Hussain et al. Journal of Nanoparticle Research. 15 (2013) 1676.

[4] Y. Zhang et al. Applied Surface Science. 276 (2013) 769–775.

[5] This study was financed in part by the Coordenação de Aperfeiçoamento de Pessoal de Nível Superior - Brasil (CAPES) – Finance Code 001; and this research was supported by FAPESP (#2022/03219-2) and CNPq (#310846/2022-6; #150759/2024-0).

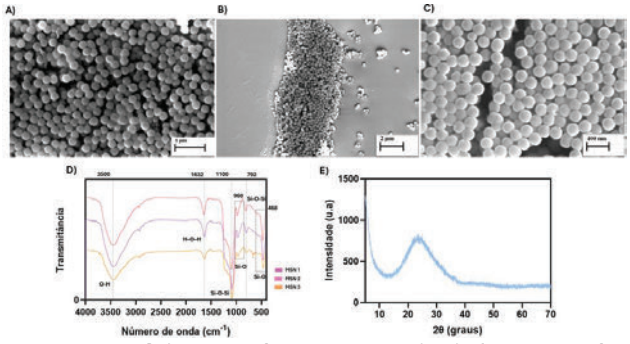


Figure 1. A, B, and C) Scanning Electron Microscopy (SEM) of mesoporous silica nanoparticles. **D)** Fourier Transform Infrared Spectroscopy (FTIR) of mesoporous silica nanoparticles.; **E)** X-ray Diffraction (XRD) of mesoporous silica nanoparticles.

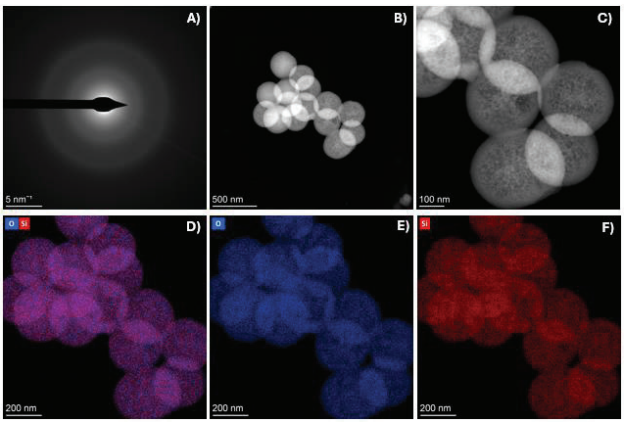


Figure 2. Transmission Electron Microscopy (TEM) images of mesoporous silica nanoparticles. **A)** Electron diffraction; **B)** Morphology; **C)** Porosity; **D)** Mapping; **E)** Oxygen composition in the sample; **F)** Silicon composition in the sample.

Synthesis and Microstructural Analysis of Ti-Nb Based Composites for Orthopedic Implants

Carlos Eduardo da Silva[1], Vinícius Richieri Manso Gonçalves[2], Carlos Roberto Grandini[1], Gerson Santos de Almeida[3], William Fernando Zambuzzi[3], Sophia Alexandra Tsipas[4], Paulo Noronha Lisboa-Filho[1], Diego Rafael Nespeque Corrêa[1]

[1] São Paulo State University (UNESP), School of Sciences, Campus Bauru, Laboratory of Anelasticity and Biomaterials, Bauru, SP, Brazil; [2] Federal University of São Carlos (UFSCar), Department of Materials Engineering, São Carlos, SP, Brazil; [3] São Paulo State University (UNESP), Institute of Biosciences, Campus Botucatu, Department of Chemistry and Biochemistry, Bauru, SP, Brazil; [4] University Carlos III of Madrid, Department of Materials Science and Engineering, IAAB, Leganés, Spain

Recently, Ti-Nb alloys have shown promise for orthopedic implants, as the combination of titanium's and niobium's properties enhances the implant's biocompatibility [1]. However, with constant use of the implant, the material eventually wears down, leading to various problems, such as implant loosening or even issues with ion release into the body [2], [3]. Based on this, the project aims to evaluate the Ti-Nb alloy reinforced with boron carbide (B_4C), which improves wear resistance; in addition, the reinforcement increases the alloy's Vickers hardness and reduces its modulus of elasticity. In this case, a combination of ceramic and metal properties makes it hard yet malleable; furthermore, the Titanium Matrix Composite (TMC) also demonstrated good biocompatibility. The alloys were produced by electric arc melting; in this process, B_4C reacts with titanium, forming titanium carbide (TiC) and titanium boride (TiB), thereby hardening the phases. Figure 1 shows scanning electron microscopy (SEM) images and optical microscopy images. Figure 2 shows the transmission electron microscopy (TEM) image, in which EDS analysis was performed in the region of interest to identify which structure represents TiC and which represents TiB. Furthermore, the alloy's microstructure could be observed in greater detail; in addition, ASTAR analysis was performed, as shown in Figure 3, which confirms the observed microstructure [4]. Keywords: Biomaterials, metal matrix composites, mechanical behavior, wear resistance.

References

[1] M. Z. Al Mahmud, M. H. Mobarak, N. Hossain, M. A. Islam, and M. T. Rayhan, "Emerging breakthroughs in biomaterials for orthopedic applications: A comprehensive review," Dec. 01, 2023, *Elsevier B.V.* doi: 10.1016/j.bprint.2023.e00323.

[2] M. M. Soliman *et al.*, "Stress transfer, stress shielding, and micro-movement analysis in the implanted femoral bone region with various hip implant stem materials: A finite element approach," *Mater. Today Commun.*, vol. 41, Dec. 2024, doi: 10.1016/j.mtcomm.2024.110932.

[3] V. R. M. Gonçalves *et al.*, "Micro-arc oxidation treatment applied on the surface of β Ti[sbnd]Nb matrix composites as a strategy to modulate cellular behavior," *Surf. Coat. Technol.*, vol. 506, Jun. 2025, doi: 10.1016/j.surfcoat.2025.132113.

[4] Financial support: FAPESP #2026/07285-0, #2024/19591-3, #2024/03308-0.

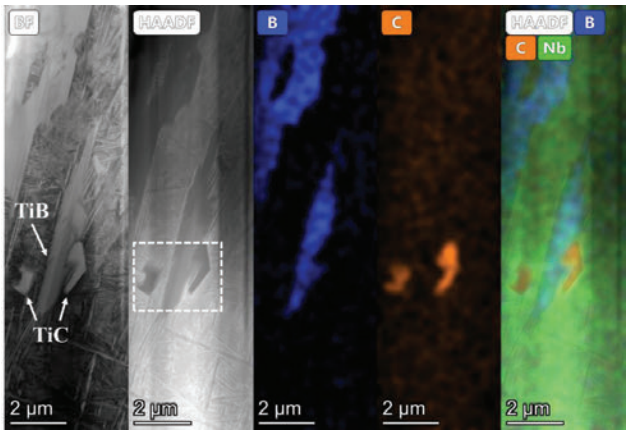


Figure 2. Chemical elemental mapping of the FIBed 5% lamella acquired STEM-BF and STEM-HAADF modes.

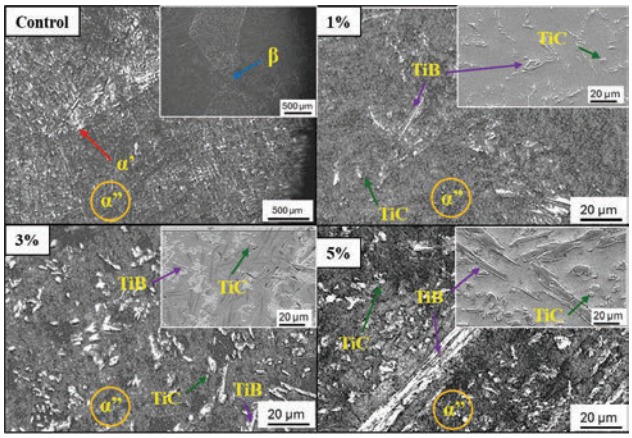


Figure 1. Microstructural analysis of the TMC samples under optical imaging

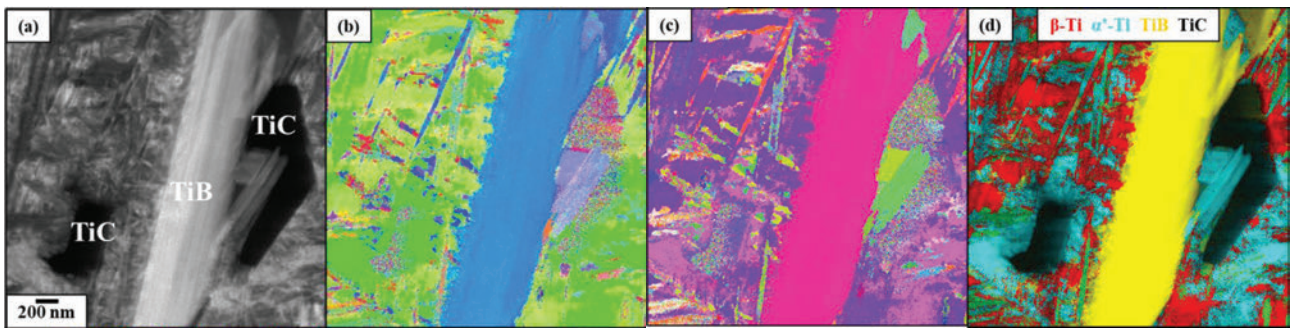


Figure 3. TEM-ASTAR analysis of TMC samples of Ti-15Nb alloy matrix with 5% B_4C addition

Tracking Impact and Expanding Access in a Core Microscopy Facility: The LIMicro-IQ Experience

Hugo C. Loureiro[1*], Leandro de Abreu[1], Raquel E. Miller[1], Rene A. N. Silva[1], Ana Flávia Nogueira[1], Camila A. Rezende[1], Daniela Zanchet[1]

[1] Institute of Chemistry, Universidade Estadual de Campinas.
*E-mail: hugocl@unicamp.br

The LIMicro-IQ (Microscopy Core Facility of the Institute of Chemistry, UNICAMP, https://www.iqm.unicamp.br/institucional/infraestrutura/cemuiq/limicro/, part of the Unicamp Microscopy Network (RMU), supports a wide range of research groups, external institutions, and industry partners through its advanced microscopy infrastructure. The facility houses a Quanta FEG 250 SEM (Thermo Fisher Scientific), a FlexAFM system (Nanosurf) with electrical modes (KPFM, c-AFM), and a MicroTime 200 confocal system (PicoQuant), for advanced time-resolved fluorescence techniques (TCSPC, FLIM, FRET, FCS). Complementary infrastructure includes a sputter coater, an ultramicrotome, and a cryo-ultramicrotome. At LIMicro, microscopy techniques are applied to a diverse range of materials, including photovoltaic materials, catalysts, thin films, nanoparticles, environmental samples, biological specimens, and soft matter such as polymers and cellulose derivatives. Recent years have shown increasing demand for STEM-in-SEM imaging using the Quanta FEG 250, which offers the highest resolution on the instrument and is used for particle size analysis, morphological evaluation, and pre-screening for TEM. There is also growing interest in analyzing biological and high-water-content materials, such as hydrogels, which are often incompatible with high vacuum. The Quanta's environmental SEM (ESEM) mode, which uses water vapor in the chamber, enables the analysis of these delicate samples and allows in-situ studies of dynamic transformations—e.g., hydration and degradation of perovskites—providing valuable nanoscale insights. To ensure consistent infrastructure management and broad access, all multiuser instruments at IQ-UNICAMP are housed in Institutional Laboratories, with centralized scheduling through a public online booking system. This allows both internal and external users to view equipment calendars and usage history, supporting transparency and efficient resource utilization. Between 2022 and mid-2026, more than 6000 instrument hours were logged at LIMicro. During this period, access was offered to over 100 internal users from 40 research groups at IQ-UNICAMP and 15 from IFGW-UNICAMP (Institute of Physics Gleb Wataghin), as well as to external academic and industrial clients via the *Central Analítica* system. Industry collaborations accounted for 20% of total usage, with 43% from pharmaceutical, 17% chemical, 12% automotive, and 13% other sectors. External academic access included six UNICAMP institutes/engineering schools and ten other Brazilian research institutions. In 2024, the facility implemented a revised training protocol, which includes preparatory study materials and a written evaluation required before hands-on training. Post-training assessments are completed via online forms, enabling technical staff to track user progress and support autonomy. The number of trained users has increased from 15 to 44 on SEM, and from 0 to 16 on AFM between late 2022 and mid-2026. As part of its training strategy, LIMicro also organizes courses, seminars, and hands-on workshops, with active participation from the technical team. These initiatives aim not only to expand the user base but also to enhance user qualification and promote more effective experimental design and data interpretation. LIMicro is actively involved in scientific outreach, including live demonstrations of optical and electron microscopy (via remote SEM access) at events such as *UNICAMP de Portas Abertas*, *Ciência e Arte nas Férias* and *Futuras Cientistas*, designed to engage students and the public in scientific thinking and instrument-based discovery.

A key innovation in facility management was the implementation of a Research Resource Identifier (RRID: SCR_024633) in early 2024, to address the challenge of quantifying core facility impact. Citation models and experimental procedure templates were developed for each equipment mode and made available via QR codes, email signatures, and the LIMicro website. In 2 years, 27 publications have cited the facility using its RRID. This system has greatly simplified publication tracking and was extended to other institutional laboratories at IQ as part of a broader citation policy. The LIMicro experience illustrates how strategic infrastructure management and active user engagement can maximize the research and societal impact of microscopy core facilities [2].

References

[1] The LIMicro infrastructure was funded by FAPESP, CNPq and PRP-Unicamp

[2] The authors thank LIMicro (RRID:SCR_024633) from CEMUIQ-UNICAMP for technical support.



Figure 1. LIMicro page on Core Marketplace.

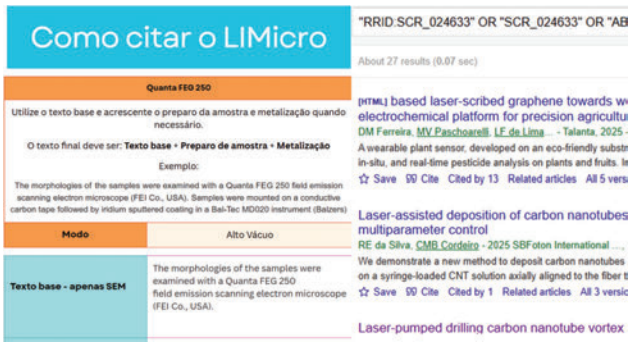


Figure 2. Citation model for the Quanta FEG 250 (left) and RRID-based search on Google Scholar (right), illustrating the implementation and traceability of facility usage (RRID: SCR_024633).

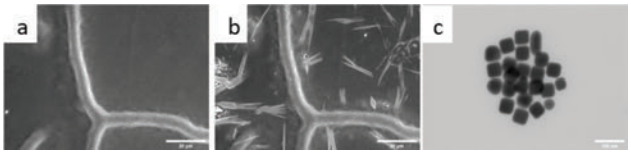


Figure 3. Examples of LIMicro applications: a) ESEM image of perovskite at 60% RH – time 0 min; b) ESEM image of perovskite at 60% RH after 15 min; c) STEM-in-SEM image of AuNP

Use of SEM imaging to characterize the effect of adding helium to the welding gas in TIG welding of superduplex stainless steel - XII MICROMAT 2026

Diel Silva Botão[1*], Eustáquio de Souza Baêta Junior[1], Camila Alves Pelicarto da Silva Botão[1], Frederico Garcia Bindi de Lacerda[1], Jonas Gabriel Ramos da Silva Ataliba[2], André Rocha Pimenta[1,2]

[1] Programa de Pós-Graduação em Engenharia Mecânica (PPG-EM) – Universidade do Estado do Rio de Janeiro;
[2] Laboratório de Instrumentação e Simulação Computacional LISCOMP – Instituto Federal do Rio de Janeiro.
*E-mail: dielbotao@gmail.com

Duplex stainless steels (DSS) are increasingly used in the oil and gas industries, as well as in the energy and chemical sectors, markets in which carbon steels and austenitic stainless steels have traditionally been the primary materials [1]. The main characteristic of DSS lies in its high corrosion resistance combined with high mechanical strength. These properties result from a combination of factors, such as the balance between the ferritic (~50%) and austenitic (~50%) phases in their microstructure, as well as the presence of alloying elements that increase resistance to pitting corrosion [2]. The ferritic phase exhibits higher mechanical strength, while the austenitic phase contributes to the material's toughness and weldability. The heat treatment of austenitic-ferritic steels still faces significant challenges, as it is necessary to maintain the balance between the phases and prevent the precipitation of deleterious phases, such as sigma (σ), chi (χ), alpha line (α'), and nitrides, which degrade mechanical properties and corrosion resistance [3]. In the specific case of autogenous TIG welding, the technological challenges are even more significant due to the tendency for high volumetric fractions of ferrite to form, as well as the potential formation of nitrides. In this context, several studies are investigating the development of new techniques, equipment, and process parameters that contribute to improved productivity and reduced costs. Among these approaches, the analysis of the influence of the chemical composition of the shielding gas during the welding of DSS steels stands out [4]. The influence of shielding gas composition on microstructural properties is widely addressed in the literature, with consistent results regarding both material quality and mechanical performance [5], [6]. In this regard, the present study evaluated the influence of adding helium to the shielding gas in autogenous TIG welding of UNS S32750 superduplex stainless steel. Samples using a commercial shielding gas composed of Ar + 2% N and an experimental shielding gas composed of Ar + 2% N + 30% He were used. Circumferential welds were performed using the automated TIG process at a current of 60 A and pulsed current with 30 Hz. For microstructural characterization, scanning electron microscopy (SEM) in backscattered electron (BSE) mode was employed. The ferrite and austenite phases, as well as the presence or absence of deleterious phases, were characterized using only polished samples. Chromium nitrides were observed after electrochemical attack using a 10% oxalic acid solution. The SEM images were taken using the mosaic feature, which automatically generates multiple images in a matrix format and then combines them into a single high-resolution image of the entire welded joint. Figures 1 and 2, show the welded joint without He and with 30% of He, respectively. Figures 1(a) and 2(a) were made without etching, and Figures 1(b) and 2(b) etching with 10% oxalic acid. In both welded joints, no deleterious phases were observed, neither in the fusion zone nor in the HAZ. The high-resolution mosaic enabled investigation of the entire HAZ, not just a small region, as is usually done in SEM images. The macro also allowed measuring the width and depth of the weld joint. The addition of He increased the width of the weld joint from 4.0 to 4.4 mm, while the depth remained unchanged at 1.2 mm. On the other hand, the He increases the amount of nitrides, as seen in Figure 1(b) and 2(b).

References

[1] M. A. Valiente Bermejo *et al.*, "Effect of shielding gas on welding performance and properties of duplex and superduplex stainless steel welds", *Weld. World*, v. 59, n. 2, p. 239–249, mar. 2015, doi: 10.1007/s40194-014-0199-7.

[2] P. Sathiya, S. Aravindan, R. Soundararajan, e A. Noorul Haq, "Effect of shielding gases on mechanical and metallurgical properties of duplex stainless-steel welds", *J. Mater. Sci.*, v. 44, n. 1, p. 114–121, jan. 2009, doi: 10.1007/s10853-008-3098-8.

[3] E. Akbarzadeh, K. Yurtışık, C. Hakan Gür, T. Saeid, e R. Tavangar, "Influence of Shielding Gas on the Microstructure and Mechanical Properties of Duplex Stainless Steel in Wire Arc Additive Manufacturing", *Met. Mater. Int.*, v. 30, n. 7, p. 1977–1996, jul. 2024, doi: 10.1007/s12540-023-01623-3.

[4] B. Mvola e P. Kah, "Effects of shielding gas control: welded joint properties in GMAW process optimization", *Int. J. Adv. Manuf. Technol.*, v. 88, n. 9, p. 2369–2387, fev. 2017, doi: 10.1007/s00170-016-8936-2.

[5] Y. Hu e J. Xue, "Effects of Flowrate of Additional Shielding Gas on the Properties of Welded Seam Using Twin-Wire GMAW Welding for Duplex Stainless Steel", *Metals*, v. 13, n. 7, p. 1224, jul. 2023, doi: 10.3390/met13071224.

[6] K. Wang, C. Shao, X. Jiao, J. Zhu, Z. Cai, e C. Li, "Investigation on Microstructure and Properties of Duplex Stainless Steel Welds by Underwater Laser Welding with Different Shielding Gas", *Materials*, v. 14, n. 17, p. 4774, jan. 2021, doi: 10.3390/ma14174774.

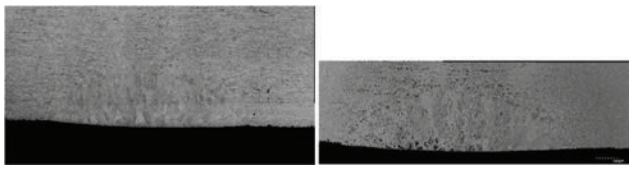


Figure 1. Sample without He in the shielding gas. (a) without etching; (b) etching with 10% oxalic acid.

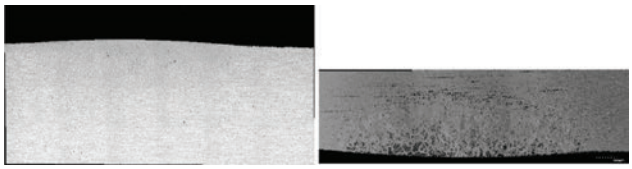


Figure 2. Sample with He in the shielding gas. (a) without etching; (b) etching with 10% oxalic acid.

ÍNDICE DE AUTORES

A

Abreu, Leandro de – 102
Afonso, Conrado Ramos de Moreira – 82
Afonso, Conrado Ramos Moreira – 273147
Afonso, Conrado R. M. – 383941434449537075 85 98
Afonso, C. R. M. – 64
Aguillera, Gabriel E. G. P. – 93
Akasaki, Jorge Luis – 89
Almeida, Gerson S. – 93
Almeida, Gerson Santos de – 101
Almeida, Juliana M. P. – 94
Almeida, Luiz Henrique de – 4055
Amigó-Borras, Vicente – 96
Antonialli, Armando Italo Sette – 30
Antunes, Débora R. – 60
Antunes, Débora Ribeiro – 37
Aquino, José M. – 86
Araujo, Leonardo Sales – 55
Araújo, Victor dos Santos Pena de – 79
Ataliba, Jonas Gabriel Ramos da Silva – 103
Aviles, David Jose – 26
Aviles, David Jose Barreto – 76

B

Bacalhau, José Britti – 4344
Baêta Junior, Eustáquio de Souza – 103
Barbieri, Renan – 23
Barbosa, Maciel – 42
Barud, Hernane – 42
Basaglia, Marcos V. – 67
Becker, Daniela – 78
Bedoch, Audrey Marie – 81
Bento, Gabriel Souza – 55
Berenguel, Otavio – 29
Béreš, Miloslav – 75
Bettini, Jefferson – 29
Bettini, Sílvia H. P. – 67
Bisatto, Rubens – 52
Biscalchim, Érica R. – 60
Biscalchim, Érica Rennó – 100
Bortolleto, Marcelo – 89
Botão, Camila Alves Pelicarto da Silva – 103
Botão, Diel Silva – 103
Botta, Walter J. – 62
Botta, Walter José – 61
Botta, W. J. – 50
Braga, Diogo Pedrino – 2526687680
Braghin, João G. M. – 86
Burke, Grace – 32

C

Caillier, Bruno Bruno – 42
Camargo, Gabriel M. de – 49
Cameirão, Ana Rodrigues – 94
Campestrini, Lucas – 78
Campos, José Brant de – 88
Canabarro, Beatriz Rodrigues – 90
Caram, Rubens – 66
Cardoso, Giovana Collombaro – 3196
Cardoso, Priscila Carvalho Borba – 88
Carvalho, Cássia C. De – 86
Carvalho, Leticia Pinheiro Muniz de – 90
Casarin, Bruno M. – 415385
Cavalcante, Luiz A. F. – 6097
Cavalcante, Luiz Aparecido Ferreira – 57
Collombaro, Giovanna Cardososo – 71
Connolly, Brian – 32
Cordeiro, Marco A. L. – 35
Correa, Diego Rafael Nespeque – 27317172737982 84
Corrêa, Diego Rafael Nespeque – 3669778399101
Correa, Diego R. N. – 70
Corrêa, Diego R. N. – 93

Costa, Carlos Alberto Rodrigues – 29
Coury, Francisco – 32
Coury, Francisco Gil – 34456591
Cruz, Sandra – 42

D

Dalmônico, Gisele M. – 52
Decol, Marindia – 78
Dias, Renan – 39
Dias, Renan A. F. – 384143445385
Diniz, Gustavo – 83
Diniz, Gustavo da Silva – 71
Duro, Lucas D. – 4153

E

Eduardo, Bernado P. – 87
Eduardo, Bernardo Pompermayer – 28
Elias, Vinicius Felippe – 45
Elias, Vinícius Felippe – 34
Ersen, Ovidiu – 52
Escuder, Angel Vicente – 96

F

Fabiano Filho, Marcelo – 74
Fagundes Jr, José Gedael – 4859
Farina, Marcos – 2452
Fernandes, João Paulo Cosas – 92
Fernandes, Paula – 42
Ferraz, Mariana de Brito – 61
Firmo, Letícia K. M. – 59
Fiuza, Tanna Elyn Rodrigues – 29
Folgueras, Marilena Valadares – 78
Fontes, Marina – 42
Forini, Mariana M. L. H. – 376097
Forini, Mariana Monteiro de Lima Honorato – 57100
França, Rodrigo de Oliveira – 2676
Freitas, Júlia R. de – 60
Freitas, Júlia Rodrigues de – 57

G

Gallego, Juno – 4859
Gonçalves, Raquel P. – 52
Gonçalves, Vinícius Richieri Manso – 27101
Gonçalves, Vinicius R. M. – 93
Gouveia, Guilherme. L. De – 86
Gouveia, Guilherme Lisboa de – 5163
Graceto, Augusto de Souza – 30
Grandini, Carlos R. – 7093
Grandini, Carlos Roberto – 273136697172737779
8283849699101
Grillo, Renato – 37576097100
Gualti, Stella Machado – 47

H

Hernandes, Antônio C. – 94
Herrmann, Paulo S. P. – 58
Heuser, Vinycius Tavares – 88
Hoeldtke, Adriane – 23

I

Ihiawakrim, Dris – 52

J

Janeček, Miloš – 66
Janes, Danilo Biazon – 29
Jardim, Paula M. – 87
Jardim, Paula Mendes – 2890
Junior, Amaro G. B. – 52

K

Kliauga, Andrea – 80
Kliauga, Andrea Madeira – 25
Kliauga. Andrea Madeira – 68
Koga, Guilherme Yuuki – 81
Kuroda, P. A. B. – 64
Kuroda, Pedro Akira Bazaglia – 3177

L

Lacerda, Frederico Garcia Bindi de – 103
Lages, Vanessa P. – 52
Laurentiz, Rosangela S. – 97
Leal, Jaderson Rodrigo da Silva – 51
Leão, L. A. R. – 64
Leite, Edson Roberto – 29
Lima, Victor Max Barros da Silva de – 40
Lima, Vilma – 24
Lisboa-Filho, Paulo Noronha – 101
Longuinho, Mariana M. – 52

Loureiro, Hugo C. – 102
Lourenço, João Vitor Garcia – 75
Lourenço, Mariana L. – 3885
Lourenço, Mariana Luna – 75
Lourenço, Mariana Luno – 73
Lourenço, M. L. – 64

M

Macêdo, João Vitor Barletta – 68
Macedo, Pedro Henrique Barletta – 76
Magalhães, Danielle C. C. – 98
Magalhães, Danielle Cristina Camilo – 2580
Magalhães. Danielle Cristina Camilo – 68
Malafaia, Artur Mariano de Sousa – 26
Malmonge, José Antonio – 89
Manchester, Tristan – 32
Manreza, Carlos Eduardo – 7384
Marques, Leandra – 344565
Martins, João Pedro Ferreira – 77
Mattos, Felype Narciso de – 77
Mattoso, Ney – 23
Mayer, Gabriela C. – 62
Mazzer, Eric – 91
Mazzer, Eric Marchezini – 34
Mazzer, Herique Marchezine – 45
Medeiros, Fernanda C. – 52
Melo, Bruna Sedaca Camargo de – 29
Mendonça, Rafaela de Souza – 100
Menezes, Carlos A. – 24
Mergulhão, Marina E. M. – 92
Miller, Raquel E. – 102
Minarik, Peter – 98
Montanari, Lucina – 25
Montoro, Fabiano Emmanuel – 29

N

Nogueira, Ana Flávia – 102
Nunes, Carlos A. – 39

O

Oliveira, Mair M. M. de – 24
Oliveira, Marcelo Falcão de – 26
Oliveira, Mila Christy de – 80
Oliveira, Pedro Henrique Fernandes – 68
Oliveira, Thiago Alves de – 69
O'Meany, Manuel Amado Rodas – 96
Otani, Lucas – 91
Ottani, Vinicius Cardoso – 4344

P

Paiva, Bruno da Silva de – 88
Paiva, Thaís Lima de – 90
Paodjuenas, Lucas H. M. – 3587
Passos, João Gabriel da Cruz – 2676
Patel, Jitendra – 4344
Pedroso, O. A. – 50
Pellegrino, Vinícius Melo – 83
Pereira, Mariana S. – 3949
Peripolli, Suzana Bottega – 88
Pimenta, André Rocha – 5488103
Pintão, Carlos Alberto Fonzar – 73
Plaine, A. – 64
Plaine, Athos H. – 95
Prado, Heloiza F. Alves do – 37
Prandi, Gilberto V. – 66

Q

Quadros, Fernanda de Freitas – 313699
Quadros, Fernanda F. – 93
Queiroz, Fabio dos Santos – 4055

R

Reyes, Rodrigo A. V. – 86
Rezende, Camila A. – 102
Ribeiro, Gabriela Bugni – 6591
Ribeiro, Rafaella Martins – 28
Riga-Rocha, Beatriz A. – 97
Riga-Rocha, Beatriz Aline – 100
Rôa, Gabriel Cardoso – 36
Rodrigues, João Felipe Q. – 66
Rodrigues, Taissa Zangerolami Lopes – 4055
Rolin, Vitor S. – 48
Rossi, André L. – 52
Rossi, Karina Nogueira Zambone Pinto – 47
Rossi, Mariana C. – 49
Rovere, Carlos A. D. – 86
Rovere, Carlos Alberto Della – 2676

S

Sakanaka, Lyssa S. – 58
Saldanha, Felipe Escher – 51
Sanches, Alex Otávio – 89
Sangali, Márcio – 66
Santana, Geovanne S. – 95
Santo, Giovanna – 85
Santo, Giovanna do Espirito – 47
Santo, Giovanna E. – 4153
Santoro, Patrícia H. – 58
Santos, Breno Rocha dos – 47

Santos, Daniel G. S. dos – 434498
Santos, Jean Carlos dos – 76
Santos, Jean Pierre dos – 24
Santos, Rafael Formenton Macedo dos – 7982
Santos, R. F. M. dos – 64
Serbena, José Pedro Mansueto – 23
Serrão, Fernanda T. L. – 35
Shiki, Sidney Bruce – 30
Silva, Bismarck L. – 86
Silva, Carlos Eduardo da – 2769101
Silva, Cleiton C. – 20
Silva, Denize Maria S. e – 98
Silva, Elvis Soares da – 30
Silva, Iasmin Maciel Vieira da – 54
Silva, Isabela Maria da – 39
Silva, Leandro S. – 66
Silva, Lorena Maria da – 3445
Silva, Luccas Nunes Caetano da – 72
Silva, Matheus Henry da – 98
Silva, Rene A. N. – 102
Silva, Thiago Carvalho da – 80
Silveira, Rebecca Mederos da – 40
Simioli, Carolina de Siqueira – 63
Soares, Carolina – 26
Solorzano, Guillermo – 32
Sousa, Raul E. de – 95
Souza, Elton Jose de – 89
Souza, Samuel Lima de – 74
Spadotto, Julio – 32
Spinelli, José Eduardo – 51566386
Staffa, Lucas H. – 67
Staffa, Lucas Henrique – 92
Starck, Leticia F. – 66
Stráský, Josef – 66

T

Tavares, Leonardo Martins – 76
Taverna, María E. – 97
Teixeira, Guilherme Araújo – 46
Teixeira, Rodolfo da Silva – 66
Torrento, Jhuliene Elen Muro – 72
Torrento, Jhuliene E. M. – 70
Toschi, Vitor Meirelles Santos – 84
Tsipas, Sophia Alexandra – 101

V

Vacchi, Guilherme dos Santos – 2676
Valentim, Matheus – 66
Ventrella, Vicente A. – 4859
Ventura, Carlos Eiji Hirata – 30
Verruma-Bernardi, Marta R. – 58

W

Werckmann, Jacques G. J. – 52
Wolf, Witor – 4674

X

Xavier, Marcella Gautê Cavalcante – 56
Xavier, Vinicius P. M. – 58

Y

Yamautti, Lavínia Ayumi – 4344

Z

Zambuzzi, William Fernando – 101
Zambuzzi, Willian F. – 93
Zanchet, Daniela – 102
Zanotto, Edgar Dutra – 21
Zepon, G. – 50
Zepon, Guilherme – 61628194
Zlotea, Claudia – 61

REGISTRO FOTOGRÁFICO DO EVENTO









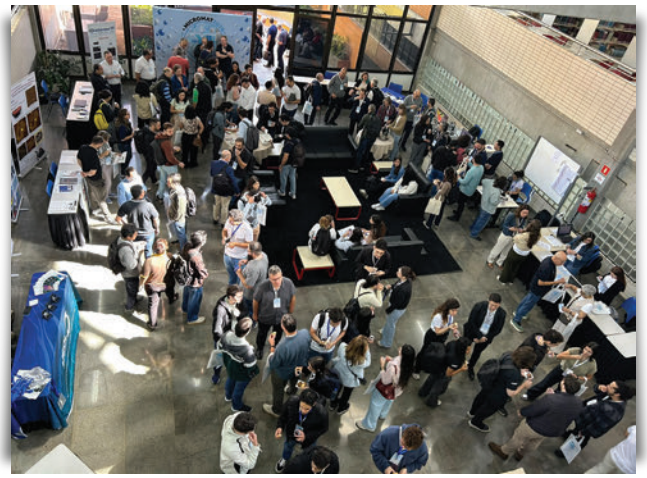





MICROMAT2026
MATERIAIS


MICROMAT2026


MICROMAT
CONGRESSO BRASILEIRO DE MICROSCOPIA DE MATERIAIS
DECTRIS
altmann
Tescan
FAPESP
SBMM
UFSCar
São Carlos - SP - UFSCar - 20 a de Julho / 2026






DECTRIS

Diamante:

JEOL

Ouro:

dp UNION

DECTRIS

ENABLING SCIENTIFIC BREAKTHROUGHS

Instrutécnica
instrumentação para pesquisa e indústria

altmann
altmann s.a. importação e comércio

Prata:

Tescan
Accelerating the Art of Discovery

Bronze:

3DLAB
INVIXITNE BY LAYER
LAYER BY LAYER

DSTL

Apoio Institucional:

DEMa
UFSCar

ppgcem
Programa de Pós-Graduação em Ciência e Engenharia de Materiais

UFSCar

Organização:

AGEVENTOS